

PHOTOINDUCED MAGNETISM IN NANOSTRUCTURES OF PRUSSIAN BLUE
ANALOGUES

By

DANIEL MATTHEW PAJEROWSKI

A DISSERTATION PRESENTED TO THE GRADUATE SCHOOL
OF THE UNIVERSITY OF FLORIDA IN PARTIAL FULFILLMENT
OF THE REQUIREMENTS FOR THE DEGREE OF
DOCTOR OF PHILOSOPHY

UNIVERSITY OF FLORIDA

2010

© 2010 Daniel Matthew Pajeroski

To all beef patties, special sauce, lettuce, cheese, pickles, onions on a sesame seed bun.

ACKNOWLEDGMENTS

My sincere thanks go out to those who helped me during the course of my PhD studies at the University of Florida. First, I would like to thank the talented chemists Dr. Franz A. Frye, Dr. Justin E. Gardner, Matthieu F. Dumont, and Matthew J. Andrus for generously providing valuable chemistry insights and samples. I appreciate the help afforded by my predecessor in Professor Meisel's lab, Dr. Ju-Hyun Park, as well as students in the neighboring low temperature labs, Dr. Byoung-Hee Moon and Dr. Pradeep Bhupathi from Professor Lee's lab, and Kyle Thompson from Professor Ihas' lab. I would like to thank cryogenic engineers Greg Labbe and John Graham for running the helium liquefier and providing time and plumbing for trouble-shooting cryogenic issues. Thanks also go out to electrical engineers Larry Phelps, Pete Axson, and Rob Hamersma of the UF Physics electronics shop for valuable insight, electronic components in a pinch and for fixing broken equipment. I would like to thank Brent Nelson and David Hansen from UF Physics Information Technology. I would like to thank Don Brennan, Tim Noland, and Jay Horton for help with technical issues in the New Physics Building and around lab B133. I would like to thank program assistants Dori Faust, Darlene Latimer, Kristin Nichola, Denise Carlton, and Carolyn Grider. I would like to thank Mark Link, Ed Storch, Bill Malphurs, and Mike Herlevich of the UF Physics instrument shop for incisive design critiques and superior craftsmanship when building custom apparatus. I would like to thank Ben Pletcher of the UF Major Analytical Instrumentation Center for the TEM images and EDS data. I would like to thank Professor Steve Hill, Dr. Andrew Ozarowski, and Dr. Saitti Datta of the NHMFL for help with the magnetic resonance studies. I would like to thank Dr. Steve Nagler, Dr. Jerel Zaretsky, Dr. V. Ovidiu Garlea, Dr. Lou Santodonato, Chris Redmon, and the

entire sample environment team of the ORNL for help with the neutron scattering experiments. I would like to thank the teachers of courses I took, as well as fellow students who were essential to the learning process. I would like to thank my thesis committee members, Professors Alan T. Dorsey, Hai-Ping Cheng, Yoonseok Lee, Daniel R. Talham and Mark W. Meisel. I would like to thank Professor Talham for his time and insight, specifically during Chem-Phys group meetings. Finally, I would like to thank Professor Mark W. Meisel for his advice and his dedication to providing me with research and learning opportunities.

This work was supported, in part, by the National Science Foundation (NSF) through DMR-0701400 and the NHMFL via cooperative agreement with NSF DMR-0654118 and the State of Florida. The research at Oak Ridge National Laboratory's High Flux Isotope Reactor was sponsored by the Scientific User Facilities Division, Office of Basic Energy Sciences, U. S. Department of Energy.

TABLE OF CONTENTS

	<u>page</u>
ACKNOWLEDGMENTS.....	4
LIST OF TABLES.....	11
LIST OF FIGURES.....	12
LIST OF ABBREVIATIONS.....	19
ABSTRACT.....	22
CHAPTER	
1 INTRODUCTION.....	24
1.1 Experimental Techniques.....	25
1.2 Theoretical Methods.....	26
1.3 Quantitative Analysis of Magnetization in Prussian Blue Analogues.....	27
1.4 Cobalt Hexacyanoferrate Nanoparticles.....	28
1.5 Thin Films of Prussian Blue Analogues.....	29
1.6 Heterostructures of Prussian Blue Analogues.....	30
2 EXPERIMENTAL TECHNIQUES.....	32
2.1 Sample Environment.....	33
2.1.1 Vacuum Equipment.....	33
2.1.1.1 Pumps.....	33
2.1.1.2 Pumping Lines.....	36
2.1.1.3 Vacuum Gauges.....	36
2.1.1.4 Oil Mist Filters and Fore-line Traps.....	36
2.1.1.5 O-rings.....	37
2.1.2 Cryostats.....	38
2.1.2.1 Bath Cryostats.....	38
2.1.2.2 Continuous Flow Cryostats and Cryogenic Inserts.....	38
2.1.2.3 Closed Cycle Refrigerators.....	39
2.1.3 Superconducting Magnets.....	39
2.1.3.1 Magnet Construction.....	40
2.1.3.2 Magnet Operation.....	Error! Bookmark not defined.
2.1.4 Light Guides.....	43
2.2 Detection Methods.....	43
2.2.1 SQUID magnetometer.....	43
2.2.1.1 Superconducting QUantum Interference Devices.....	43
2.2.1.2 Quantum Design MPMS XL Magnetometer.....	45
2.2.1.2 Remnant Fields and Degaussing the MPMS.....	47
2.2.2 Additional Methods Performed at UF.....	48

2.2.2.1	Atomic Force Microscopy	48
2.2.2.2	Carbon, Hydrogen and Nitrogen Combustion	49
2.2.2.3	Energy Dispersive X-Ray Spectroscopy	49
2.2.2.4	Fourier-Transform Infrared Spectroscopy	51
2.2.2.5	Inductively Coupled Mass Spectrometry	52
2.2.2.6	Transmission Electron Microscopy	53
2.2.2.7	Ultraviolet and Visible Spectroscopy	55
2.2.2.8	X-Ray Powder Diffraction	56
2.2.3	National Laboratories	57
2.2.3.1	Electron Magnetic Resonance at the NHMFL	57
2.2.3.2	HB1A Neutron Triple-Axis Spectrometer at HFIR	59
2.2.3.3	HB2A Neutron Powder Diffractometer at HFIR	61
2.2.3.4	Inelastic Neutron Scattering on SEQUOIA at SNS	62
2.3	Custom Apparatus	62
2.3.1	SQUID Probe with Low temperature Rotation and Optical Fibers	62
2.3.1.1	Probe Specifications and Design	63
2.3.1.2	Probe Material Properties	66
2.3.1.3	Operation	68
2.3.1.4	Conclusions	71
2.3.2	Neutron Scattering Probe for Photoinducing Opaque Powders	71
3	THEORETICAL METHODS	73
3.1	Quantum Mechanics of Transition Metal Ions	74
3.1.1	Coulomb Interaction and the Multi-Electron Ion	75
3.1.2	Ligand Field Theory	78
3.1.3	Spin-Orbit Coupling	82
3.1.4	Zeeman Splitting	84
3.1.5	Superexchange Interaction	85
3.1.6	Mean-Field Theory	86
3.2	Tight-Binding Approximations	88
3.2.1	Extended Hückel Theory	89
3.2.2	Ligand Field Theory	92
3.2.3	Superexchange Interaction	92
3.2.4	Infrared Vibrational Spectroscopy	92
3.3	Fitting Algorithms	93
3.3.1	Least Squares	93
3.3.2	Levenberg-Marquardt	95
3.3.3	Rietveld Refinement	96

4	QUANTITATIVE ANALYSIS OF MAGNETIZATION IN COMPLEX CYANIDES.....	99
4.1	Synthesis and Chemical Composition.....	100
4.2	Spectroscopy	100
4.3	Magnetic Susceptibility	102
4.4	Microscopic Probe of Magnetization	103
4.5	Fitting Magnetization.....	104
4.5.1	$K_3Cr(CN)_6$	105
4.5.2	$K_3Fe(CN)_6$	106
4.5.3	$Cs_{2.8}Ni_4[Cr(CN)_6]_4 \cdot nH_2O$	108
4.5.4	$Co_4[Fe(CN)_6]_3 \cdot nH_2O$	109
5	COBALT HEXACYANOFERRATE NANOPARTICLES	112
5.1	Nanoparticles of Rubidium Cobalt Hexacyanoferrate.....	115
5.1.1	Introduction.....	116
5.1.2	Synthesis and Chemical Composition	116
5.1.3	Structure.....	117
5.1.3.1	Transmission Electron Microscopy	117
5.1.3.2	Fourier Transform Infrared Spectroscopy	118
5.1.4	Magnetization	119
5.1.5.1	DC Susceptibility.....	120
5.1.5.2	DC Magnetization	122
5.1.5.3	AC Susceptibility.....	123
5.1.5	Discussion	124
5.1.6	Conclusions.....	127
5.2	Nanoparticles of Potassium Cobalt Hexacyanoferrate	128
5.2.1	Introduction.....	128
5.2.2	Synthesis and Chemical Composition	130
5.2.2.2	Fourier Transform Infrared Spectroscopy	130
5.2.3	Structure.....	132
5.2.3.1	Transmission Electron Microscopy	132
5.2.3.2	X-Ray Diffraction.....	133
5.2.3.3	Neutron Diffraction.....	135
5.2.4	Magnetization	140
5.2.4.1	Quenched High Temperature DC Susceptibility	141
5.2.4.2	Quenched Low Temperature DC Susceptibility	142
5.2.4.3	Quenched Low Temperature Magnetization.....	143
5.2.4.4	Isothermal Relaxation	144
5.2.4.5	Photoinduced Low Temperature DC Susceptibility.....	145
5.2.4.6	Photoinduced Low Temperature Magnetization	146
5.2.5	Discussion	147
5.2.5.1	Details of Modeling	147
5.2.5.1	Size Dependence of Thermal Quenching.....	150
5.2.5.2	Photoinduced versus Quenched States.....	151
5.2.5.3	Resulting Schema of Bulk and Nanoparticles.....	152
5.2.6	Conclusions.....	154

6	THIN FILMS OF PRUSSIAN BLUE ANALOGUES	155
6.1	Introduction	155
6.2	Rb _{0.7} Ni _{4.0} [Cr(CN) ₆] _{2.9} ·nH ₂ O Thin Films	158
6.2.1	Sample Characterization	158
6.2.1.1	Chemical Composition	158
6.2.1.2	AFM	159
6.2.1.3	FT-IR	159
6.2.1.4	UV-Vis	160
6.2.2	Magnetization	161
6.2.2.1	DC Susceptibility in 100 G	162
6.2.2.2	DC Magnetization in 40 kG	163
6.2.2.3	DC Magnetization Field Dependence	164
6.2.2.4	Magnetization Process	164
6.2.2.5	DC Magnetization Angular Dependence	166
6.2.3	Electron Magnetic Resonance	166
6.2.3.1	EMR Temperature Dependence	167
6.2.3.2	EMR Angular Dependence	174
6.2.3.3	EMR Frequency Dependence	177
6.2.4	X-ray Diffraction	178
6.3	Additional Prussian Blue Analogue Thin Films	178
6.3.1	Rb _{0.6} Co _{4.0} [Cr(CN) ₆] _{2.9} ·nH ₂ O Thin Films	179
6.3.2	Rb _{0.7} Cu _{4.0} [Cr(CN) ₆] _{2.9} ·nH ₂ O Thin Films	181
6.3.3	Rb _{0.3} Zn _{4.0} [Cr(CN) ₆] _{2.8} ·nH ₂ O Thin Films	184
6.3.4	Rb _{0.9} Ni _{4.0} [Fe(CN) ₆] _{2.8} ·nH ₂ O Thin Films	186
6.3.5	Rb _{0.7} Co _{4.0} [Fe(CN) ₆] _{2.8} ·nH ₂ O Thin Films	188
6.3.6	Rb _{0.5} Cu _{4.0} [Fe(CN) ₆] _{2.7} ·nH ₂ O Thin Films	189
6.3.7	Rb _{0.5} Zn _{4.0} [Fe(CN) ₆] _{2.8} ·nH ₂ O Thin Films	191
6.4	Discussion	191
6.4.1	Rb _{0.7} Ni _{4.0} [Cr(CN) ₆] _{2.9} ·nH ₂ O Thin Films	192
6.4.2	Additional Prussian Blue Analogue Thin Films	204
6.5	Conclusions	206
7	HETEROSTRUCTURES OF PRUSSIAN BLUE ANALOGUES	207
7.1	Solid Solutions of Cobalt Hexacyanoferrate	207
7.1.1	Introduction	207
7.1.2	Synthesis and Chemical Composition	211
7.1.3	Transmission Electron Microscopy	212
7.1.4	Infrared Spectroscopy	213
7.1.5	X-Ray Diffraction	216
7.1.6	Mean-Field Calculations	219
7.1.6.1	Low Temperature Magnetization in the Mean-Field	219
7.1.6.2	Mean-field Magnetic Susceptibility and Spin-Crossover	221
7.1.7	Magnetic Measurements	222
7.1.7.1	Low Temperature DC Susceptibility	223
7.1.7.2	DC Magnetization	226

7.1.7.3	High Temperature DC Susceptibility.....	228
7.1.7.4	Physically Mixed $x = 0.66$ compound.....	230
7.1.8	Discussion.....	232
7.1.8.1	Photoinduced Decrease in Magnetization.....	232
7.1.8.2	Scaling of Magnetic Properties.....	235
7.1.8.3	Spin-Crossover Dilution.....	238
7.1.8.4	Mean-Field Predictions versus Observations.....	242
7.1.9	Conclusions.....	244
7.2	Heterostructured Films Containing Cobalt Hexacyanoferrate.....	245
7.2.1	Introduction.....	245
7.2.2	Synthesis.....	247
7.2.3	Magnetization of Nickel Hexacyanochromate and Cobalt Hexacyanoferrate Heterostructures.....	248
7.2.3.1	Slow Deposition Multilayer Films.....	248
7.2.3.2	Stacked Films.....	250
7.2.3.3	Thin Sandwiched Films.....	253
7.2.3.4	Thick Sandwiched Films.....	257
7.2.4	40/40/40 Heterostructure.....	260
7.2.4.1	40/40/40 film, 10 kG Temperature Sweeps.....	262
7.2.4.2	40/40/40 film, Transmission Electron Microscopy.....	263
7.2.4.3	40/40/40 film, Energy Dispersive X-ray Spectroscopy.....	264
7.2.4.4	40/40/40 film, X-ray Powder Diffraction.....	265
7.2.4.5	40/40/40 film, Infrared Spectroscopy.....	266
7.2.5	Capping Layers of Cobalt and Chromium Hexacyanochromates.....	267
7.2.5.1	Magnetization of Cobalt Hexacyanochromate and Cobalt Hexacyanoferrate Sandwich Heterostructures.....	267
7.2.5.2	Magnetization of Chromium Hexacyanochromate and Cobalt Hexacyanoferrate Sandwich Heterostructures.....	268
7.2.6	Discussion.....	269
7.2.7	Conclusion.....	275
8	SUMMARY AND CONCLUSIONS.....	276
APPENDIX		
A	UNITS.....	281
B	LOW TEMPERATURE ROTATION PROBE DRAWINGS.....	282
C	COPYRIGHT RELEASE FORMS.....	297
LIST OF REFERENCES.....		
		306
BIOGRAPHICAL SKETCH.....		
		316

LIST OF TABLES

<u>Table</u>	<u>page</u>
2-1	Magnetic response of candidate probe materials for optical rotator magnetization probe 67
4-1	Parameters to be used in modeling magnetization data for $\text{Cs}_{2.8}\text{Ni}_4[\text{Cr}(\text{CN})_6]_4n\text{H}_2\text{O}$, $\text{Co}_4[\text{Fe}(\text{CN})_6]_3n\text{H}_2\text{O}$, $\text{K}_3\text{Cr}(\text{CN})_6$, and $\text{K}_3\text{Fe}(\text{CN})_6$ 104
5-1	Synthesis and chemical composition of rubidium cobalt hexacyanoferrate nanoparticles. 117
5-2	Magnetic properties of rubidium cobalt hexacyanoferrate nanoparticles..... 125
5-3	The microscopic states relevant to $\text{K}_j\text{Co}_k[\text{Fe}(\text{CN})_6]_l \cdot n\text{H}_2\text{O}$ 129
5-4	The macroscopic states relevant to $\text{K}_j\text{Co}_k[\text{Fe}(\text{CN})_6]_l \cdot n\text{H}_2\text{O}$ 129
5-5	Metal oxidation states of bulk powder and nanoparticles, in addition to fitting parameters used for 131
5-6	Chemical composition and characteristic sizes of potassium cobalt hexacyanoferrate nanoparticles and bulk powder 132
5-7	Magnetic properties of quenched potassium cobalt hexacyanoferrate nanoparticles and bulk powder 151
5-8	Magnetic properties of photoinduced potassium cobalt hexacyanoferrate nanoparticles and bulk powder 152
6-1	Molecular formulas of films measured and techniques used 179
7-1	Molecular formulas and unit cell parameters for $\text{Na}_\alpha\text{Co}_x\text{Ni}_{1-x}[\text{Fe}(\text{CN})_6]_\beta \cdot n\text{H}_2\text{O}$. 212
7-2	Nickel hexacyanochromate and cobalt hexacyanoferrate heterostructures studied..... 248

LIST OF FIGURES

<u>Figure</u>		<u>page</u>
1-1	Illustration of constrained geometries in nanostructures.....	29
1-2	Illustration of designer heterogeneous geometries in nanostructures.....	31
2-1	Illustrations showing operation of standard pumps that can be found in a cryogenic laboratory	35
2-2	Illustration of a superconducting solenoid magnet.....	41
2-3	Illustration of a SQUID magnetometer circuit	45
2-4	Illustration of SQUID magnetometer pickup coils	46
2-5	Remnant fields and degaussing the MPMS.....	47
2-6	AFM schematic.....	48
2-7	A schematic of a combustion train for CHN analysis	49
2-8	EDS schematic.....	50
2-9	FT-IR schematic.....	52
2-10	ICP-MS schematic.....	53
2-11	TEM schematic.....	54
2-12	UV-Vis spectrometer schematic	55
2-13	XRD schematic.....	56
2-14	Theoretical EMR schematic.....	58
2-15	Experimental EMR schematic.....	59
2-16	The triple-axis spectrometer at HFIR on beamline HB1A	60
2-17	The neutron powder diffractometer at HFIR on beamline HB2A.....	61
2-18	The SEQUOIA inelastic time-of-flight spectrometer at SNS	62
2-19	Photographs of the optical rotation probe for use in a SQUID magnetometer....	64
2-20	Magnetization versus field for potential optical rotation probe materials.....	67

2-21	A circuit diagram of the control board for the automated operation of the custom probe using a stepper motor	70
2-22	Magnetization versus rotation angle measured with the custom probe for two different magnetite samples at 300 K (a) and 2 K (b)	70
2-23	Photoirradiation of powdered neutron scattering samples.....	72
2-24	Photoirradiation of powdered neutron scattering samples using tumbler probe .	72
3-1	The energy differences between different d^5 Fe^{3+} free-ion terms arising from electron-electron repulsion as a function of the Racah repulsion parameter B...	78
3-2	The octahedral coordination geometry	79
3-3	The energy of a molecular term as a function of the octahedral splitting parameter, Δ , for a d^5 ion, such as Fe^{3+}	81
3-4	Energy shift plotted versus the tetragonal distortion parameter, δ	82
3-5	Energy splitting of the octahedral hexacyanoferrate $^2T_{2g}$ ground state.....	84
3-6	The Zeeman splitting versus applied magnetic field for the spin-orbit split $^2T_{2g}$ -like ground state of hexacyanoferrate	85
3-7	The effect of superexchange on magnetization	88
3-8	The cyanide molecule.....	91
4-1	The cubic complex cyanide Prussian blue analogue structure	101
4-2	UV-Vis of $Rb_{0.7}Ni_{4.0}[Cr(CN)_6]_{2.9}\cdot nH_2O$	102
4-3	Measurement of magnetic ordering temperature in $Cs_{2.8}Ni_4[Cr(CN)_6]_4\cdot nH_2O$, $Co_4[Fe(CN)_6]_3\cdot nH_2O$, $K_3Cr(CN)_6$, and $K_3Fe(CN)_6$	103
4-4	Magnetic properties of $K_3Cr(CN)_6$	106
4-5	Magnetic properties of $K_3Fe(CN)_6$	108
4-6	Magnetic properties of $Cs_{2.8}Ni_4[Cr(CN)_6]_4\cdot nH_2O$	109
4-7	Magnetic properties of $Co_4[Fe(CN)_6]_3\cdot nH_2O$	110
5-1	Prussian blue analogue structure	113
5-2	A detail of the photoexcitation processes in $K_{0.2}Co_{1.4}[Fe(CN)_6]\cdot 6.9H_2O$	114
5-3	TEM of $Rb_jCo_k[Fe(CN)_6]_l\cdot nH_2O$ nanoparticles.....	118

5-4	FT-IR absorption spectra of $\text{Rb}_j\text{Co}_k[\text{Fe}(\text{CN})_6]_l \cdot n\text{H}_2\text{O}$ nanoparticles.....	119
5-5	The temperature dependences of the low field, 100 G, susceptibilities of $\text{Rb}_j\text{Co}_k[\text{Fe}(\text{CN})_6]_l \cdot n\text{H}_2\text{O}$ nanoparticles	121
5-6	The $T = 2$ K magnetization versus magnetic field sweeps of $\text{Rb}_j\text{Co}_k[\text{Fe}(\text{CN})_6]_l \cdot n\text{H}_2\text{O}$ nanoparticles	122
5-7	The temperature dependences of the real (χ') and imaginary (χ'') ac susceptibilities of $\text{Rb}_j\text{Co}_k[\text{Fe}(\text{CN})_6]_l \cdot n\text{H}_2\text{O}$ nanoparticles	123
5-8	Ordered magnetic components of the smaller batches	126
5-9	FT-IR spectra of bulk and nanoparticles of K-Co-Fe	131
5-10	TEM of K-Co-Fe	133
5-11	XRD of K-Co-Fe	135
5-12	Neutron scattering of K-Co-Fe.....	136
5-13	Neutron diffraction as a function of temperature for K-Co-Fe.....	138
5-14	Magnetic neutron scattering in K-Co-Fe.....	139
5-15	Temperature dependent magnetic moment of quenched states for K-Co-Fe... ..	141
5-16	Magnetic ordering of quenched states in K-Co-Fe	142
5-17	Magnetization versus field of quenched states for K-Co-Fe	143
5-18	Relaxation of magnetization in quenched states of K-Co-Fe.....	144
5-19	Magnetic ordering of photoinduced states in K-Co-Fe.....	145
5-20	Magnetization versus field of photoinduced states for K-Co-Fe	146
5-21	Linearization of modeling K-Co-Fe	148
5-22	Ordering temperatures and coercive fields of batches in different macroscopic statesercivities for the nanoparticles, as well as an increase in the coercivity of the P state as compared to the Q state	153
5-23	Microscopic schema based upon all data.....	153
6-1	Prussian blue analogue structure	155
6-2	The multiple sequential adsorption method that can be used for generating thin films of Prussian blue analogues	156

6-3	Different orientations of the magnetic thin films with respect to the applied magnetic field are expected to have different behavior	157
6-4	AFM of thin films.....	159
6-5	Room temperature FT-IR spectroscopy measurements of the cyanide stretches present in Ni-Cr materials	160
6-6	UV-Vis spectroscopy of Ni-Cr materials	161
6-7	Temperature dependent magnetization of Ni-Cr materials	162
6-8	Temperature dependent magnetization of Ni-Cr materials at high fields	163
6-9	Field dependent magnetization of Ni-Cr materials.....	164
6-10	Magnetizing process of thin Ni-Cr film	165
6-11	Magnetizing process of thick Ni-Cr film	165
6-12	Magnetizing process of Ni-Cr powder.....	165
6-13	Angle dependence of magnetization in Ni-Cr materials.....	166
6-14	EMR lines of Ni-Cr powder	169
6-15	Results of fitting EMR lines of Ni-Cr powder.....	169
6-16	EMR lines of Ni-Cr thin film perpendicular	170
6-17	Results of fitting EMR lines of Ni-Cr thin film perpendicular	170
6-18	EMR lines of Ni-Cr thin film parallel	171
6-19	Results of fitting EMR lines of Ni-Cr thin film parallel.....	171
6-20	EMR lines of Ni-Cr thick film perpendicular	172
6-21	Results of fitting EMR lines of Ni-Cr thick film perpendicular	172
6-22	EMR lines of Ni-Cr thick film parallel	173
6-23	Results of fitting EMR lines of Ni-Cr thick film parallel	173
6-24	EMR lines of Ni-Cr thin film as a function of angle.....	175
6-25	Results of fitting EMR lines of Ni-Cr thin film as a function of angle	175
6-26	EMR lines of Ni-Cr thick film as a function of angle	176

6-27	Results of fitting EMR lines of Ni-Cr thick film as a function of angle.....	176
6-28	EMR lines of Ni-Cr thick film as a function of angle in lower field	177
6-29	Results of fitting EMR lines of Ni-Cr thick film as a function of angle in lower field.....	178
6-30	Ligand field levels of Co-Cr.....	180
6-31	Magnetic susceptibility of Co-Cr thin film.....	181
6-32	Ligand field energies of Cu-Cr	182
6-33	Magnetic susceptibility of Cu-Cr thin film	183
6-34	UV-Vis of Cu-Cr thin film	184
6-35	Ligand field energies of Zn-Cr	185
6-36	Magnetization of Zn-Cr versus field	186
6-37	Ligand field energies of Ni-Fe.....	187
6-38	Magnetic susceptibility of Ni-Fe thin films.....	188
6-39	Ligand field energy levels and rotational magnetism of Co-Fe	189
6-40	Ligand field energies of Cu-Fe.....	190
6-41	Magnetic susceptibility of Cu-Fe thin films.....	191
6-42	Demagnetizing fields in films magnetized perpendicular to surface normal.....	195
6-43	Demagnetizing fields in films magnetized parallel to surface normal.....	195
6-44	Fitting Magnetization of Ni-Cr films in low field	197
6-45	Fitting Magnetization of Ni-Cr films in high field.....	198
6-46	Thickness dependence of thin films.....	199
6-47	EMR lines of Ni-Cr thin films and powder	203
7-1	The $\text{Na}_\alpha\text{Ni}_{1-x}\text{Co}_x[\text{Fe}(\text{CN})_6]_\beta \cdot n\text{H}_2\text{O}$ material	210
7-2	Typical TEM micrographs for samples reported in Table 7-1 for different values of x	213

7-3	FT-IR spectra and fitting parameters of $\text{Na}_\alpha\text{Ni}_{1-x}\text{Co}_x[\text{Fe}(\text{CN})_6]_\beta \cdot n\text{H}_2\text{O}$ as a function of x	215
7-4	Full XRD diffractograms of $\text{Na}_\alpha\text{Ni}_{1-x}\text{Co}_x[\text{Fe}(\text{CN})_6]_\beta \cdot n\text{H}_2\text{O}$	217
7-5	XRD of the $x = 1$ $\text{Na}_\alpha\text{Ni}_{1-x}\text{Co}_x[\text{Fe}(\text{CN})_6]_\beta \cdot n\text{H}_2\text{O}$	218
7-6	Room temperature XRD reflection with background subtracted and intensity normalized to show the continuous evolution with x	218
7-7	Photoinduced magnetization of $\text{Na}_\alpha\text{Ni}_{1-x}\text{Co}_x[\text{Fe}(\text{CN})_6]_\beta \cdot n\text{H}_2\text{O}$	225
7-8	Molar magnetic susceptibility of $\text{Na}_\alpha\text{Ni}_{1-x}\text{Co}_x[\text{Fe}(\text{CN})_6]_\beta \cdot n\text{H}_2\text{O}$ as a function of time irradiated at 5 K and 10 G, measured in a SQUID.....	226
7-9	Checking for asymmetry in the hysteresis loop as a possible explanation of the reduction in H_C for the $x = 0.66$ sample	228
7-10	Magnetization versus field for $\text{Na}_\alpha\text{Ni}_{1-x}\text{Co}_x[\text{Fe}(\text{CN})_6]_\beta \cdot n\text{H}_2\text{O}$	227
7-11	Thermal induced changes in magnetization of $\text{Na}_\alpha\text{Ni}_{1-x}\text{Co}_x[\text{Fe}(\text{CN})_6]_\beta \cdot n\text{H}_2\text{O}$	229
7-12	Microscopic versus macroscopic mixing.....	231
7-13	Magnetization of macroscopically mixed $\text{Na}_\alpha\text{Ni}_{1-x}\text{Co}_x[\text{Fe}(\text{CN})_6]_\beta \cdot n\text{H}_2\text{O}$	231
7-14	Field dependence of photoinduced magnetization for $\text{Na}_\alpha\text{Ni}_{1-x}\text{Co}_x[\text{Fe}(\text{CN})_6]_\beta \cdot n\text{H}_2\text{O}$	234
7-15	Scaling of magnetic properties of $\text{Na}_\alpha\text{Ni}_{1-x}\text{Co}_x[\text{Fe}(\text{CN})_6]_\beta \cdot n\text{H}_2\text{O}$	235
7-16	Superexchange in $\text{Na}_\alpha\text{Ni}_{1-x}\text{Co}_x[\text{Fe}(\text{CN})_6]_\beta \cdot n\text{H}_2\text{O}$	237
7-17	Charge transfer induced spin transition parameters for $\text{Na}_\alpha\text{Ni}_{1-x}\text{Co}_x[\text{Fe}(\text{CN})_6]_\beta \cdot n\text{H}_2\text{O}$	239
7-18	Amount of CTIST materials in $\text{Na}_\alpha\text{Ni}_{1-x}\text{Co}_x[\text{Fe}(\text{CN})_6]_\beta \cdot n\text{H}_2\text{O}$	240
7-19	FT-IR parameters in $\text{Na}_\alpha\text{Ni}_{1-x}\text{Co}_x[\text{Fe}(\text{CN})_6]_\beta \cdot n\text{H}_2\text{O}$	241
7-20	Comparison of ferromagnetic versus antiferromagnetic Co-Fe components....	243
7-21	Modification of superexchange energy in $\text{Na}_\alpha\text{Ni}_{1-x}\text{Co}_x[\text{Fe}(\text{CN})_6]_\beta \cdot n\text{H}_2\text{O}$	244
7-22	A scheme showing synthesis of a heterostructured thin film using multiple sequential adsorption cycles.	246
7-23	Magnetization of slow deposition multilayer films	249

7-24	Magnetization of 10/10 Co-Fe/Ni-Cr thin film oriented parallel.	251
7-25	Magnetization of 10/10 Co-Fe/Ni-Cr thin film oriented perpendicular.	251
7-26	Magnetization of 10/10 Ni-Cr/Co-Fe thin film oriented parallel	252
7-27	Magnetization of 10/10 Ni-Cr/Co-Fe thin film oriented perpendicular	252
7-28	Magnetization of 10/5/10 Ni-Cr/Co-Fe/Ni-Cr thin film oriented parallel.....	254
7-29	Magnetization of 10/5/10 Ni-Cr/Co-Fe/Ni-Cr thin film oriented perpendicular...	254
7-30	Magnetization of 10/10/10 sandwich film versus temperature.	255
7-31	Photoinduced magnetization of 10/10/10 film oriented perpendicular	256
7-32	Photoinduced magnetization of 10/10/10 film oriented perpendicular	256
7-33	Magnetization of 40/40/40 Ni-Cr/Co-Fe/Ni-Cr heterostructure.....	258
7-34	Magnetization of 20/40/20 Ni-Cr/Co-Fe/Ni-Cr heterostructure.....	259
7-35	Magnetization of 40/20/40 Ni-Cr/Co-Fe/Ni-Cr heterostructure.....	260
7-36	Magnetization data of the 40/40/40 sandwich Ni-Cr/Co-Fe/Ni-Cr PBA film	261
7-37	10 kG temperature sweeps of 40/40/40 Ni-Cr/Co-Fe/Ni-Cr	262
7-38	Transmission electron microscopy of the 40/40/40 Ni-Cr/Co-Fe/Ni-Cr heterostructure..	263
7-39	An energy dispersive x-ray line scan of the 40/40/40 heterostructure	264
7-40	X-ray powder diffraction of a 40/40/40 heterostructure.....	265
7-41	Cyanide stretching energies in the infrared	266
7-42	Magnetization data of Co-Cr/Co-Fe/Co-Cr heterostructures	268
7-43	Magnetization data of Cr-Cr/Co-Fe/Cr-Cr heterostructures	269
7-44	Photoexcitation of Co-Fe	271
7-45	Distortions in Ni-Cr	272
7-46	Anisotropy in Ni-Cr	274

LIST OF ABBREVIATIONS

A	Alkali cation
AC	alternating current
AFM	Atomic force microscopy
AQ	Aqueous solution
B	Magnetic field
CHN	Carbon hydrogen nitrogen
CLB	Chemistry Lab Building
CN	Cyanide
CTIST	Charge transfer induced spin transition
DC	Direct current
EDS	Energy dispersive spectroscopy
EMF	Electromagnetic field
emu	Electromagnetic unit
EMR	Electron magnetic resonance
EXAFS	Extended x-ray fine structure
FC	Field cooled
FCC	Face centered cubic
FT-IR	Fourier transform infrared
FWHM	Full-width-half-maximum
G	Gauss
<i>H</i>	Magnetizing field
HB	HFIR Beamline
H _c	Coercive field
HFIR	High Flux Isotope Reactor

HS	High spin
HT	High temperature
ICP-MS	Inductively coupled mass spectrometry
K	Kelvin
lb	Pound
LCAO	Linear combination of atomic orbitals
LS	Low spin
LT	Low temperature
m	meter
M	Transition metal
M'	Transition metal
MAIC	Major Analytical Instrumentation Center
MPMS	Magnetic Properties Measurement System
NHMFL	National High Magnetic Field Laboratory
NMR	Nuclear magnetic resonance
NPB	New Physics Building
OD	Outer diameter
ORNL	Oakridge National Laboratory
Pa	Pascale
PBA	Prussian blue analog
PVP	Polyvinylpyrrolidone
RMS	Root mean squared
S	Spin quantum number
SCO	Spin crossover
SEM	Scanning electron microscopy

SEQUOIA	an inelastic diffractometer at SNS, after the Native American chief
SNS	Spallation Neutron Source
SQUID	Superconducting quantum interference device
T	Tesla or Temperature (depending upon context)
T_C	Magnetic ordering temperature
T_{CTIST}	Temperature around which the thermal spin crossover centers, $(T_{up}+T_{down})/2$
T_f	Freezing temperature associated with spin-glass materials
T_{up}	Temperature at which half of the spin crossover material has transitioned in the heating cycle
T_{down}	Temperature at which half of the spin crossover material has transitioned in the cooling cycle
TEM	Transmission electron microscopy
UF	University of Florida
UV-Vis	Ultraviolet and Visible (spectroscopy)
XRD	X-ray diffraction
ZFC	Zero field cooled
χ	Magnetic susceptibility
XRD	X-ray diffraction

Abstract of Dissertation Presented to the Graduate School
of the University of Florida in Partial Fulfillment of the
Requirements for the Degree of Doctor of Philosophy

PHOTOINDUCED MAGNETISM IN NANOSTRUCTURES OF PRUSSIAN BLUE
ANALOGUES

By

Daniel Matthew Pajerowski

August 2010

Chair: Mark W. Meisel

Major: Physics

A wide range of experimental and theoretical investigations have been made on nanostructures of Prussian blue analogues, and a variety of results have been obtained. Most notably, a novel photoeffect has been observed in $\text{Rb}_j\text{Co}_k[\text{Fe}(\text{CN})_6]_l \cdot n\text{H}_2\text{O}$ / $\text{Rb}_j\text{Ni}_k[\text{Cr}(\text{CN})_6]_l \cdot n\text{H}_2\text{O}$ Prussian blue analogue heterostructured films, and this effect persists up to ~ 75 K, which is an unprecedented high temperature for photocontrol in this class of compounds. This engineering of the high- T_C heterostructures was made possible by insight gained from studying other nanostructured Prussian blue analogues. Specifically, solid solutions of $\text{Na}_\alpha\text{Ni}_{1-x}\text{Co}_x[\text{Fe}(\text{CN})_6]_\beta \cdot n\text{H}_2\text{O}$ proved that the sign and the magnitude of photoinduced magnetization can be tuned with chemical formula. In addition, these solid solutions elucidated the effect that diluting the lattice has on the magnetic properties of the photomagnet. By studying nanoparticles of $\text{Rb}_j\text{Co}_k[\text{Fe}(\text{CN})_6]_l \cdot n\text{H}_2\text{O}$, a size-dependent scaling of magnetic ordering temperatures and coercive fields was established, with “bulk” long-range magnetic order occurring in particles larger than ~ 25 nm. In parallel work, nanoparticles of $\text{K}_j\text{Co}_k[\text{Fe}(\text{CN})_6]_l \cdot n\text{H}_2\text{O}$ showed a reduction in bistable material with decreasing particle size. The magnetic anisotropy of sequential adsorption Prussian blue analogue films proved to be

complicated, and required a plethora of probes to tease out the inherent properties. Many analogues were studied, and magnetostatic, g-factor, and magnetocrystalline effects were identified in different samples, depending upon the magnetic ions. In addition to a discussion about characterization of these nanostructured Prussian blue analogues, a review of the relevant theoretical and experimental techniques is presented. For example, the design and implementation of a custom magnetometer probe with fiber optics and automatic sample rotation is noteworthy and is discussed. Furthermore, the design of a custom optic probe for use with photoinducible opaque powders in neutron scattering experiments is included. Theoretical tools and numerical investigations that were employed to understand the experimental results are overviewed, with specific attention given to properly parameterizing the photoinduced systems. Detailed models of Prussian blue analogue materials are presented. Specific examples showing the potential ambiguity of assigning superexchange constants based on magnetization in the presence of first order orbital angular momentum are also discussed, and one example is the photomagnetic $\text{Rb}_j\text{Co}_k[\text{Fe}(\text{CN})_6]_l n\text{H}_2\text{O}$. Finally, experimental techniques, which include AFM, CHN, EDS, EMR, FT-IR, ICP-MS, neutron scattering, SQUID magnetometry, TEM, UV-Vis spectroscopy, and XRD, are reviewed for the purpose of understanding the data presented.

CHAPTER 1 INTRODUCTION

To begin, magnetism is central to all discussion in this thesis. From a purely scientific standpoint, magnetism fascinates because it is an inescapable manifestation of quantum mechanics. Among fundamental physical concepts, magnetism is of particular importance technologically, most especially for the storage of information in memory devices. Modern memory storage is done with oxides or alloys that require high temperatures for synthesis, and memory is written using other magnetic materials. Currently, potential alternative materials are being investigated with much vigor, with the hopes of either having similar performance using cheaper manufacturing than industry standards or improved performance with limited increase in expense. Of the many alternative possibilities, molecule based complex cyanides are the focus of this work. Compared to metallurgical synthesis, the room temperature and pressure wet chemistry required for complex cyanides is cheap and user-friendly. In addition, while standard methods may be used to write to these materials, the magnetization of the complex cyanides can also be changed by the application of external light, heat, and pressure [1-2]. Possible benefits of the complex cyanides include potentially storing bits in individual nanometer sized molecules, as well as the fast, three dimensional write ability that would be awarded by using photons, instead of magnetic field induced torque, to write. The problem can then be stated as the search to understand the magnetization of the complex cyanides and to see how practical the goals of an optically controlled cyanometallate memory storage device may be.

More specifically for this dissertation, the main thrust of the research has been studying the effects of incorporation of complex cyanides into nanostructures. The

nanostructures studied include nanoparticles, thin films, and heterostructures of thin films, along with atomically mixed solid solutions of bulk materials. Novel photomagnetic effects of the nanostructures and phenomena related to the effects will be discussed in detail in the main chapters of the thesis.

On a practical note, this thesis is written at a level so as to be accessible to someone with an undergraduate education in a physical science, with the possible need for additional reading to understand the details of certain subsections. No details will be given on the experimental and theoretical topics covered in typical curricula, and the interested reader is directed to standard texts on the subjects [3-4]. In addition, the units will generally be c.g.s., except in cases where precedent dictates otherwise for ease of comparison. When plotting magnetic fields, μ_0 will be suppressed for readability.

The structure of the dissertation is such that Chapters 2 and 3 provide specific, pertinent background information that may be helpful to fully understand the new measurements and materials that are presented in Chapters 5, 6, and 7. Chapter 4 is somewhat between the experimental chapters and the background chapters, as it illustrates essential concepts and treats data already present in the literature to a quantitative analysis based upon tools outlined in the background sections.

1.1 Experimental Techniques

Experimental methods are presented in Chapter 2. While DC magnetization measurements make up the majority of data presented in this thesis, complementary techniques are essential to achieve in depth understanding of magnetization results. In the modern world, many apparatus for probing solids have been honed to a high level of

sophistication, and an adequately educated scientist can either participate in collaborations or simply step in as a guest to use the desired equipment. Therefore, part of the experimental methods chapter consists of an encyclopedia of the experimental procedures utilized. As external lab facilities with well supported user programs were essential to some investigations, including national laboratories and other labs at the University of Florida, capabilities as well as the locations of the equipment have been documented. Furthermore, more substantial space is allotted for procedures where the author has made significant contributions. In particular, an artisanal rotation probe to study the angular dependence of magnetization in thin films is detailed. Also, as photoinduced magnetization has been one of the most exciting topics studied, advancements on magnetization optic probes and neutron scattering optic probes are also presented.

1.2 Theoretical Methods

Physics is an experimental science. On the other hand, theoretical work is essential for potential predictive power and insight into experimental results. What can provide greater joy than finding the additional term necessary to not only accurately fit a puzzling data set but to actually open up a whole new avenue of experiments? While complicated first principles theories can dazzle with their power, well parameterized Hamiltonians tractable to the average physicist are light and elegant at their best (but misleading and confusing at their worst). In Chapter 3, starting with a bare atom, the relevant interactions will be introduced using the magnetically ubiquitous iron as a bellwether. In vacuum, the first-order energy of an atom is determined by electron-electron Coulomb repulsion and the Pauli exclusion principle. Additional corrections, such as relativistic effects and spin-orbit coupling can provide additional

structure to the energy spectrum. Next, if a molecule forms with a single magnetic ion, the bare ionic energies will be affected by the presence of the additional non-magnetic atoms, the so-called ligands. Dubbed ligand field theory, the changes in the electronic energy levels of the ions in the molecule have been found to be caused by both electrostatic and covalent interactions [5]. The situation becomes increasingly complex as more magnetic ions are introduced to molecules and allowed to interact with one another. Magnetic interactions, mediated through the non-magnetic ligands in a coordination network, further perturb the energy levels and can even lead to macroscopic correlation of magnetic moments throughout a compound. This long-range magnetic order can have many exotic properties of its own, as well as technological implications for information storage.

1.3 Quantitative Analysis of Magnetization in Prussian Blue Analogues

To provide a strong foundation for the chapters discussing even more complicated nanostructured materials, the magnetic properties of nickel hexacyanochromate and cobalt hexacyanoferrate, the two compounds most thoroughly studied, will be described in Chapter 4 using machinery presented in the theoretical methods chapter. The detailing of two materials of nearly identical structures having different magnetic ions will hopefully reinforce the need to understand the quantum mechanical theories that can accurately describe this type of magnetism. To begin, the paramagnetic precursors, $K_3[Cr(CN)_6]$ and $K_3[Fe(CN)_6]$, will be analyzed, stressing the single-ion properties of the molecules, which remain relevant in the more complicated energy spectra of the full complexes. Subsequently, an analysis of the $Ni_{4.0}[Cr(CN)_6]_{3.0} \cdot nH_2O$ and $Co_{4.0}[Fe(CN)_6]_{3.0} \cdot nH_2O$ materials will be presented along with how magnetization as a

function of temperature and magnetic field may be explained as resulting from the magnetic energy levels of the ions.

1.4 Cobalt Hexacyanoferrate Nanoparticles

The first set of new materials studied consist of nanoparticles of the photomagnetic $\text{Rb}_j\text{Co}_k[\text{Fe}(\text{CN})_6]_l \cdot n\text{H}_2\text{O}$ Prussian blue analogue. Partially motivated by the “room at the bottom” approach to science, magnetic nanoparticles (Figure 1-1) are relevant to the development of memory storage devices as memory media are made increasingly dense and finite size effects may help or hinder device performance. The photoinduced magnetism of $\text{K}_{0.2}\text{Co}_{1.4}[\text{Fe}(\text{CN})_6] \cdot 6.9\text{H}_2\text{O}$ was first discovered in a bulk powder, showing long-range magnetic order that was modified with the application of light [1]. More recently, researchers have been synthesizing photomagnetic nanoparticles, however, no long-range order was observed [6] [7]. It was not until nanoparticles of $\text{Rb}_j\text{Co}_k[\text{Fe}(\text{CN})_6]_l \cdot n\text{H}_2\text{O}$ were synthesized with fine size control that a size dependent study of photomagnetic nanoparticle magnetic properties was performed. This work showed modifications of the coercive fields and the ordering temperatures as a function of size, spanning the regimes from bulk-like to superparamagnetic properties [8]. Further size-dependent studies were performed on $\text{K}_j\text{Co}_k[\text{Fe}(\text{CN})_6]_l \cdot n\text{H}_2\text{O}$ magnets, which can be trapped into different magnetic states by varying the cooling rates [9]. Details of the experiments, including magnetization, x-ray diffraction, neutron diffraction, AC-susceptibility, infrared spectroscopy and energy dispersive x-ray spectroscopy, will be presented in Chapter 5.

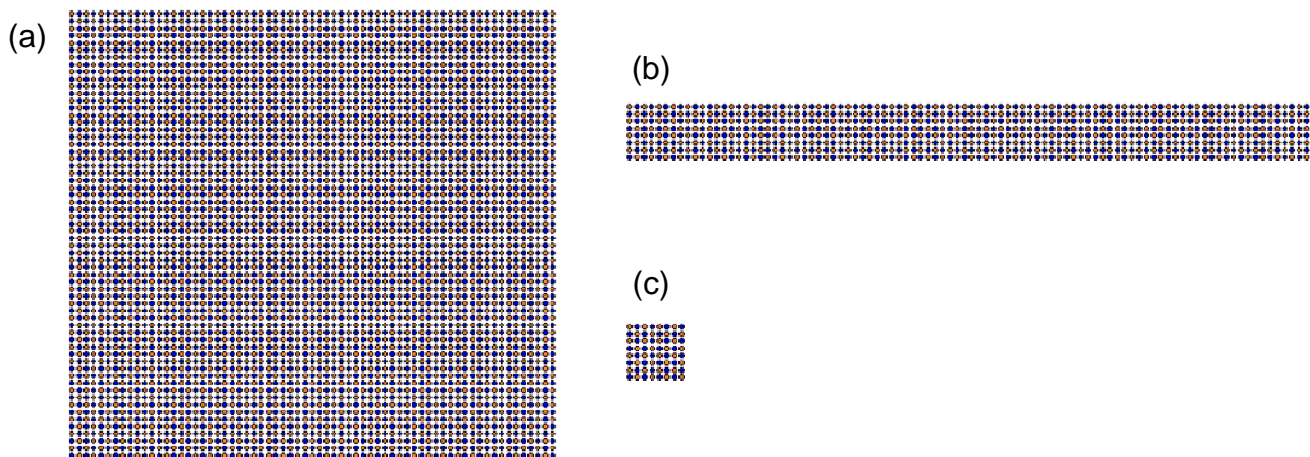


Figure 1-1. Illustration of constrained geometries in nanostructures. Schematic projections of (a) bulk, (b) thin films, and (c) nanoparticles are shown.

1.5 Thin Films of Prussian Blue Analogues

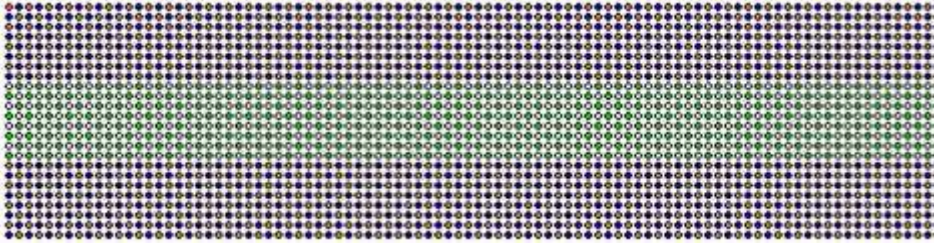
While nanoparticles limit the size of a material in all three spatial dimensions, thin films are the result of limiting the size of only one spatial dimension. In effect, the thin film shape breaks symmetry along the shortened axis (Figure 1-1), and one might expect this broken symmetry to be reflected in the material properties. For both optical applications and memory device applications, thin films are important. Previously, the photoinduced magnetism of $\text{Rb}_7\text{Co}_k[\text{Fe}(\text{CN})_6]_l \cdot n\text{H}_2\text{O}$ thin films were studied, finding an anisotropy of the photoinduced magnetization [10]. This chapter focuses mainly on thin films of $\text{Rb}_7\text{Ni}_k[\text{Cr}(\text{CN})_6]_l \cdot n\text{H}_2\text{O}$ that do not possess photoinduced magnetism, but do have a high ordering temperature, between 60 and 90 K, and a simpler magnetic ground state. Additional films were also studied, substituting different transition metals and studying how the magnetic anisotropy is affected. The goal of the study was not only to characterize the specific films in question, but to provide insight into the general issue of the anisotropy in complex cyanide thin films. The current understanding of this phenomenon, as well as detailed experimental studies, including magnetization,

magnetic microwave resonance, UV-Vis spectroscopy, infrared spectroscopy, x-ray diffraction, scanning electron microscopy and atomic force microscopy, will be presented in Chapter 6.

1.6 Heterostructures of Prussian Blue Analogues

Using the knowledge base compiled during the photomagnetic nanoparticle and thin film studies, an entirely different class of heterostructured materials were synthesized and investigated. The main idea was to take the useful properties from two different materials and to put them together in a new meta-material that possess both of the desirable properties of the constituents. It is interesting that when materials are combined, new unexpected properties can evolve, not native to either parent compound. Two different types of heterostructures were studied, solid solutions and multi-layered thin films, Figure 1-2. Two exciting results were a $\text{Na}_\alpha\text{Co}_x\text{Ni}_{1-x}[\text{Fe}(\text{CN})_6]_\beta \cdot n\text{H}_2\text{O}$ powder, in which the sign of the photoinduced magnetism can be tuned with chemical formula, and a $\text{Rb}_j\text{Co}_k[\text{Fe}(\text{CN})_6]_l \cdot n\text{H}_2\text{O} / \text{Rb}_j\text{Ni}_k[\text{Cr}(\text{CN})_6]_l \cdot n\text{H}_2\text{O}$ heterostructured film, which has photomagnetic effects at unprecedented temperatures for Prussian blue analogues. The experimental magnetization, x-ray diffraction, infrared spectroscopy, transmission electron microscopy, and energy dispersive x-ray spectroscopy measurements will be presented in Chapter 7, along with descriptions of the present understanding of the underlying heterostructure properties.

(a)



(b)

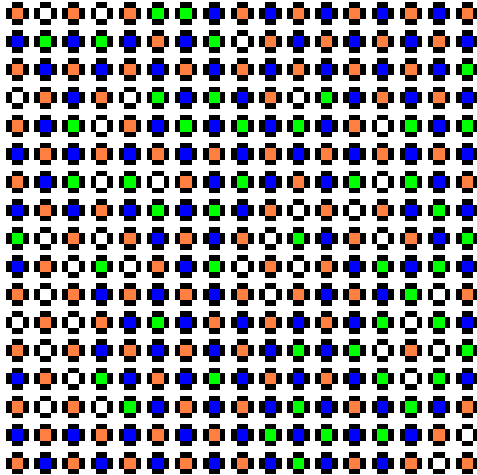


Figure 1-2. Illustration of designer heterogeneous geometries in nanostructures. Schematic projections of (a) a thin film heterostructure and a (b) solid solution heterostructure are shown.

CHAPTER 2 EXPERIMENTAL TECHNIQUES

Perhaps experimental physics may be understood as the harnessing of well documented physical phenomenon to further investigate the less well known properties of matter. A certain level of understanding of the apparatus used is necessary for a rigorous analysis of results. This understanding not only allows the experimentalist to identify the correct piece of equipment to probe the property of interest, but immensely aids in the ability to recognize and avoid spurious results in the forthcoming data. This chapter seeks to survey the experimental techniques utilized in taking the data shown in later chapters.

In Section 2.1, sample environments will be discussed, followed by a summary of the detection methods in Section 2.2. Methods are sorted according to the physical location where the apparatus is located, with those performed in Professor Meisel's lab in the New Physics Building (NPB) Room B133 outlined in Subsection 2.2.1, those performed in Professor Talham's lab in the Chemistry Lab Building (CLB) Room 404, techniques at the Major Analytical Instrumentation Center (MAIC) at the University of Florida or other external labs in Subsection 2.2.2, and, finally, probes located at national labs in Subsection 2.2.3. Within these detection sections, methods are ordered alphabetically. Finally, Section 2.3 will be devoted to custom probes designed by the author and used to collect data presented in the dissertation. Detailed machine drawings and additional photographs of the custom equipment are relegated to the appendices.

2.1 Sample Environment

Sample environment is a crucial aspect of experimental physics [11-14]. For the data to be presented in the following chapters, the three most relevant parameters are temperature, magnetic field, and the application of light to the sample. Specifically, relevant vacuum technology, cooling schemes, superconducting magnets, and photoirradiation methods will be described in the following subsections.

2.1.1 Vacuum Equipment

Vacuum equipment is necessary in cryogenic applications for many reasons. The two most relevant examples are the need to evacuate sample and insulation spaces, and to reduce the vapor pressure over liquid helium in order to reach temperatures below 4.2 K. Proper pumping of all cold spaces is important because an atmosphere with significant proportions of gas will impede cooling power.

2.1.1.1 Pumps

Rotary pumps are the workhorses of the cryogenic laboratory. The pumping mechanism is purely mechanical in nature, consisting of a series of vanes that force air from the inlet to the exhaust as the pump turns, Figure 2-1 (a). Routine base pressures of 10^{-2} or 10^{-3} mbar can be reached, with maximum working pressures of a few hundred mbar, or 1 bar in spurts. Rotary pumps are available in many different sizes, with throughputs ranging from less than $1 \text{ m}^3/\text{hour}$ to a few tens of m^3/hour .

Rotary pumps are often used as roughing pumps before more sophisticated vacuum technology is recruited, backing pumps for diffusion or turbo pumps, or for reducing the vapor pressure over a liquid helium bath. Roughing pumps are required in many instances as technologies with lower base pressures often have lower maximum operating pressures. Diffusion pumps must have a back-pressure below 0.1 mbar or oil

can back-stream into the vacuum system ruining expensive equipment, while turbo pumps with too large of a pressure differential can bend a fin, permanently ruining the pump. Sometimes it is desirable to arrange two rotary pumps of different sizes in stages in order to achieve base pressures down to 10^{-4} mbar.

Most rotary pumps have a gas-ballast. When opened, a gas-ballast causes the pump to work extra hard, thereby heating the oil. This heat helps remove any water that may have condensed in the pumping system when pumping a cryostat that has been exposed to air or has been left unused for a long time. Most surfaces release adsorbed water vapor when the pressure is reduced, and without the proper use of a gas-ballast, the long term base pressure of the system will suffer.

Oftentimes, it is necessary to reach pressures lower than those achievable by rotary pumping technology for proper thermal insulation of a cryostat. Oil diffusion pumps are capable of reaching pressures down to 10^{-7} mbar, but, as mentioned previously, have maximum working pressures of about 0.1 mbar and must be backed with a rotary pump. Air is moved by the use of heated oil vapors that create a high-velocity stream to guide air from the inlet to the exhaust. This stream is created in practice by use of a resistive heating element at the base, and either air, water, or liquid nitrogen cooling of the walls, Figure 2-1 (b). Pumps are generally fitted with a cold trap to help remove water from the vacuum space while simultaneously preventing pump oil contamination of the cryostat or sample space.

The other main pumping technology for reaching high vacuum is the turbomolecular pump, Figure 2-1 (c). Turbomolecular pumps are capable of reaching pressures down to 10^{-8} mbar, and must also be backed with a rotary pump. One

important aspect of the turbo pump is the dependence of pumping speed and base pressure upon the mass of the gas being pumped. Therefore, heavy oil molecules are pumped especially well, but helium actually has one of the poorest ratios for turbo pumps and it is due to this mass effect that diffusion pumps can outperform turbo pumps in helium applications.

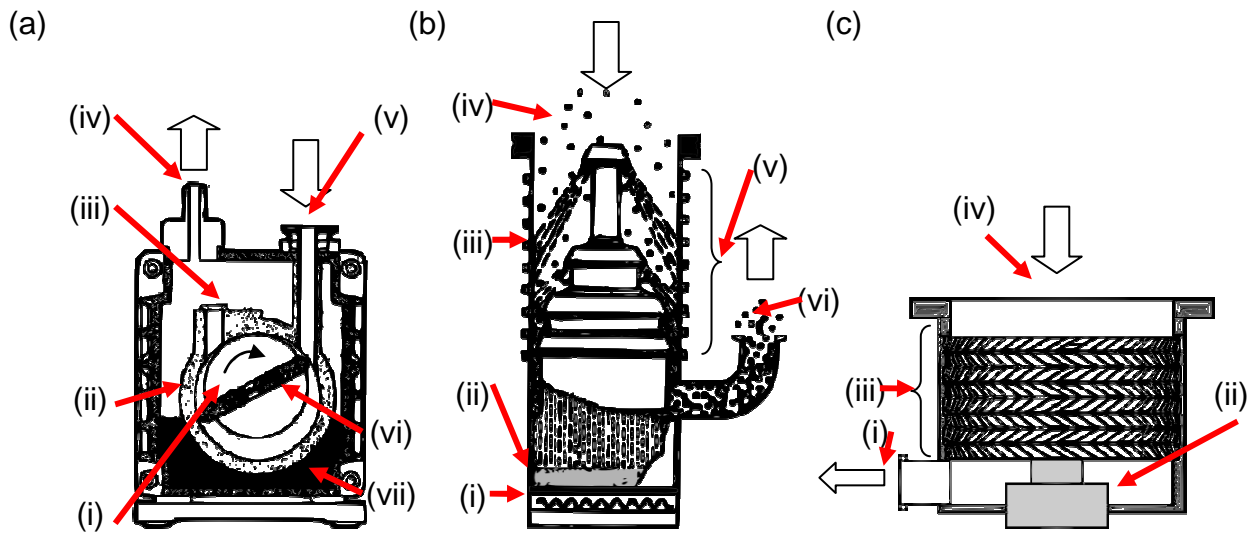


Figure 2-1. Illustrations showing operation of standard pumps that can be found in a cryogenic laboratory. (a) A schematic cutaway showing the main design elements of a rotary pump, (i) the rotor, (ii) the stator, (iii) the exhaust valve, (iv) the exhaust outlet, (v) the pump inlet, (vi) the vanes, and (vii) the pump oil bath. (b) A schematic cutaway showing the main design elements of an oil diffusion pump, (i) the heater, (ii) the hot oil, (iii) cooling elements, (iv) the low-pressure inlet, (v) different compression stages of the oil vapor jets, and (vi) the exhaust. Oil is represented by dashed lines and the pumped molecules by small circles. (c) A schematic cutaway showing the main design elements of a turbomolecular pump, including the (i) exhaust, (ii) motor, (iii) turbines, and (iv) low-pressure intake. These images were generated by the author and inspired by standard texts on the subject [11-14].

2.1.1.2 Pumping Lines

If pumps are analogous to the voltage source in a pumping circuit, then pumping lines are the resistive wires. In order to achieve the maximum pumping power at the vacuum space, lines with minimal impedance are of the highest importance. Ideally, lines are metal for high vacuum, as plastics can be permeable to helium gas. Pumping lines should be free of adsorbed impurities, and therefore it is ideal to clean lines with a volatile substance, like acetone. Finally, the cross-sectional area of the lines should be large enough to ensure that the displacement throughput of the lines is larger than that of the pump being used.

2.1.1.3 Vacuum Gauges

Vacuum in the range of 1 to 1000 mbar can easily be measured with a simple spring loaded dial gauge. However, for higher vacuum, pressure is generally measured with a Pirani gauge in the range of 10 mbar to 10^{-3} mbar, and a Penning gauge in the range 10^{-2} to 10^{-7} mbar. Pirani gauges consist of a wire filament in contact with the atmosphere, and depending upon the gas concentration, different thermal conductivity in the gauge is measured. Penning gauges measure the ion conductivity across a large voltage drop. It is important to remember that the calibration of these high vacuum gauges is dependent on the type of gas used in the system.

2.1.1.4 Oil Mist Filters and Fore-line Traps

In order to remove the oil vapors present in the exhaust gas of a rotary pump, oil mist filters are used. This filtration is for three important reasons: first, there is a health hazard associated with the inhalation of oil mist; second, oil mist may contaminate plumbing, pressure gauges, and flow-meters behind the pump; and third, since UF has a helium recovery system, it is desirable to limit the amount of oil that must be removed

in the recovery laboratory. Filters can either be coalescing or centrifugal. Centrifugal filters are mainly utilized for price reasons but have the downside that they must be drained occasionally. Fore-line traps are used on the inlet of a rotary pump to reduce the amount of oil back-streaming up the pumping line. These must also be changed regularly as traps saturate with oil over time.

2.1.1.5 O-rings

Any time two pieces of vacuum equipment are joined together, a seal must be made. Ideally, joints would be soldered or welded, but oftentimes setups are dynamic, so temporary seals are used. These may be o-ring seals, or different varieties of a flare fitting.

For o-rings, the material to be used is the most important aspect of the seal. Nitrile rubber is the ubiquitous o-ring material used in modern day vacuum technology, most simply because it is the best seal for the price. Nitrile has a working temperature range from -40°C to 120°C . Silicone rubber has a higher temperature range of workability, -100°C to 250°C , however it is not used in the cryogenic apparatus because it is permeable to helium gas. Butyl rubber is another o-ring material that has a low gas permeability. It can be used down to -60°C , but is a little more expensive than nitrile. Fluoroelastomers, such as Viton, are used for higher temperatures but is more expensive and less ductile than nitrile. It has a working temperature range from -20°C to 200°C . Teflon can also be used to make seals, but one has to always be wary of the dodgy mechanical properties and large thermal contractions. For low temperature o-rings, indium seals are ideal because of the similar thermal expansion coefficient of the indium and the metal cryogenic apparatus.

2.1.2 Cryostats

Helium is the mainstay refrigerant for any researcher looking to reach temperatures below 70 K. Specifically, the more common ^4He isotope is capable of reaching temperatures down to 1 K, due to its thermodynamic phase diagram.

Depending upon needs and availability, liquid helium cryostats or closed cycle cryostats are used.

2.1.2.1 Bath Cryostats

The simplest cryostat configuration is a bath cryostat, consisting of a large volume of cryogen (tens of liters) thermally insulated from ambient temperature. More complicated setups may include internal structure, such as a continuous flow cryostat, to allow for greater control of sample temperature. Regardless of the internal structure, bath cryostats require substantial shielding to achieve the necessary thermal insulation for economical experiments. Shielding generally consists of a radiative shield thermally anchored to either a liquid nitrogen or helium gas cooled shield. Currently, the boil-off rates are comparable for nitrogen or helium gas shielded systems.

2.1.2.2 Continuous Flow Cryostats and Cryogenic Inserts

While it is possible to pump on the entire bath to reduce the temperature below 4.2 K, it is common practice to thermally isolate a smaller volume, which has been equipped with radiation shielding, to be pumped on while leaving the bath at 4.2 K. These volumes are a type of continuous flow cryostat called variable temperature inserts that allow for separate temperature control of the bath and the sample space. This separation of sample and bath spaces allows for cooling without the need for large displacements of gas and reduces the ~35% boil-off of liquid necessary to reach the lambda point (2.17 K) to a small fraction of the bath [13]. Of course, this convenience

requires an additional level of complexity, in which a stream of super-cooled gas in conjunction with a resistive heater are able to achieve stability over wide ranges of temperature. Helium is drawn from the bath through an impedance line (which is sometimes variable), and the temperature of the insert is controlled by using a resistive heater and pump to control the pressure within the insert. Cooling is achieved as the cold gas flows over the sample and out through the exhaust to the pump. Additional stability can be achieved at the expense of a longer relaxation time constant when changing temperatures by putting a heat exchanger between the cold gas and the sample.

2.1.2.3 Closed Cycle Refrigerators

While bath cryostats require an external liquefier and the transfer of liquid helium into the apparatus, closed cycle refrigerators offer an increasingly popular alternative. The most common type of refrigeration cycle used is one of the Gifford-McMahon type. Grossly, they consist of a closed circuit of helium gas, a probe, and a compressor. During operation, helium is alternatively compressed and allowed to expand at tens of Hertz, using the entropy of the expansion to cool the sample. Depending upon the type of shielding employed and the power of the compressor, temperatures as low as 5 K can be routinely reached in these instruments. Potential drawbacks of closed cycle refrigerators are the coupling of the compressor vibrations to the experiment, maintenance of the compressor, and the comparatively high initial cost of the setup when compared to a continuous flow cryostat.

2.1.3 Superconducting Magnets

Perhaps the highest impact application for superconductors is in the wire of superconducting magnets. At the expense of refrigeration, magnets with

superconducting wire are capable of magnetic fields in the neighborhood of 20 T without the need for high voltage power supplies. The most common winding geometries for superconducting lab magnets are a continuous solenoid or split pair, Figure 2-2. While solenoids allow for the best field homogeneity, for neutron scattering it is necessary to have access to the sample perpendicular to the magnetic field.

2.1.3.1 Magnet Construction

Due to the need for high current densities, most commercial magnets utilize type I superconductors. In order to increase the critical field, alloying is employed, as impurity sites act as local flux pinning minima. In addition, the wire is generally multi-filamentary to further prevent dissipative flux jumping. The most common superconducting wire is the NbTi alloy, because it is cheap, ductile, and has a high supercurrent density even in strong fields. Using only NbTi, fields up to 9 T at 4.2 K or 11 T at 2.2 K can be routinely reached. To get in the neighborhood of 20 T, the magnet wire must operate at or below the lambda point (2.17 K), and the inner windings must be made from the more expensive and brittle Nb₃Sn alloy.

Magnetic field homogeneity is always a concern, and standard superconducting solenoids have flat magnetic field profiles over a centimeter at the center field up to one part per thousand. To achieve higher homogeneity, many modern systems utilize compensating coils to combat the field gradients produced from the finite nature of the wound solenoids. For finer adjustment, shim coils can tune the homogeneity of the center field to 1 part in 10⁵ for series shims and as good as 1 part in 10⁷ for tunable shims. Finally, counter-wound cancellation coils may be fit on the ends of a magnet to help cancel stray fields at distances away from the center of the magnet. Overall, the

case is slightly worse for split pair magnets, where field homogeneity is typically an order of magnitude lower for analogous setups.

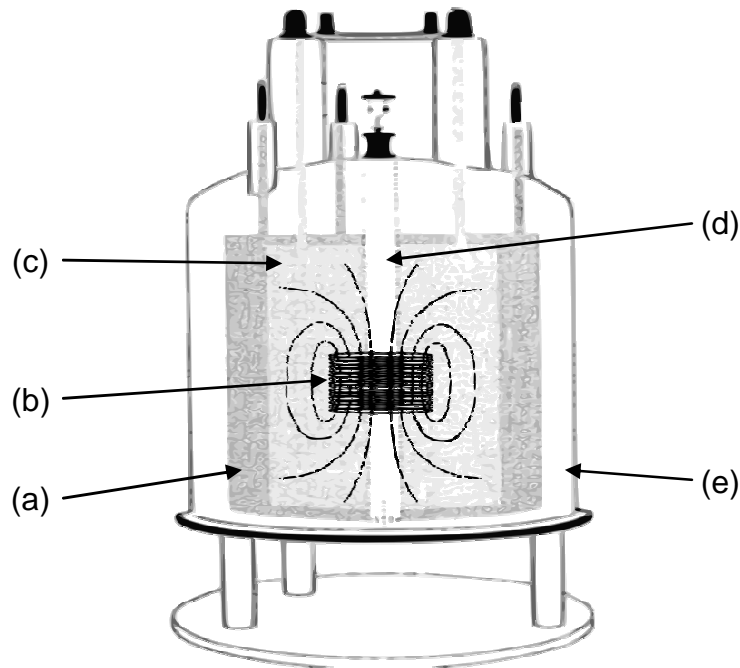


Figure 2-2. Illustration of a superconducting solenoid magnet. A schematic cutaway showing the main design elements of a superconducting solenoid, including (a) a nitrogen jacket, (b) the magnetic coils, (c) the helium bath, (d) the magnet bore, and (e) the vacuum isolation space. This image was generated by the author and inspired by standard texts on the subject [11] [14].

2.1.3.1 Magnet Operation

Perhaps the most important thing to remember when working around and using a superconducting magnet is the huge amount of energy held within the structure, of the order of a megajoule. This enhanced awareness of magnetic forces is especially true in split pair setups, where large mechanical reinforcements are needed to stop the pairs from joining together. Due to their small resistances, superconducting coils are able to produce huge back EMF's when the current is ramped up or down. This inductance forces users to ramp at sufficiently slow rates to avoid transitioning the wires to the

normal state, thereby quenching the magnet and potentially damaging expensive equipment. If the wires do phase transition to the normal state, the large amount of energy stored in the circuit must then be dissipated. It is not uncommon to see a plume of helium from the magnet bath vent during a quench. All modern magnets have measures in place to avoid the most destructive consequences of a quench. The so-called superconducting winding protection circuit is, most simply, resistive elements put in parallel with the magnet windings, thereby shorting the magnet once a quench has occurred.

Happily, unlike resistive magnets, superconducting magnets do not require the application of an external voltage to maintain current flow. Practically, this aspect is often exploited in superconducting magnets to limit helium boil-off during operation by the use of a persistent magnet mode. The persistence mode is when there is still supercurrent in the coils, but the external power supply has been turned off. To allow for persistence as well as ramping of the field, a superconducting switch is wired in parallel to the main coil windings, and a small heater is placed near the switch. When charging the magnet, heat is applied, causing the switch to go normal and therefore acting effectively as a broken wire in the circuit, dropping all applied voltage over the magnet coils. For the persistent mode, heat is removed from the superconducting switch, thereby isolating the coils, so the external power supply can then be slowly ramped down and turned off, leaving a persistent supercurrent in the windings. It is important to remember that if the field is to be changed after entering the persistent mode, the power supply must be ramped to the correct voltage corresponding to the current in the magnet, and the superconducting switch must then be activated before

any changes in the voltage across the magnet circuit can be made. Typical decay rates in persistent mode are 100 $\mu\text{T}/\text{hour}$.

2.1.4 Light Guides

For photoinduced studies of magnetization and structural changes, it is necessary to have a way to get light from a room temperature halogen light source, with typical powers of 1 or 2 mW, down into the cold space of a cryostat. For small scale probes, optical fibers from Ocean Optics, Model 200 UV-Vis, OD $\sim 270 \mu\text{m}$ were used. These fibers are ideal because they are flexible, are thermally insulating, and are easily arranged to direct light onto small samples. For larger scale probes, fiber optics are no longer ideal or even economically feasible. In these cases, solid quartz rods were used as light guides; although they are not flexible, much larger amounts of light can be guided down to the sample space.

2.2 Detection Methods

With sample environment considerations in one hand, the other obvious element to an experimental study is the detection methodology itself. With the large amount of scientific infrastructure already in place, experimentation often comes down to keen identification of the correct probe and the conditions to extract the material properties of interest. In the following subsections, the Superconducting QUantum Interference Device (SQUID) magnetometer that was used most heavily, auxiliary methods performed in other labs, and probes located at national lab facilities will be overviewed.

2.2.1 SQUID magnetometer

2.2.1.1 Superconducting QUantum Interference Devices

Superconducting QUantum Interference Devices (SQUIDs) are highly precise amplifiers, often utilized in magnetometers due to their sensitivity to magnetic fields

weaker than 10^{-14} T [15] [16]. A clear example of the precision of SQUIDs is their ability to detect, and actually discover, that flux is quantized in units of

$$\varphi_0 = \frac{h}{2e} = 2.0678 \times 10^{-15} T \cdot m^2 \quad 2.1$$

where h is Planck's constant, and e is the charge quanta. SQUID devices are based upon Josephson junctions, which consist of two superconducting regions connected by a weak link that allows quantum tunneling between the two regions without bulk transport.

Josephson junctions are generally made from niobium or niobium alloy superconductors, such as NbSe₂ or NbTi. While originally a point contact using a sharp-ended screw was used, modern day junctions are microbridges using patterned lithography. Current and voltage can then be measured across the weak link created at the point contact.

The Josephson junction alone does not act as a magnetometer, so it must be included in a larger SQUID circuit, Figure 2-3. The basic aspects of a SQUID circuit are a transformer coil, which is large enough to interact with the sample, coupled to a signal coil, which is manufactured symmetrically with a radio-frequency detector coil. The signal coil and detector coils are connected through a weak link, allowing flux coupling. Magnetic flux changes arising from a magnetic sample induce current in the transformer, and these changes couple directly to the detector coil via mutual inductance. Finally, the radio-frequency voltage across the detector coil can be measured, after going through a conditioning circuit, and fit to extract the field associated with the sample.

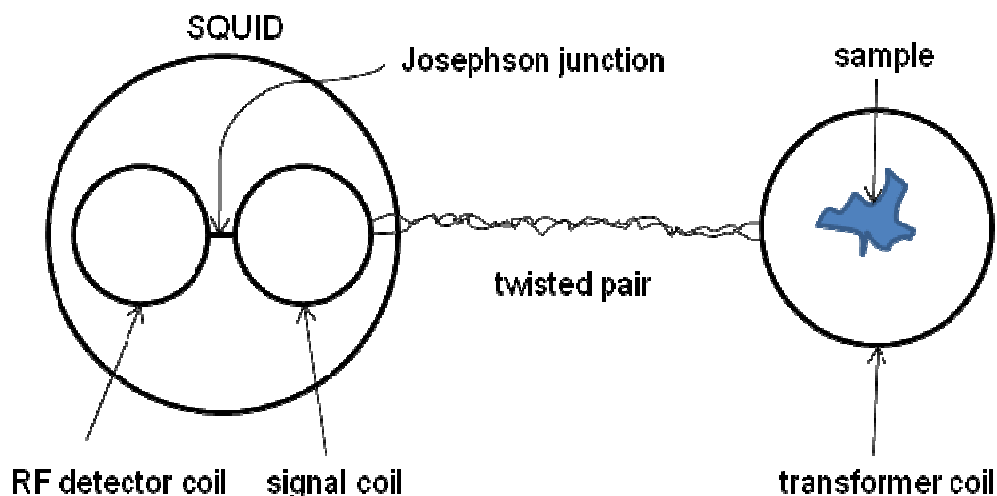


Figure 2-3. Illustration of a SQUID magnetometer circuit. A circuit set up to detect flux changes resulting from a magnetic sample, utilizing the high sensitivity afforded by a SQUID amplifier.

2.2.1.2 Quantum Design MPMS XL Magnetometer

Two different commercial magnetometers from Quantum Design were used for the DC- and AC-SQUID measurements, an MPMS-5S and an MPMS-XL [17-19]. The MPMS-5S, located in the New Physics Building Room B20, is the older of the two and is equipped with an AC detection board, a 5 T superconducting magnet equipped with a field reset, magnetic shielding, and a pumped ^4He cryostat. The MPMS-XL, located in the New Physics Building Room B133, is newer and has the added benefit of a 7 T superconducting magnet. An additional advantage of the MPMS-XL is a low temperature impedance allowing for the continuous operation at base temperatures lower than 2 K, but the XL is not equipped with any of the other additional features of the 5S model.

Powder samples were mounted in either diamagnetic gelcaps or on sticky tape to increase the optical cross-section for photoinduced experiments. Commercial straws were used as a diamagnetic sample rod to allow translation of the sample through the

SQUID magnetometer detector coils. In general, backgrounds were subtracted based upon the known mass susceptibility of the sample holders, but in many cases, background contributions were insignificant.

The Quantum Design magnetometers utilized a second derivative transformer coil to measure sample flux and to couple to the SQUID, Figure 2-4. The advantage of the multiple coil setup is from the inherent background subtraction of any signal that is a longer wavelength than the ~ 4 cm long transformer. These noise sources will simply cause, for example, a positive voltage in the top coil, a negative voltage in the second, a negative voltage in the third, and a positive voltage in the fourth coil, summing to zero [18].

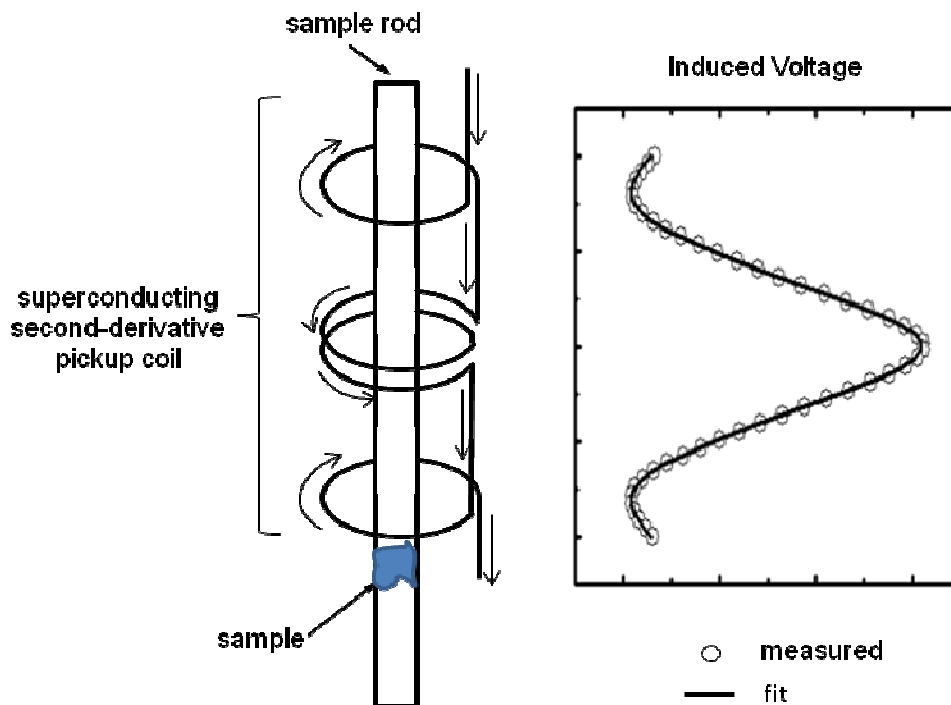


Figure 2-4. Illustration of SQUID magnetometer pickup coils. The superconducting second derivative pickup coil used in the MPMS magnetometer and the voltage induced as a function of the position of a magnetic sample within the coils.

2.2.1.2 Remnant Fields and Degaussing the MPMS

For probing magnetic systems with weak anisotropy, the use of small fields may be necessary. The fields can be measured using a custom Hall probe for the SQUID magnetometer (based on a Toshiba THS118E chip) developed by the author. The use of the standard “oscillate” option on the MPMS provides “zero field” of ~ 10 G, Figure 2-5 (a). However, this level of error uncertainty can be undesirable at times, when a manual degaussing sequence can be employed instead. The specific degaussing method depends on the recent history of the magnet. An example of a degauss sequence would consist of high resolution charging between -40 kG, 30 kG, -20 kG, 10 kG, -5 kG, 2.5 kG, 1 kG, 500 G, -250 G, 100 G, -75 G, 50 G, -25 G, 10 G, -10 G, 0, 5 G, -5 G, 0. The results of this sequence give a different field profile with a smaller magnitude of ~ 1 G, Figure 2-5 (b). It is also important to wait a sufficient amount of time for eddy currents to dissipate, since superconducting magnets have long time constants because of a large inductance combined with a small resistance.

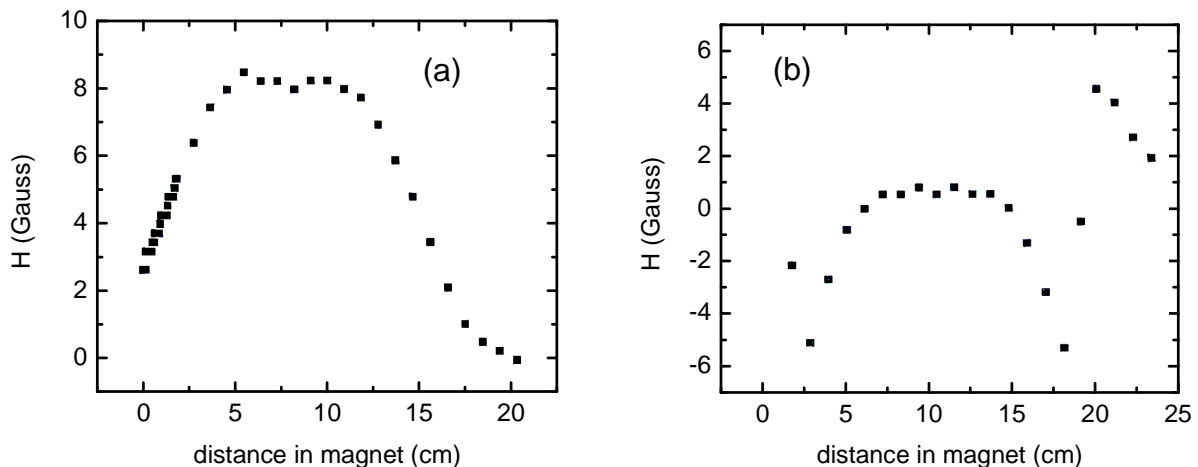


Figure 2-5. Remnant fields and degaussing the MPMS. (a) The field in the magnet after a standard oscillate to zero protocol, with center field ~ 8 cm. (b) The field in the magnet after a manual degaussing sequence, with center field ~ 10 cm.

2.2.2 Additional Methods Performed at UF

2.2.2.1 Atomic Force Microscopy

Atomic Force Microscopy (AFM) is a highly sensitive scanning probe microscopy that was used to characterize the surface morphology of thin films [20]. All AFM studies were performed on a Digital Instruments multimode scanning probe microscope in Professor Talham's Chemistry Lab in CLB Room 404. Roughly a square centimeter of film was cut and placed under the scanning tip. The scanning tip is a sharp point attached to the end of a cantilever, which in turn is connected to the feedback electronics that monitor the height of the tip over the surface to help prevent tip crashes onto the sample, Figure 2-6. Nanometer scale changes in the deflection of the tip are detected by a laser coupled to a photodiode.

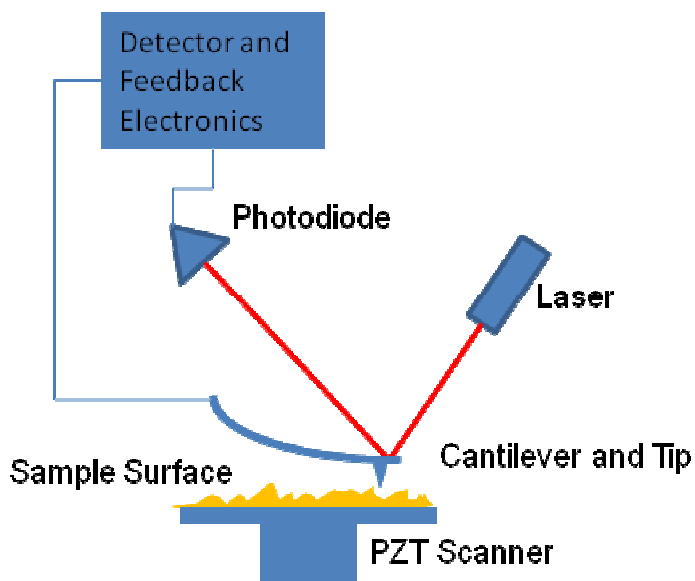


Figure 2-6. AFM schematic. The sample tip scans over a material, revealing details of the surface morphology.

2.2.2.2 Carbon, Hydrogen, and Nitrogen Combustion

Carbon, Hydrogen, and Nitrogen combustion analysis (CHN) was utilized to determine light atom (with 2p electrons) concentrations for selected samples [21]. All CHN was performed at the University of Florida Spectroscopic Services laboratory. Roughly 3-5 milligrams of sample are used and destroyed in the measurement process. To achieve controlled combustion, the sample is sealed in an oxygen atmosphere and external heat is applied. As atoms are released, they flow through a series of columns containing a water trap, a carbon dioxide trap, and a nitric oxide trap, Figure 2-7. By measuring the masses of the different traps after combustion of the sample is complete, the analytical determination of the chemical make-up is possible with straightforward calculations.

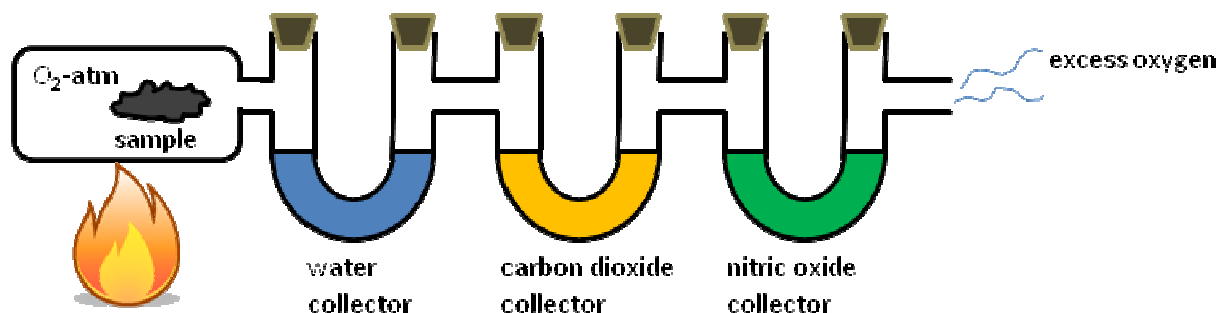


Figure 2-7. A schematic of a combustion train for CHN analysis.

2.2.2.3 Energy Dispersive X-Ray Spectroscopy

Energy Dispersive X-ray Spectroscopy (EDS or EDX) was the primary analytical technique used for determining relative concentrations of “heavy” atoms (containing 3d electrons) for selected samples [22]. All results reported herein were recorded on a JOEL 2010F Super-Probe, housed at the Major Analytical Instrumentation Center (MAIC) at the University of Florida (UF). Only micrograms of samples are necessary to

perform the measurements, with mounting achieved by deposition of microliter quantities of sample containing solution on holey-carbon TEM grids purchased from Ted Pella, Inc. Simplistically, the experimental apparatus required are an electron gun with proper magnetic lenses and an inelastic x-ray detector, Figure 2-8 (a). In this method, a beam of electrons is focused on the sample, with a finite probability of incident electrons ejecting bound electrons. If the ejected electron was from an inner shell, the atom will seek the new ground state, emitting energy in the form of a photon in the process, Figure 2-8 (b). These photons can then be collected and analyzed by a detector, revealing the electronic transitions present. A typical spectrum consists of x-ray counts as a function of energy. As each atom has a unique electronic structure, the electronic transitions present in the experimental x-ray spectrum are diagnostic of the chemical composition of the sample.

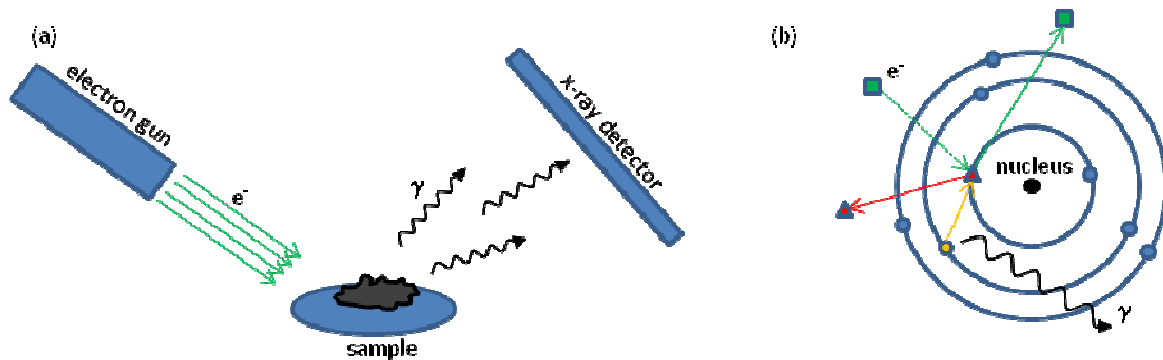


Figure 2-8. EDS schematic. (a) Experimental setup of EDS. (b) Microscopic effect showing incident electron (green square) hitting bound electron (red triangle) causing it to be ejected. The atom then relaxes down to the ground state by filling in electrons, one example is displayed (yellow circle), and emitting x-rays to conserve energy.

2.2.2.4 Fourier-Transform Infrared Spectroscopy

Fourier Transform InfraRed (FT-IR) spectroscopy, in the middle of the spectrum, is the study of how light with wavelengths from $4,000\text{ cm}^{-1}$ to around 400 cm^{-1} interacts with matter [23]. All measurements were performed on a mid infrared Nicolet 6700 spectrometer located in CLB Room 411. Powder samples were either mounted in pressed KBr pellets or sandwiched between two salt-plates for the study of materials that were sensitive to pressure. Thin film samples were run with no additional modifications. As with all spectroscopic methods, infrared spectroscopy is sensitive to transitions between discrete energy levels for the material being irradiated. These energy levels can be either vibrational or electronic in origin, and for this work, vibrational modes were of primary accessibility and interest. Interferometers are the basis of an infrared spectrometer, which consists of a broad-band source, a beam-splitter, a fixed mirror, a movable mirror, a sample, and a detector, Figure 2-9 (a). Spectra are obtained as a function of moveable mirror position. Fourier transform spectroscopy is so called because it consists of sending a pulse of radiation with many frequency components through the sample to the detector, which registers the signal in the time domain (technically the moveable mirror position domain). Finally, a Fourier transform is performed to obtain the spectra in the frequency domain, Figure 2-9 (b).

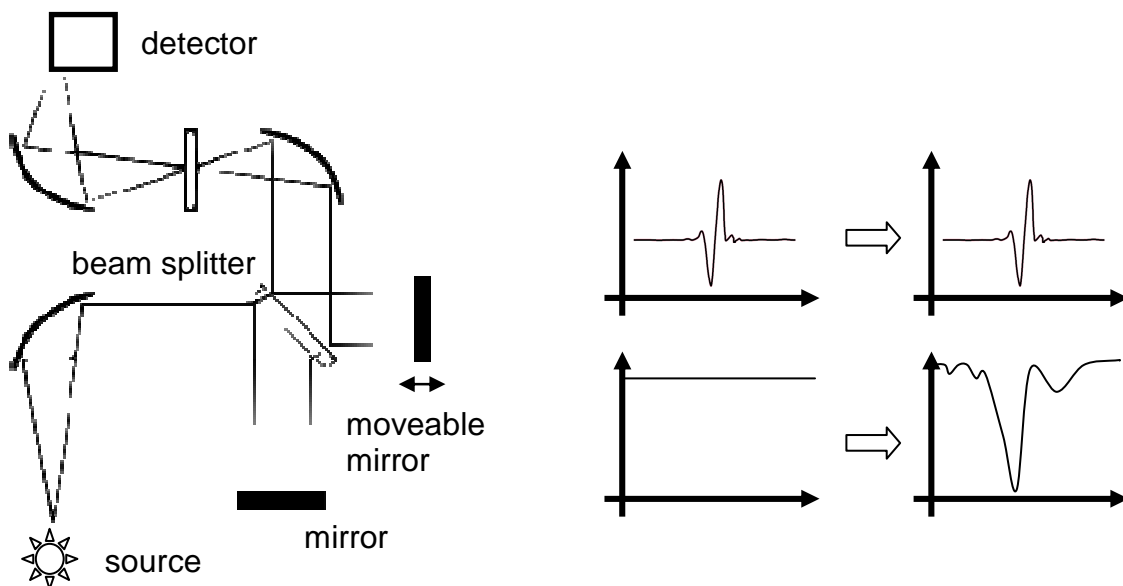


Figure 2-9. FT-IR schematic. (a) A schematic of a typical Fourier transform infrared spectrometer. (b) A schematic showing how the high-spectral-content pulse is modified after passing through the sample, and subsequently is Fourier transformed to give a spectrum in frequency space.

2.2.2.5 Inductively Coupled Mass Spectrometry

Inductively Coupled Plasma Mass Spectrometry (ICP-MS) is an analytical chemical technique used to determine the concentrations of metals, and some non-metals, with a high sensitivity. For example, detection limits are less than a picogram per second for transition metals [24]. ICP-MS results were obtained using a Thermo-Finnigan Element-2 spectrometer located at the UF Department of Geology. Samples were prepared for ICP-MS by dissolving them in trace metal grade nitric acid. This chemical dissolution is necessary in order to aerosolize the sample for when it is introduced into the plasma chamber. This aerosol enters an argon environment of the chamber and is subsequently exposed to powerful radio frequency radiation, converting the gas into a plasma, Figure 2-10. Argon is chosen because of the much higher first ionization potential, compared to all elements except He, F, and Ne. It is the dynamics

of the argon and sample plasma that provide for sample explosion and subsequent ionization. Once ionization is complete, the RF field also serves to delineate ions having different charge to mass ratios, and thus determine the elemental content of the sample.

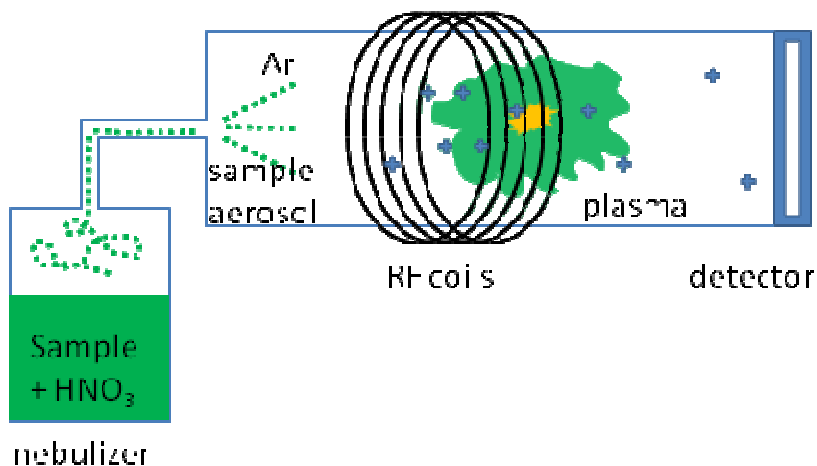


Figure 2-10. ICP-MS schematic. The sample dissolved in acid is aerosolized in a nebulizer and introduced into an argon environment, in which it flows into an ionizing RF field, and the ions are subsequently detected via mass spectrometry.

2.2.2.6 Transmission Electron Microscopy

Patterned after the more traditional light transmission microscopy, Transmission Electron Microscopy (TEM) allows for resolution of a few Å's, owing to the short deBroglie wavelength of the electrons [25]. All results reported herein were recorded on a JOEL 2010F Super-Probe, housed at the Major Analytical Instrumentation Center (MAIC) at the University of Florida (UF). Only micrograms of samples are necessary to perform the measurements, with mounting achieved by the deposition of microliter quantities of sample containing solution on various holey-carbon TEM grids purchased from Ted Pella, Inc. A representative setup consists of an electron gun, conditioning lenses, and an imaging screen, Figure 2-11. Electrons are generated at a thermionic

electron gun. This source is then focused by the use of magnetic lenses, in which the trajectory of the charged particles is bent by the presence of the applied field. Electrons next travel through an aperture to avoid background from large angle particles. Subsequently, the focused electrons are scattered by the matter present in the sample, creating a negative image of the sample in the electron beam. The objective optic serves to focus the image, and the objective aperture again cuts off high-angle scatterers. The image is then enlarged by the intermediate and projector lenses onto the imaging screen, where electrons interact with phosphor to produce light that can be recorded with standard camera techniques. These methods have been utilized to obtain light-field, dark-field, and diffraction data on the samples discussed in the following chapters.

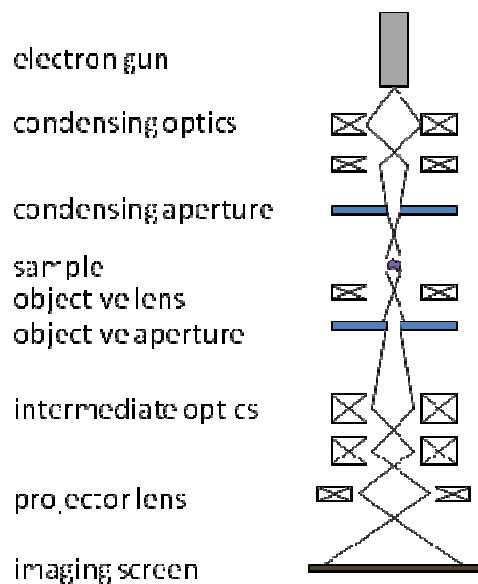


Figure 2-11. TEM schematic. Electrons travel from the top to the bottom, with the waist of the beam represented by the solid lines, and magnets represented by boxes with exes in them.

2.2.2.7 Ultraviolet and Visible Spectroscopy

Spectroscopy in the UltraViolet and Visible range (UV-Vis) is useful for studying coordination networks because the wavelengths of approximately 200 to 800 nm probe energy scales of 6.21 to 1.24 eV, which are comparable to the energies separating different multi-electron magnetic energy levels [26]. A typical spectrometer consists of a source, a monochromator, the sample space, a photodetector, and a computer interface, Figure 2-12. Two different machines located in the Chemistry Lab Building were used, a room temperature device, and a spectrometer equipped with a close-cycle cryostat for temperature dependent studies. The source consists of two elements, a tungsten halogen for wavelengths above 320 nm and a deuterium arc lamp for wavelengths below 320 nm. Monochromators are made up of a diffraction grating and a series of filters to remove higher order diffractions. Samples are mounted using quartz slides for thin films and quartz cuvettes for solutions. The detector is a silicon photodiode. Spectra are then recorded as ASCII delimited files.

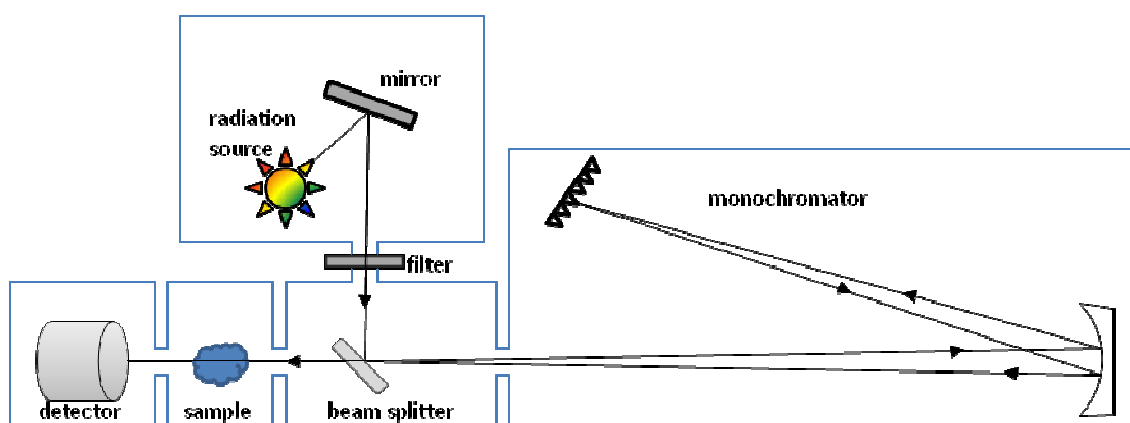


Figure 2-12. UV-Vis spectrometer schematic. More complicated setups may include conditioning optics, multiple sources and references beams, for example.

2.2.2.8 X-Ray Powder Diffraction

X-Ray Diffraction (XRD) is used to find the average positions of heavy atoms in a wide range of samples [27]. All samples studied were polycrystalline, so the XRD Philips APD 3720 2θ powder diffractometer located in MAIC Room 117 was used. A standard Cu K_{α} source is used, producing a dominant wavelength of 1.54 Å (933 eV) x-rays by applying voltages near the ionization energy of the K (1s) to L_3 ($1p_{3/2}$) transition in Cu. For good signal to noise on organometallic compounds, tens of milligrams are desirable, but samples on the order of one milligram show clear, refinable Bragg peaks. Samples were mounted on a 25 mm x 47 mm glass slide purchased from Ted Pella Inc., and immobilized using a 1 cm² piece of double-sided sticky tape in the center of the slide. In XRD, the lattice planes within ordered crystals satisfy the condition of constructive interference when the path length difference between x-rays scattering from different lattice layers is an integer multiple of the incident wavelength, Figure 2-13. For randomly oriented polycrystalline samples, all lattice planes are effectively probed at the same time, the disadvantage is that the experimental integration over crystalline angles reduces the amount of structural information.

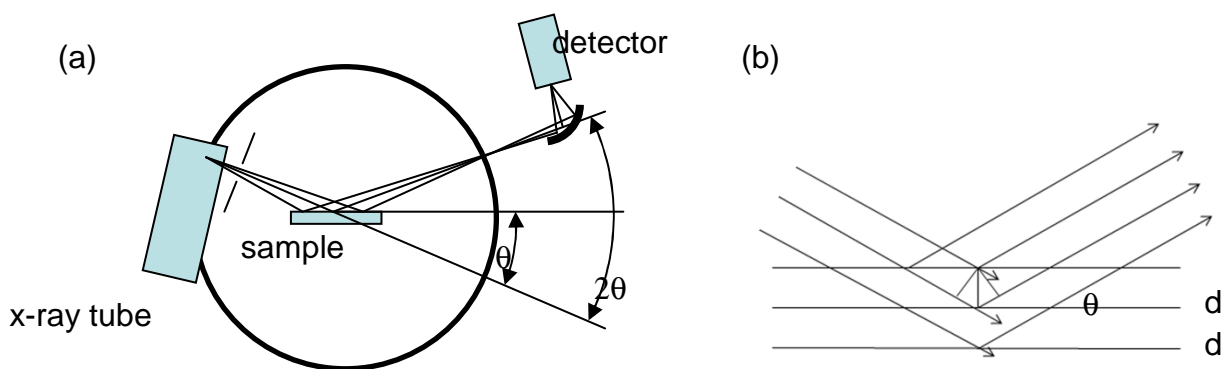


Figure 2-13. XRD schematic. A schematic showing how incident x-rays gain an extra path length of $2d\sin(\theta)$ when scattering off of evenly spaced planes a distance d apart.

2.2.3 National Laboratories

National Laboratory user facilities are an important resource for the modern research scientist and the author feels fortunate to have been able to visit a few different facilities. For the materials studied in this thesis, measurements were carried out at the National High Magnetic Field Laboratory (NHMFL) in Tallahassee, Florida, and the Oak Ridge National Laboratory (ORNL) in Oak Ridge, Tennessee. High field Electron Magnetic Resonance (EMR) studies were performed at NHMFL, Neutron Diffraction (ND) studies were performed at the High-Flux Isotope Reactor (HFIR) at ORNL on the triple-axis spectrometer on beamline HB1A and the neutron powder diffractometer on beamline HB2A, and Inelastic Neutron Scattering (INS) was performed at the Spallation Neutron Source (SNS) on the fine-resolution Fermi chopper spectrometer at beamline 17. Online at full-power since 1966, the 85 megawatt HFIR source is unique because it has the highest flux, of the order of a million neutrons/cm²s on most beamlines, of any reactor based source of neutrons for condensed matter research in the United States. Neutrons at the HFIR are in the thermal spectrum, with a small portion of cold neutrons available. On the other hand, the SNS is still in the process of being commissioned as of this writing, but is expected to have record neutron fluxes available for studying materials. Unlike the HFIR, the SNS uses spallation to create bursts of neutrons with a wide range of energies, and as such, the spectrometers must operate in time-of-flight mode.

2.2.3.1 Electron Magnetic Resonance at the NHMFL

Electron Magnetic Resonance (EMR) experiments were performed in Professor Stephen Hill's lab at the NHMFL, using a resonant cavity insert to a Quantum Design Physical Property Measurement System (PPMS) equipped with a 5 T magnet. For

approximately a square centimeter of sample, Prussian blue analogue films require about 400 cycles, which is an arrangement that may also be achieved by using multiple films of less than 400 cycles. For powder resonance, approximately a milligram of a Prussian blue analogue magnet is required. Resonant absorption of external microwave radiation for electron systems can be easily understood in the context of energy splittings to be presented in the next chapter. Briefly, if an electron is placed in a magnetic field, there is a difference in energy between the parallel and antiparallel orientations of the spin vector with respect to the field vector, Figure 2-14 (a). When the energy difference between the two orientations is in resonance with external radiation, spins may be excited from the lower energy level to the upper one, resulting in the absorption of the incident radiation, which may be measured experimentally, Figure 2-14 (b).

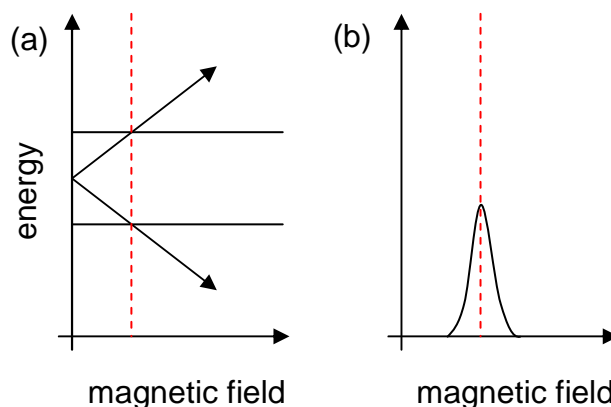


Figure 2-14. Theoretical EMR schematic. (a) The simplest energy level splitting of an $S = 1/2$ spin species as a function of magnetic field. The horizontal lines indicate the microwave energy, and the dashed red line indicates the resonance condition. (b) The increase in cavity absorbance when the resonance condition is met.

The apparatus necessary for performing resonant absorption experiments is generalized in Figure 2-15. The first essential ingredient is a tunable external magnetic field that is large enough to split the energy levels of the system to separations excitable by an external radiation source, which is the second essential ingredient. Furthermore, the sample is often placed in a resonant cavity to further amplify the effects of absorption. To measure absorption, the ratio of the microwave intensity before the sample and after the sample can be compared.

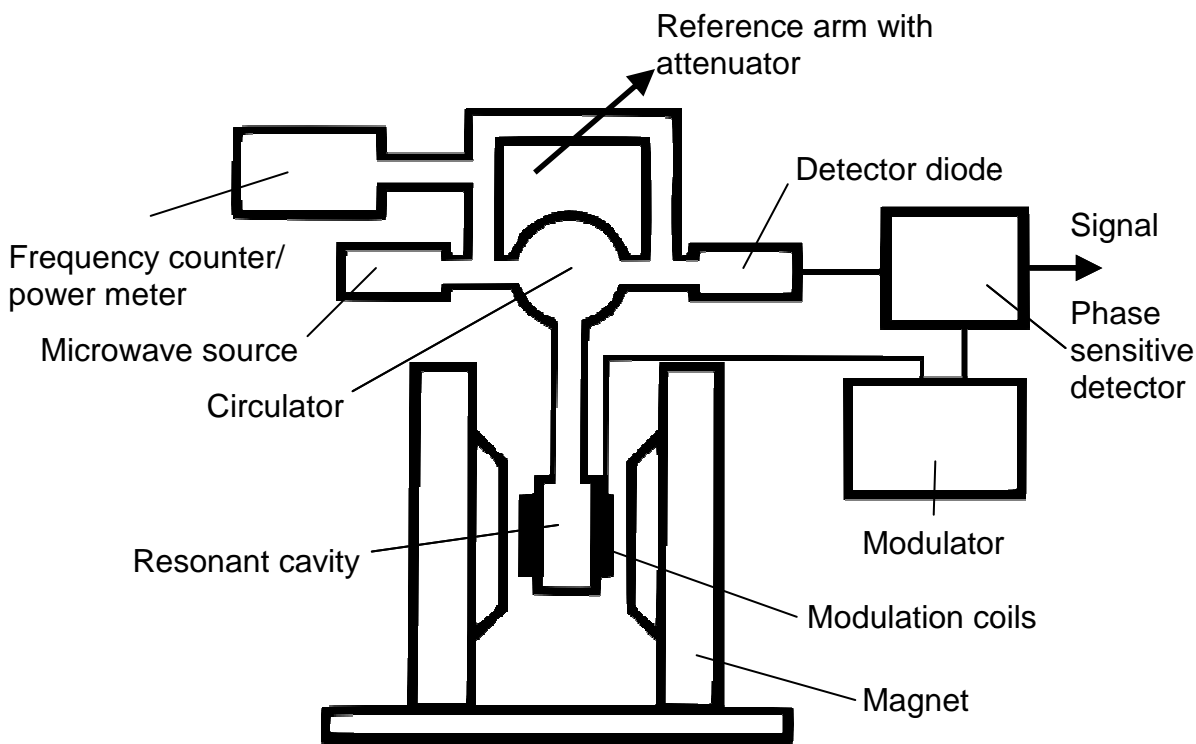


Figure 2-15. Experimental EMR schematic. The key features are a microwave source, a resonant cavity, a magnet, and a detector.

2.2.3.2 HB1A Neutron Triple-Axis Spectrometer at HFIR

The Fixed-Incident Energy Triple-Axis Spectrometer on beamline HB1A at HFIR (Figure 2-16) is ideal if the exact energies and momenta of interest in a sample are

known. Approximately five grams of deuterated Prussian blue analogue powder are required for HB1A. Momentum transfers from 0.2 to 4.9 \AA^{-1} can be measured in elastic mode, and energy transfers from roughly -35 meV to 11 meV at $q = 3 \text{ \AA}^{-1}$ can be measured in inelastic mode. In the best case, energy resolutions of $\sim 0.5 \text{ meV}$ are possible. This beamline has one of the most intense, with a flux at the sample of $\sim 2 \times 10^7 \text{ neutrons/cm}^2\text{s}$, and cleanest beams at the reactor, due in part to the pyrolytic graphite monochromator system, which fixes the incident energy at 14.6 eV. In addition to the monochromator, HB1A has a variety of analyzers to help condition the beam, with analyzer angles able to be ranged from -60° to 120° , as well as the option to place a sapphire filter in the beam before the monochromator. A variety of collimators are available at different portions of the beam, before the monochromator the collimation is 48', between the monochromator and the sample, collimators of 10', 20', 30' or 40' may be used, between the sample and the analyzer, collimators of 10', 20', 30', or 40' may be used, and finally between the analyzer and the detector, collimators of 70' or 140' are available. The fixed detectors give access to scattering angles from -5° to 120° . Finally, the maximum beam size on HB1A is 40 mm x 150 mm.

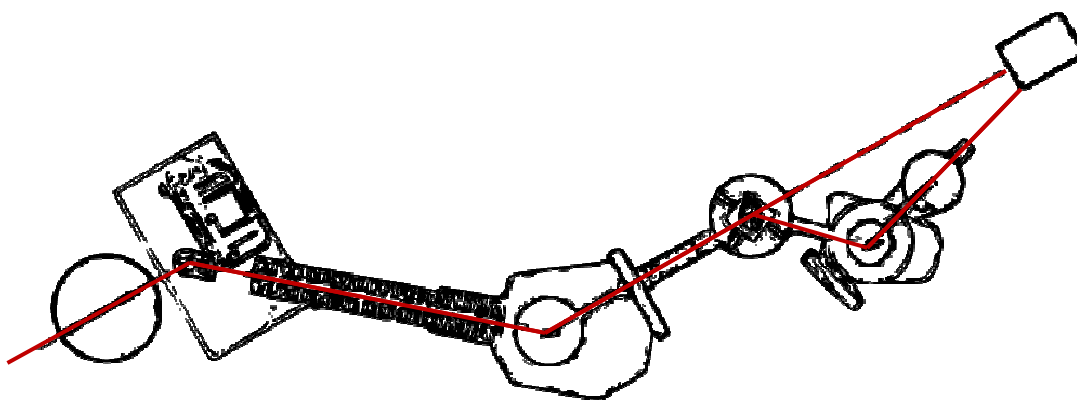


Figure 2-16. The triple-axis spectrometer at HFIR on beamline HB1A. Here, the red lines show the neutron beam.

2.2.3.3 HB2A Neutron Powder Diffractometer at HFIR

The Neutron Powder Diffractometer on beamline HB2A at HFIR (Figure 2-17) is optimized to take powder patterns, as opposed to the triple-axis machine. Approximately three grams of deuterated Prussian blue analogue powder are required for HB2A. This spectrometer is useful to refine crystal and magnetic structures. The detectors are 44 movable ^3He tubes setup to detect intensities in a Debye-Scherrer geometry. As the detectors are situated, they give access to 0° to 150° scattering angles, although the lower end may be plagued by air-scattering and the high end is weak due to the structure factors of samples. The monochromator is germanium and is capable of providing three different incident wavelengths, 1.54 Å, 2.41 Å, or 1.12 Å. The collimator may be left out of the beam, giving 12' collimation, or 16', 21' or 31' collimators may be used, at the expense of intensity. The beam is optimized for samples with a $25 \times 25 \text{ mm}^2$ cross-sectional area, but it may be masked with borated plastics if smaller samples are necessary. Finally, the maximum resolution is about 0.2° or $2 \times 10^{-3} \Delta d/d$, where d is the real space distance between lattice planes.

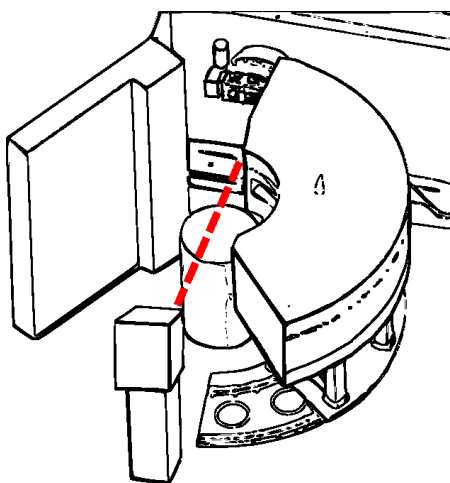


Figure 2-17. The neutron powder diffractometer at HFIR on beamline HB2A. Here, the red lines show the neutron beam.

2.2.3.4 Inelastic Neutron Scattering on SEQUOIA at SNS

Inelastic Neutron Scattering was performed on the SEQUOIA spectrometer (Figure 2-18) at SNS. Approximately five grams of deuterated Prussian blue analogue powder are required for SEQUOIA. Operating in time-of-flight mode, two choppers are utilized, a T_0 chopper to block the unwanted high-energy neutrons resulting from spallation, and a Fermi chopper to choose the incident energy range. This setup allows for an incident energy range from 10-2000 meV, but it may be possible to increase the upper limit. The energy resolution varies from 1% to 5%, getting worse in the higher energy limit. This fine energy resolution is due to the 5.5-6.3 m sample to detector distance.

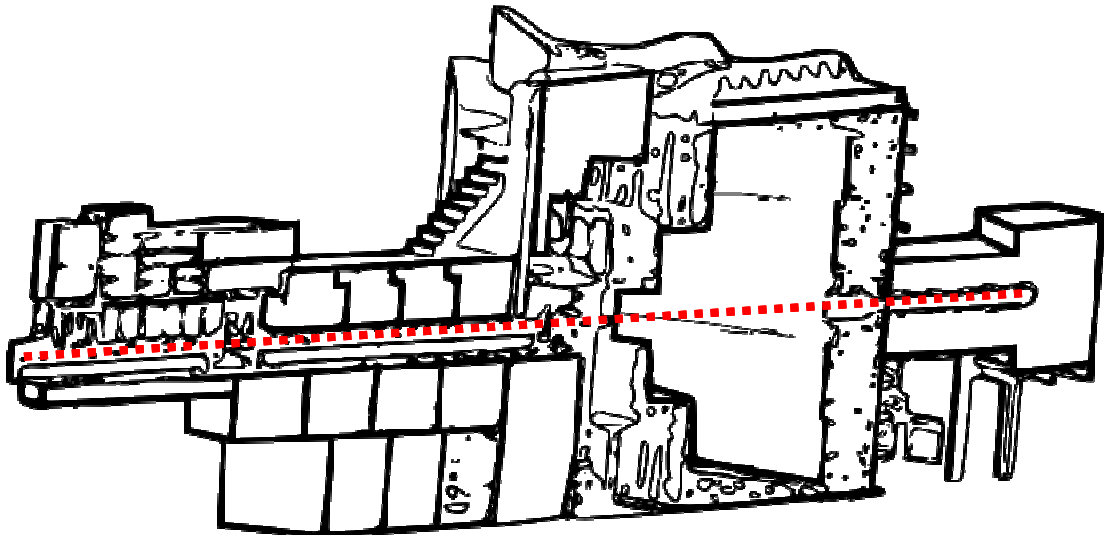


Figure 2-18. The SEQUOIA inelastic time-of-flight spectrometer at SNS. Here, the red line is the neutron beam.

2.3 Custom Apparatus

2.3.1 SQUID Probe with Low temperature Rotation and Optical Fibers

In order to study materials with magnetic anisotropy as well as photo induced magnetism, a new probe has been developed [28]. *In situ* sample rotation is a valuable tool to measure the angular dependence of the magnetization. Additionally, there is an

ongoing research effort to study materials that show changes in magnetization with applied light. Specifically, samples showing photoinduced magnetization as well as magnetic anisotropy have been identified [10] [29]. Therefore, an experimental setup that is able to measure magnetizations down to low temperatures, while affording *in situ* sample irradiation and rotation, is beneficial.

There are a few inherent difficulties one has to be aware of when setting up such a system. A probe that is suitable for use with commercial SQUID magnetometers was designed because signals can be quite small, i.e. 10^{-6} emu and less. Although using a commercial setup was considered most promising, it puts significant size and weight constraints on the probe and, most importantly, on the sample space. Also, because of the small signals involved, a minimization of the background signal from the probe is sought. Finally, care has to be taken that the system can operate at temperatures below the boiling point of ^4He . Thermal contraction and expansion of parts must be taken into account, as well the need to keep parts movable while minimizing heating. As an important part of developing the experimental setup, possible construction materials have been characterized. A probe that meets the desired specifications has been built and tested. Probe specifications, design, materials data, and operation will be presented and discussed.

2.3.1.1 Probe Specifications and Design

The probe setup is shown in Figure 2-19. Detailed machine drawings of the probe can be found in Appendix B. Sample rotation is uniaxial about an axis perpendicular to the applied magnetic field. Rotation is done with a line connecting the low temperature sample holder to a cylinder at ambient temperature, with an additional line for resetting.

Operation can be completely manual, manually controlled by a stepper motor, or automated by using computer controls for the stepper motor. Commands can be initiated in commercial software by using control data bits that are insignificant. For example, scan length parameters ranging from 4.00001 cm to 4.001 cm can be mapped onto 100 different commands and subsequently read by the stepper motor control program. A fiber optic cable allows for irradiation.

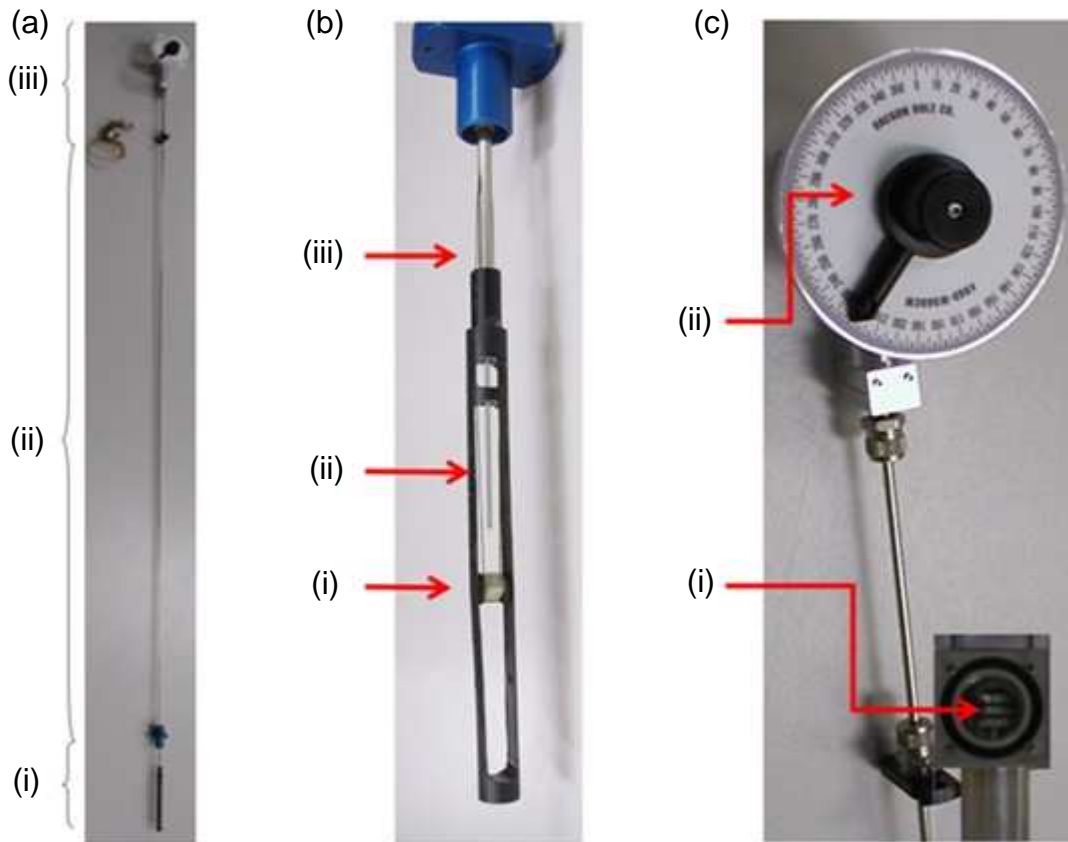


Figure 2-19. Photographs of the optical rotation probe for use in a SQUID magnetometer. (a) There are three main sections of the probe: (i) a low temperature end that sits within the SQUID coils and magnet bore and houses the rotating sample stage, (ii) a shaft that seats within an o-ring for movement of the probe through the SQUID coils that connects the high and low temperature spaces, and (iii) a head that contains the active rotation element and other probe elements. (b) A photograph of the low temperature end of the probe displays the (i) drive lines, (ii) the optic fiber, and (iii) the sample rotation cell. (c) A photograph of the top end of the probe shows (i) the drive spool, clearly visible through a clear plastic seal, and (ii) the manual dial for angular control.

The head of the probe must be light enough to accommodate the servo that translates the entire probe vertically to move the sample through the SQUID coils. The housing is aluminum because of its density, strength, and machinability. The drive shaft is beared by a slide-seal assembly consisting of o-rings and plastic spacers. Vacuum is achieved by the use of rubber o-rings for the drive shaft seal, the connection of the probe head to the shaft, and for the two additional access ports, one on the top and one on the side. The o-rings themselves do not keep the vertical position of the probe head static, so a quick connect of Teflon ferrules is attached to the probe head and can be tightened at the desired height; this variability in height can be quite useful to accommodate additional slack that may be introduced by the different thermal contraction of the long sections between room temperature and low temperature. Stycast 2850GT black epoxy seals the clear holes made for the optical fiber.

The shaft of the probe is constrained to be 0.12" (0.305 cm) OD for use in a commercial QD-MPMS SQUID magnetometer, allowing the commercial shaft seal assembly to be used. Most of the shaft is stainless steel for strength, but the bottom portion is quantalloy to minimize the background signal. The shaft is attached to the low temperature end with epoxy. For the drive lines, fishing materials were of prime consideration because they are non-metallic, thin, and strong. To decide between monofilament or braided lines, two exemplary products were studied: Spiderwire 8 lb monofilament (mono-line) and Spectra PowerPro 15 lb (braided-line). The braided-line was chosen for its larger Young's modulus, since stretching of the lines can lead to errors in sample angles. Although there is a larger magnetic signal associated with the

braided-line, the amount near the SQUID coils is only ≈ 10 milligrams. Magnetic and mechanical properties of the lines are summarized in the next subsection.

For the low temperature end of the probe, the main pieces are a yoke and a rotatable sample stage. Delrin was chosen for its compromise of strength and small magnetic signal. The yoke is long enough to be locally symmetric with respect to translations vertically through the detector coils, minimizing its flux contributions. The rotation stage is a hollow cylinder beared by plastic on plastic, with all but $\approx 90^\circ$ open for accessibility during irradiation. The drive strings are attached to the rotation stage via nylon set screws. The magnetic properties of black DelrinTM acetal polymer, brown VespelTM polyimide, and white nylon are summarized in the next subsection.

2.3.1.2 Probe Material Properties

During the design process, several candidate materials were investigated. Magnetic properties were measured in a Quantum Design MPMS-XL SQUID magnetometer, and the results are summarized in Table 2-1 and Figure 2-20. All samples were mounted in uniform straws using press fits, so no background signal was subtracted. Annealing of the Delrin was attempted in case additional magnetism was coming from free bonds [30], but no obvious change in the susceptibility was observed. Temperature sweeps were done at 100 G, 1 kG, and 1 T between 2 K and 300 K. Field sweeps were done at 2 K, 10 K, and 100 K for fields up to 7 T. The magnetic susceptibility results could be well fit to a semi-empirical formula,

$$\chi = \frac{C}{T} + L \cdot T + D \quad . \quad 2.2$$

Table 2-1. Magnetic response of candidate probe materials for the optical rotator magnetization probe. Remnant magnetizations (M_{REM}) are in emuG/gram, C is emuK/gram, L is emu/gramK, and D is emu/gram.

	T (K)	H (T)	mono-line	braided-line	Vespel	Delrin	nylon
C	2-300	1e-2	9.1068e-07	1.0671e-05	5.3498e-07	7.2737e-07	1.5198e-07
L	2-300	1e-2	-4.2817e-10	-4.1188e-09	-5.9675e-12	8.7623e-11	-8.5243e-11
D	2-300	1e-2	-1.3229e-07	2.5228e-06	8.2524e-07	8.2636e-08	-3.3978e-07
C	2-300	1e-1	1.8156e-07	6.9705e-06	5.1355e-07	2.6522e-07	9.1798e-08
L	2-300	1e-1	-1.0635e-10	-2.6259e-10	1.1519e-10	-6.5593e-12	-1.1522e-11
D	2-300	1e-1	-4.6009e-07	3.0526e-07	6.0252e-08	-3.8065e-07	-3.9787e-07
C	2-300	1	1.6334e-07	6.2278e-06	4.8105e-07	2.3244e-07	8.1238e-08
L	2-300	1	-9.9114e-11	-5.5029e-10	-8.5564e-11	-3.8665e-11	-1.5503e-11
D	2-300	1	-6.0505e-07	-4.6172e-07	-3.8356e-07	-5.0794e-07	-4.0962e-07
M_{REM}	2	7 → 0	5.4541e-05	2.3989e-04	1.5669e-04	4.7316e-05	6.2121e-06
M_{REM}	10	7 → 0	4.3157e-05	2.2723e-04	1.0041e-04	2.1461e-05	1.3669e-05
M_{REM}	100	7 → 0	-1.5032e-05	1.0743e-04	3.3839e-06	6.8093e-06	4.1010e-06

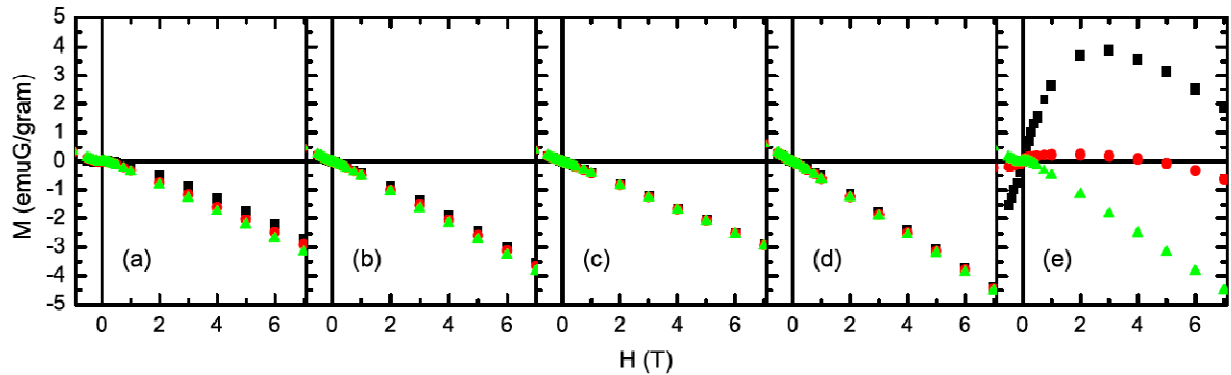


Figure 2-20. Magnetization versus field for potential optical rotation probe materials. Magnetization as a function of field measured at 100 K (green Δ), 10 K (red \bullet) and 2 K (black \blacksquare) for the mono-line (a), braided-line (b), Vespel (c), Delrin (d), and nylon (e).

Additionally, for the drive lines, some mechanical properties were investigated. Force constants were examined at room temperature to test the line deformation in response to an applied force. The mono-line has a diameter of 0.010 in (0.254 mm) and a measured Young's modulus of 1.4 GPa, which is lower than 2.3 GPa reported to us by Berkley Fishing in a private communication. The braided-line has a diameter of 0.007 in (0.1778 mm) and a measured Young's modulus of 68 GPa, which is close to the 73 – 124 GPa range reported by Honeywell for different Spectra fibers [31].

2.3.1.3 Operation

Use of the custom rotation probe is more complicated than simply using a standard MPMS sample rod. First, the user must mount the sample at the bottom of the probe, while being careful not to let grease touch the axles of the rotation cell. Next, if the fiber optic cable is desired, the side head having the fiber optic cable must be in place rather than a blank. The user must decide what form of angular control is to be used, manual, manual with the stepper motor, or automated with the stepper motor. For simple manual control, the dial will be mounted on the probe head, but for stepper motor control, the dial is removed and the stepper motor mounted in its stead. Good practice consists of testing rotation on the bench at room temperature before operation.

Extreme care must be taken as to the extent to which the probe is rotated in one direction or the other, as without such care, the user may over rotate the probe and cause damage. Generally, one should completely load one end of the spool to prepare for rotation in the opposite direction. Insertion of the probe into the SQUID should utilize the custom counterbalance and preset weight, at which point standard practices should be followed. Once the probe has been cooled to the desired temperatures, careful tensioning of the control line should be checked, since slack may be introduced upon

cooling. Tensioning may be adjusted by the set of ferrules attaching the probe head to the shaft. By the same token, if slack was taken up at cold temperatures, the user must remember to add slack to the probe before warming. If only one direction of rotation is desired, the issue of slack is less important.

If manual operation is to be used, the probe has now been completely prepared for use. If stepper motor control is to be utilized, additional steps are necessary. The driver board (Figure 2-21) must be set-up, consisting of the 12 V power supply for the motor, the 5 V power supply for the logic, and cables connecting to the probe and (if desired) the computer parallel port. To begin controlling the probe via board-only (i.e. no computer control) automated operation, make sure that switch SW3 is up. Set SB1-1, SB1-3 and SB1-5 to “up”; SB1-2 and SB1-4 can be changed at the discretion of the user. Whenever changes are made to the board’s inputs, depressing SW1 (the master reset) may be necessary. To begin controlling the probe with computer automated operation, make sure switch SW3 is in the down position. Set SB1-1, SB1-2, and SB1-5 to “down;” SB1-3 and SB1-4 can be changed at the discretion of the user. Connect the computer controller cable to CN3, making sure that position 1 is placed in the GND terminal and position 4 is placed on the CLK terminal. The bits can then be written to by the parallel port using the computer’s logic power. The “Stepper Motor Control.vi” on the SQUID computer can now be used for automated control of the motor and simultaneous data acquisition with MPMS MultiVu.

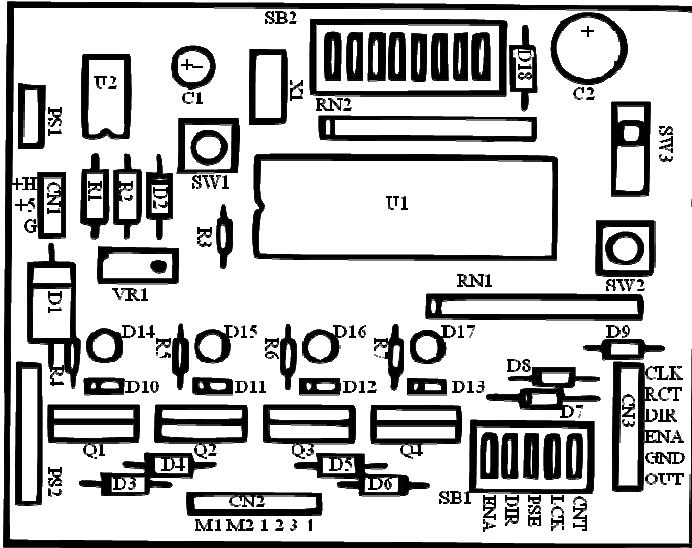


Figure 2-21. The schematic of the circuit control board for the automated operation of the custom probe using a stepper motor. Circuit elements use standard shorthand notation for, “C” for capacitors, “D” for diodes, “R” for resistors, “CN” for plugs, “SB” for switch banks, “SW” for switches.

To verify successful probe operation, a piece of magnetite with the magnetic axis aligned perpendicular to the axis of rotation was measured without any applied field. Sample rotation was tested through greater than 360° and at temperatures down to 2 K, Figure 2-22 (a). Sample irradiation was also tested using thin films of $A_j\text{Co}_k[\text{Fe}(\text{CN})_6]_l \cdot n\text{H}_2\text{O}$ oriented parallel to an applied magnetic field of 100 G at 5 K, as seen in Figure 2-22 (b).

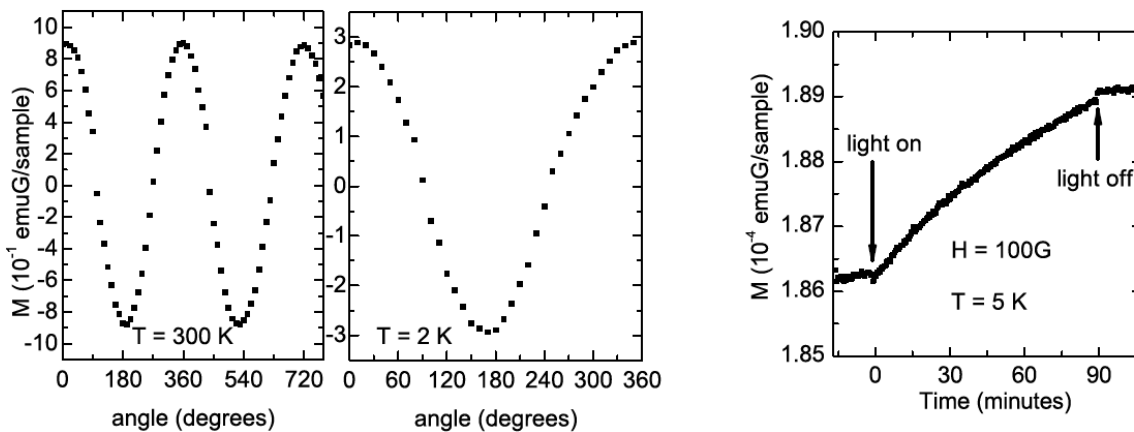


Figure 2-22. Magnetization versus rotation angle measured with the custom probe for two different magnetite samples at 300 K (a) and 2 K (b). (b) Magnetization versus time for thin films of $A_j\text{Co}_k[\text{Fe}(\text{CN})_6]_l \cdot n\text{H}_2\text{O}$. Light was introduced to the sample at $t = 0$ minutes and turned off at $t = 90$ minutes.

2.3.1.4 Conclusions

The ability to photoirradiate and rotate samples *in situ* while using the convenient setup of a commercial magnetometer has been demonstrated and represents a combination of previously unreported features. Probe materials and design have been presented with the hopes of providing insight to others who are investigating the photomagnetic properties of new materials. Future improvements may be made to the probe by more carefully etching the materials to remove possible magnetic impurities introduced by the machining process.

2.3.2 Neutron Scattering Probe for Photoinducing Opaque Powders

One final project is the photoinducing of opaque powders for neutron scattering. As this endeavor is a new experimental undertaking, a probe must be developed to provide the necessary sample environment. As of this writing, the development of a second generation of prototypes for the neutron light experiments are underway. The novel part of the sample design consists of a low temperature tumbler that allows for opaque particles to be exposed to light as a function of time, without the problem of surface particles blocking light from the rest of the sample. A schematic of the problem and proposed solution can be seen in Figure 2-23 and Figure 2-24. The expertise gained in rotating samples at low temperature with the custom SQUID probe described in the above section, as well as more standard photoinduced magnetism probes for the SQUID is invaluable in the development of such a probe.

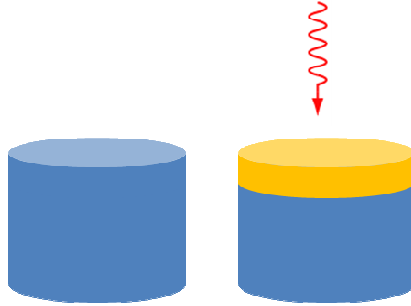


Figure 2-23. Photoirradiation of powdered neutron scattering samples. Because the powders to be photoinduced are opaque, the top layer of the powder may be photoexcited, but the majority of the sample does not become photoexcited because it does not receive any radiation. The dark state of the sample is represented by dark blue and the photoexcited state is represented by yellow.

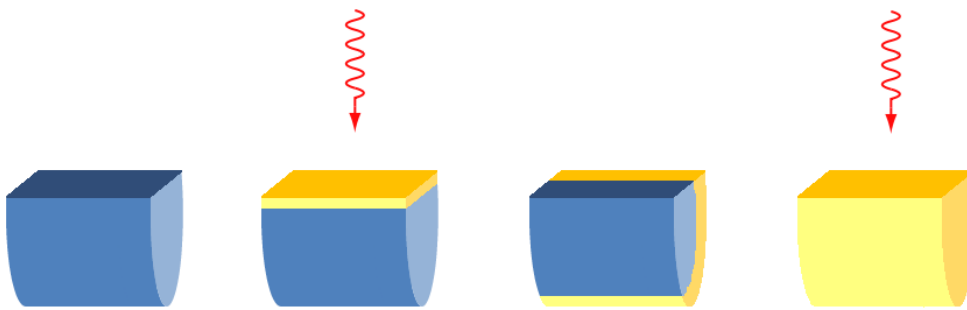


Figure 2-24. Photoirradiation of powdered neutron scattering samples using tumbler probe. To mitigate the problem of opacity, powders are instead mounted in a quartz tumbler cell that may be rotated about one axis. As irradiation starts, the same problem as a fixed cell is encountered, with the top layer blocking light from reaching the majority of the sample. However, the cell can rotate and tumble the previous top layer to be on the bottom. After a sufficiently long time, all powder within the cell will be photoexcited and measured. The dark state of the sample is represented by dark blue and the photoexcited state is represented by yellow.

CHAPTER 3 THEORETICAL METHODS

While this thesis is experimentally driven, the interpretation of experimental results is eternally intertwined with the theoretical methods that seek to explain them. This desire for more fundamental explanations of data is the main reason that an experimentalist must delve into the realm of theory, where even simple models can be predictive and further drive the experimental research. The ideology behind the theoretical applications employed in this work is not always to obtain precise quantitative explanations of results, but often to glean information from results that is not otherwise obvious using semi-empirical, transparent methods. The different experimental techniques introduced in Chapter 2 require varying degrees of post processing in order to extract the desired information, and while methods such as microscopy provide information even to the untrained eye, spectroscopy and magnetization data can be exceedingly complex and can require detailed modeling. As the studies undertaken are explicitly of the photoinduced magnetism of a coordination network, the theories presented seek to provide additional insight into this problem.

First, in Section 3.1, the general machinery of the quantum mechanical interpretation of transition metal ions within a localized picture is presented, with the different relevant energies in the system introduced one at a time. Next, Section 3.2 consists of a more *ab initio* approach that is still accessible to experimentalists, the tight-binding set of theories. Finally, in Section 3.3, the ubiquitous fitting routines based upon least-squares type methods are discussed.

3.1 Quantum Mechanics of Transition Metal Ions

The discussion will take place in a building block mode, with examples and asides inserted where convenient. Of particular interest is the calculation of energy levels, and how these energies change with the application of an external magnetic field, as these two pieces of information can be probed directly by experiment. Roughly, one can begin with a single, free ion and work from the simple hydrogen-like picture, studying the electron-electron interactions as additional electrons are added to build up a multi-electronic wavefunction. Next, it is necessary to invoke the so-called ligand field theory, as the electrostatic interaction and covalency of the ligands with the magnetic ion will add additional structure to the energy levels. The familiar spin-orbit coupling and Zeeman splitting terms from quantum mechanics are then discussed in the context of transition metal ion energy levels. From here, interacting ions are considered, via the superexchange interaction, and the many-body ground state is approximated, via mean-field theory. Finally, the motivating interpretation of experimental electron magnetic resonance, inelastic neutron scattering, UV-Vis spectroscopy, and magnetization measurements are put forward. Of high interest is the magnetization example, in which the quantum mechanical treatment discussed is applied to a novel piece of experimental data, namely the field dependence of the magnetic moment in potassium ferricyanide. While these methods are old, the advent of modern computers allows for simultaneous diagonalization of many interactions without the need to invoke perturbation theory, allowing old problems to be re-visited with more power and to provide more insight.

3.1.1 Coulomb Interaction and the Multi-Electron Ion

The hydrogen atom is a standard model, even for more complicated atomic systems, such as the transition metals [32]. However, even within this framework, building multi-electron wavefunctions is non-trivial. Therefore, the standard practice is to learn the empirical set of Hund's rules to formulate the terms that constitute a multi-electron ion [4]. These rules can be summarized as follows.

- (1) Within an electron configuration, the ground state is the term with the maximum multiplicity, and, strictly speaking, the maximum value of the spin quantum number.
- (2) Within a given spin configuration, the ground state is the term with the largest value of the angular momentum quantum number.
- (3) Finally, for less than half-filled valence shells, the ground state is the term with the least total angular momentum, and for more than half-filled shells, the ground state is the term with the most total angular momentum.

However, these empirical rules represent the obfuscated surface of the underlying Coulombic interactions and wavefunction antisymmetrization that govern the energy levels of multi-electron ions on a more fundamental level [33]. To treat the problem using the machinery of quantum mechanics, one must start with the Coulomb repulsion term,

$$V_{e-e}(i,j) = \sum_{i>j=1}^n \frac{e^2}{r_{12}} , \quad 3.1$$

where e is the charge of the electron, r_{12} is the distance between two electrons, and the sum is over all interactions within the ion. As this potential represents a pair-wise electron-electron interaction, the interaction integral can be expressed as

$$\left\langle AB \left| \frac{e^2}{r_{12}} \right| CD \right\rangle = \iint \psi_A^*(r_1) \psi_B^*(r_2) \frac{e^2}{r_{12}} \psi_C(r_1) \psi_D(r_2) dV_1 dV_2 \quad , \quad 3.2$$

where ψ is a single-electron wavefunction of a hydrogen-like atom, the subscripts denote distinct orbitals, and the integral is over all space. The treatment discussed here only considers the valence electrons of the ion, and ignores higher order effects, such as potential 4s-3d electron interactions. Practically, the integral in Equation 3.2 is calculated by expanding $V_{e-e}(i,j)$ in terms of the natural basis of the wavefunctions, which are spherical harmonics. After a few lines of calculus and the application of angular momentum selection rules,

$$\left\langle AB \left| \frac{e^2}{r_{12}} \right| CD \right\rangle = \delta(m_s^A, m_s^C) \delta(m_s^B, m_s^D) \delta(m_l^A + m_l^B, m_l^C + m_l^D) \times \sum_{k=0}^{\infty} c^k(l^A m_l^A, l^C m_l^C) c^k(l^D m_l^D, l^B m_l^B) \cdot R^k(ABCD) \quad , \quad 3.3$$

where the c^k terms are the angular integrals and the R^k terms are the radial integrals, and details of these calculations can be found in Condon and Shortley's book [34]. It is worth noting that the diagonal elements are defined as

$$J(A,B) = \left\langle AB \left| \frac{e^2}{r_{12}} \right| AB \right\rangle \quad , \quad 3.4$$

the Coulomb integral, and

$$K(A,B) = \left\langle AB \left| \frac{e^2}{r_{12}} \right| BA \right\rangle , \quad 3.5$$

the exchange integral. For equivalent electrons, $R^k(ABCD) = F^k$, where the F^k terms are referred to as the Condon and Shortly electron repulsion parameters. The c^k integrals are standard spherical harmonic overlaps, and these can be calculated. Practically, at this point, one has arrived at a single-ion Hamiltonian where these F^k terms are parameters that can be used to fit to experimental data to learn about the physics and chemistry of a given ion. Precedents show that the inclusion of only $k = 2$ and $k = 4$ terms is sufficient to parameterize the interaction [34].

A different treatment by Racah is more general and provides a slightly different parameterization of the electron-electron interactions [35]. While the derivation itself is more complicated, the Racah parameters themselves are slightly more pleasing because energy differences between terms of the same multiplicity within a given configuration only depend upon the Racah parameter B, while in the Condon-Shortley scheme, two parameters are used. However, separations between terms of different multiplicities involve both Racah parameters B and C. The electron-electron repulsion parameters in the two frameworks have a simple linear relationship,

$$B = F^2 - 5F^4 , \quad \text{and} \quad 3.6$$

$$C = 35F^4 . \quad 3.7$$

In practice, the energies and wavefunctions corresponding to the different states of the multi-electron single-ion can be solved within the matrix formulation of quantum mechanics on a personal computer. For the free Fe^{3+} ion, $B = 1,029 \text{ cm}^{-1}$ and $C/B = 4.1$ (giving $C \sim 4,220 \text{ cm}^{-1}$) [5]. An interaction diagram showing the splitting of the terms as

electron-electron repulsion is turned on is shown in Figure 3-1. It is worth noting that when the Fe^{3+} forms the hexacyanoferrate complex significant to this thesis, $B = 535 \text{ cm}^{-1}$ and $C = 4,219 \text{ cm}^{-1}$ [5].

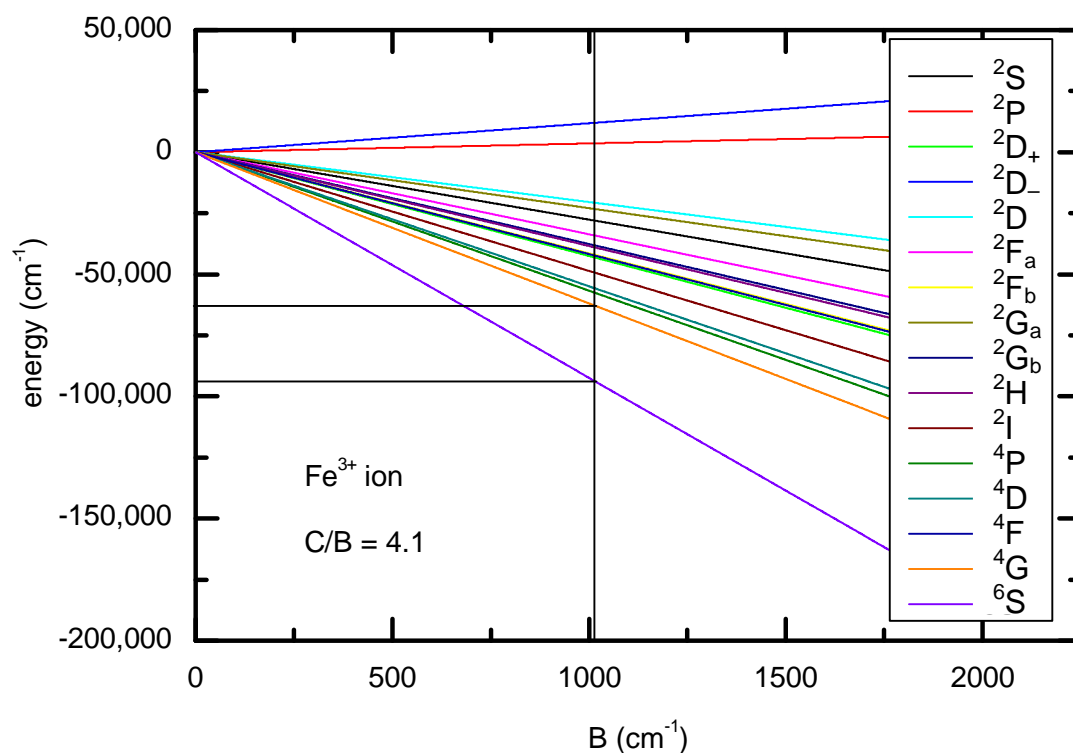


Figure 3-1. The energy differences between different $d^5 \text{Fe}^{3+}$ free-ion terms arising from electron-electron repulsion as a function of the Racah repulsion parameter B . The vertical line corresponds to the standard value for free Fe^{3+} [5].

3.1.2 Ligand Field Theory

While spin orbit coupling is a logical next single ion energy to be considered, for the 3d transition metals, the energy shifts due to interactions with surrounding ions in a molecule provide a larger perturbation, and therefore they will be considered [5] [36].

While originally, the interactions between the ion in question and the surrounding ligands were treated in the framework of an electrostatic interaction [37], quantitative

analysis has shown that most (but not all!) energy shifts are in fact due to covalency between the ions. Since both treatments are not usually performed *ab initio*, but rather semi-empirically, it is a matter of taste as to which approach provides the most personal insight. Herein, the picture where energy shifts are due to wavefunction overlap, the angular overlap model [5], will be employed. Octahedral coordination is relevant to the networks considered in this thesis, Figure 3-2, so a brief outline of such an interaction will be undertaken.

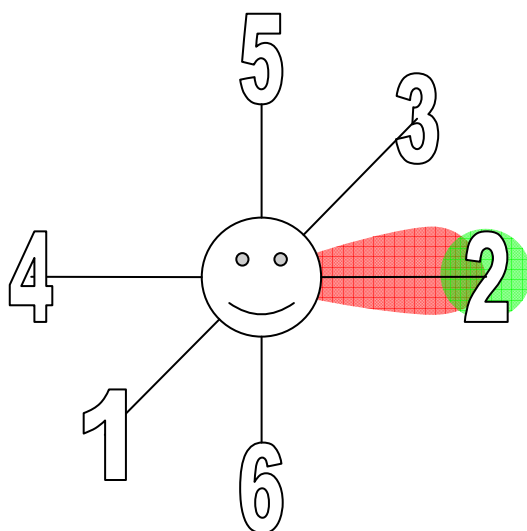


Figure 3-2. The octahedral coordination geometry. An octahedrally coordinated smiley metal ion is shown, with an overlap between a lobe of the central, red, 3d orbital with an s-wave, green, ligand orbital shown for site 2. The numbers are relevant to the Hamiltonian angular overlap parameters discussed in the text.

Taking atomic wavefunctions on ligand and ion sites, overlap integrals can be generated for each metal-ligand interaction, giving a generic angular overlap interaction matrix for an orthoaxial molecule,

$$H_{\text{ligand}} = \begin{bmatrix} \frac{3}{4}[e_{\sigma}(1)+e_{\sigma}(2)+e_{\sigma}(3)+e_{\sigma}(4)] & \frac{\sqrt{3}}{4}[e_{\sigma}(1)+e_{\sigma}(3)-e_{\sigma}(2)-e_{\sigma}(4)] & 0 & 0 & 0 \\ \frac{\sqrt{3}}{4}[e_{\sigma}(1)+e_{\sigma}(3)-e_{\sigma}(2)-e_{\sigma}(4)] & e_{\sigma}(5)+e_{\sigma}(6)+\frac{1}{4}[e_{\sigma}(1)+e_{\sigma}(2)+e_{\sigma}(3)+e_{\sigma}(4)] & 0 & 0 & 0 \\ 0 & 0 & e_{\pi x}(1)+e_{\pi x}(4)+e_{\pi y}(2)+e_{\pi y}(3) & 0 & 0 \\ 0 & 0 & 0 & e_{\pi y}(1)+e_{\pi y}(6)+e_{\pi x}(5)+e_{\pi x}(3) & 0 \\ 0 & 0 & 0 & 0 & e_{\pi x}(2)+e_{\pi x}(6)+e_{\pi y}(5)+e_{\pi y}(4) \end{bmatrix}, \quad 3.8$$

where a basis of $d_{x^2-y^2}$, d_{z^2} , d_{xy} , d_{xz} , and d_{yz} was used, with e_{σ} and e_{π} denoting overlap of the ion with σ and π orbitals of the i^{th} ligand. The x and y subscripts denote directions of the overlap of the ligand assuming a right handed coordinated system with the z-axis vector from the ligand to the ion. For π bonding that is symmetric with respect to rotations about the metal to ligand bond axis, these overlap energies are degenerate. For O_h symmetry, the standard crystal field splitting parameter of the t_{2g} and e_g strong-field-limit orbitals is simply $\Delta = 3e_{\sigma} - 4e_{\pi}$.

In practice, a Kronecker tensor product of the single-electron ion-ligand Hamiltonian, H_{ligand} , must be made for each electron to be considered. Finally the eigen problem can be solved on a standard personal computer. For a $d^5 \text{Fe}^{3+}$ ion in a symmetric octahedral field, the splitting of the free-ion states due to the ligand interaction can be calculated, Figure 3-3. It is interesting to note that under the influence of a sufficiently strong metal-ligand interaction, the ground state actually comes from the 2I term, rather than the free-ion ground state 6S term, for example, carbon ligated Fe^{3+} .

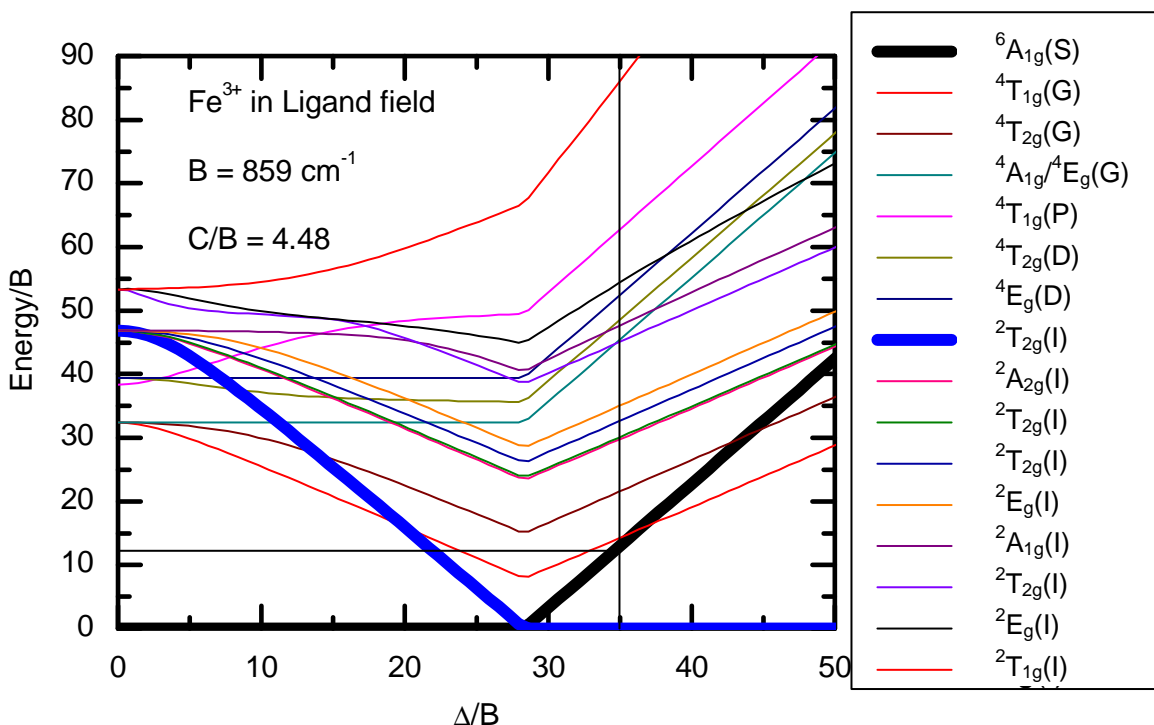


Figure 3-3. The energy of a molecular term as a function of the octahedral splitting parameter, Δ , for a d^5 ion, such as Fe^{3+} . A typical value for $\text{Fe}(\text{CN})_6^{3-}$ is denoted by the vertical line, showing a ${}^2T_{2g}$ ground state separated from the next excited state by roughly $10,000 \text{ cm}^{-1}$.

In addition to the splitting shown in Figure 3-3, due to a symmetrical octahedral field, lower symmetries further lift the degeneracies. For example, a tetragonal distortion serves to separate states of different total angular momentum within a given ligand field multiplet. For the ${}^2T_{2g}$ $\text{Fe}(\text{CN})_6^{3-}$ ground state term, such a distortion is exemplified in Figure 3-4. Lower symmetries of the six-fold ligand field are also possible, such as a trigonal distortion. However, in practice these distortions may be small, or they may serve to overparameterize the problem in such a way as to render the meaning of the high-order distortion parameters unclear. For the molecules under consideration in this thesis, a tetragonal distortion is sufficient to capture the salient features of the energy spectrum.

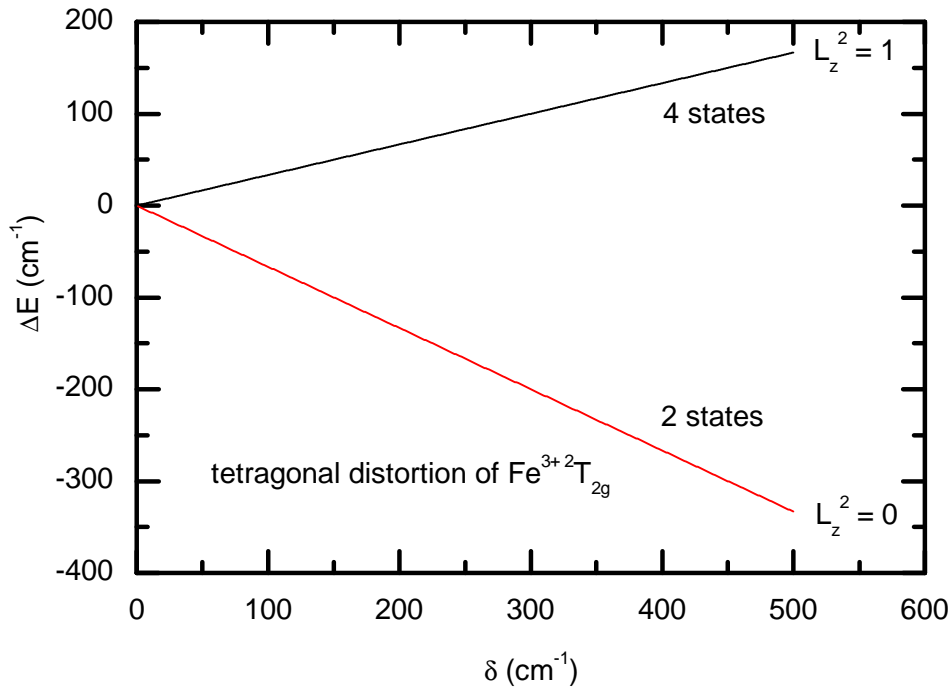


Figure 3-4. Energy shift plotted versus the tetragonal distortion parameter, δ . Specifically, for a $d^5 2T_{2g} Fe(CN)_6^{3-}$ ground term.

3.1.3 Spin-Orbit Coupling

Spin-orbit coupling arises from the magnetostatic interactions of the inherent spin angular momentum of an electron with the orbital angular momentum [4]. The hydrogen-like single electron Hamiltonian

$$H_{\text{single, S-O}} = \xi \mathbf{l} \cdot \mathbf{s} \quad , \quad 3.9$$

where ξ is the single electron spin-orbit coupling parameter, \mathbf{l} is the angular momentum, and \mathbf{s} is the spin moment. The single electron spin-orbit coupling parameter scales linearly with the effective charge of the nucleus, and therefore becomes more important the heavier the ion is. For multiple electron ions, the spin-orbit interaction energy becomes

$$H_{\text{S-O}} = \sum_i \xi(i) \mathbf{l}_i \cdot \mathbf{s}_i = \lambda \kappa \mathbf{L} \cdot \mathbf{S} \quad , \quad 3.10$$

where λ is the multi-electron spin-orbit coupling parameter, and Stephens' reduction factor κ has been introduced to take into account the quenching of orbital angular momentum due to the ligands. The angular momentum reduction factor can vary between zero and one, depending upon the local environment, and it is often somewhere in between. The multiple-electron spin-orbit parameter is related to the single-electron parameter as

$$\lambda = \pm \xi / 2S \quad , \quad 3.11$$

with a plus sign for less than half-full shells, and the minus sign for greater than half-full shells, as for the latter, the picture is one of positively charged holes [5] [33].

In practice, the solution of this spin-orbit Hamiltonian is analogous to those posed in the previous sections. For a $d^5 \text{Fe}^{3+}$ ion in a symmetric octahedral field of cyanides, it was shown that the ground state is a well separated ${}^2T_{2g}$, Figure 3-3. The effect of the spin-orbit coupling on this term can be calculated as the interaction is turned on, and for different values of the reduction parameter, κ (Figure 3-5).

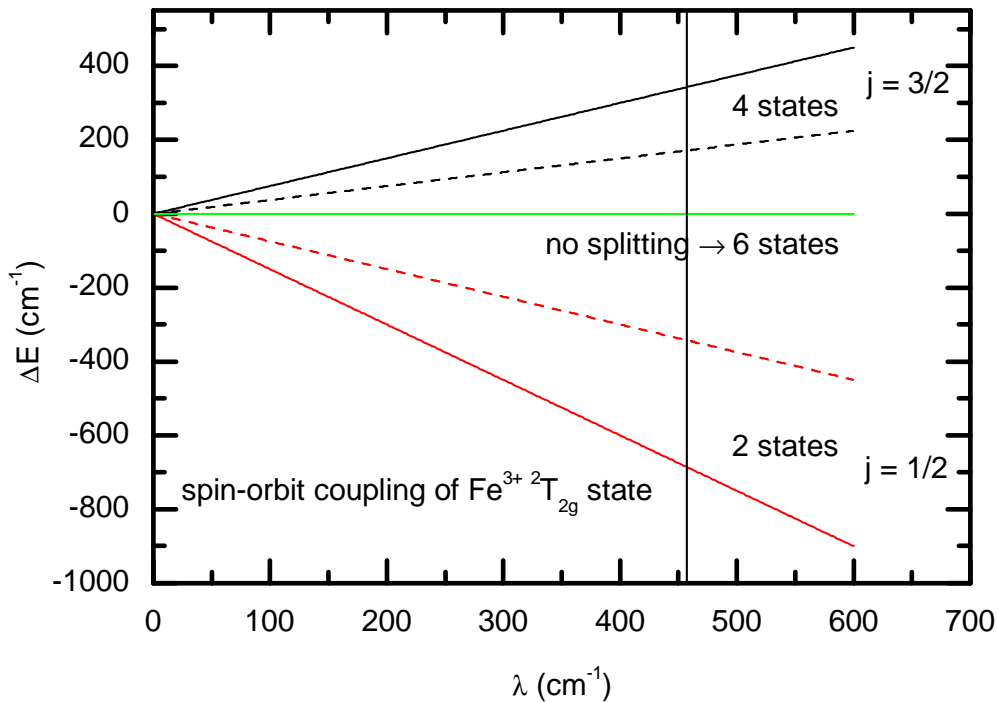


Figure 3-5. Energy splitting of the octahedral hexacyanoferrate ${}^2T_{2g}$ ground state. Energies are shown for $\kappa = 1$ (solid lines), the $\kappa = 0$ totally quenched (green line), and a partially quenched $\kappa = 0.5$ state (dashed lines). In the presence of spin-orbit coupling, the six-fold degeneracy of the ${}^2T_{2g}$ state is lifted for different values of the total angular momentum, j . The vertical line at 460 cm^{-1} is the free ion value of spin orbit coupling [5]. Clearly if the orbital moment is completely quenched, spin-orbit coupling has no effect.

3.1.4 Zeeman Splitting

The response of a magnetic ion to an external magnetic field is called the Zeeman effect [4]. This effect can be written in the straightforward fashion

$$H_{Zeeman} = \mu_B H (\kappa L_z + 2S_z) \quad , \quad 3.12$$

where μ_B is the Bohr magneton, H is the applied magnetic field, κ is the orbital reduction parameter, L_z is the component of the angular momentum along the magnetic field, and S_z is the component of the spin angular momentum along the magnetic field.

Experimentally, this term is the smallest yet considered, with maximum interaction energies of $\sim 10\text{ cm}^{-1}$ for fields less than 10 T. However, this term is

essential when considering the magnetization of a sample, since changes in energies with applied magnetic field are detected with a magnetometer. The effect of this term on spin-orbit split ${}^2T_{2g}$ -like ground state of the hexacyanoferrate ion can be calculated for different values of the orbital reduction factor, Figure 3-6.

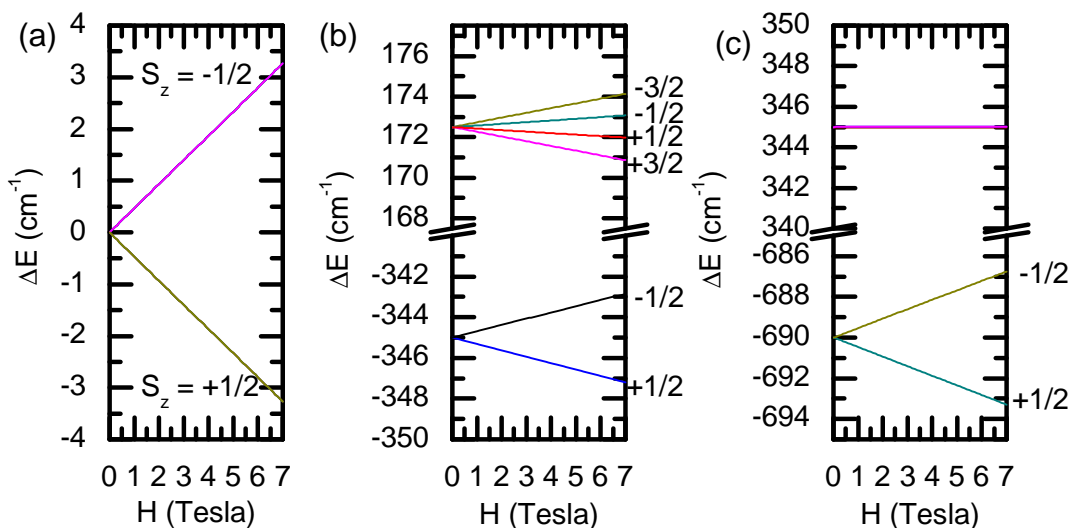


Figure 3-6. The Zeeman splitting versus applied magnetic field for the spin-orbit split ${}^2T_{2g}$ -like ground state of hexacyanoferrate. Energies are shown for (a) $\kappa = 0$, with no angular momentum, (b) $\kappa = 0.5$, the angular momentum is partially quenched, and the magnetic field splits the $j = 3/2$ into a quartet and the $j = 1/2$ into a doublet, and (c) $\kappa = 1$, with no quenching of the angular moment, the $j = 3/2$ term is robust and the $j = 1/2$ term is split into a doublet.

3.1.5 Superexchange Interaction

Superexchange is a result of second-order perturbation theory. It is the most relevant ion-ion interaction for coordination compounds, like those studied in this thesis. The superexchange interaction arises from a mutual wavefunction overlap with a shared ligand and two ionic centers. While the connectivity can be greater than two-fold and span an entire lattice, superexchange is still a two body exchange interaction. This interaction can give rise to a splitting between the singlet and triplet states of a dimer, effectively aligning the spins parallel or anti-parallel. Using the molecular orbital theory

model put forward by Hoffman [38], the leading terms in the superexchange energy can be written in terms of the integrals between dimer A and dimer B, such that

$$E_{\text{triplet}} - E_{\text{singlet}} = J_{AB}^{\text{superexchange}} = -2K_{AB} + \frac{(2h_{AB})^2}{J_{AA} - J_{AB}} \quad , \quad 3.13$$

where K and J are the familiar exchange and Coulomb integrals previously introduced (Equations 3.4 and 3.5), and h_{AB} is difference of ionization potentials of the dimer A and dimer B magnetic orbitals. Since the exchange integral is always positive, the first term in Equation 3.13 leads to ferromagnetic interaction, and the second term in Equation 3.13 leads to antiferromagnetic interaction. For multiple magnetic orbitals, the contributions can be summed, to first order. This model effectively reproduces the empirical Goodenough-Kanamori rules for the sign of superexchange, where the interactions are ferromagnetic for orthogonal orbitals and antiferromagnetic for orbitals with substantial overlap [39].

3.1.6 Mean-Field Theory

If the superexchange interaction is present to an appreciable degree, the problem becomes a many-body system of all ions in the lattice. Many body problems cannot be solved exactly, but by invoking a mean-field approximation to the free energy, many features of the many-body ground state can be reproduced [40] [41] [42] [43]. For simplicity, considering only the superexchange of spins associated with nearest transition metal neighbors, designated as *n.n.*, under the influence of an applied magnetic field, the Hamiltonian has the form

$$H = -2 \sum_{i,j=n.n} J_{ij} S_i \cdot S_j + g\mu_B H \sum_i S_i \quad , \quad 3.14$$

where J is an exchange constant (not to be confused with the Coulomb integral, please note context), g is the Landé factor, μ_B is the Bohr magneton, S is the electronic spin, and H is the applied field. The mean-field expansion of the spin operator gives

$$H \approx H_{MF} = -2 \sum_{i,j=n.n.} J_{ij} \langle S_i \rangle \cdot S_j - 2 \sum_{i,j=n.n.} J_{ij} S_i \cdot \langle S_j \rangle + 2 \sum_{i,j=n.n.} J_{ij} \langle S_i \rangle \cdot \langle S_j \rangle + g\mu_B H \sum_i S_i \quad , \quad 3.15$$

where $\langle S \rangle$ denotes an average spin polarization value. For the case of a spatially independent average spin polarization, one can further simplify the problem to a diagonal Hamiltonian,

$$H_{MF} = -2 \sum_i 2ZJ_0 \langle S \rangle \cdot S_i + 2ZJ_0 N \langle S \rangle^2 + g\mu_B H \sum_i S_i \quad , \quad 3.16$$

where Z is the number of nearest neighbors, J_0 is the scalar exchange constant, and N is the total number of spins.

Expressions for the average spin polarization can be derived by minimizing the free energy with respect to variation of the spin polarization, yielding,

$$\langle S \rangle = S \cdot B_S \left(\frac{g\mu_B S H_{ext}}{k_B T} + \frac{2ZJ}{k_B T} S \cdot \langle S \rangle \right) \quad , \quad 3.17$$

where B_S is the Brillouin function [44], k_B is the Boltzmann constant, and $\langle \dots \rangle$ denotes an average. Equation 3.17 is transcendental and therefore cannot be solved exactly, but must be done numerically. For the specific example of a lattice of Fe^{3+} ions with spin-orbit split ${}^2T_{2g}$ -like ground states and fully quenched angular momentum, the resulting solutions for values of $g\mu_B H_{ext}/k_B = 0.01$ and $2Z/k_B = 1$ are shown in Figure 3-7.

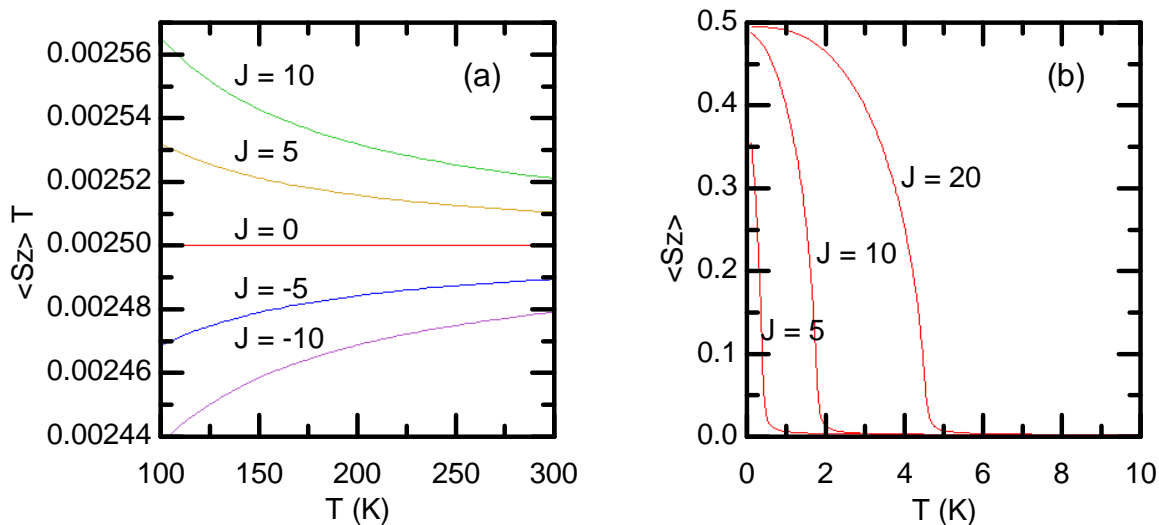


Figure 3-7. The effect of superexchange on magnetization. (a) The effect of superexchange on the average spin value along the magnetic field above the magnetically ordered state is shown for an $S = 1/2$, Fe^{3+} ion for both ferromagnetic ($J > 0$) and antiferromagnetic interactions ($J < 0$), Equation 3.17. (b) The average spin value along the magnetic field shows sharp increases corresponding to long-range magnetic order, with increasing ordering temperatures for increasing values of the superexchange parameter, J . Here only ferromagnetic examples are shown, as antiferromagnetic samples have no net magnetic moment in their ordered state.

It should be mentioned that disorder and random effects can give rise to complicated and highly degenerate microstates, such as the spin-glass (relevant to Prussian blue analogues), but a detailed discussion of these effects cannot be simply understood by any low-energy theories, and are therefore beyond the scope of this thesis [45] [46]. It is worth noting that external stimuli, such as sufficiently strong magnetic fields, can tune a disordered system away from a spin-glass-like state towards more standard magnetic states.

3.2 Tight-Binding Approximations

While the previous section outlining semi-empirical methods of quantum mechanics is useful, an additional level of understanding can be gained by a more fundamental approach to calculation of energy levels. Because the coordination

networks studied can be understood in terms of a perturbed molecular orbital picture, as opposed to an itinerant electron picture, tight-binding approximations are appropriate to approximate the energy levels of the systems. The most common tight-binding approximation is using a linear combination of atomic orbitals (LCAO), and a further approximation is the extended Hückel theory [47]. While quantitative results are not expected with these methods, oftentimes qualitative features of the systems can be reliably reproduced. Specifically, tight-binding methods are useful for understanding the nature of the chemical bonding in a system. In the following, a simple example of the carbon and nitrogen interaction leading to a CN molecule will be outline first. Next, specific examples of tight-binding calculations to approximate ligand fields, superexchange interactions, and force-fields between atoms will be discussed. This final point is relevant when interpreting infrared vibrational spectroscopy data, often used to delineate between different types of heterobinuclear moieties present in Prussian blue analogues.

3.2.1 Extended Hückel Theory

The Schrödinger equation can often be written down for a complex system, but rarely solved exactly. Three standard approximations are employed in solving the Schrödinger equation within the Hückel formalism. First, the Born-Oppenheimer approximation assumes that electrons move in a field of fixed nuclei, due to the disparate masses of the two types of particles. Second, the independent particle approximation makes the assumption that the total many-electron wave function can be written down as a product of the single-electron wave functions. Third, only the valence electrons are considered in the calculation, as the electrons in filled orbitals are mostly inert.

Aside from specific fitting of experimental data, tight-binding calculations of molecules act as a sandbox from which valuable chemical intuition may be extracted. Each molecular orbital is given as a linear combination of atomic orbitals. The basis set used is spherical harmonics for the angular part of the wavefunction, and Slater-type orbitals for the radial part of the wave function. Slater-type orbitals are a further approximation to the hydrogen-like orbitals in which

$$R(r) = Nr^{n-1}e^{-\zeta r} \quad , \quad 3.18$$

where N is a normalization factor, n is the principle quantum number, and z is a semi-empirical parameter that characterizes the diffuseness of the orbital. For more diffuse orbitals, such as the 3d set, a double-zeta expansion is used consisting of a linear combination of two Slater-type orbitals. The problem is then reduced to an eigen problem for the coefficients of the atomic orbitals in the basis set,

$$HC = SCE \quad , \quad 3.19$$

where H is a square matrix containing the one electron energy integrals (analogous to those discussed in Section 3.1.1 on electron repulsion within the Condon and Shortley regime), and C is the coefficient matrix, S is the matrix of overlap integrals, and E is the diagonal matrix of orbital energies. In practice, the coefficient matrix is found by the variational method to minimize the total energy of the system. The core matrix elements of the single electrons are given by atomic energies, and for the off-diagonal elements, by the Wolfsberg and Helmholz approximation,

$$H_{ij} = \frac{1}{2}K(H_{ii} + H_{jj})S_{ij} \quad , \quad 3.20$$

where S is the overlap integral, and K is a scaling parameter introduced to account for the increased overlap in molecules. While the fundamental calculation of K is not done, experimental studies of ethane by Hoffman showed that $K = 1.75$ is suitable [47].

A somewhat straightforward example involving the bonding of carbon and nitrogen to form the cyanide molecule, which is highly relevant to the cyano-bridged networks studied in this thesis, will now be presented. The calculation involves the four valence atomic orbitals of carbon $C(2s)$, $C(2p_x)$, $C(2p_y)$, and $C(2p_z)$, and the four valence atomic orbitals of nitrogen $N(2s)$, $N(2p_x)$, $N(2p_y)$, and $N(2p_z)$. Therefore the cyanide molecule will have a basis set of 8 atomic wave functions, and Equation 3.18 will require the inversion of 8×8 matrices. The solution to Equation 3.18 gives both the molecular orbitals and their energies, which are shown in Figure 3-8. The lowest anti-bonding orbital, the π^* , is especially important to the magnetization of the Prussian blue analogues, because it acts as a strong electron acceptor on the carbon-dominated molecular orbitals and mediates the superexchange between metal ions.

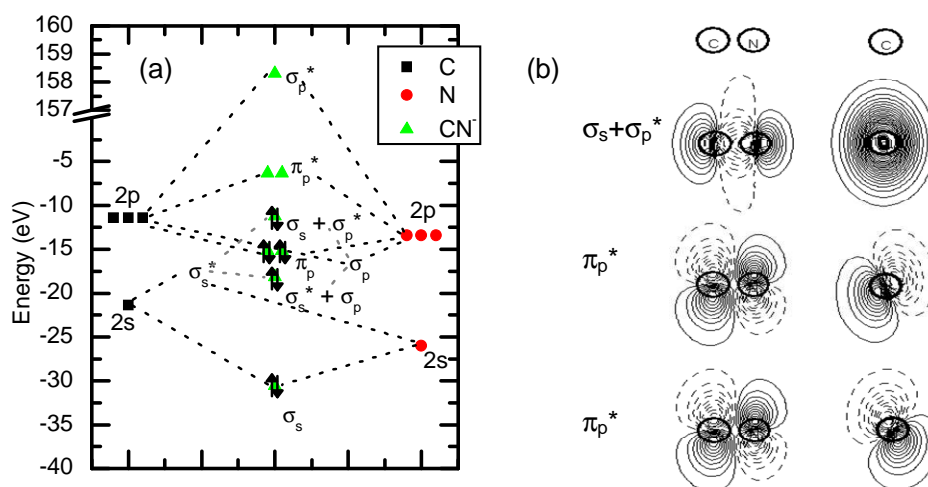


Figure 3-8. The cyanide molecule. (a) An extended Hückel interaction diagram shows how carbon and nitrogen are able to lower their energy by forming a cyanide molecule. (b) An illustration of the π_p^* and $\sigma_s + \sigma_p^*$ orbitals of the CN molecule relevant for the formation of extended cyano-bridged coordination networks.

3.2.2 Ligand Field Theory

While the parameters used in ligand field theory are best utilized as fitting parameters to experimental data, it is also possible to calculate them from fundamental principles. However, calculating from first principles is a difficult problem. It is not surprising that qualitative methods such as LCAO methods are unable to provide quantitative predictions for the desired parameters, and more complicated methods such as Density Function Theory (DFT) are not, themselves, parameterized in such a way to make the ligand field theory parameters assignable from these calculations. However, it is desirable to glean qualitative trends from first principles to help explain experimental trends, such as the relative ligand field strengths of different atoms and the effects of distortions on the ligand field. Two specific examples will be briefly introduced: (1) the difference in the octahedral ligand field splitting parameter for a $\text{Co}(\text{NC})_6^{4-}$ molecule compared to the $\text{Fe}(\text{CN})_6^{3-}$ molecule, and (2) the effect of tetragonal distortions on the energy levels of a $\text{Ni}(\text{NC})_6^{4-}$ and $\text{Cu}(\text{NC})_6^{4-}$ molecules.

3.2.3 Superexchange Interaction

The superexchange interaction introduced in Section 3.1.5 was again dealt with completely as an empirical parameter. Like the ligand field splitting parameters, the qualitative changes in the superexchange constant may be investigated with extended Hückel theory.

3.2.4 Infrared Vibrational Spectroscopy

Quantitative theoretical analysis of the cyanide stretching frequencies in Prussian blue analogues is still lacking. This situation is unfortunate, given the high degree to which scientists use cyanide stretching frequencies as diagnostic tools to assign oxidation states and coordination numbers in cyanometallate compounds. Although a

quantitative solution should be possible using modern density functional theories, such a study is beyond the scope of this thesis, and instead a tight-binding analysis was attempted in order to understand the trends observed. Unfortunately, the tight-binding approximations are inadequate for this level of structure determination and no meaningful information could be extracted from the studies.

3.3 Fitting Algorithms

More often than not, experimental scientists are forced to deal with overdetermined systems. The classic example of an overdetermined system is a data set with many points that a researcher would like to fit to a function having fewer parameters than there are data points. This situation happens all the time, daily for many people. All is not lost, especially if one has access to a math machine, such as a standard personal computer. The ubiquitous technique employed is a method of least squares.

In Section 3.3.1, the general procedure of least squares fitting is overviewed. In Section 3.3.2, the Levenberg-Marquardt algorithm that was extensively employed for fitting functions in this thesis is discussed. In Section 3.3.3, the specific example of least squares fitting used to fit all diffraction data in the thesis, the Rietveld method, is overviewed.

3.3.1 Least Squares

The process of fitting data comes down to minimizing the difference between the function that is fit and the data. These differences are called the residuals of the fit. The name “least squares” refers to the fact that, in this method, a square of the difference between the data and the fitting function is used [48]. The squared difference is used instead of the absolute difference for the simple reason that this allows the

residuals of the fit to be treated as a continuous differentiable quantity. An important thing to remember when using this method is that the squaring of the residuals effectively weights outliers stronger than other data. Therefore, if data points are known to be erroneous they should be excluded, or one can additionally weight the residuals by the known experimental errors involved.

A straightforward derivation can illustrate these points. The least square fit parameter, S , is defined as the sum of the square of the residuals

$$S = \sum_{i=1}^n r_i^2 \quad , \quad 3.21$$

where there are n discrete data points. Explicitly, these residuals are the difference between the experimental data and the fitting function,

$$r_i = y_i - f(x_i, \beta) \quad , \quad 3.22$$

which depends upon the independent experimental variable and the fitting parameters.

This parameter may be minimized by setting the derivative with respect to changes in the function parameters equal to zero.

$$\frac{\partial S}{\partial \beta_j} = 2 \sum_{i=1}^n r_i \frac{\partial r_i}{\partial \beta_j} = 0, j = 1, \dots, m \quad , \quad 3.23$$

where there are m parameters. By substituting Equation 3.22 into Equation 3.23, one gets

$$-2 \sum_{i=1}^n r_i \frac{\partial f(x_i, \beta)}{\partial \beta_j} = 0, j = 1, \dots, m \quad . \quad 3.24$$

If the function $f(x_i, \beta)$ depends linearly upon the fit parameter,

$$f(x_i, \beta) = \sum_{j=1}^m \beta_j F_j(x_i) \quad , \quad 3.25$$

the derivative is straightforward

$$\frac{\partial f(x_i, \beta)}{\partial \beta_j} = F_j(x_i) \quad . \quad 3.26$$

If a tensor is defined such that

$$X_{ij} \equiv F_j(x_i) \quad , \quad 3.27$$

The solution to the linear least square problem becomes clear, namely

$$\beta = (X^T X)^{-1} X^T y \quad . \quad 3.28$$

3.3.2 Levenberg-Marquardt

While the linear least squares case is straightforward, complicating issues arise when the function in question is nonlinear, and a more complicated approach must be used. Here the Levenberg-Marquardt algorithm can be utilized [49] [50]. In order to find the minimum of a function $F(x)$ that is a sum of squares of nonlinear functions, $f_i(x)$, i.e.

$$F(x) = \frac{1}{2} \sum_{i=1}^m [f_i(x)]^2 \quad . \quad 3.29$$

Let the Jacobian of $f_i(x)$ be denoted $J_i(x)$, then the Levenberg-Marquardt method searches in the direction given by the solution p to the equations

$$(J_k^T J_k + \lambda_k I) p_k = -J_k^T f_k \quad , \quad 3.30$$

where λ_k are nonnegative scalars and I is the identity matrix.

3.3.3 Rietveld Refinement

Rietveld refinement was used to interpret powder diffraction patterns from neutron and x-ray scattering experiments [51]. Specifically, the GSAS [52] and EXPGUI [53] computer programs were used for all refinements. This technique refers to the use of least squares fitting of experimental data with theoretical models, and it is called refinement because it can only modify parameters within a given test model, rather than predict the appropriate model *a priori*. In essence, the refinement consists of minimizing the function which depends upon the square of the difference between the fit and the data, such that

$$F(R) = \sum_i W_i(\text{experiment} - c \times \text{model})^2 \quad , \quad 3.31$$

where W_i is the statistical weight and c is an overall scale factor. Because of this short-coming, crystallographers must test many different models to arrive at a solution.

Practically, most of the information that goes into a Rietveld refinement comes from the Bragg condition for constructive interference of scattered waves

$$Q = \frac{4\pi \sin(\theta)}{n\lambda} \quad , \quad 3.32$$

where Q is the momentum transfer, θ is the scattering angle, n is the order of the reflection, and λ is the incident wavelength. Or, conversely, the Bragg condition can be reformulated as the Laue condition

$$\vec{k} \cdot \vec{R} = \frac{1}{2} \vec{K} \quad ,$$

where \vec{k} is the incidence wave vector, and \vec{K} is the momentum transfer ($\vec{K} \equiv \vec{k}' - \vec{k}$, where \vec{k}' is the final wave vector). For a powder pattern, the Bragg reflections can be thought of in terms of the Ewald sphere [42]. The Ewald sphere is the surface generated by rotating the incident wave-vector through the origin and testing to see if a reciprocal lattice point lies on the surface of the sphere at a distance $|\vec{K}|$ from the origin, thus satisfying the Laue condition. The random distribution in a powder sample averages over all possible scattering angles, so that each reciprocal lattice vector generates a sphere of radius $|\vec{K}|$. This powder scattering sphere will intercept the Ewald sphere to create a circle, so long as $|\vec{K}|$ is less than $2|\vec{k}|$. The vector between a point on the intersecting circle and the end of the incident wave vector is the final momentum \vec{k}' , that satisfies the Laue scattering condition. Formally,

$$|\vec{K}| = 2|\vec{k}| \sin\left(\frac{\theta}{2}\right) , \quad 3.34$$

therefore, by measuring the angular dependence of the scattered intensities of a powder, information about all Bragg reflections corresponding to reciprocal lattice vectors shorter than $2|\vec{k}|$ is available.

While the gross features are captured by the positions of the reflections, the intensities of the reflection contain important information about the structure of the atoms within a unit cell. The geometric structure factor modulates the intensities by

$$S(\mathbf{K}) = \sum_{j=1}^n e^{i\mathbf{K} \cdot \vec{d}_j} , \quad 3.35$$

where $S(\mathbf{K})$ is the geometric structure factor, and \vec{d}_j are the positions of the atoms within the unit cell. This structure factor can diminish observed Bragg peaks due to interference between waves scattered within a given unit cell. For neutron refinements, an additional magnetic factor due to the spin scattering must be added to the atomic scattering.

Finally, aside from the position and intensities of the Bragg reflections, information is also contained in the shape of the lines. Crystallite size can serve to broaden the lines, as a departure from infinite space symmetry occurs. This final point is particularly relevant to nanostructured materials.

CHAPTER 4 QUANTITATIVE ANALYSIS OF MAGNETIZATION IN COMPLEX CYANIDES

Using the experimental and theoretical machinery described in the previous two sections, a quantitative analysis of the magnetization in select Prussian blue analogues and their paramagnetic precursors can be made. The two magnets of particular interest to this thesis are $\text{Cs}_{2.8}\text{Ni}_4[\text{Cr}(\text{CN})_6]_4 \cdot n\text{H}_2\text{O}$, which has a high ordering temperature of 60 to 90 K [54], and $\text{Co}_4[\text{Fe}(\text{CN})_6]_3 \cdot n\text{H}_2\text{O}$, which can display photoinduced magnetism when proper proportions of interstitial ions are included in the lattice [1]. In addition, paramagnetic precursors of these materials, $\text{K}_3\text{Cr}(\text{CN})_6$ and $\text{K}_3\text{Fe}(\text{CN})_6$, will be presented for comparison. A well parameterized Hamiltonian, whose components may be determined by experimental measurements, is sought. Specifically, electron spectroscopy, magnetic neutron diffraction, and magnetization measurements are sufficient to fully determine the relevant Hamiltonian for magnetization in these systems. As for most problems, many paths to a possible solution may exist, and the best approach may depend upon personal taste and the availability of resources. One recipe of the many possible is outlined in this chapter.

The author would like to stress the dangers of using improper, incomplete, or misunderstood recipes when modeling the magnetization of the systems in question. For example, the change in magnetic susceptibility as a function of temperature may be due to multiple effects, including spin-orbit coupling, structural distortions, and superexchange. If the model is underdetermined, it may be impossible to separate the different contributions. In the same vein, the use of simple equations without a full understanding of their derivation should be avoided at all costs. A common culprit is the Curie-Weiss formula, $\chi = C/(T-\theta)$, where the assumption that all deviations from high

temperature Curie-like behavior come only from superexchange is often assumed by the unaware researcher, even in systems with first order orbital angular momentum. This issue, and others, may be avoided if proper companion measurements to magnetization are performed, where the Hamiltonian to be considered contains only well understood parameters.

In Section 4.1, spectroscopy experiments, designed to determine the single-ion parameters are discussed. These measurements help in determining possible spin and orbital states for ions. In Section 4.2, magnetization measurements performed to detect the presence of magnetic order are presented. In Section 4.3, microscopic probes of the magnetic structure are presented. Finally, in Section 4.4, known parameters are summarized and a fit of the magnetization data is presented.

4.1 Synthesis and Chemical Composition

The precursor materials were used without modification after purchase from Acros. The powders of $\text{Cs}_{2.8}\text{Ni}_4[\text{Cr}(\text{CN})_6]_4 \cdot n\text{H}_2\text{O}$ and $\text{Co}_4[\text{Fe}(\text{CN})_6]_3 \cdot n\text{H}_2\text{O}$ were synthesized by Matthieu F. Dumont. Chemical formulae were determined using ICP-MS for the relative ratios of all elements excepting hydrogen, which was determined by multiplying the oxygen content by two. The ICP-MS was performed by Complete Analysis Laboratories, Inc. (www.calilabs.com).

4.2 Spectroscopy

Even before beginning a spectroscopy experiment, it is useful to have knowledge of the general atomic environment and structure of the material. For Prussian blue analogues, a good starting point is always the simple cubic structure that was assigned after single-crystal diffraction studies of Prussian blue [55]. The structure consists of metal ions linked by cyanides in a unit cell with two metals, Figure 4-1. From this space

model, the point symmetry and local environments of the magnetic atoms can then be determined.

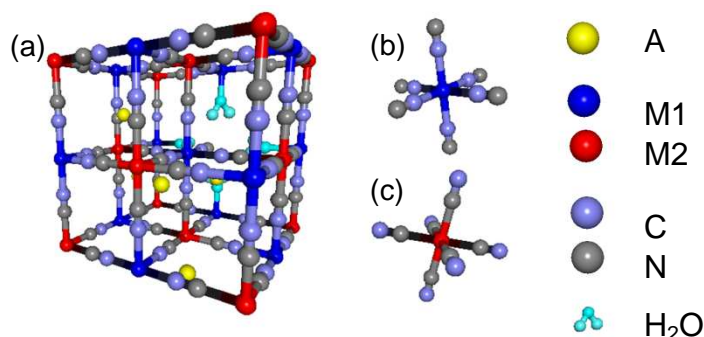


Figure 4-1. The cubic complex cyanide Prussian blue analogue structure. (a) A representation of the crystal structure of a generic Prussian blue analogue, $A_rM1_k[M2(CN)_6]_r \cdot nH_2O$. (b) The $M1(NC)_6$ molecular sub-unit to be considered for single-ion excitations. (c) The $M2(CN)_6$ molecular sub-unit to be considered for single-ion excitations.

Two different types of spectroscopy may be applied to the materials in question, INS for excitations from ~ 25 meV to ~ 1 eV (spanning the energies of spin-orbit coupling and structural distortions) and UV-Vis for excitations from ~ 1 eV to ~ 6 eV (for which ligand field interactions and electron repulsion are relevant energies). Inelastic neutron scattering has not yet been exploited for complex cyanides, but at the end of May 2010, a collaboration between UF and ORNL should remedy this lack of data. Ultraviolet and Visible spectroscopy, on the other hand, has been performed on $Cs_{2.8}Ni_4[Cr(CN)_6]_4 \cdot nH_2O$, $Co_4[Fe(CN)_6]_3 \cdot nH_2O$, $K_3Cr(CN)_6$, and $K_3Fe(CN)_6$. Results are conclusive for determining the ligand field splittings of nickel and chromium ions, Figure 4-2. However, iron has transitions from the π of the CN^- to the d-levels of the metal in the same energy range. The ligand to metal transitions have much larger probabilities than d-d transitions, rendering the standard UV-Vis spectroscopic determination of iron ligand field states with standard UV-Vis spectrometers difficult.

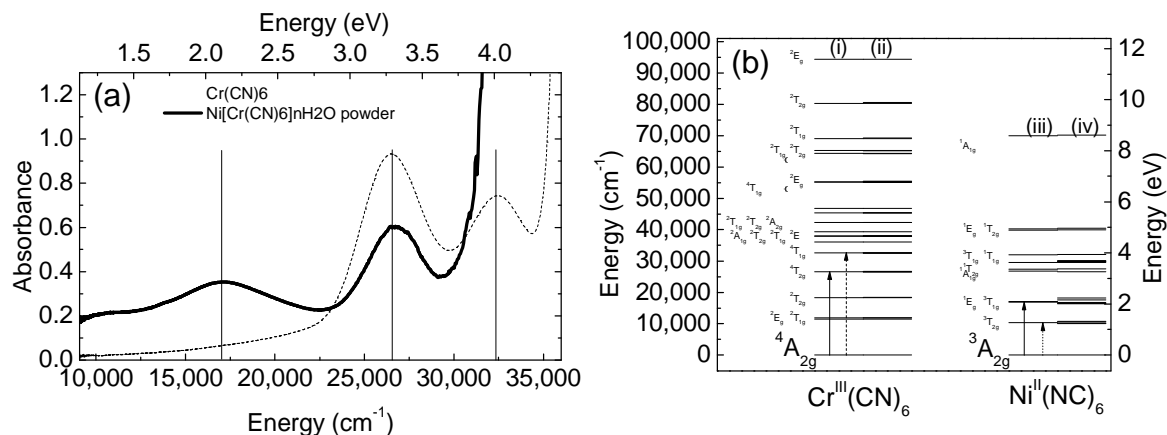


Figure 4-2. UV-Vis of $\text{Rb}_{0.7}\text{Ni}_{4.0}[\text{Cr}(\text{CN})_6]_{2.9}\cdot n\text{H}_2\text{O}$. (a) Room temperature UV-Vis spectroscopy measurements of the d-d transitions present in 10 mM $\text{Cr}(\text{CN})_6$ precursor (---), and a 10 mM $\text{Rb}_{0.7}\text{Ni}_{4.0}[\text{Cr}(\text{CN})_6]_{2.9}\cdot n\text{H}_2\text{O}$ powder with background subtracted by using the functional form of a diamagnetic $\text{Rb}_{0.5}\text{Zn}_{4.0}[\text{Fe}(\text{CN})_6]_{2.8}\cdot n\text{H}_2\text{O}$ (—). (b) Using the transitions shown in Figure 4-2 (a), a multiplet calculation can be performed to show the electronic energy levels for the Ni^{2+} and Cr^{3+} ions in the Prussian blue network. Chromium energy levels are shown for (i) no spin-orbit coupling and (ii) using reported values of spin-orbit coupling for the free ion [5]. Nickel energy levels are shown for (iii) no spin-orbit coupling and (iv) using reported values of spin-orbit coupling for the free ion [5].

4.3 Magnetic Susceptibility

The next experiment consists of a temperature dependent magnetic susceptibility measurement down to the lowest temperatures available. The point of this measurement is to look for anomalies in the shape that may be characteristic of magnetic phase transitions. The magnetization data for $\text{K}_3\text{Cr}(\text{CN})_6$ and $\text{K}_3\text{Fe}(\text{CN})_6$ do not show any anomalies, whereas the Prussian blue analogues, $\text{Cs}_{2.8}\text{Ni}_4[\text{Cr}(\text{CN})_6]_4\cdot n\text{H}_2\text{O}$ and $\text{Co}_4[\text{Fe}(\text{CN})_6]_3\cdot n\text{H}_2\text{O}$, show divergence of the magnetic susceptibility at ~ 90 K and ~ 13 K, respectively, Figure 4-3. These transition temperatures may be used to estimate the magnitude of the superexchange parameter using mean-field theory,

$$T_C = \frac{\sqrt{Z_A Z_B} |J_{AB}|}{3k_B} \sqrt{S_A(S_A+1)S_B(S_B+1)} \quad , \quad 4.1$$

where T_C is the ordering temperature, Z is the number of nearest neighbors, J is the superexchange constant, S is the spin quantum number, and k_B is the Boltzmann constant. It is important to note that Equation 4.1 can only give the magnitude of the superexchange parameter, but not the sign.

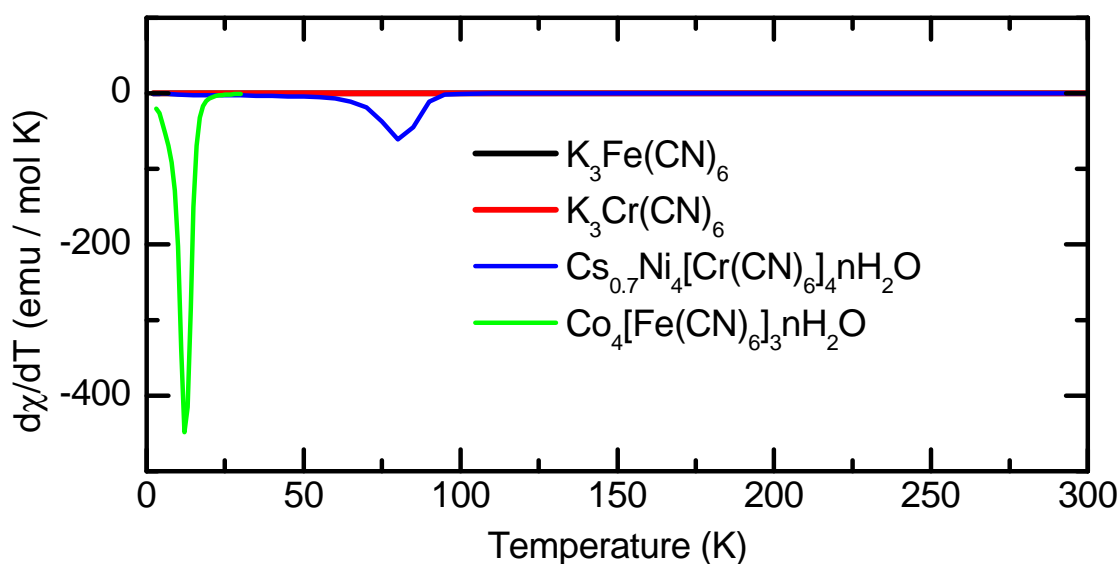


Figure 4-3. Measurement of magnetic ordering temperature in $\text{Cs}_{2.8}\text{Ni}_4[\text{Cr}(\text{CN})_6]_4 \cdot n\text{H}_2\text{O}$, $\text{Co}_4[\text{Fe}(\text{CN})_6]_3 \cdot n\text{H}_2\text{O}$, $\text{K}_3\text{Cr}(\text{CN})_6$, and $\text{K}_3\text{Fe}(\text{CN})_6$. A derivative of the DC magnetic susceptibility, in an applied field of 100 G, as a function of temperature is shown to display magnetic transitions, from paramagnetic to either ferromagnetic or ferrimagnetic states. The $\text{K}_3\text{Fe}(\text{CN})_6$ and $\text{K}_3\text{Cr}(\text{CN})_6$ materials are seen to be paramagnetic from 2 K to 300 K. The $\text{Cs}_{2.8}\text{Ni}_4[\text{Cr}(\text{CN})_6]_4 \cdot n\text{H}_2\text{O}$ and $\text{Co}_4[\text{Fe}(\text{CN})_6]_3 \cdot n\text{H}_2\text{O}$ materials show divergence of the magnetic susceptibility at ~ 13 K and ~ 90 K, respectively.

4.4 Microscopic Probe of Magnetization

While magnetization or specific heat measurements can determine the magnitude of the superexchange constant, true determination of the magnetic structure requires a microscopic probe. One possible probe is magnetic neutron diffraction.

Neutron diffraction of $\text{Cs}_{2.8}\text{Ni}_4[\text{Cr}(\text{CN})_6]_4 \cdot n\text{H}_2\text{O}$ has been performed, and a ferromagnetic structure was found [56]. For $\text{Co}_4[\text{Fe}(\text{CN})_6]_3 \cdot n\text{H}_2\text{O}$, an x-ray magnetic circular dichroism measurement has been reported [57], however the electronic transitions present in the spectra are not well enough understood to be quantitatively modeled, and macroscopic magnetic susceptibility data was relied upon for analysis of the microscopic data. For this reason, it is crucial to perform a study of the magnetic structure of $\text{Co}_4[\text{Fe}(\text{CN})_6]_3 \cdot n\text{H}_2\text{O}$ using a more easily modeled probe, such as neutron diffraction, where the relevant interactions are understood. The proposal to perform such an experiment has been accepted and is scheduled to be performed at ORNL on the HB2A beamline of HFIR in May 2010.

4.5 Magnetization Fitting

At this point, a parameter set is available for the different compounds, Table 4-1. Here, certain parameters could not be determined from the available measurements, but plausible estimates can be made based upon spectroscopic and nephelauxetic series [5]. Once the ground term has been assigned, the first order relevant energy scales are spin-orbit coupling and superexchange.

Table 4-1. Parameters to be used in modeling magnetization data for $\text{Cs}_{2.8}\text{Ni}_4[\text{Cr}(\text{CN})_6]_4 \cdot n\text{H}_2\text{O}$, $\text{Co}_4[\text{Fe}(\text{CN})_6]_3 \cdot n\text{H}_2\text{O}$, $\text{K}_3\text{Cr}(\text{CN})_6$, and $\text{K}_3\text{Fe}(\text{CN})_6$. Δ is the octahedral splitting parameter, B and C are electron repulsion parameters, ζ is the spin-orbit coupling parameter, κ is the orbital reduction factor, J is the superexchange parameter, and the ground states have been calculated based upon the previous parameters. Units are all in cm^{-1} , unless specified.

complex	Δ	e_π	e_σ	B	C	ζ	κ	J	ground state
$\text{Co}^{2+}(\text{NC})_6$	11,000	0	3,667	885	4,253	515	0-1.5	± 13 K	$^4\text{T}_{2g}$
$\text{Fe}^{3+}(\text{CN})_6$	35,000	-1,000	10,333	535	4,219	460	0-1		$^2\text{T}_{2g}$
$\text{Ni}^{2+}(\text{NC})_6$	11,000	0	3,667	1,044	4,594	630	-	$+90$ K	$^3\text{A}_{1g}$
$\text{Cr}^{3+}(\text{CN})_6$	26,000	-1,000	7,333	933	3,732	275	-		$^4\text{A}_{1g}$

Magnetization [3] [58] is one of the more complex quantities to critically understand because it does not just depend upon the energy levels of a system, but rather how those energy levels respond to an applied magnetic field

$$M = -\frac{dE}{dH} \quad . \quad 4.2$$

One can use Boltzmann statistics to calculate the average magnetization resulting from the thermal population of a set of calculated energy levels, E_i ,

$$\langle M \rangle = \frac{\sum_i \left(-\frac{dE_i}{dH} \right) e^{-E_i/k_B T}}{\sum_i e^{-E_i/k_B T}} \quad . \quad 4.3$$

For the magnetization calculations in this section, the well separated, ligand-field ground term will be used as a starting point.

4.5.1 $K_3Cr(CN)_6$

First, consider the magnetization of the $K_3Cr(CN)_6$ material. The parameters in Table 4-1 suggest that a good Hamiltonian to calculate magnetization between 2 K and 300 K may be

$$H = \mu_B H (2S_z) \quad , \quad 4.4$$

where μ_B is the Bohr magneton, H is the external magnetic field, and S_z is the spin moment along the field direction. The agreement between model calculations, using Equation 4.4, and experiments is astonishing, as no fitting parameters are used, Figure 4-4. The slight deviations between experiment and model may be due to errors in background subtraction, or second order spin-orbit coupling effects coming from mixing with excited states of similar symmetry. The decrease in the χT values at low

temperatures is real, present in both the model and the experimental, and is due to a violation of the $H/T \ll 1$ limit for Curie behavior.

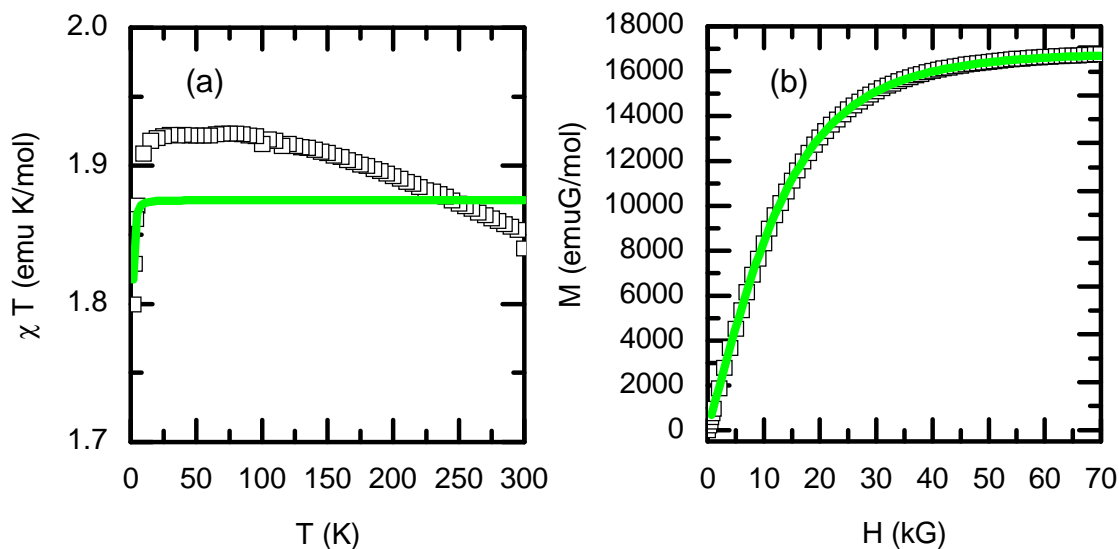


Figure 4-4. Magnetic properties of $K_3Cr(CN)_6$. (a) χT versus T and (b) magnetization versus field for $K_3Cr(CN)_6$, from a SQUID magnetometer experiment (\square), and model calculations (—).

4.5.2 $K_3Fe(CN)_6$

The next material, $K_3Fe(CN)_6$, has unquenched orbital angular momentum that gives an additional level of complexity. In light of this orbital contribution, a plausible Hamiltonian is then

$$H = \mu_B H (\kappa L_z + 2S_z) + \lambda (\kappa L \cdot S) \quad , \quad 4.5$$

where μ_B is the Bohr magneton, H is the external magnetic field, λ is the spin-orbit coupling constant, L_z is the orbital moment along the field direction, S_z is the spin moment along the field direction, and κ is the orbital reduction parameter. While structural distortions might exist (and in the most rigorous case, should be included), for simplicity, these effects may be approximated by the κ parameter. It is also noteworthy that the use of powder data makes additional parameterization suspicious. The experimental data of $K_3Fe(CN)_6$ may be compared to a model without orbital

contributions (Equation 4.4) and one with orbital contributions (Equation 4.5), Figure 4-5. The failure of the spin-only model to reproduce the magnitude of the magnetization as a function of field and temperature is striking for this material, in contrast with $K_3Cr(CN)_6$. The fact that the moment is anomalously large at high temperatures and small at low temperatures is a suggestive signature of the presence of orbital moments and spin-orbit coupling. With spin-orbit coupling parameters of $\sim 100 \text{ cm}^{-1}$ for the iron series ions, the width of the energy multiplet is nearly equal to the thermal difference between 300 K and 2 K. Discrepancies of the fit can be attributed to the known structural transition at 70 K and the lack of a structural distortion parameter in the fitting Hamiltonian. These higher-order effects go beyond the scope of the current discussion and analysis.

These data clearly illustrate two important lessons for fitting magnetic data of organometallic compounds. First, a simple application of $\chi = C/(T - \theta)$ would yield $\theta \sim 40 \text{ K}$, although spin correlations of that magnitude can be completely ruled out by the absence of a divergence in the susceptibility in the relevant temperature range. Second, a simple application of a spin-only Hamiltonian with a scaled g-factor cannot reproduce the data, unless an appreciable temperature dependence of the effective g-factor was introduced.

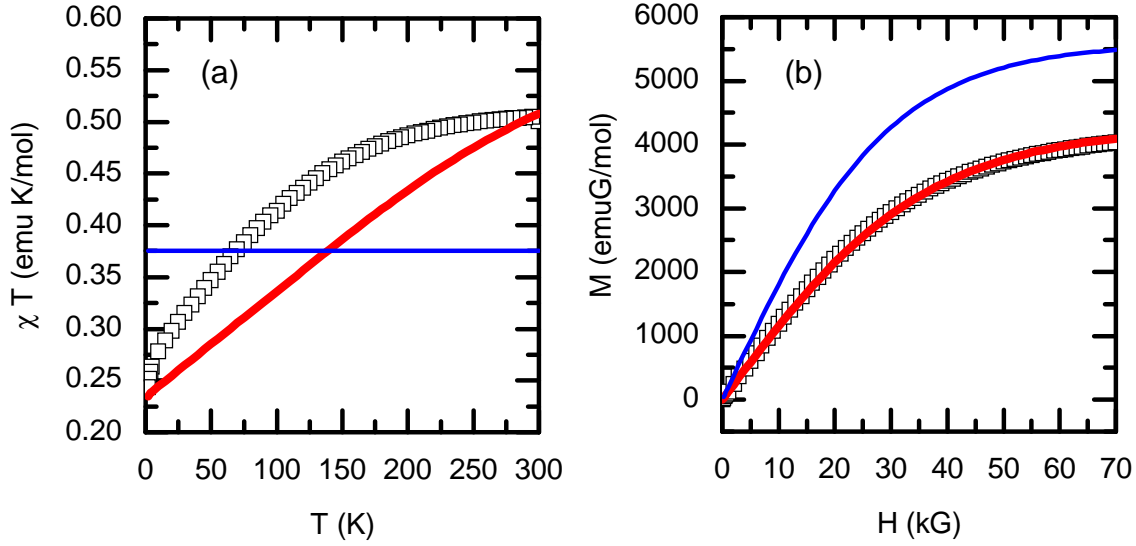


Figure 4-5. Magnetic properties of $\text{K}_3\text{Fe}(\text{CN})_6$. (a) χT versus T and (b) magnetization versus field for potassium ferricyanide, from a SQUID magnetometer experiment (\square), a simple model with only Zeeman splitting of the $^2T_{2g}$ ground state ($—$), and a model including both spin-orbit interaction and Zeeman splitting of the ground state ($—$). A reduction parameter of $3/4$ was found to fit best. It is clear that even qualitative features of the data cannot be fit without spin-orbit coupling.

4.5.3 $\text{Cs}_{2.8}\text{Ni}_4[\text{Cr}(\text{CN})_6]_4 \cdot n\text{H}_2\text{O}$

The next material to be considered is $\text{Cs}_{2.8}\text{Ni}_4[\text{Cr}(\text{CN})_6]_4 \cdot n\text{H}_2\text{O}$. This material possesses two magnetic ions, Ni^{2+} and Cr^{3+} , that both have orbital singlet ground states. Therefore, to first order, orbital angular momentum should not affect the magnetization. However, the observed divergence of the magnetic susceptibility and subsequent neutron diffraction studies showed strong spin-spin correlations associated with superexchange. Therefore, a reasonable Hamiltonian should be

$$H = \mu_B H (2S_z) - 2 \sum_{i,j=n.n.} J_{ij} \mathbf{S}_i \cdot \mathbf{S}_j \quad , \quad 4.6$$

where μ_B is the Bohr magneton, H is the external magnetic field, λ is the spin-orbit coupling constant, S_z is the spin moment along the field direction, and J is the superexchange parameter. The many body portion of Equation 4.6 can be

approximated with a mean-field solution, as described in Section 3.1.6. In addition, demagnetizing effects will be present in the low field magnetically ordered data and the phenomenological approach described in Section 6.4.1, that scales the magnetization by a domain factor will be used. Good global agreement of the magnitude and shape of the model calculation compared to the experimental data is found, Figure 4-6.

Deviations near the onset of magnetic order are expected due to the approximate nature of the mean-field approach. Additional differences may be due to 2nd order orbital momentum effects, notorious for these ions [36].

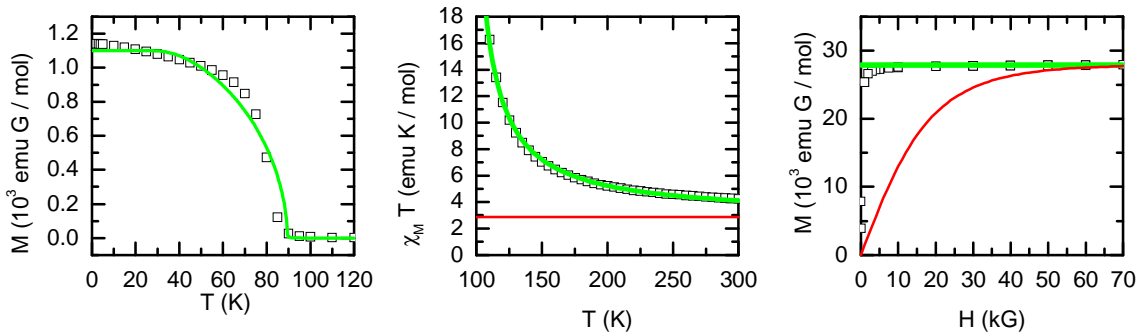


Figure 4-6. Magnetic properties of Cs_{2.8}Ni₄[Cr(CN)₆]₄·nH₂O. (a) Magnetization versus temperature, (b) χT versus temperature, and (c) magnetization versus field for Cs_{2.8}Ni₄[Cr(CN)₆]₄·nH₂O, from a SQUID magnetometer experiment (\square), a mean-field model taking into account interacting spins (---), and a model neglecting spin-spin interactions (---).

4.5.4 Co₄[Fe(CN)₆]₃·nH₂O

Co₄[Fe(CN)₆]₃·nH₂O is the final, most complicated material to be considered. As seen by the parameters in Table 4-1, Co₄[Fe(CN)₆]₃·nH₂O has both spin-spin correlations and first order orbital angular momentum. A reasonable Hamiltonian to try modeling the system is

$$H = \mu_B H (\kappa L_z + 2S_z) + \lambda (\kappa \mathbf{L} \cdot \mathbf{S}) - 2 \sum_{i,j=n.n.} J_{ij} \mathbf{S}_i \cdot \mathbf{S}_j \quad , \quad 4.7$$

where μ_B is the Bohr magneton, H is the external magnetic field, λ is the spin-orbit coupling constant, L_z is the orbital moment along the field direction, S_z is the orbital

moment along the field direction, J is the superexchange parameter and κ is the orbital reduction parameter. Like the $\text{Cs}_{2.8}\text{Ni}_4[\text{Cr}(\text{CN})_6]_4 \cdot n\text{H}_2\text{O}$, the many body interaction is solved using mean-field theory, and the low field, ordered state is expected to be multi-domain. The author is currently in the process of debugging his full-fledged code for this Hamiltonian, so at this point, only high temperature expansion fits are made. Similar to the paramagnetic $\text{K}_3\text{Fe}(\text{CN})_6$ precursor that has one of the chromophores present in $\text{Co}_4[\text{Fe}(\text{CN})_6]_3 \cdot n\text{H}_2\text{O}$, first an illustrative attempt to fit the data using a spin-only formula is made, Figure 4-7. For all fits, both signs of J will be used in order to see which one produces smaller residuals.

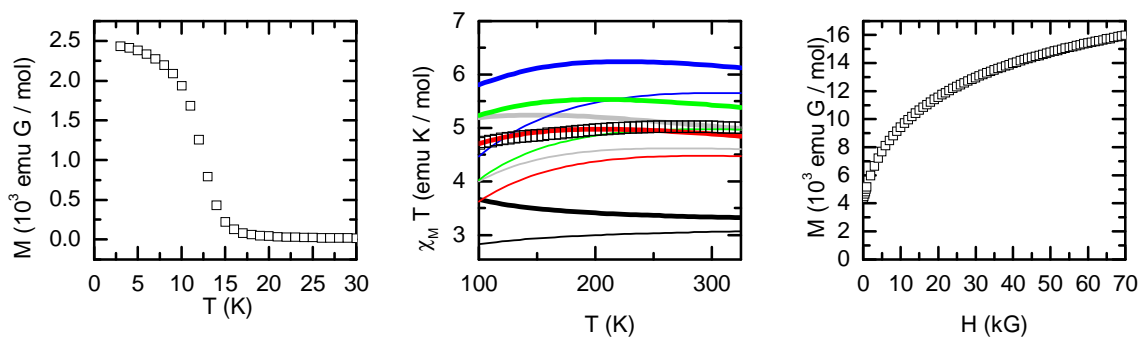


Figure 4-7. Magnetic properties of $\text{Co}_4[\text{Fe}(\text{CN})_6]_3 \cdot n\text{H}_2\text{O}$. (a) Magnetization versus temperature, (b) χT versus temperature, and (c) magnetization versus field for $\text{Co}_4[\text{Fe}(\text{CN})_6]_3 \cdot n\text{H}_2\text{O}$ (actually normalized to $\text{Co}_{1.5}[\text{Fe}(\text{CN})_6] \cdot n\text{H}_2\text{O}$ to compare directly to literature), from a SQUID magnetometer experiment (\square), a model without orbital moments (—), and different models having degrees of quenching of the orbital moments, with full moments on Co and Fe (—), reduced orbital momentum on the Fe (—), reduced orbital momentum on the Co (—), and reduced orbital moments on both ions (—). Here, bold lines correspond to ferromagnetic models and thin lines correspond to ferrimagnetic models.

While the antiferromagnetic J can reproduce the shape of the susceptibility as a function of temperature quite well without needing to include orbital moments, the magnitude of the magnetization is terribly wrong, Figure 4-7. This disagreement is good reason to include orbital moments, as in the originally hypothesized formula,

Equation 4.7. The magnitude of the magnetization after including first order angular momentum is in much better agreement with experimental data. Perhaps surprisingly, the shape can now also be reproduced with a ferromagnetic J , as a decrease in the susceptibility with temperature now also takes place because of the depopulation of high orbital momentum states, just as in $K_3Fe(CN)_6$. Preliminary fits of the field dependence yield similar conclusions. One tell-tale sign of orbital contributions in these compounds is the finite slope of magnetization at high magnetic fields, which is absent in systems with first order orbital singlets.

In the end, the $Co_4[Fe(CN)_6]_3 \cdot nH_2O$ fitting is the most complicated, but most intriguing as well. Although χT decreases with temperature, an observation that has lead scientists to conclude antiferromagnetic interactions based upon application of the Curie-Weiss law, a full fit that properly concludes orbital contributions actually suggests *ferromagnetic interactions may be present*. Whichever the case, these questions should be answered with the inelastic neutron scattering and magnetic diffraction experiments scheduled at ORNL at the end of May 2010.

CHAPTER 5 COBALT HEXACYANOFERRATE NANOPARTICLES

Nanotechnology represents an exciting new frontier of science, and the study of nanoparticles is bound to uncover additional scientifically and technologically relevant phenomenon in the coming years. Nanoparticles are materials between a few nanometers and a few hundred nanometers, and often behave differently from microparticles and bulk crystals of the same material. For this reason, nanoparticles of the photoactive Prussian blue analogue cobalt hexacyanoferrate were studied and presented in this thesis. Different interstitial cations were used to investigate different material properties, as the choice of rubidium, potassium, or sodium has subtle effects on the magnetization of the host material. These results for the nanoparticles are best understood within the greater context of past studies on similar bulk materials.

The investigation of the magnetism of Prussian blue, $\text{Fe}_4[\text{Fe}(\text{CN})_6]_3 \cdot n\text{H}_2\text{O}$, and related analogues has a rich history [59] [60], dating back to 1928 [61]. Measurements down to liquid helium temperatures identified the transition in Prussian blue to be long-range ferromagnetic order [62-64], but an understanding of the magnetic interactions remained elusive until the 1970s, when x-ray [65] and neutron [55] diffraction data identified the crystal structure and the spin transfer from high-spin Fe^{3+} to low-spin Fe^{2+} . Subsequent to this identification, the class of isostructural, face centered cubic cyanometallates were dubbed Prussian blue analogues, Figure 5-1.

Interest in Prussian blue analogues was renewed by the 1996 discovery of long-lived, photoinduced magnetism in $\text{K}_{0.2}\text{Co}_{1.4}[\text{Fe}(\text{CN})_6] \cdot 6.9\text{H}_2\text{O}$ [1]. A flurry of experimental and theoretical research has elucidated the fundamental nature of the phenomena in three-dimensional bulk materials [66] [67]. In the following a brief

summary of the photoinduced magnetization mechanism elucidated by these studies will be presented.

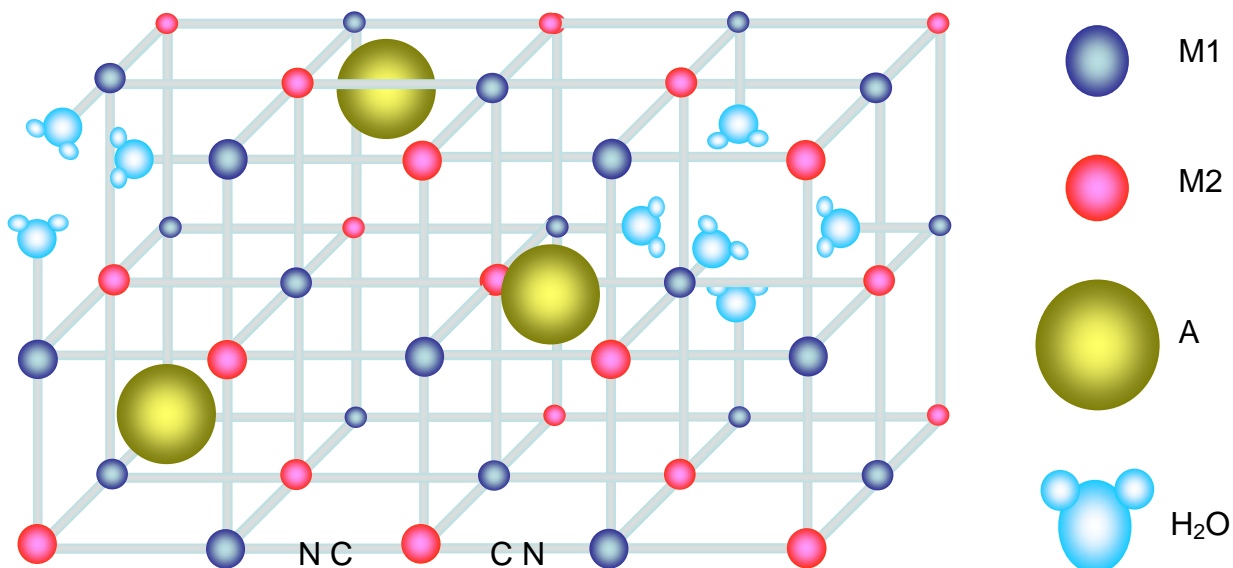


Figure 5-1. Prussian blue analogue structure. Prussian blue analogues have a chemical formula of $A_jM1_k[M2(CN)_6]_l \cdot nH_2O$, j, k, l and n are constrained by charge balance. Cations ($A = Cs^+, Rb^+, K^+, Na^+$) are incorporated based upon the number of M2 vacancies. M2 vacancies are coordinated by water as shown. The distance between M1 and M2 is generally $\sim 5 \text{ \AA}$.

Magnetic transitions in cobalt hexacyanoferrate systems depend strongly on the single-ion parameters introduced in Section 3.1. Iron is in a strong ligand field of carbon and is therefore found to be either Fe^{3+} (LS, $S = 1/2$) or Fe^{2+} (LS, $S = 0$). Cobalt is in an intermediate ligand field of nitrogen and is found to be either Co^{2+} (HS, $S = 3/2$) or Co^{3+} (LS, $S = 0$). The nomenclature of the following is such that pairs displaying defined local minima in configuration space with respect to energy have a “0” appending their label and short-lived metastable states are appended with a prime.

$Co^{3+}Fe^{2+}$ ($S_{Co} = 0, S_{Fe} = 0, S_{tot} = 0$) is the diamagnetic LS0 pair and

$Co^{2+}Fe^{3+}$ ($S_{Co} = 3/2, S_{Fe} = 1/2, S_{tot} = 1$) is the ferrimagnetic HS0 pair with a

superexchange through the bridging cyanides. $Co^{3+}Fe^{2+}$ ($S_{Co} = 1, S_{Fe} = 0, S_{tot} = 1$) is the

intermediate HS' pair and $\text{Co}^{2+}\text{Fe}^{3+}$ ($S_{\text{Co}} = 1/2$, $S_{\text{Fe}} = 1/2$, $S_{\text{tot}} = 0$) is intermediate the LS' pair. Other pairings, appearing to be oxidized and reduced species when compared to HS0 and LS0, exist mainly at the boundary of HS and LS pairs and at surfaces where metal coordination numbers change. There are also structural differences between the different pairs, with LS0 being the shortest ($\sim 10 \text{ \AA}$ Co-Co) and HS0 being the longest ($\sim 10.2 \text{ \AA}$ Co-Co) [68].

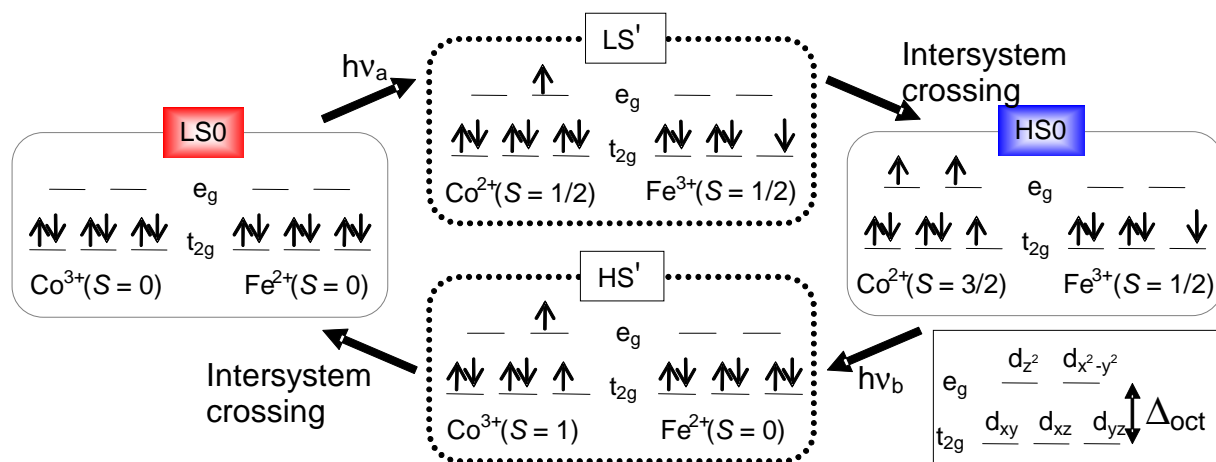


Figure 5-2. A detail of the photoexcitation processes in $\text{K}_{0.2}\text{Co}_{1.4}[\text{Fe}(\text{CN})_6] \cdot 6.9\text{H}_2\text{O}$. Strong-field e_g and t_{2g} orbitals are used for simplicity.

The ability to increase magnetization with blue light and decrease it with red light can be understood as changing the relative populations of LS0 and HS0 in the sample, Figure 5-2. To increase the magnetization in $\text{K}_{0.2}\text{Co}_{1.4}[\text{Fe}(\text{CN})_6] \cdot 6.9\text{H}_2\text{O}$, an LS0 state is irradiated with blue light, exciting an electron from Fe to Co, giving LS'. The LS' state then transitions to the metastable HS0 state, separated from LS0 by an energy barrier of the order of 1 eV [1] [69]. To decrease the magnetization in $\text{K}_{0.2}\text{Co}_{1.4}[\text{Fe}(\text{CN})_6] \cdot 6.9\text{H}_2\text{O}$, HS0 regions are irradiated with red light, exciting an electron from Co to Fe, giving HS'. The HS' state then transitions to the metastable LS0 state, separated from HS0 by an energy barrier of the order of 1 eV [1] [69].

In this chapter, starting with Section 5.1, nanoparticles of rubidium cobalt hexacyanoferrate will be discussed, with specific attention to finite size effects on the photoinduced magnetism and magnetically ordered states. In the subsections of 5.1, synthesis and chemical composition (5.1.2), structure (5.1.3), and magnetization (5.1.4) will be presented and discussed (5.1.5). Second, Section 5.2 compares nanoparticles and bulk powder of cobalt hexacyanoferrate. This potassium cation system is interesting because it allows for clear thermal transitions and thermal quenching of magnetic states in addition to photoinduced magnetization. Within Section 5.2, synthesis and chemical composition (5.2.2), structure (5.2.3), and magnetization (5.2.4) are to be presented and discussed (5.2.5). Finally, in Section 5.3, sodium cobalt hexacyanoferrate nanoparticles showing large thermal hysteresis are discussed to show the size dependence of this effect.

5.1 Nanoparticles of Rubidium Cobalt Hexacyanoferrate

Nanoparticles of rubidium cobalt hexacyanoferrate ($\text{Rb}_j\text{Co}_k[\text{Fe}(\text{CN})_6]_r \cdot n\text{H}_2\text{O}$) were synthesized using different concentrations of the organic ligand polyvinylpyrrolidone (PVP) to produce four different batches of particles with characteristic diameters ranging from nominally 3 to 13 nm. Upon illumination with white light at 5 K, the magnetization of these particles increases. In addition, the magnetic properties, namely the long-range ferrimagnetic ordering temperature (T_C) and the coercive field (H_C), of the nanoparticles evolve with preparation protocol. At 2 K, particles with diameters less than 10 nm are in the superparamagnetic limit. This work was published, in part, in the *New Journal of Physics* (<http://www.iop.org/EJ/journal/NJP>). Those sections contained within the NJP article

are copyright of the IOP (copyright release form in Appendix C) and the online abstract can be found at <http://www.iop.org/EJ/abstract/1367-2630/9/7/222/> [8].

5.1.1 Introduction

Numerous efforts to synthesize nanoparticles of Prussian blue analogues have been made, but only a few examples of photoinduced magnetism have been reported, including work that isolated $K_jCo_k[Fe(CN)_6]_r \cdot nH_2O$ particles, with typical diameters of 8–10 nm, within a silica xerogel [6], and other research producing 11 nm × 70 nm nanorods of $Mo(CN)_8Cu_2$ protected by polyvinylpyrrolidone (PVP) [7]. In each case, although photoinduced magnetism was observed, the particles did not exhibit long-range order.

This section reports $Rb_jCo_k[Fe(CN)_6]_r \cdot nH_2O$ nanoparticles, protected by PVP, that exhibit photoinduced magnetism for all sizes and that possess long-range ordering, with coercive fields ranging between 0.25–1.5 kG, in the larger particles. From the data, the superparamagnetic limit at 2 K is identified, and the magnetic signal generated from particles in this limit can be estimated for the different batches of particles.

5.1.2 Synthesis and Chemical Composition

The nanoparticles were synthesized by Dr. Franz Frye, modifying the procedure described by Uemura and coworkers [70] [71]. The Prussian blue analogue powder is encapsulated in a polyvinylpyrrolidone polymer (PVP) during synthesis. By varying the amount of PVP (Table 5-1), the protocol produced specimens with different sizes and distributions. After 30 minutes of stirring, the solution was allowed to sit for one week. To isolate the particles, three volumes of acetone were added to the synthesis solution, which was centrifuged, and then further washed with acetone and dried under vacuum.

Chemical analysis was obtained from a combination of CHN combustion analysis and inductively coupled plasma mass spectroscopy (ICP-MS), and the resulting formula are listed in Table 5-1, along with the ratio of the PVP repeat unit per cobalt. The concentration of H₂O was estimated by considering the measured Fe vacancies and charge balance.

Table 5-1. Synthesis and chemical composition of rubidium cobalt hexacyanoferrate nanoparticles.

Batch	Starting PVP (g)	Resulting chemical formula	PVP:Co ratio	Diameter (nm)
A	1.0	Rb _{1.9} Co ₄ [Fe(CN) ₆] _{3.2} · 5.8 H ₂ O	360	3.3 ± 0.8
B	0.5	Rb _{1.8} Co ₄ [Fe(CN) ₆] _{3.2} · 5.8 H ₂ O	200	6.9 ± 2.5
C	0.2	Rb _{1.7} Co ₄ [Fe(CN) ₆] _{3.2} · 5.8 H ₂ O	60	9.7 ± 2.1
D	0.1	Rb _{0.9} Co ₄ [Fe(CN) ₆] _{2.9} · 6.6 H ₂ O	20	13.0 ± 3.2

5.1.3 Structure

In order to characterize the nanoscopic nature of the samples, transmission electron microscopy (TEM) and fourier transform infrared (FT-IR) spectroscopy was performed. Other techniques that would provide analysis of large sample sizes, such as dynamic light scattering of samples in suspension, were tried but lacked the requisite resolution for the size regimes and distributions of interest.

5.1.3.1 Transmission Electron Microscopy

For the transmission electron microscopy (TEM) studies, a 50 µL aliquot of the suspension was diluted 2000 times, and 8 µL of the diluted suspension was placed on a holey carbon grid. Selected area electron diffraction was compared to powder x-ray diffraction patterns to confirm the structure [72]. Using Image J imaging software [73],

the TEM images were analyzed to obtain the particle size distributions shown in Figure 5-3, similar size distributions have been obtained for Prussian blue nanoparticles protected by PVP [74]. These data were fit to a log-normal function that yielded the characteristic diameters shown in Table 5-1.

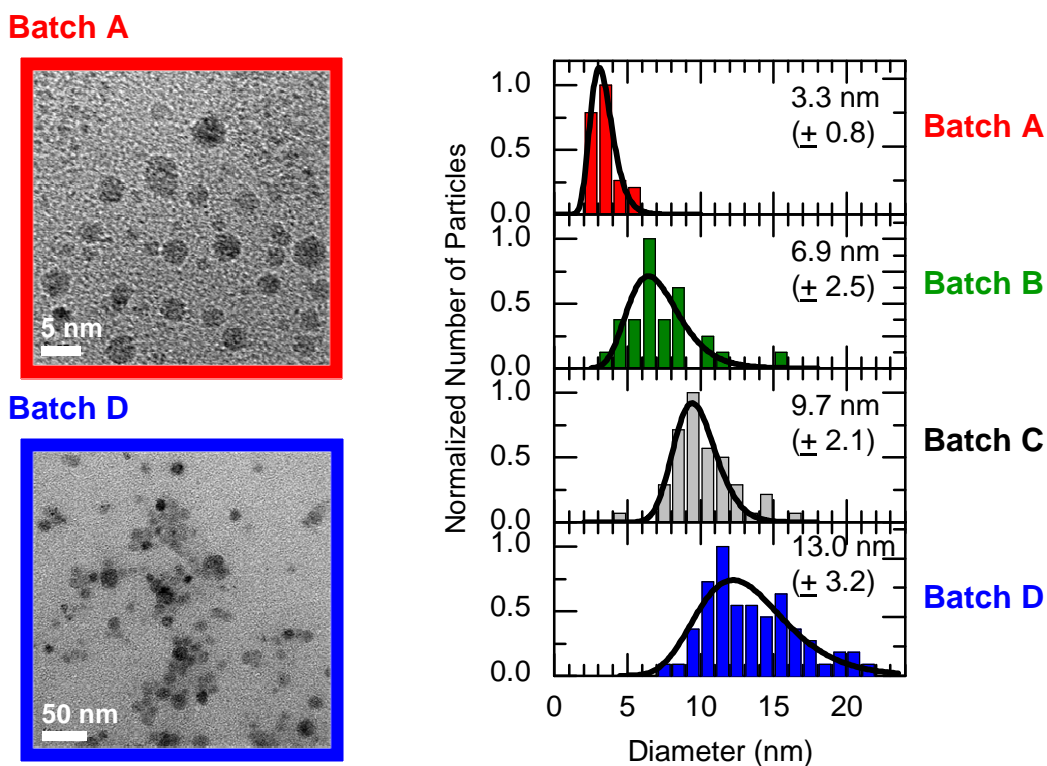


Figure 5-3. TEM of $\text{Rb}_7\text{Co}_4[\text{Fe}(\text{CN})_6]_r \cdot n\text{H}_2\text{O}$ nanoparticles. (left) Typical TEM images. (right) The particle distributions, normalized to the largest bin, versus diameter for the four batches of particles, see Table 5-1. The total number of particles for each distribution, smallest to largest, is 44, 27, 53, and 62, respectively. The solid lines are the results of log-normal fits that provide the characteristic diameters shown for each distribution.

5.1.3.2 Fourier Transform Infrared Spectroscopy

FT-IR was performed on samples analogous to those studied in more detail in the following subsections, Figure 5-4. Similar synthesis protocols yielded batches with characteristic diameters, d , of $d \sim 240$ nm (a 'bulk' powder), $d \sim 13$ nm (nanoparticles analogous to Batch D), and $d \sim 3$ nm nanoparticles (analogous to Batch A). It was

necessary to synthesize new samples as these studies were performed after the original samples had degraded over time. The FT-IR spectrum of the pure cobalt hexacyanoferrate displays peaks near 2163, 2120, 2090, and 2040 cm^{-1} , corresponding to the cyanide stretches of the $\text{Co}^{2+}\text{Fe}^{3+}$ (HS), $\text{Co}^{3+}\text{Fe}^{2+}$ (LS), $\text{Co}^{2+}\text{Fe}^{2+}$ (reduced) and linkage isomerized $\text{Co}^{2+}\text{Fe}^{2+}$ phases, respectively [75]. As the size of the particle is reduced, the intensity of the HS peak near 2163 cm^{-1} decreases, while that of the LS and reduced peaks near 2120 and 2090 cm^{-1} emerge and grow.

$\frac{A}{w\sqrt{\pi/2}}e^{-2\left(\frac{x-xc}{w}\right)^2}$	(a) d ~ 240 nm 'bulk'			(b) d ~ 13 nm 'Batch D'			(c) d ~ 3 nm 'Batch A'		
xc (cm^{-1})	2157	2122	2088	2156	2116	2088	2088	2120	2160
w (cm^{-1})	17.6	18.41	22.3	15.7	35.9	45.2	42.8	38.6	15.4
A (arb. Units)	0.72	0.04	0.24	0.22	0.23	0.52	0.28	0.60	0.12

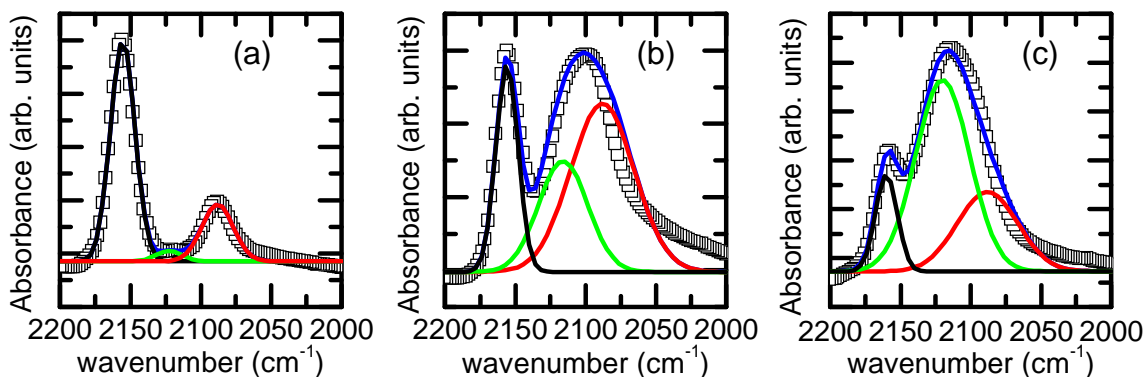


Figure 5-4. FT-IR absorption spectra of $\text{Rb}_x\text{Co}_k[\text{Fe}(\text{CN})_6]_r.n\text{H}_2\text{O}$ nanoparticles. (a) d ~ 240 nm 'bulk' powder, (b) d ~ 13 nm nanoparticles analogous to Batch D, and (c) d ~ 3 nm nanoparticles analogous to Batch A. Fits to Gaussian lines are shown for HS (—), LS (—), reduced (—), and total intensity (—), and the values of the fitting parameters are tabulated.

5.1.4 Magnetization

The quantity of central interest is magnetization. To this end, a standard commercial SQUID magnetometer was employed. The samples were mounted to

commercial transparent tape and could be irradiated with light from a room temperature, halogen source by using a homemade probe equipped with a bundle of optical fibers [76]. Background contributions from the holder and tape are independently measured and subtracted from the data.

5.1.5.1 DC Susceptibility

The temperature dependences of the DC magnetic susceptibilities, $\chi(T)$, of the four batches of particles are shown in Figure 5-5. The magnetic signals are expressed per mole of Prussian blue analogue (PBA), Table 5-1. The dark state ZFC data were obtained after cooling in zero applied field from 300 K, while the dark state FC data were taken after cooling in 100 G from 300 K. The light state was established after field cooling the samples from 300 K to 5 K in 100 G and subsequently irradiating with light for 5 hours. The light state FC data were obtained after cooling from 30 K in 100 G.

All samples reported show a photoinduced increase in their magnetic signals and ordering temperatures, and the strength of the change is correlated with the size of the particles. The differences between the FC susceptibilities of the light and dark states, $\Delta\chi = \chi_{FC}^{light} - \chi_{FC}^{dark}$, are plotted in the insets of Figure 5-5; finite values can only arise from the photoinduced magnetism.

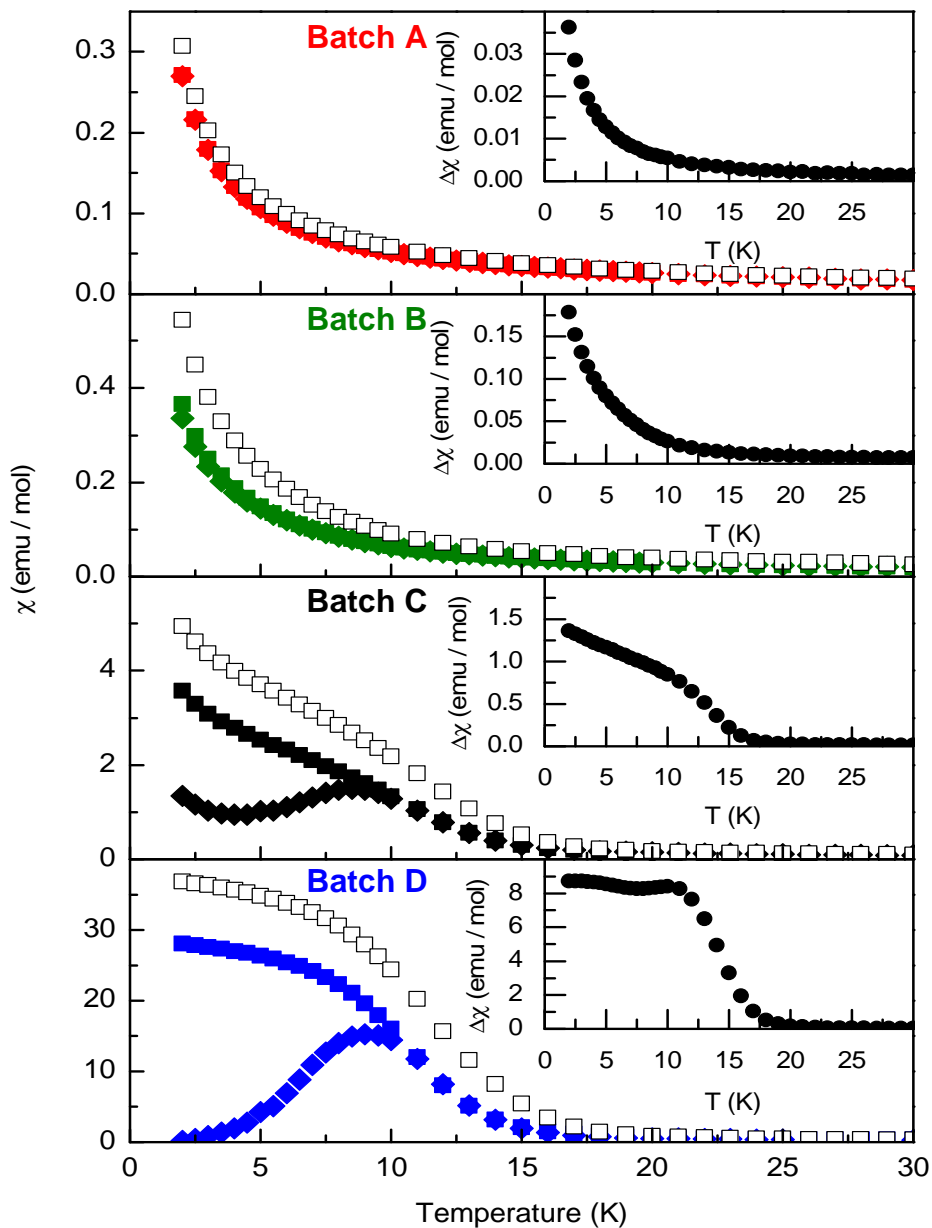


Figure 5-5. The temperature dependences of the low field, 100 G, susceptibilities of $\text{Rb}_7\text{Co}_\kappa[\text{Fe}(\text{CN})_6]_r \cdot n\text{H}_2\text{O}$ nanoparticles. The zero-field cooled (ZFC) dark (◆), field-cooled (FC) dark (■), and FC light (□) states of each batch produced are shown. The insets display the differences between the FC light and dark states, as described in the text. Finite values for this difference can only arise from photoinduced magnetism.

5.1.5.2 DC Magnetization

The field dependences of the DC magnetization, $M(H)$, of the four batches of particles are shown in Figure 5-6. The magnetic signals are expressed per mole of Prussian blue analogue (PBA), Table 5-1. The dark and light states are the same as for the DC susceptibility measurements. All samples reported show a photoinduced increase in their coercive fields and saturation magnetizations, and the strength of the change is correlated with the size of the particles.

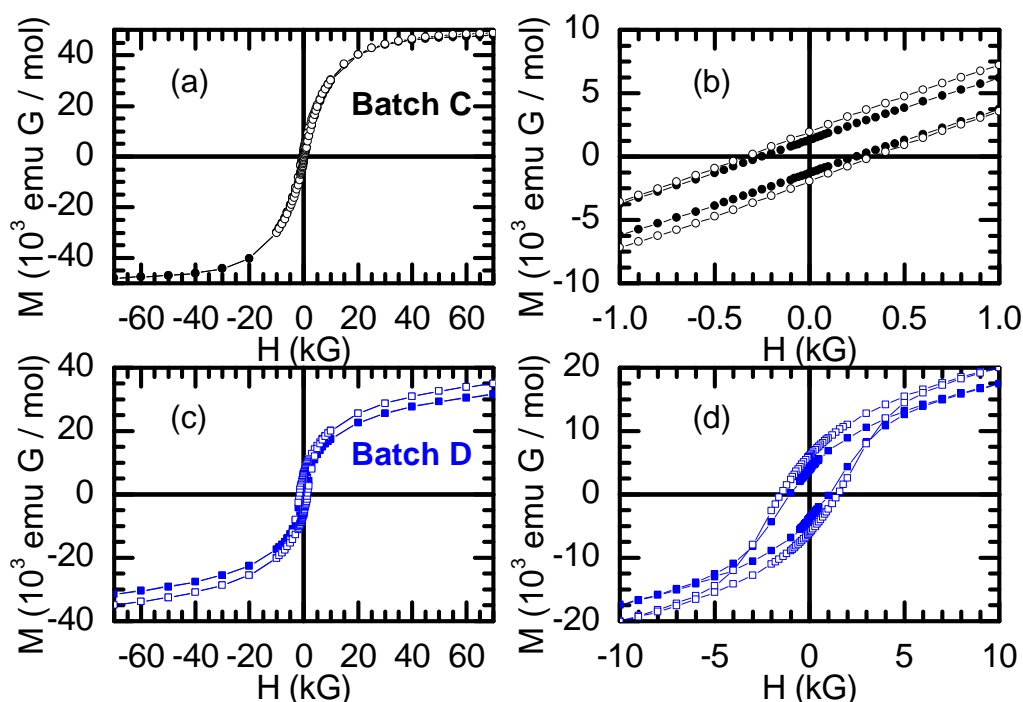


Figure 5-6. The $T = 2$ K magnetization versus magnetic field sweeps of $\text{Rb}_7\text{Co}_\kappa[\text{Fe}(\text{CN})_6]_r \cdot n\text{H}_2\text{O}$ nanoparticles. Here Batch C for (a) high fields and (b) the field region relevant to the hysteresis in both light (\square) and dark (\blacksquare) states are shown. In addition, Batch C for (a) high fields and (b) the field region relevant to the hysteresis in both light (\circ) and dark (\bullet) states. The coercive fields, H_C , for the light and dark states for each batch are listed in Table 5-2, and the lines are guides for the eyes.

5.1.5.3 AC Susceptibility

The temperature dependences of the real (χ') and imaginary (χ'') ac susceptibilities of the ZFC dark states, i.e. primordial states, of all four batches are shown in Figure 5-7.

The phenomenological parameter for frequency dependence of the peak is

$$\beta = \frac{\Delta T_f}{T_f \Delta(\log \omega)}, \quad 5.1$$

where T_f is the freezing temperature given by the cusp in $\chi'(T)$ and ω is the angular frequency, is 0.024 ± 0.004 for batches C and D, and this observation is consistent with spin glass or cluster glass behavior [77] [78].

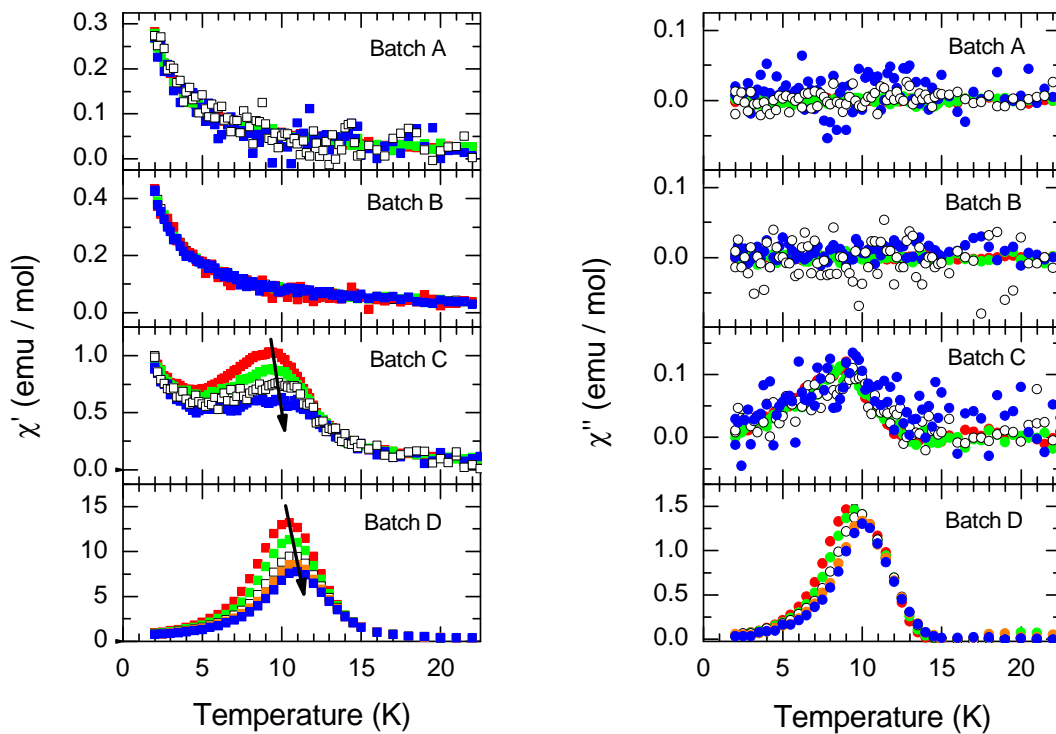


Figure 5-7. The temperature dependences of the real (χ') and imaginary (χ'') ac susceptibilities of $\text{Rb}_7\text{Co}_4[\text{Fe}(\text{CN})_6]_n\text{H}_2\text{O}$ nanoparticles. Zero field cooled dark states were measured with no applied static field and an alternating field of 4 G, except for batch D, which was measured in 1G. The frequency dependence was studied at 1 Hz (■), 10 Hz (■), 100 Hz (□), and 1 kHz (■) for all batches, except for batch D, which has an additional measurement at 333 Hz (■). Arrows are guides for the eyes and pass through the peaks.

5.1.5 Discussion

It is important to recall that the photoinduced magnetic properties of the Prussian blue analogues depends upon a spin crossover effect and the presence of vacancies that allow crystalline flexibility [57][79-85]. More specifically for the $\text{Rb}_j\text{Co}_k[\text{Fe}(\text{CN})_6]_l \cdot n\text{H}_2\text{O}$ nanoparticles, the spins can exist in either of two arrangements. The low-spin state consists of Fe^{2+} ($S = 0$) and Co^{3+} ($S = 0$), while the high-spin state possesses Fe^{3+} ($S = 1/2$) and Co^{2+} ($S = 3/2$). Depending on the local chemical environment due to the values of j, k, l , and n in the chemical formula, the Fe and Co spins can be locked into either their high-spin or low-spin states for all accessible temperatures. Alternatively, with the proper tuning of constituent elements, the Fe and Co ions can exist in high-spin states at room temperature and then experience a crossover to their low-spin states at approximately 150 K. This spin crossover phenomenon prepares the system for the possibility of experiencing photoinduced magnetism. However, since the spin crossover effect may not be 100% efficient, some regions remain locked in their high-spin states, giving rise to the magnetic signals observed for the dark state of the particles. When irradiated, the low-spin regions are photoinduced to the high-spin magnetic state, resulting in a growth of the magnetic domain. This scenario is supported by the frequency dependent ac susceptibility studies, and by the local probe investigations of others [68] [86].

Two main features, onset of long-range magnetic order and increasing net magnetization, are important when considering the evolution of material properties due to the increasing average size of the separate batches. The ordering temperatures of the particles and the magnetic susceptibility are both seen to decrease as particles become smaller, Figure 5-5. This scaling of magnetization is linked to an increased

diamagnetic-surface to magnetically-active-volume ratio at smaller particle sizes. This contention is supported by the FT-IR spectra, which show an increase in the LS and reduced content as particle size decreases, although the precise location of these moieties cannot be gleaned from such methods. At low temperatures, the high-spin Fe and Co ions interact antiferromagnetically, giving rise to a ferrimagnetic transition at T_C [87]. For the magnetic data shown in Figure 5-5 and Figure 5-8, the onset of this transition can be estimated, and these macroscopic temperatures are listed in Table 5-2. Therefore, it is plausible that particles larger than a critical size will allow domains large enough to approach bulk-like magnetic properties. Conversely, smaller particles may put limits on allowed domain size, suppressing the ordering temperature. Microscopically, if the size of the magnetic domains is less than or of the order of the magnetic coherence length, then a spectrum of T_C values can be expected until the superparamagnetic limit is achieved.

Table 5-2. Magnetic properties of rubidium cobalt hexacyanoferrate nanoparticles.

Batch	Diameter (nm)	T_C^{dark} (K)	T_C^{light} (K)	H_C^{dark} (G)	H_C^{light} (G)
A	3.3 ± 0.8	< 2	< 2	< 10	< 10
B	6.9 ± 2.5	~10	~13	~15	~30
C	9.7 ± 2.1	13	17	250	330
D	13.0 ± 3.2	19	22	1000	1500

Consider the magnetic properties of the samples presented in conjunction with the TEM analysis. Batch A has no observed coercivity and follows Curie-like behavior. Batches B and C show a combination of Curie-tail and partial ordering with a reduced T_c (Figure 5-5 and 5-8), as well as finite coercive fields. Finally, the active sites in Batch D are almost entirely ferrimagnetically ordered with the largest coercive field of all batches presented. In addition, the differences between the FC and ZFC data for the dark state in batch D is consistent with spin glass or cluster glass behavior [77] [78], in accord with the presence of large magnetic domains.

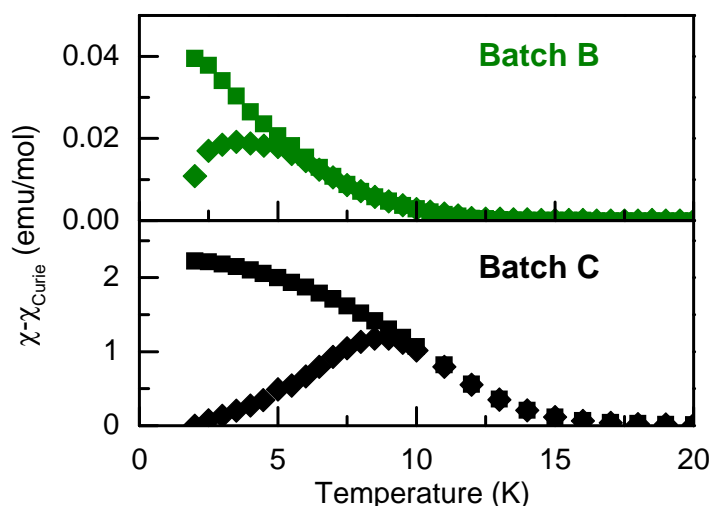


Figure 5-8. Ordered magnetic components of the smaller batches. The ZFC (◆) and FC (■) dark states show a signal associated with long-range order for the two batches (Batch B and Batch C) displaying a mix of magnetic behavior after subtracting the Curie-like contribution.

Based upon fitting the macroscopic magnetization data available in the Curie-like contributions at low temperature, the superparamagnetic contribution for each of the four batches of nanoparticles (smallest to largest) is 100%, 90%, 50%, and 10%. Consequently, at least down to 2 K, nanoparticles with sizes below ~ 10 nm are in the superparamagnetic limit. These interpretations are consistent with the M versus H

measurements performed at 2 K, where significant coercive fields, H_C , and remnant magnetization values are observed for the two largest sets of particles but not for the two smallest sets of particles, Figure 5-6 and Table 5-2. It is interesting to note that even at 70 kG, there is still a finite slope to the magnetization, and this slope actually gets larger with particle size. Two plausible explanations for this behavior exist:

(1) there is local flipping of minor Fe spins to be aligned with the increasing field, without a clear spin-flip field due to the disordered nature of the magnetism, and (2) there is a field dependent magnetic moment on either the cobalt or iron sites due to the first order angular momentum not being completely quenched by the crystal environment (as detailed in Chapter 4).

5.1.6 Conclusions

In conclusion, four different sizes of $Rb_xCo_k[Fe(CN)_6]_r \cdot nH_2O$ nanoparticles protected by PVP were synthesized and characterized. Each batch of particles is photoinducible, but the strength of this effect, as well as other global properties, e.g. T_C and H_C , are correlated with the intrinsic particle size distributions of each batch. The combination of photoinduced magnetism and nanosized Prussian blue analogue particles with finite coercive fields is unique and establishes a length scale limit of ~10 nm diameter for these properties. Since publication, these findings have been used to understand the results of additional nanoparticle studies [88] [89].

5.2 Nanoparticles of Potassium Cobalt Hexacyanoferrate

Nanoparticles and bulk powder of potassium cobalt hexacyanoferrate ($K_xCo_k[Fe(CN)_6]_r \cdot nH_2O$) were synthesized by changing the density of reactants in solution, without using surfactant, excluding additional experimental uncertainties from estimating the amount of surfactant present. Bulk powder with characteristic diameters, d , of $d \sim 200$ nm and nanoparticles of $d \sim 27$ nm were studied. Both sizes show photoinduced magnetization and the ability to trap magnetic states by thermal quenching. However, the magnetic properties are modified in the nanoparticles, showing less total magnetization, greater magnetic coercivities, and longer isothermal relaxation constants. In addition, macroscopic differences between photoinduced and thermally quenched low temperature magnetic states of $K_xCo_k[Fe(CN)_6]_r \cdot nH_2O$ are presented for the first time. Magnetic data is complemented by infrared spectroscopy, transmission electron microscopy, x-ray powder diffraction, and temperature dependent neutron diffraction. This work is expected to be submitted for publication at a later date.

5.2.1 Introduction

While there are reports of photoswitchable nanoparticles by other groups [6] [7], as well as a study of rubidium cobalt hexacyanoferrate nanoparticles that the author co-authored [8], these studies focused mainly on the low temperature magnetically ordered state. However, charge transfer induced spin transitions (CTIST) between the high-spin (HS) and low-spin (LS) states can also be incited by changing the temperature [1]. The relevant states to be considered for these transitions are summarized in Table 5-3 and Table 5-4.

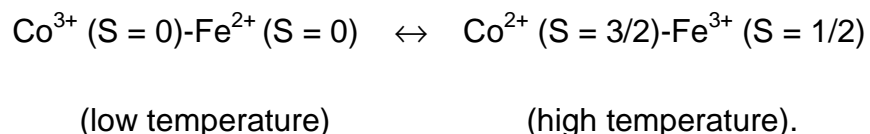
Table 5-3. The microscopic states relevant to $K_xCo_k[Fe(CN)_6]_l \cdot nH_2O$.

microstate shorthand	oxidation states	bond length (Å)	Co spin	Fe spin
HS	$Co^{2+}-NC-Fe^{3+}$	10.3	3/2	1/2
LS	$Co^{3+}-NC-Fe^{2+}$	10.0	0	0
'reduced'	$Co^{2+}-NC-Fe^{2+}$	10.3	3/2	0

Table 5-4. The macroscopic states relevant to $K_xCo_k[Fe(CN)_6]_l \cdot nH_2O$.

macrostate shorthand	Meaning	realization	expected microstates
Q	Quenched	rapid cooling to 100 K at ~100 K/min	mostly HS, some LS
P	Photoinduced	photoirradiation at temperatures below 100 K	mostly HS, some LS
G	low temperature Ground state	slow cooling at ~1 K/min to 100 K	LS

In the high temperature limit (~300 K), most Co–NC–Fe pairs will be in a HS ($S = 1$) state. Upon reaching a sufficiently low temperature (~200 K), Co–NC–Fe pairs begin transitioning to the LS state, and the process can be summarized as



The K cation samples are of particular interest because it was shown that in addition to photoinducing, thermal quenching can trap variable amounts of HS pairs [9] [76]. In the extreme limit of cyanide bridged molecular cobalt iron, it was found that quenched and photoinduced states are identical [90]. While the quenched and

photoinduced states in Na cation, bulk powders have been studied by x-ray diffraction [68], and quenching has been studied with magnetic susceptibility, Mössbauer spectroscopy [91] and specific heat [92], no systematic study has been presented on the macroscopic measurements of such a material or of how finite size effects might play a role and further elucidate the fundamental mechanisms involved.

This thesis chapter reports on $K_xCo_k[Fe(CN)_6]_l \cdot nH_2O$ (henceforth K-Co-Fe) nanoparticles, synthesized without surfactant, that exhibit photoinduced magnetism and thermal quenching of magnetic states for characteristic diameters, d , of $d \sim 27$ nm and $d \sim 200$ nm batches of nanoparticles. Clear modifications of the magnetic properties with size are observed and macroscopic differences between the photoinduced and thermally quenched magnetic states are detected.

5.2.2 Synthesis and Chemical Composition

Bulk K-Co-Fe Prussian blue analogue powders were prepared by Dr. Justin E. Gardner and Matthew J. Andrus, using procedures previously described by Shimamoto and coworkers [84]. Nanoparticles of K-Co-Fe Prussian blue analogues were synthesized Dr. Justin E. Gardner and Matthew J. Andrus, by modifying the procedures previously reported by Yamada and coworkers [93]. In order to estimate the chemical formulae, EDS and CHN were performed on the samples, and the results are part of Table 5-5.

5.2.2.2 Fourier Transform Infrared Spectroscopy

Infrared spectroscopy of cobalt hexacyanoferrates are typically performed in the energy region of the cyanide stretch of the compound, where the structure evolves due to the changing oxidation states of the coordinating metals of the cyanide, Figure 5-9. The first peak at 2160 cm^{-1} represents the $Fe^{3+}(LS)-CN-Co^{2+}(HS)$ stretch, while the

second broad peak is a combination of the $\text{Fe}^{2+}(\text{LS})\text{-CN-Co}^{3+}(\text{LS})$ and $\text{Fe}^{2+}(\text{LS})\text{-CN-Co}^{2+}(\text{HS})$ stretches which appear at 2115 cm^{-1} and 2090 cm^{-1} , respectively. Nanosized powders are known to exhibit spectra with a smaller $\text{Fe}^{3+}/\text{Fe}^{2+}$ ratio [8] [94]. Results of fitting the FT-IR spectra are detailed in Table 5-5.

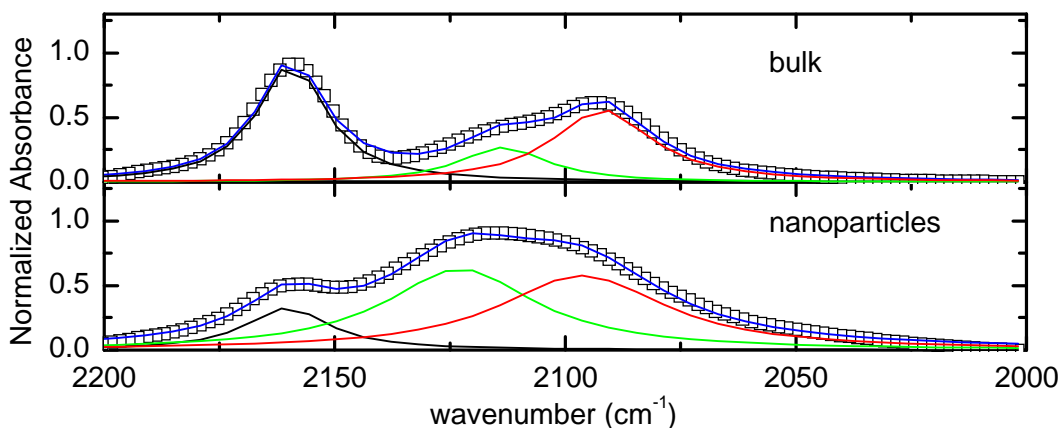


Figure 5-9. FT-IR spectra of bulk and nanoparticles of K-Co-Fe. The nanoparticles show a reduction in the amount of switchable material, the leftmost peak.

Table 5-5. Metal oxidation states of bulk powder and nanoparticles, in addition to fitting parameters used for Figure 5-9. Fits are to a Gaussian function for the lines,

$$\text{i.e. } \frac{A}{w\sqrt{\pi/2}} e^{-2\left(\frac{\omega-\omega_0}{w}\right)^2}.$$

Sample	Oxidation States	ω_0 (cm^{-1})	W (cm^{-1})	A (l cm^{-1})
bulk	$\text{Co}^{3+}_{0.25}\text{Co}^{2+}_{0.75} [\text{Fe}^{2+}(\text{CN})_6]_{0.18}[\text{Fe}^{3+}(\text{CN})_6]_{0.56}$	2159.4 ± 0.2	19.78 ± 0.3	21.6 ± 0.3
		2125.0 ± 1.1	18.7 ± 2.2	5.9 ± 1.0
		2095.9 ± 0.8	32.1 ± 1.3	25.0 ± 1.0
nano	$\text{Co}^{3+}_{0.07}\text{Co}^{2+}_{0.93}[\text{Fe}^{2+}(\text{CN})_6]_{0.32}[\text{Fe}^{3+}(\text{CN})_6]_{0.36}$	2162.4 ± 3.7	32.7 ± 8.8	13.0 ± 9.3
		2123.2 ± 1.3	36.5 ± 9.8	37.5 ± 18.8
		2096.7 ± 2.9	45.7 ± 5.5	33.0 ± 10.3

5.2.3 Structure

The macrostructure of the samples were characterized with HR-TEM, in order to estimate the average particle size. XRD at room temperature was performed to show the structure of the heavier elements. Temperature dependent neutron diffraction from 5 K to 300 K was performed on the $d \sim 27$ nm nanoparticles to probe the structural transition and to look for magnetic scattering. While structural transitions correlated to changes in the magnetic states have been observed in the bulk, they have yet to be reported for samples showing finite size effects.

5.2.3.1 Transmission Electron Microscopy

For the transmission electron microscopy (TEM) studies, a 50 μL aliquot of the suspension was diluted 2000 times, and 8 μL of the diluted suspension was placed on a holey carbon grid. The TEM images were analyzed by printing on standard 8.5 in x 11 in paper and measuring particles by hand with a digital caliper to obtain the particle size distributions shown in Figure 5-10, and similar size distributions have been obtained for Prussian blue nanoparticles protected by PVP [8] [74]. This size analysis method was found to yield the same results as the previous method in which a computer program was used, however the paper method involved less eye-strain and the ability to perform the measurements while enjoying Florida sunshine. These data were fit to a log-normal function that yielded the characteristic diameters shown in Table 5-6.

Table 5-6. Chemical composition and characteristic sizes of potassium cobalt hexacyanoferrate nanoparticles and bulk powder.

Sample	Chemical Formula	Diameter (nm)
bulk	$\text{K}_{0.39} \text{Co}^{3+}_{0.25} \text{Co}^{2+}_{0.75} [\text{Fe}^{2+}(\text{CN})_6]_{0.18} [\text{Fe}^{3+}(\text{CN})_6]_{0.56} \cdot 3.30 \text{H}_2\text{O}$	200 ± 38
nano	$\text{K}_{0.32} \text{Co}^{3+}_{0.07} \text{Co}^{2+}_{0.93} [\text{Fe}^{2+}(\text{CN})_6]_{0.32} [\text{Fe}^{3+}(\text{CN})_6]_{0.36} \cdot 3.30 \text{D}_2\text{O}$	27.4 ± 5.7

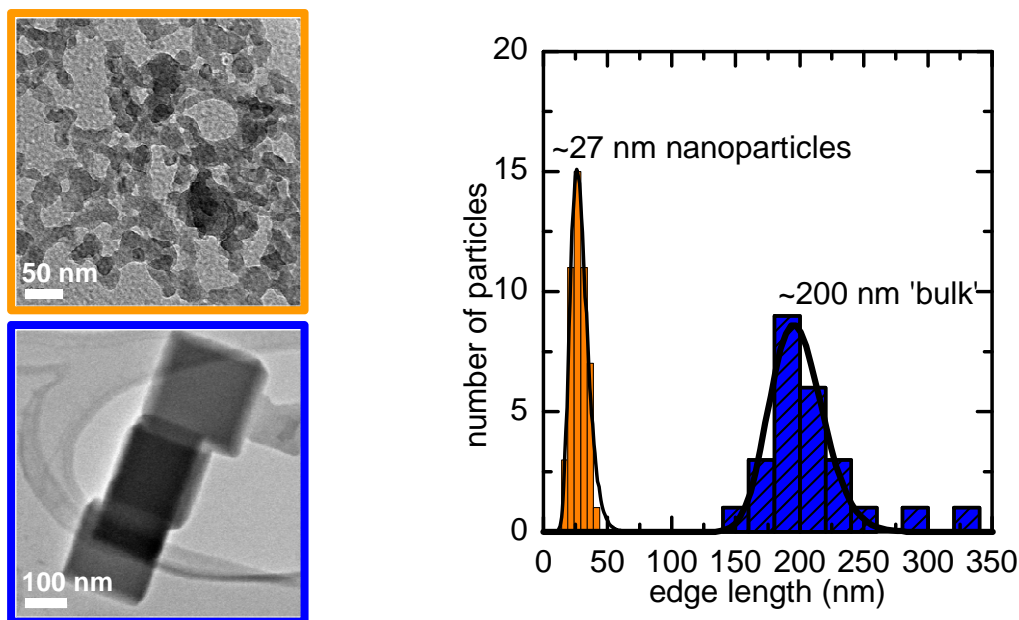


Figure 5-10. TEM of K-Co-Fe. (left) Typical TEM images are shown. (right) The particle distributions, versus diameter for the bulk and small particles, see Table 5-6. The solid lines are the results of log-normal fits that provide the characteristic diameters shown for each distribution.

5.2.3.2 X-Ray Diffraction

To investigate the lattice constants and crystal structure, a Philips APD 3720 powder diffractometer, housed in the Major Analytical Instrument Center at the University of Florida, was used to perform room temperature x-ray diffraction (XRD) using a Cu K_{α} source. It is worth noting that two lines, 1.54056 Å and 1.54441 Å, are present for the K-edge of Cu, and stripping of the weaker $K_{\alpha 2}$ line was performed, however the line-widths are so large for these samples that such an analysis is not necessary. Diffraction studies on similar compounds have assigned the HS unit cell to ~10.3 Å and the LS unit cell to ~10.0 Å [68]. As extended x-ray fine structure (EXAFS)

measurements have shown that the Co-N distance is most sensitive to the changing oxidation states of a Co-NC-Fe pair [95] [96], the $\text{Fe}^{3+}(\text{LS})\text{-CN-Co}^{2+}(\text{HS})$ and $\text{Fe}^{2+}(\text{LS})\text{-CN-Co}^{2+}(\text{HS})$ moieties should have similar lengths near $\sim 10.3 \text{ \AA}$. Between 10-20 mg of the same samples used for all other characterizations were mounted on glass slides and pressed onto squares of double-sided cellophane tape of $\sim 2.3 \text{ cm}^2$. The room temperature x-ray powder diffractograms, shown in Figure 5-11, were used to model the structure by a Rietveld refinement using the EXPGUI [53] interface for GSAS [52]. In order to approximate the complicated Prussian blue analogue structure, a single-phase model with $Fm\bar{3}m$ (No. 225) space group symmetry was used. Specifically, the cobalt and nickel atoms were forced to occupy the same site. Atomic occupancies were set by the experimentally determined chemical formulas, excepting the oxygen atoms of the interstitial waters that were allowed to vary as the samples may have dehydrated or hydrated between synthesis and diffraction. The same site symmetries as in Prussian blue were used, where the iron vacancies were replaced by the six coordinated oxygen atoms of the ligand water molecules [65]. Placement of the oxygen atoms of the interstitial water molecules at the $32f$ Wyckoff position [68] and a relatively small percentage at the $192i$ position was found to yield a robust local minima during refinement procedure.

The bulk powder shows one phase, with a lattice constant of 10.35 \AA and a FWHM of 0.12° for the (2, 2, 0) reflection. The nanoparticles show two phases, with lattice constants of 10.31 \AA and 10.07 \AA and a FWHM of 0.5° for the (2, 2, 0) reflection.

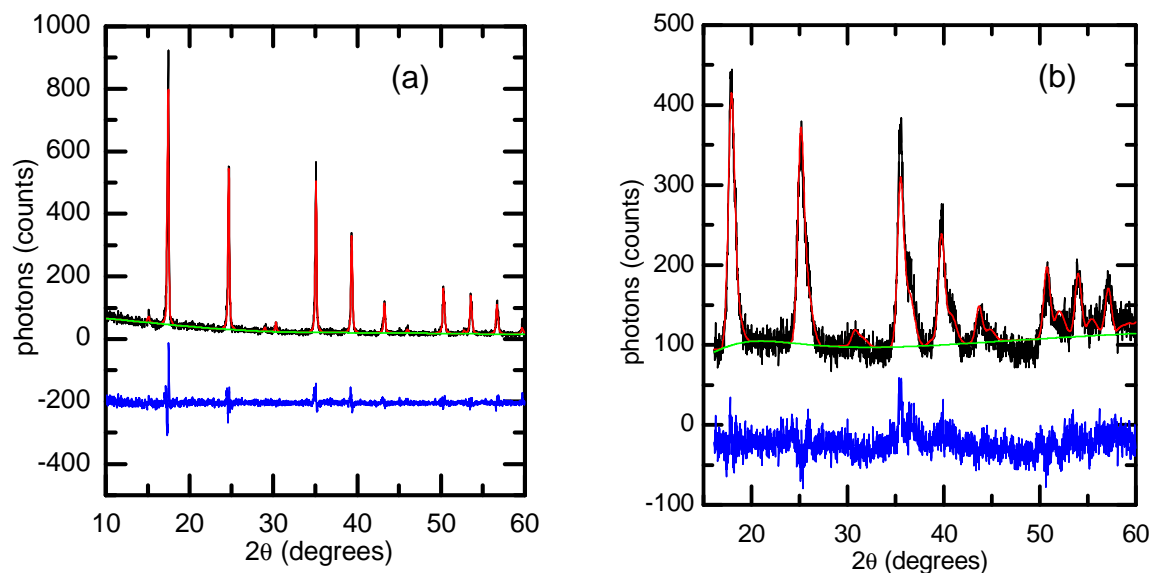


Figure 5-11. XRD of K-Co-Fe. Room temperature x-ray powder diffractograms of (a) bulk and (b) nanoparticles of K-Co-Fe. The wavelength is 1.54 Å. The nanoparticles clearly show two peaks, a larger peak accounting for 65% of the scattering near 10.313 Å corresponding to the HS and ‘reduced’ phases, and a smaller peak accounting for the remaining 35% of the structured peak near 10.068 Å corresponding to the LS phase. Experimental counts are shown in black, with Rietveld refinements in red, and residuals of the fit below the data in blue. Peak nomenclature is described in Table 5-3.

5.2.3.3 Neutron Diffraction

As compared to x-ray diffraction, neutron diffraction is more sensitive to light elements and may also scatter off local magnetic moments in a lattice. In order to probe the structure of the quenched phase in nanoparticles, as compared to the bulk materials that have already been studied [68], 5 grams of deuterated K-Co-Fe were used. A full neutron powder diffraction pattern of the nanoparticles gives the same unit cell parameters as x-rays, Figure 5-12. Quenching the sample by quickly inserting into a liquid helium filled cryostat ($\Delta T/\Delta \text{time} \sim 100 \text{ K/min}$) shows clear changes in the diffraction pattern, corresponding to the thermally quenched state (Q). Upon warming to 200 K, a transition of the unit cell to the low temperature ground state (G) can be seen,

Figure 5-13 (a). Conversely, by slowly cooling the sample from room temperature at ~ 1 K/min, a transition from the high temperature equilibrium phase (RT) to the G state is observed, Figure 5-13 (b).

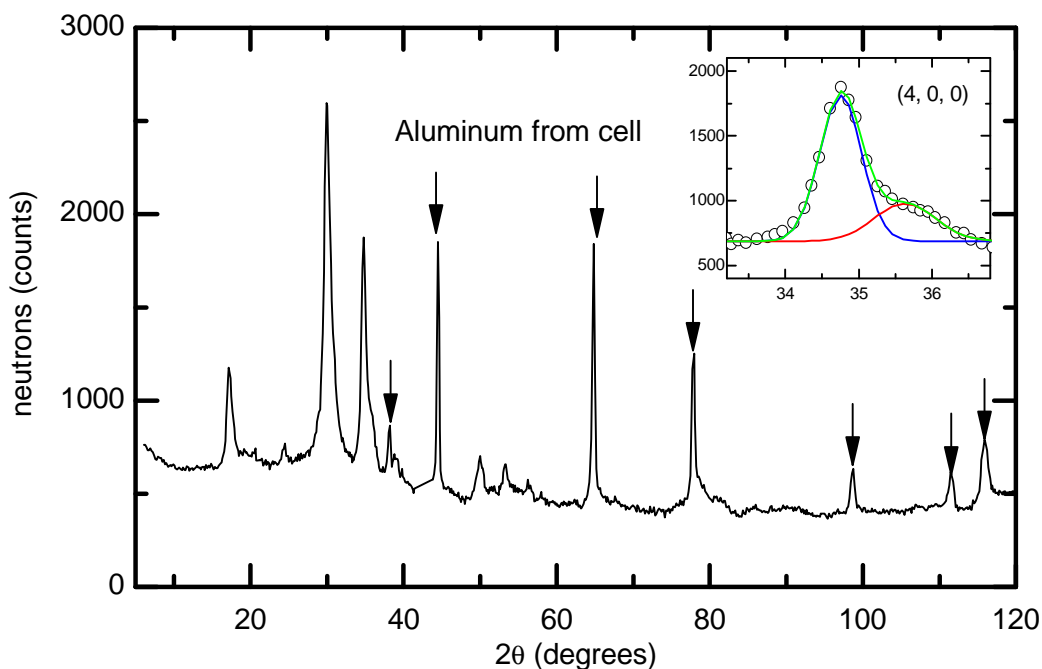


Figure 5-12. Neutron scattering of K-Co-Fe. Room temperature neutron powder diffractograms of nanoparticles of K-Co-Fe are shown. The nanoparticles clearly show two peaks, a larger peak accounting for 73% of the scattering near 10.312 \AA corresponding to the HS and 'reduced' phases, and a smaller peak accounting for the remaining 27% of the structured peak near 10.061 \AA corresponding to the LS phase. (inset) The (4, 0, 0) reflection showing the structure of the reflections, experimental counts are shown as white circles, with a HS/'reduced' peak in blue and the LS peak in red. Peak nomenclature is described in Table 5-3.

These peaks can be fit with a three phase model analogous to that used for the infrared measurements, with the HS, LS, and 'reduced' components taken into account. Unfortunately, the neutron data is more convoluted due to the HS and 'reduced' phases having the same lattice constant and the overlap of the lines due to the structural disorder in the samples. To mitigate this issue, the LS component was fit with a temperature independent lattice constant, and this assumption is corroborated by a set

of fits done with free parameters showing no clear trend in the LS unit cell parameter. On the other hand, the HS unit cell parameter shows a clear dependence on the high-spin fraction and must be allowed to vary. Although both a Lorentzian and Gaussian character is present in the peaks, and in fact the Gaussian nature is somewhat stronger, a Lorentzian shape was used to fit the temperature dependence to avoid insurmountable variable co-variance as the HS/'reduced' and LS lines get close at lower temperatures. The results of fitting the lines yield the temperature dependences of the lattice constants, Figure 5-13 (c) and the amount of scattering associated with each unit cell, Figure 5-13 (d). The full-width-half-maximum values did not shown any clear trends above the noise.

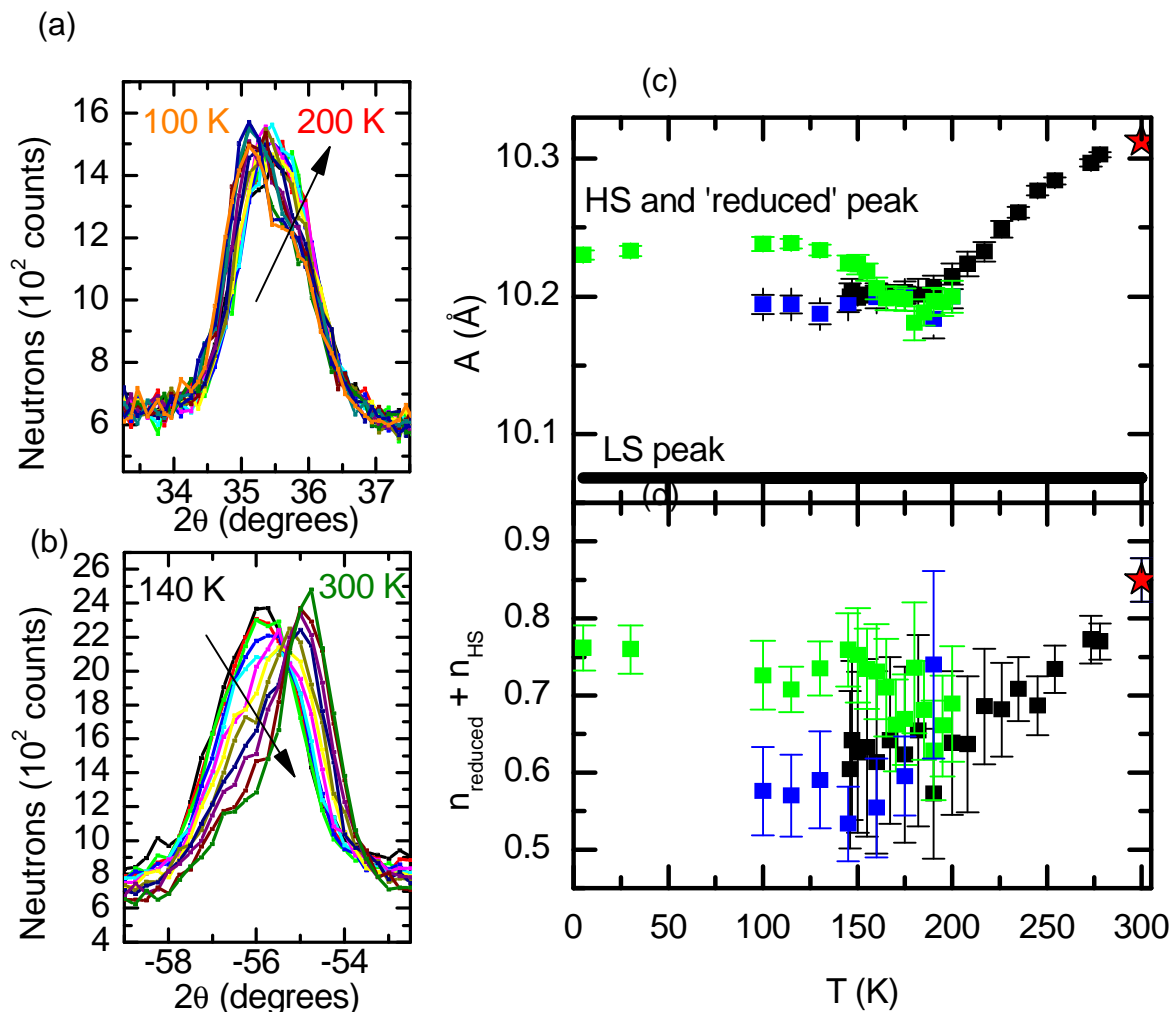


Figure 5-13. Neutron diffraction as a function of temperature for K-Co-Fe. The evolution of the structure is seen by tracking the (4,0,0) reflection for (a) warming after quenching to 100 K and (b) warming after slowly cooling at ~ 1 K/min. Results of fitting these reflections can be seen in the temperature dependence of (c) the unit cell size and (d) the fraction of high spin and 'reduced' material, $n_{\text{HS}} + n_{\text{reduced}}$, having the larger lattice constant. Quenching is shown in green, slow-cooling in blue, and room temperature as a red star for data taken at HFIR on HB2A ($\lambda \sim 1.54$ Å), data taken slow cooling on HB1A ($\lambda \sim 2.36$ Å) is black. The different horizontal axes on the raw scattering data is due to slightly different ways of counting the angle on the experimental detector bank, and these angles have been kept as they were recorded by the machines.

Finally, an attempt was made to observe magnetic scattering of the nanoparticles, in order to elucidate the magnetic structure. The expected nature of the scattering was modeled by positioning point spins on the nuclear positions of the metals and comparing the magnetic signal for parallel and antiparallel alignment, Figure 5-14 (a). A main result of the model calculations is that the relative intensity of the first two peaks is different for the ferrimagnetic versus ferromagnetic states. However, any magnetic scattering present, as potentially evidenced by the difference between the spectra at 5 K in the magnetically ordered state and 30 K in the paramagnetic state, was smaller than the experimental resolution of the setup used, Figure 5-14 (b). In addition, no difference was observed between 0.5 T and 5 T at 5 K.

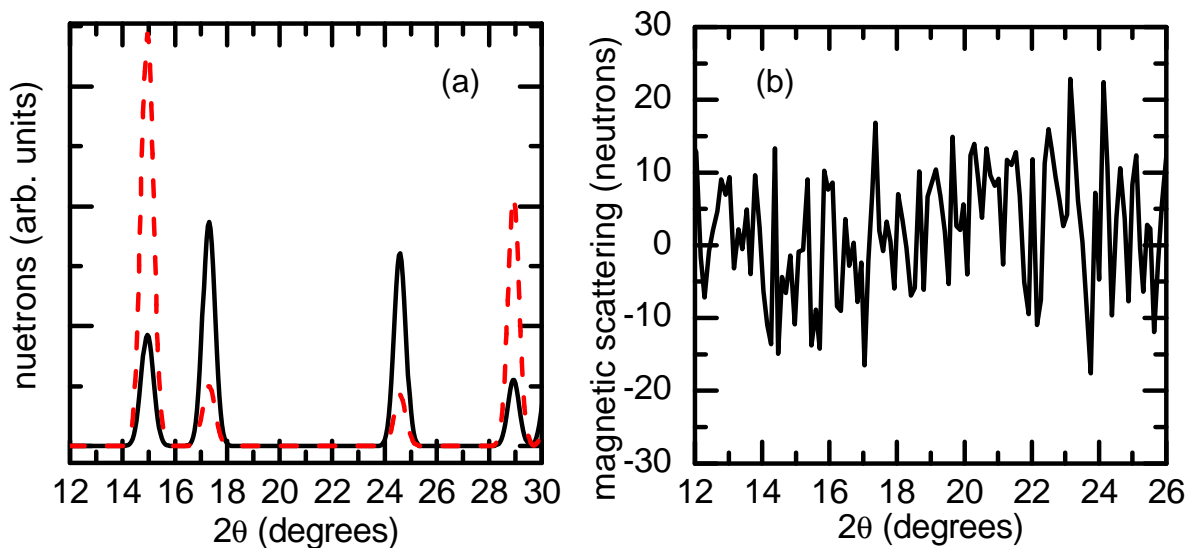


Figure 5-14. Magnetic neutron scattering in K-Co-Fe. (a) Calculated magnetic scattering for K-Co-Fe predicting different intensities for ferromagnetic (—) and ferrimagnetic (---) structures are shown for an incident wavelength of 1.54 Å. (b) Experimental observed magnetic scattering contribution taken as the difference between the magnetically ordered state at 5 K and the magnetically disordered state at 30 K.

5.2.4 Magnetization

Magnetization is a key parameter to further probe the quenched state (Q), low temperature ground state (G), and photoinduced states (P), which are defined explicitly in Table 5-4. To this end, a standard commercial SQUID magnetometer was employed. For photoinduced measurements, the samples were mounted to commercial transparent tape and could be irradiated with light from a room temperature, halogen source by using a homemade probe equipped with a bundle of optical fibers [76]. Background contributions from the holder and tape are independently measured and subtracted from the data. For the quenching measurements, in order to achieve better signal to noise in the paramagnetic states, gelcaps were packed with powder and mounted on a standard sample holder. Backgrounds from the gelcaps were subtracted based upon the mass susceptibility of an analogous gelcap.

5.2.4.1 Quenched High Temperature DC Susceptibility

The temperature dependences of the DC magnetic susceptibility temperature product, $\chi(T) T$, in the paramagnetic limit are shown in Figure 5-15. The magnetic signals are expressed per mole, Table 5-6. Quenching was achieved by stabilizing the cryostat temperature to 100 K, and quickly inserting the sample. While infinitely slow-cooling will reach the true G state, this was realized experimentally by quenching to 100 K, warming to 200 K at less than 1 K/min, and subsequently cooling again to 100 K, warming to 200 K at less than 1 K/min, and subsequently cooling again.

Both samples show a clear trapping of magnetic states with thermal quenching, and the ability to trap the magnetic states is correlated with the size of the particles. In fact, the room temperature HS content of the samples, n_{HS} , is strongly affected by the particle size.

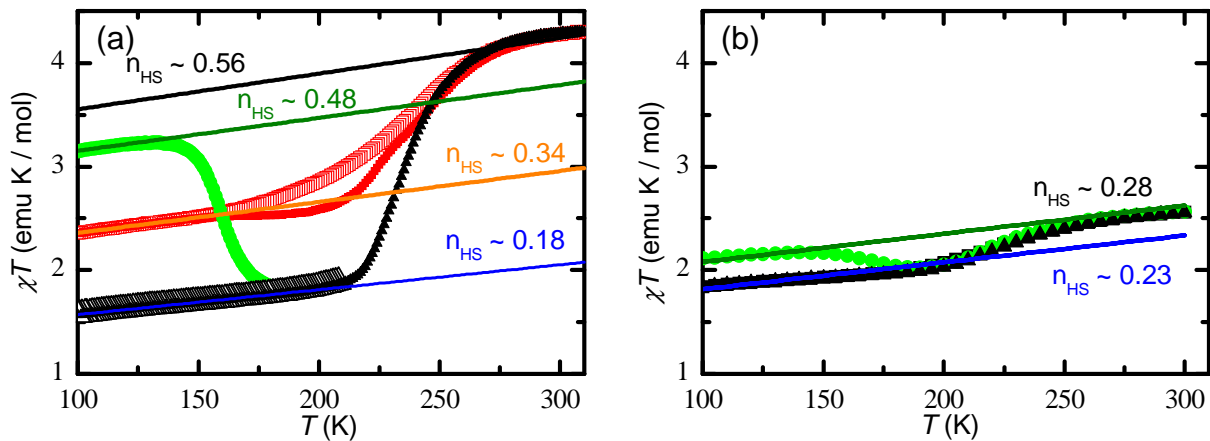


Figure 5-15. Temperature dependent magnetic moment of quenched states for K-Co-Fe. The temperature dependences of χT are shown in the paramagnetic state at 5 kG for Q (●), intermediately quenched (■), and G states (▲) of (a) ~200 nm particles and (b) ~27 nm particles. A clear reduction in the magnetism in the quenched state can be seen for the smaller, ~27 nm nanoparticles. Solid lines are fits to extract the HS fraction (n_{HS}), and the details of the fits are described in the text.

5.2.4.2 Quenched Low Temperature DC Susceptibility

The temperature dependences of the DC magnetic susceptibilities, $\chi(T)$, in the ordered state before and after thermal quenching are shown in Figure 5-16. The magnetic signals are expressed per mole, Table 5-6. Quenched states were achieved by stabilizing the cryostat temperature to 100 K, and inserting the sample. The G state was reached by quenching to 100 K, warming to 200 K at less than 1 K/min, and subsequently re-cooling. The ZFC data were obtained after cooling in zero applied field from 100 K, while the dark state FC data were taken after cooling in 100 G from 100 K.

Both samples show an increase in their magnetic signals as more spins are thermally trapped by quenching, and the strength of the change is correlated with the size of the particles. Inset of Figure 5-16 show a weak increase in the magnetic ordering temperature for the Q states compared to the G states.

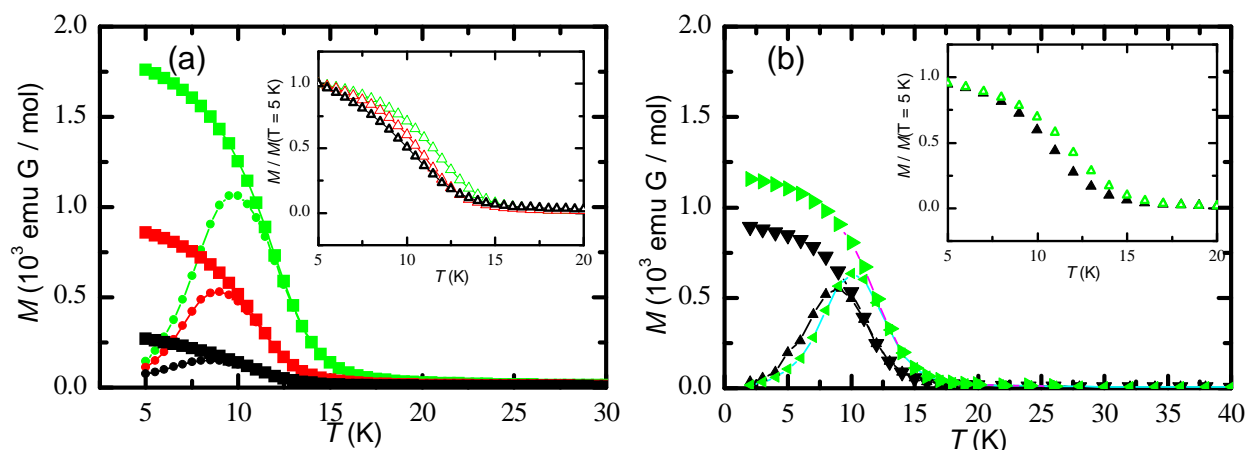


Figure 5-16. Magnetic ordering of quenched states in K-Co-Fe. The temperature dependences of the FC and ZFC DC magnetization, M , are shown in the ordered state at 100 G for Q (\bullet), intermediately quenched (\blacksquare), and G states (\blacktriangle) of (a) ~ 200 nm particles and (b) ~ 27 nm particles. A clear reduction in the magnetism in the quenched state can be seen for the smaller, ~ 27 nm nanoparticles. The ordering temperatures of both samples are similar. (inset) The FC susceptibility normalized to the low temperature limit is shown to more clearly display the changing ordering temperatures.

5.2.4.3 Quenched Low Temperature Magnetization

The temperature dependences of the DC magnetization, $M(H)$, before and after thermal quenching are shown in Figure 5-17. The magnetic signals are expressed per mole, Table 5-6. The history of the cooling is the same as for the DC susceptibility measurements. Both samples show clear increases in their high field magnetization with quenching, and a weak increase in the coercive fields. The ~ 27 nm nanoparticles have a much larger coercive field than the ~ 200 nm nanoparticles.

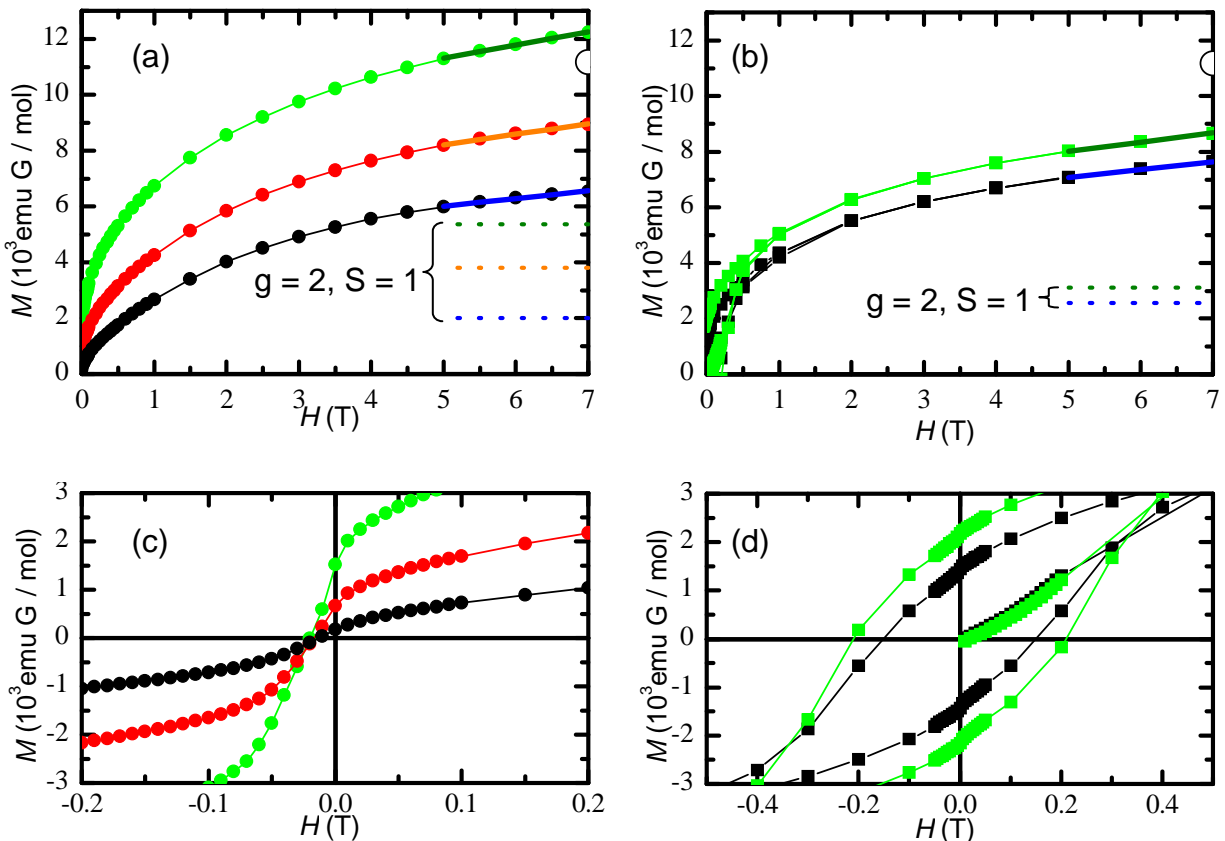


Figure 5-17. Magnetization versus field of quenched states for K-Co-Fe. The $T = 2$ K magnetization versus magnetic field sweeps are shown in the ordered state at 100 G for Q (\bullet), intermediately quenched (\blacksquare), and G states (\blacktriangle) of (a) ~ 200 nm particles and (b) ~ 27 nm particles. The coercive fields, H_C , strongly depend upon the size of the particle, as shown in the expanded views for (c) ~ 200 nm particles and (d) ~ 27 nm particles.

5.2.4.4 Isothermal Relaxation

The time dependences of the DC magnetic susceptibility temperature product, $\chi(T) T$, of the quenched states in the paramagnetic limit are shown in Figure 5-18. The magnetic signals are expressed per mole, Table 5-6. Thermal quenching was achieved by stabilizing the cryostat temperature to 100 K, and quickly inserting the sample. Three different isothermal relaxation temperatures were chosen for each sample. Both samples show non-exponential relaxation of the metastable Q state at elevated temperatures, and the nanoparticles show elongated relaxation times.

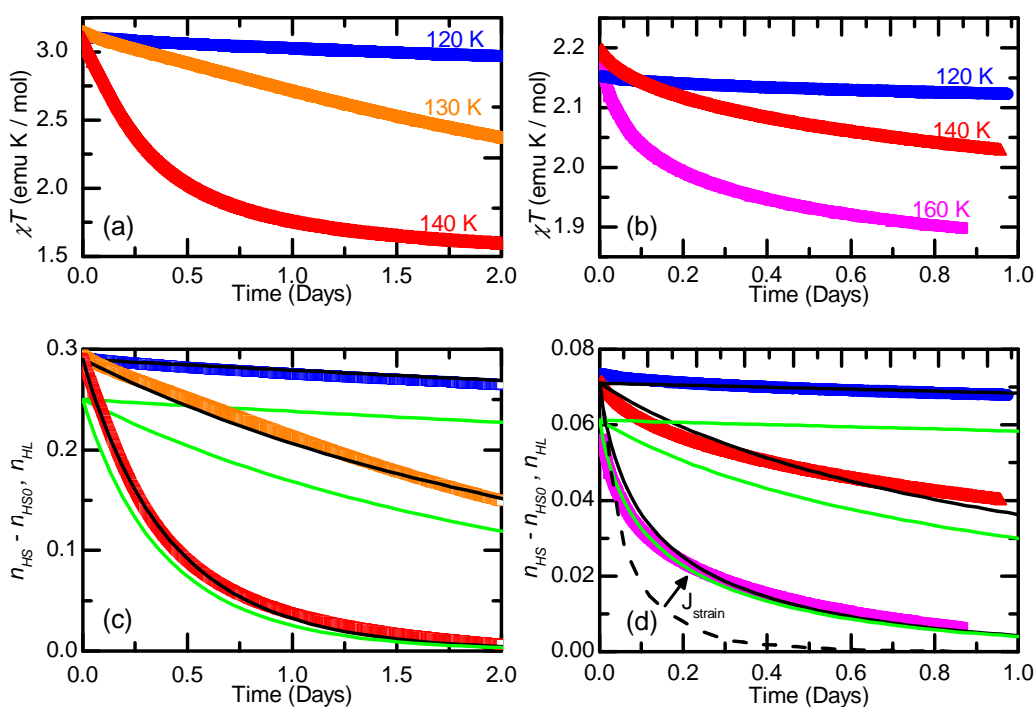


Figure 5-18. Relaxation of magnetization in quenched states of K-Co-Fe. (a) The time dependences of χT in 5 kG is shown for the Q state of the ~ 200 nm particles for 120 K (\bullet), 130 K (\blacksquare), and 140 K (\blacktriangle). (b) The time dependences of χT in 5 kG is shown for the Q state of the ~ 27 nm particles for 120 K (\bullet), 140 K (\blacksquare), and 160 K (\blacktriangle). Using the χT data, the active HS fraction, $n_{HS} - n_{HS0}$, can be extracted and fit (—) to extract the HS-LS mixing parameter, n_{HL} (—), and the semi-empirical spin-crossover parameters, which are shown for (c) ~ 200 and (d) ~ 27 nm particles. In order to fit the ~ 27 nm particle data, an additional parameter for the strain due to ‘reduced’ states must be added to reproduce the relaxation. Details of models used for the fits are explained in the text.

5.2.4.5 Photoinduced Low Temperature DC Susceptibility

The temperature dependences of the DC magnetic susceptibilities, $\chi(T)$, in the ordered state before and after photoirradiation are shown in Figure 5-19. The magnetic signals are expressed per mole, Table 5-6. The light state was established after field cooling the samples from 300 K to 5 K in 100 G and subsequently irradiating with light for 5 hours. The ZFC data were obtained after cooling in zero applied field from 100 K, while the dark state FC data were taken after cooling in 100 G from 100 K. The light state FC data were obtained after cooling from 30 K in 100 G.

Both bulk and nanoparticle samples showed a dramatic increase in the magnetic ordering temperature. The nanoparticles show a reduced ordering temperature compared to the bulk powder due to finite size effects. The differences between the FC susceptibilities of the P and G states are plotted in the insets of Figure 5-19.

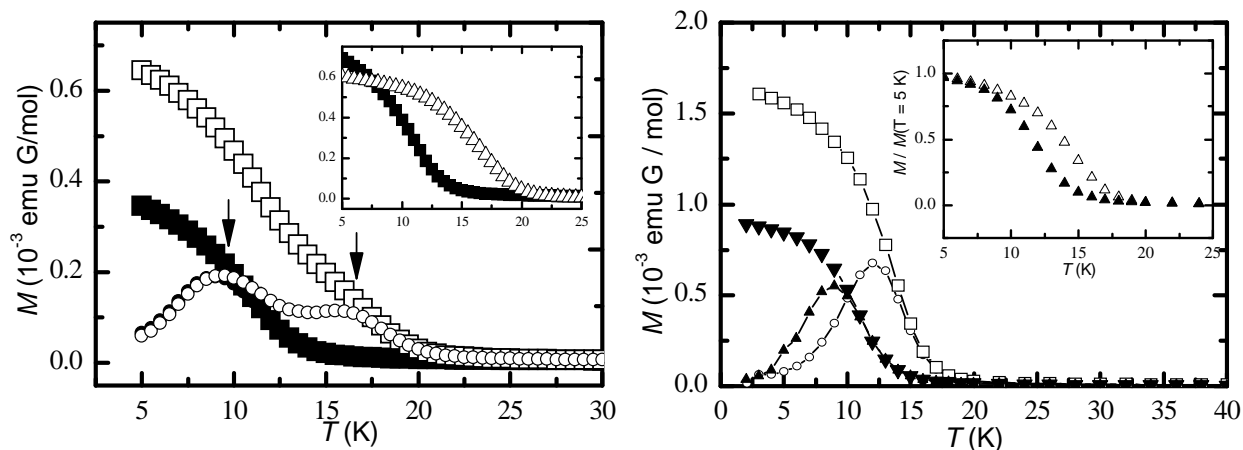


Figure 5-19. Magnetic ordering of photoinduced states in K-Co-Fe. The temperature dependences of the FC and ZFC DC susceptibility, χ , are shown in the ordered state at 100 G for ground states (\blacksquare) and photoinduced (\square) of (a) ~ 200 nm particles and (b) ~ 27 nm particles. Clear increases in the magnetic signals after photoirradiation are present. The arrows point out photoinduced and ground state magnetic signals, most likely due to inhomogeneity of photoirradiation. (inset) The FC susceptibility normalized to the low temperature limit is shown to more clearly display the changing ordering temperatures.

5.2.4.6 Photoinduced Low Temperature Magnetization

The temperature dependences of the DC magnetization, $M(H)$, are shown in Figure 5-20. The magnetic signals are expressed per mole of Prussian blue analogue (PBA), Table 5-6. The history of the cooling is the same as for the DC susceptibility measurements. Both samples show clear increases in their high field magnetization with quenching, and a weak increase in the coercive fields. The ~ 27 nm nanoparticles have a much larger coercive field than the ~ 200 nm nanoparticles.

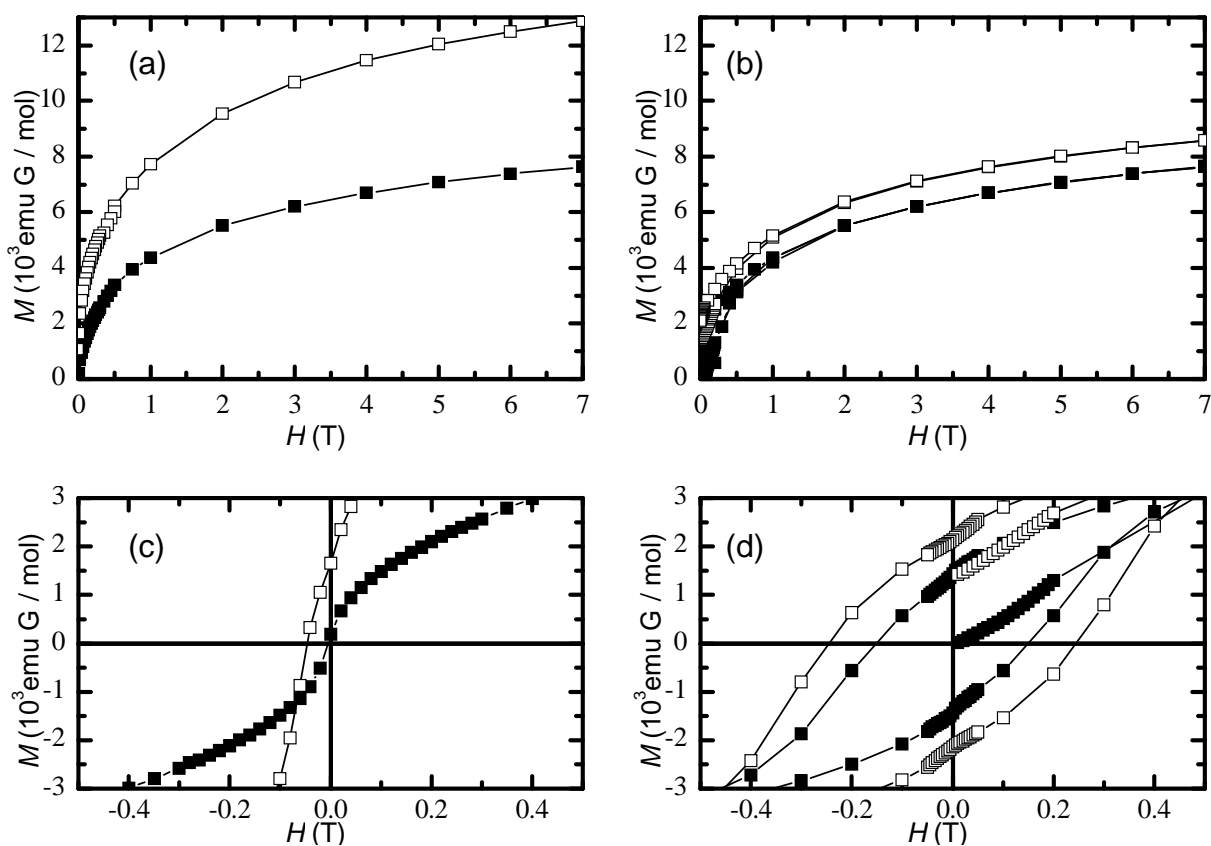


Figure 5-20. Magnetization versus field of photoinduced states for K-Co-Fe. The $T = 2$ K magnetization versus magnetic field sweeps are shown in the ordered state at 100 G ground states (\blacksquare) and photoinduced (\square) of (a) ~ 200 nm particles and (b) ~ 27 nm particles. The coercive fields, H_C , strongly depend upon the size of the particle, and to illustrate this clearly zoomed plots are shown for (c) ~ 200 nm particles and (d) ~ 27 nm particles. Lines are guides for the eyes.

5.2.5 Discussion

First, details of the models used to interpret the data will be introduced. Second, the size dependence of the quenching effect will be discussed. Third, the difference between the photoinduced and quenched states, and particularly how the nanoparticles add to this understanding, will be given. Finally, a schema of the particles that can qualitatively reproduce the previous points will be presented.

5.2.5.1 Details of Modeling

While it is possible to model the complicated system of temperature dependent moments and superexchange interactions using a combination of ligand field theory and mean-field theory, a more transparent and simple approach will be applied for the analysis of the magnetization data presented. A few assumptions are necessary for the simple model and are

- (1) χT versus T is assumed to be linear in the range from 100 K to 300 K,
- (2) the oxidation states at room temperature are taken from the infrared spectroscopy measurements,
- (3) the ground state in the bulk, reached by quenching and subsequently slow cooling, is assumed to have transitioned all switchable Fe ions into the low-spin state, and
- (4) a linear dependence of the susceptibility on the high-spin fraction is assumed.

The validity of assumption (1) is clear, to a high degree, by inspection of the data. Assumption (2) is only an assumption in the sense that the extinction coefficients of the different moieties are not exactly known. Assumption (3) is the biggest conjecture,

however, microscopic probes on analogous bulk samples show that complete transition is plausible [68]. The final assumption, the linearity of the effective moment with respect to the high-spin fraction, may not be obvious. However, this temperature dependence can be justified from mean-field theory predictions by using a plausible set of parameters and plotting the effective moment as a function of the high-spin fraction, Figure 5-21, where the approximate linearity becomes clear.

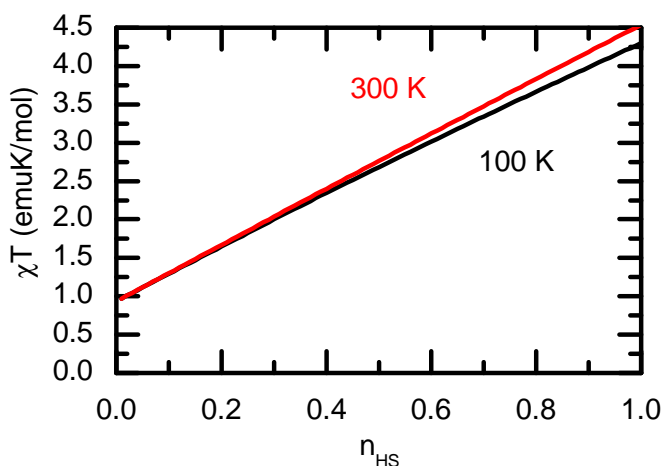


Figure 5-21. Linearization of modeling. The value of χT as a function of the high-spin fraction (n_{HS}), calculated using mean-field theory and ligand field theory and a plausible set of parameters for 100 K and 300 K shows approximately linear behavior.

The results of the aforementioned assumptions, is a semi-empirical expression for χT as a function of the high-spin fraction

$$\chi T(n_{HS}) = \frac{(1.996 + 2.591n_{HS})}{1000} T + (0.407 + 5.002n_{HS}) \quad . \quad 5.2$$

In order to study the bi-stability in the paramagnetic region, an Ising-like model for the charge transfer induced spin transition is used. For this approach, the Hamiltonian is

$$H = -J \sum_{\langle i,j \rangle} s_i s_j - \left(\frac{k_B T}{2} \ln \left(\frac{g_+}{g_-} \right) - \Delta \right) \sum_i s_i \quad , \quad 5.3$$

where $\langle i,j \rangle$ is the sum over nearest neighbors, k_B is the Boltzmann constant, T is the temperature, s is the pseudo-spin that keeps track of the CTIST state of a pair, Δ takes into account the configuration interaction due to electron-electron interaction and the ligand field, g_+ is the degeneracy of the HS state and g_- is the degeneracy of the LS state. Later, for convenience, g will be defined as the ratio $\frac{g_+}{g_-}$. Using a Bethe-Peierls-Weiss approximation, this equation can be solved to get the high-spin fraction, n_{HS} , and the relative population of the mixing of the states, n_{HL} [97].

In order to fit the magnetization curves, various constraints can be applied. To begin, the equilibrium temperature of the transition is well defined,

$$T_{eq} = \frac{2\Delta}{k \ln(g)} \quad . \quad 5.4$$

Equation 5.4 can be used to constrain the parameters of Equation 5.3. First, T_{eq} can be fixed according to the χT versus T data (~ 225 K), and the relative degeneracy of the states can be taken from specific heat measurements on similar materials ($\ln(g) \sim 12$) [92]. These constraints give a value for Δ of 1315 K. From here all parameters can be fit simultaneously to give an activation energy of 5000 K, and an interaction energy of 90 K, with a fundamental relaxation rate of $1/\tau_0 = 1/(0.12 \times 10^{12} \text{ minutes})$.

Aside from scale, the temperature dependence of the magnetization is identical in the nanoparticles and the bulk powder. Based upon this similarity, it is logical to assume that the phenomenological equilibrium parameters are the same, rather than

coincidentally modified in such a way as to give nearly identical macroscopic equilibrium states. Two models were tested by studying the relative homogeneity of the state, n_{HL} . In the first model, the amount of high-spin material was distributed through a nanoparticle volume, and in the second, the nanoparticle acted essentially as regions of a bulk powder and regions of locked pairs in 'reduced' or LS states at all temperatures. It was found that the second model, having discrete regions of trapped and bistable material, had better fits to experimental data. However, in order to more properly fit the nanoparticle relaxation data, an additional temperature dependent interaction term had to be included in the fits to account for the extended relaxation times. This interaction is proposed to be between the bistable pairs and the locked 'reduced' and LS regions in the sample. This association is consistent with the clear temperature dependence of the strain that was detected in lattice constants from the neutron scattering data.

5.2.5.1 Size Dependence of Thermal Quenching

To begin, the TEM images show clear differences in the sizes of the bulk and nanoparticle samples. Although the chemical formulae are similar, the FT-IR displays the decrease in HS material in the nanoparticles at the expense of 'reduced' and LS fractions. Neutron powder diffraction is a microscopic probe that delineated between the HS/'reduced' phases and LS phase in the nanoparticle sample as a function of temperature and provided clear evidence of the strain induced on the lattice for different degrees of thermal quenching. From the paramagnetic susceptibility, n_{HS} could be approximated, and the similarity of the equilibrium temperatures for the bulk and nanoparticles is evidence that the local chemical formula is similar for both samples. Although dramatic increases in the magnetic moment are seen with quenching, only small modifications of the coercive fields and ordering temperatures are observed,

Table 5-7. It is interesting to note that the nanoparticles actually have a significantly larger coercive field, roughly 10 times, although their magnetic ordering temperature is reduced. Isothermal relaxation experiments of the dynamics in the quenched state provide additional evidence for the similarity between the bulk and nanoparticle samples, while also displaying subtle differences due to the strain between the bistable and locked pairs in the nanoparticles.

Table 5-7. Magnetic properties of quenched potassium cobalt hexacyanoferrate nanoparticles and bulk powder.

Batch	Diameter (nm)	T_C^G (K)	T_C^I (K)	T_C^Q (K)	H_C^G (G)	H_C^I (G)	H_C^Q (G)
bulk	200 ± 38	12.3	12.4	13.8	130	165	200
nano	27.4 ± 5.7	12.4	-	15.0	1500	-	2200

5.2.5.2 Photoinduced versus Quenched states

Although the photoinduced and quenched states are identical on the molecular level [90], the resulting many-molecule state in a lattice turns out to be different for quenched or photoinduced pairs due to the interactions between molecular units. This difference can clearly be seen in the macroscopic magnetization, and the manner in which it changes under photoexcitation as compared to thermal quenching, Table 5-8. While the quenched states show little dependence of the ordering temperature and coercive field on the degree of quenching, photoexcitation brings dramatic changes to these parameters. Within the context of a mean-field picture, these differences may be due to better interconnectivity of the lattice in the photoinduced as opposed to quenched states. Also, in the photoinduced state, the difference in the ordering temperature of the bulk and nanoparticles becomes more pronounced, suggesting that the magnetic domains in the nanoparticles are being limited by structural constraints for the

photoinduced states, but not in the quenched states. This observation is consistent with the current microscopic picture of smaller domains in the quenched as compared to photoinduced states for bulk materials [68]. Furthermore, the nanoparticle data implies that the photoinduced domains in the bulk are larger than ~27 nm. In a similar way, the increased ordering temperature of the quenched nanoparticles implies the finite size is constraining trapped spins to be more interconnected in the nanoparticles.

Table 5-8. Magnetic properties of photoinduced potassium cobalt hexacyanoferrate nanoparticles and bulk powder.

Batch	Diameter (nm)	T_C^G (K)	T_C^P (K)	H_C^G (G)	H_C^P (G)
bulk	200 ± 38	12.3	19.2	130	690
nano	27.4 ± 5.7	12.4	15.7	1500	2440

5.2.5.3 Resulting Schema of Bulk and Nanoparticles

Based upon the microscopic data already discussed, as well as the macroscopic magnetization data taken as a whole, Figure 5-22, a qualitative model for the bulk and nanoparticles in the quenched and photoinduced states can be formulated, Figure 5-23. This model is consistent with the quenched and photoinduced structural domains proposed based upon microscopic x-ray diffraction experiments [68], where the magnetism in quenched states is less connected than in the photoinduced states. A consistent extension of the previous bulk model is made for the nanoparticle samples, in which size effects and surface effects now play a role in how the macroscopic magnetization manifests itself based upon the microscopic domains.

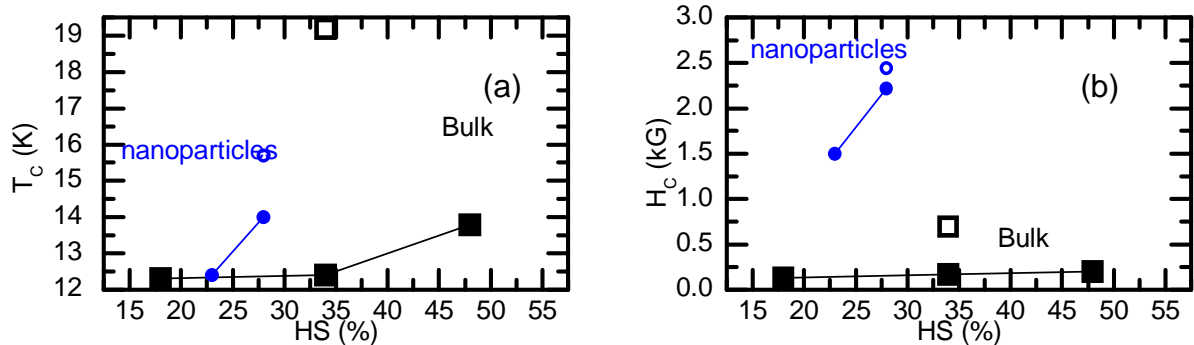


Figure 5-22. Ordering temperatures and coercive fields of batches in different macroscopic states. (a) The dependence of the coercive field upon HS, showing clear increase in coercivities for the nanoparticles, as well as an increase in the coercivity of the P state as compared to the Q state. (b) The dependence of the magnetic ordering temperature upon HS, showing an increase in the ordering temperature of the P state as compared to the Q state, as well as a suppression of the magnetic ordering temperature in the nanoparticles.

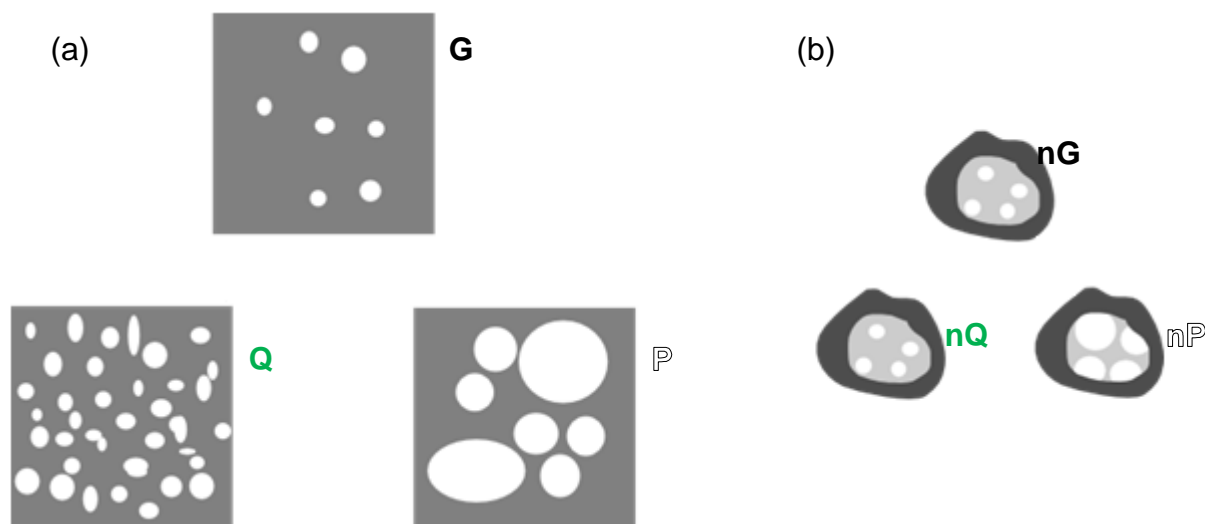


Figure 5-23. Microscopic schema based upon all data. A plausible microscopic picture is shown of the different low temperature ground state (**G**), quenched state (**Q**) and photoinduced state (**P**) in (a) the bulk powder and (b) the nanoparticles, where in the latter, the states are prefixed with “n.” In the bulk, the similar ordering temperatures of the G and Q states imply similar domain structure, as opposed to the increased ordering temperature of the P state, which implies a larger domain structure. In the nanoparticles, the nG versus nQ states are analogous to the bulk G and Q states, however in the nP state, the domains are larger giving an increased ordering temperature, but one that is reduced compared to the bulk P state.

5.2.6 Conclusions

In conclusion, bulk powder and nanoparticles of $K_xCo_k[Fe(CN)_6]_r \cdot nH_2O$ were synthesized and characterized. The experimental data was analyzed using semi-empirical methods to show clear trends suggesting that nanoparticles consist of a core-shell type distribution of states. While the particles are large enough to display long-range magnetic order, the amount of photoswitchable material is dramatically reduced. The coercive fields of the nanoparticles are enhanced more than ten times compared to the bulk.

CHAPTER 6
THIN FILMS OF PRUSSIAN BLUE ANALOGUES

6.1 Introduction

From a technological standpoint, magnetic thin films are of a high interest due to their applications in memory storage. While modern devices utilize mainly metals and alloys, the study of magnetization in thin films of coordination compounds is continuing to provide new twists on magnetic thin films [10] [29] [76] [93] [94] [98-112]. Aside from the benign conditions necessary for synthesis, compared to metallurgy, the ability for magnetic properties to be tuned with external stimuli makes these systems especially attractive. For example, Prussian blue analogues (PBAs), $A_jM1_k[M2(CN)_6]_l \cdot nH_2O$ (Figure 6-1), have been shown to display interesting behavior when in thin film geometries [10] [76] [93] [94] [100] [102].

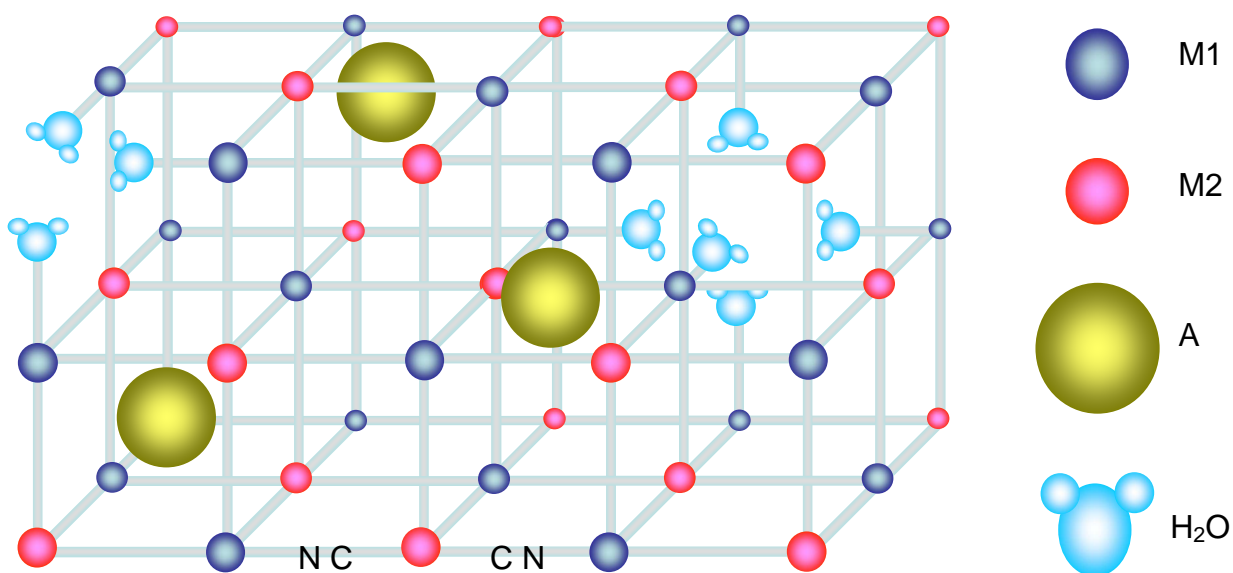


Figure 6-1. Prussian blue analogue structure. Prussian blue analogues have a chemical formula of $A_jM1_k[M2(CN)_6]_l \cdot nH_2O$, j, k, l and n are constrained by charge balance. Cations ($A = Cs^+, Rb^+, K^+, Na^+$) are incorporated based upon the number of M2 vacancies, which are coordinated by water as shown.

In this chapter, a close look is taken at the magnetic properties of PBA thin films generated by a sequential adsorption technique, Figure 6-2. This synthesis technique is attractive due to fine thickness control and the ability to change transition metal centers in a straightforward fashion. Previously, Park *et al.* had seen anisotropy in photoinduced magnetization for thin films of a $\text{Rb}_x\text{Co}_k[\text{Fe}(\text{CN})_6]_l\text{nH}_2\text{O}$ Prussian blue analogue and arrived at a plausible schematic explanation for the effect [100]. However, the $\text{Rb}_x\text{Co}_k[\text{Fe}(\text{CN})_6]_l\text{nH}_2\text{O}$ is complicated due to the ability for iron and cobalt ions to have multiple stable oxidation states, as well as the orbital angular momentum contribution to the net magnetization. Therefore, additional systems should be studied with microscopic probes to understand these films on a more fundamental level.

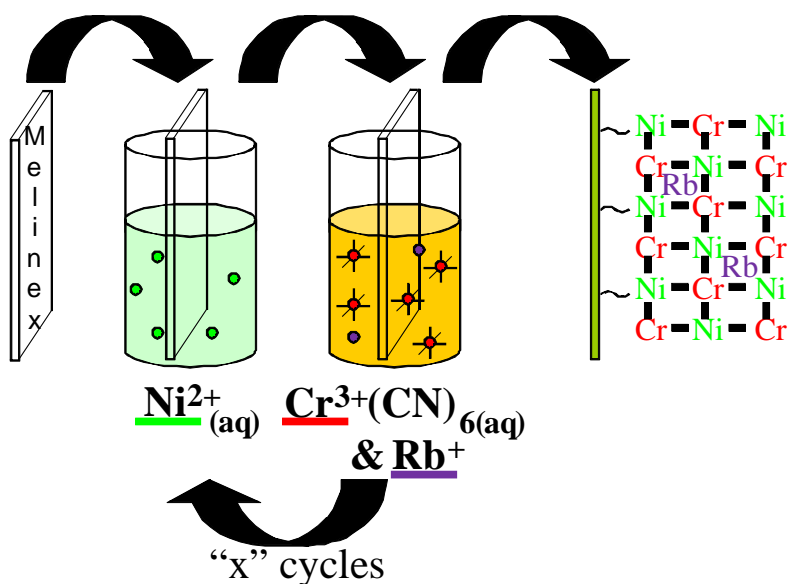


Figure 6-2. The multiple sequential adsorption method that can be used for generating thin films of Prussian blue analogues. For example, synthesis of a Ni-Cr analogue would consist of using a solid support (typically Melinex) and immersing it in an aqueous solution of hexacyanochromate, and into separate solution of Rb^+ and Ni^{2+} ions, thus depositing approximately one layer of Ni-CN-Cr. After each cycle, a simple washing with water is essential to remove excess ions. This process can be iterated to yield films of varying thicknesses and morphologies.

The hypothesis of this work is that when films are oriented at different directions with respect to an applied magnetic field, Figure 6-3, different magnetic susceptibilities will be observed due to the geometry of the samples. To this end, a series of nickel hexacyanochromate films were studied in the greatest detail, but other transition metal analogues were also studied. The main probe utilized was a SQUID magnetometer, however to get a more detailed microscopic understanding of the effects observed in the magnetization, UV-Vis, FT-IR, EMR, and XRD, among other probes, were employed. The results of these studies are to be presented in the following chapter. Portions of this work have already been published in Dr. Justin E. Gardner's thesis [93], and the main results are to be submitted for future publication.

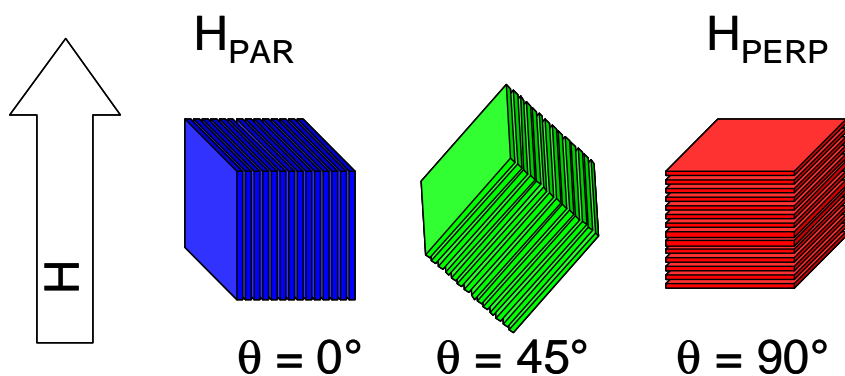


Figure 6-3. Different orientations of the magnetic thin films with respect to the applied magnetic field are expected to have different behavior.

In Section 6.2, experimental work on thin films of $\text{Rb}_{0.7}\text{Ni}_{4.0}[\text{Cr}(\text{CN})_6]_{2.9}\cdot n\text{H}_2\text{O}$ thin films is presented, including magnetization and magnetic resonance experiments. In Section 6.3, experimental data resulting from studying additional Prussian blue analogue films are given. The source of anisotropy in the different systems, as well as ion dependence, is discussed (Section 6.4) and possible future experiments are mentioned.

6.2 $\text{Rb}_{0.7}\text{Ni}_{4.0}[\text{Cr}(\text{CN})_6]_{2.9}\cdot n\text{H}_2\text{O}$ thin films

The material chosen for an in-depth study of the thin film geometry, having a Melinex solid support, was the rubidium nickel hexacyanochromate Prussian blue analogue, $\text{Rb}_j\text{Ni}_k[\text{Cr}(\text{CN})_6]_l\cdot n\text{H}_2\text{O}$. The reasons for choosing this material are three-fold. First, the samples are robust for months after synthesis, with little detectable changes in their materials properties. Second, $\text{Rb}_j\text{Ni}_k[\text{Cr}(\text{CN})_6]_l\cdot n\text{H}_2\text{O}$ has a convenient magnetic ordering temperature that is quite high for coordination networks, varying between 60 and 90 K, depending upon the stoichiometry of the sample [54]. Finally, the single-ion ground states are well defined, having stable oxidation states and no first-order orbital angular momentum.

6.2.1 Sample Characterization

To begin, thin films of nickel hexacyanochromate were characterized with scanning electron microscopy to determine the chemical formula, atomic force microscopy to determine the thickness and surface morphology, infrared spectroscopy to determine the cyanide stretching frequencies, and ultraviolet and Visible electron spectroscopy to determine the electronic structure of the ions. Results of these studies will be presented in the following sections, to set a frame of reference for magnetization, resonance, and x-ray scattering experiments.

6.2.1.1 Chemical Composition

Chemical composition was determined using scanning electron microscopy (SEM). Films were cut into squares of 1 cm^2 , mounted onto a metal puck, and coated with a thin film of carbon to enhance conductivity. The results gave chemical formulas of $\text{Rb}_{0.7}\text{Ni}_{4.0}[\text{Cr}(\text{CN})_6]_{2.9}\cdot n\text{H}_2\text{O}$ for the films, and additional details can be found in Dr. Justin E. Gardner's thesis [93].

6.2.1.2 AFM

Detailed atomic force microscopy (AFM) studies of thin films of different Prussian blue analogues were performed by Dr. Justin E. Gardner, as detailed in his thesis [93]. Briefly, the nickel hexacyanochromate analogue shows a linear dependence of thickness upon the number of deposition cycles, and an approximately linear dependence of the root-mean-square (RMS) roughness upon the number of deposition cycles, Figure 6-4. The curious dip in roughness at 20 cycles is reproducible, and likely dependent upon the inherent structural coherence of the material under the given growth conditions.

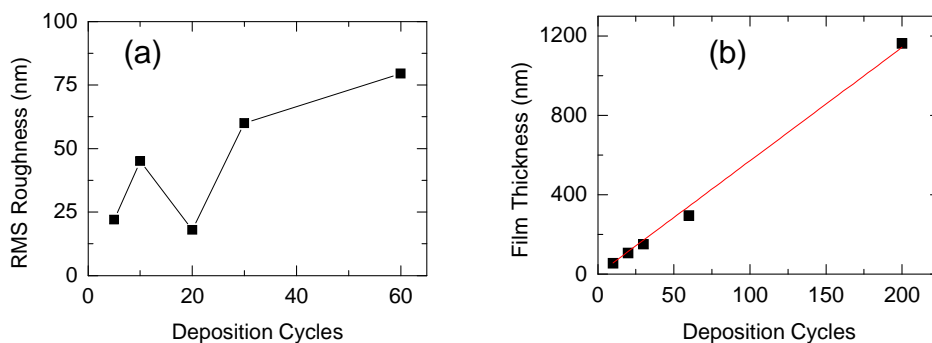


Figure 6-4. AFM of thin films. (a) Multiple sequential adsorption film roughness generally increases with number of cycles, but the 20 cycle film is smoothest. This minimum in the roughness is due to the inherent structural coherence of the material and is reproducible. (b) The thickness of the multiple sequential adsorption films is directly proportional to the number of cycles. The red line is a fit yielding 5.7 nm/cycle.

6.2.1.3 FT-IR

Fourier transform infrared (FT-IR) spectroscopy measurements provide information about the structure of cyanometallate networks, based upon the energies of the cyanide stretches. Room temperature FT-IR was performed on a $K_3Cr(CN)_6$ precursor, an 80 cycle $Rb_{0.7}Ni_{4.0}[Cr(CN)_6]_{2.9} \cdot nH_2O$ thin film, and a $Rb_{0.7}Ni_{4.0}[Cr(CN)_6]_{2.9} \cdot nH_2O$ powder. While the films could be mounted directly, the

powders were measured in diluted KBr solid solutions. The cyanide stretches associate with the $\text{Ni}^{2+}\text{-NC-Cr}^{3+}$ unit of the bulk powder and thin films were observed to be similar, Figure 6-5. The sharp peak in the precursor also appears to be present in both the thin films and the powder samples.

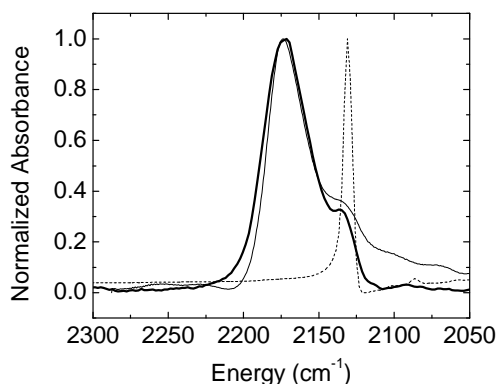


Figure 6-5. Room temperature FT-IR spectroscopy measurements of the cyanide stretches present in Ni-Cr materials. Cyanide stretches are seen in the $\text{K}_3\text{Cr}(\text{CN})_6$ precursor (---), $\text{Rb}_{0.7}\text{Ni}_{4.0}[\text{Cr}(\text{CN})_6]_{2.9}\cdot n\text{H}_2\text{O}$ powder (—), and a 80 cycle thin film of $\text{Rb}_{0.7}\text{Ni}_{4.0}[\text{Cr}(\text{CN})_6]_{2.9}\cdot n\text{H}_2\text{O}$ (-·-). The $\text{K}_3\text{Cr}(\text{CN})_6$ sample shows one clear stretch at 2131 cm^{-1} . The thin film and powder samples show peaks at 2173 cm^{-1} and 2131 cm^{-1} , with the latter being associated with free cyanides at the surface and coordinating vacancies.

6.2.1.4 UV-Vis

Electronic spectroscopy in the Visible and ultraviolet (UV-Vis) provides important information about the electronic structure of a $\text{K}_3\text{Cr}(\text{CN})_6$ precursor, an 80 cycle $\text{Rb}_{0.7}\text{Ni}_{4.0}[\text{Cr}(\text{CN})_6]_{2.9}\cdot n\text{H}_2\text{O}$ thin film and a $\text{Rb}_{0.7}\text{Ni}_{4.0}[\text{Cr}(\text{CN})_6]_{2.9}\cdot n\text{H}_2\text{O}$ powder. Room temperature UV-Vis spectroscopy shows d-d transitions associated with the molecular building blocks of the materials, Figure 6-6, namely $\text{Cr}(\text{CN})_6$ and $\text{Ni}(\text{NC})_6$. Ligand field multiplet calculations were performed using the methods described in Chapter 3. Two clear transitions are present in all samples, one for Ni^{2+} at $17,100\text{ cm}^{-1}$ corresponding to a ${}^3\text{A}_{2g}(\text{F}) \rightarrow {}^3\text{T}_{1g}(\text{F})$ type transition and one for Cr^{3+} at $26,600\text{ cm}^{-1}$ corresponding to a ${}^4\text{A}_{2g}(\text{F}) \rightarrow {}^4\text{T}_{2g}(\text{F})$ type transition. In the precursor, an additional transition at

32,600 cm^{-1} can be resolved. In the PBA film and powder, a less resolvable ${}^3A_{2g}(F) \rightarrow {}^3T_{2g}(F)$ type transition for Ni^{2+} can be seen near 10,000 cm^{-1} . There is no clear evolution from precursors, to bulk, to film, possibly due to the large line widths. All samples show ground states consistent with quenched orbital angular momentum.

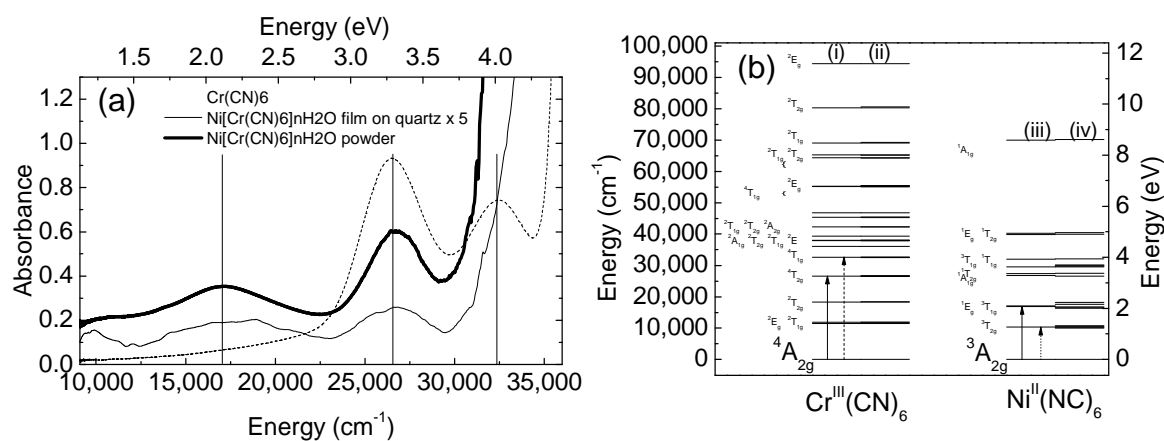


Figure 6-6. UV-Vis spectroscopy of Ni-Cr materials. (a) Room temperature UV-Vis spectroscopy measurements of the d-d transitions present in 10 mM $\text{Cr}(\text{CN})_6$ precursor (---), 10 mM $\text{Rb}_{0.7}\text{Ni}_{4.0}[\text{Cr}(\text{CN})_6]_{2.9}\cdot n\text{H}_2\text{O}$ powder with background subtracted by using the functional form of a diamagnetic $\text{Rb}_{0.5}\text{Zn}_{4.0}[\text{Fe}(\text{CN})_6]_{2.8}\cdot n\text{H}_2\text{O}$ (—), and an 80 cycle thin film of $\text{Rb}_{0.7}\text{Ni}_{4.0}[\text{Cr}(\text{CN})_6]_{2.9}\cdot n\text{H}_2\text{O}$ with background subtracted by using the functional form of a diamagnetic $\text{Rb}_{0.5}\text{Zn}_{4.0}[\text{Fe}(\text{CN})_6]_{2.8}\cdot n\text{H}_2\text{O}$ film (—). (b) Using the transitions shown in Figure 6-6 (a), a multiplet calculation can be performed to show the electronic energy levels for the Ni^{2+} and Cr^{3+} ions in the Prussian blue network. Chromium energy levels are shown for (i) no spin-orbit coupling and (ii) using reported values of spin-orbit coupling for the free ion [5]. Nickel energy levels are shown for (iii) no spin-orbit coupling and (iv) using reported values of spin-orbit coupling for the free ion [5].

6.2.2 Magnetization

A commercial magnetometer from Quantum Design was used for the DC-SQUID measurements. Powder samples were mounted in diamagnetic gelcaps, thin film samples were either stacked in boxes or measured individually in a straw without additional mounting. Commercial straws were used as a diamagnetic sample rod to allow translation of the sample through the SQUID magnetometer detector coils.

6.2.2.1 DC Susceptibility in 100 G

The low field magnetization as a function of temperature for the bulk $\text{Rb}_{0.7}\text{Ni}_{4.0}[\text{Cr}(\text{CN})_6]_{2.9}\cdot n\text{H}_2\text{O}$ and thin films of $\text{Rb}_{0.7}\text{Ni}_{4.0}[\text{Cr}(\text{CN})_6]_{2.9}\cdot n\text{H}_2\text{O}$ are shown in Figure 6-7, with both parallel and perpendicular orientations with respect to the applied magnetic field shown for the film samples. Bulk material is expressed per mole and film samples are expressed per unit area. The ZFC data were obtained after cooling in zero applied field from 300 K, while the FC data were taken after cooling in 100 G from 300 K. All samples show a change in the inflection of the magnetization versus temperature, indicative of the three dimensional magnetic order known to exist between 60-90 K, depending upon stoichiometry [54]. The thin film samples show clear anisotropy between the susceptibility in the parallel and perpendicular orientations.

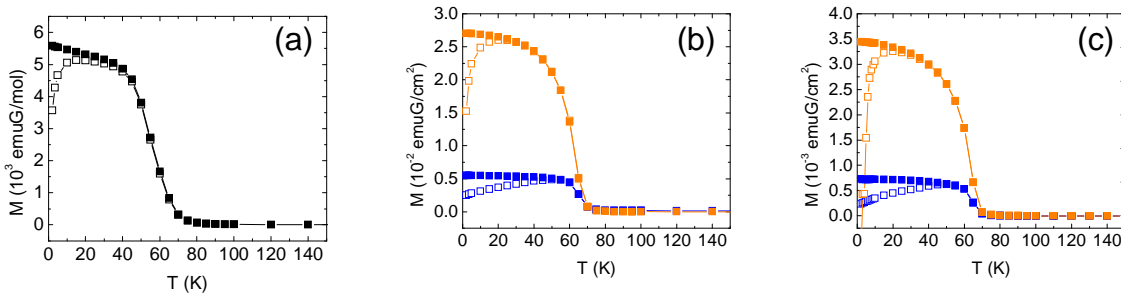


Figure 6-7. Temperature dependent magnetization of Ni-Cr materials. The temperature dependences of the low field, 100 G, magnetizations are shown for $\text{Rb}_{0.7}\text{Ni}_{4.0}[\text{Cr}(\text{CN})_6]_{2.9}\cdot n\text{H}_2\text{O}$ (a) powder, zero-field cooled (ZFC) (\square) and field-cooled (FC) (\blacksquare), (b) 400 cycle thin film, parallel ZFC (\square), parallel FC (\blacksquare), perpendicular ZFC (\square) and perpendicular FC (\blacksquare), (c) 40 cycle thin film, parallel ZFC (\square), parallel FC (\blacksquare), perpendicular ZFC (\square) and perpendicular FC (\blacksquare). Connecting lines are guides to the eye.

6.2.2.2 DC Magnetization in 40 kG

The temperature dependences of the high field magnetization for the bulk $\text{Rb}_{0.7}\text{Ni}_{4.0}[\text{Cr}(\text{CN})_6]_{2.9}\cdot n\text{H}_2\text{O}$ and thin films of $\text{Rb}_{0.7}\text{Ni}_{4.0}[\text{Cr}(\text{CN})_6]_{2.9}\cdot n\text{H}_2\text{O}$ are shown in Figure 6-8, with both parallel and perpendicular orientations with respect to the applied magnetic field shown for the film samples. Bulk material is expressed per mole and film samples are expressed per unit area. For these measurements in $H = 40$ kG, the ZFC and FC data were found to lie on top of each other. This measuring field is particularly relevant for comparison with $f \sim 116$ GHz microwave magnetic resonance experiments. All samples show the usual increased ordering temperature and a more gradual slope of the onset compared to the low field measurements. Even at these high fields, the thin film samples show clear anisotropy between the susceptibility in the parallel and perpendicular orientations.

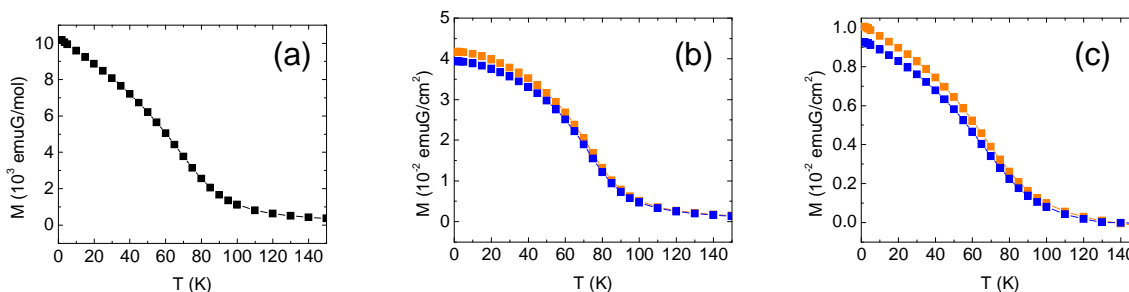


Figure 6-8. Temperature dependent magnetization of Ni-Cr materials at high fields. The temperature dependences of the high field, $H = 40$ kG, magnetizations are shown for $\text{Rb}_{0.7}\text{Ni}_{4.0}[\text{Cr}(\text{CN})_6]_{2.9}\cdot n\text{H}_2\text{O}$ (a) powder (■), (b) 400 cycle thin film, parallel (■) and perpendicular FC (■), (c) 40 cycle thin film, parallel (■) and perpendicular FC (■). Lines connecting discrete data points are guides to the eye.

6.2.2.3 DC Magnetization Field Dependence

The field dependences of the DC magnetization at $T = 2$ K for bulk $\text{Rb}_{0.7}\text{Ni}_{4.0}[\text{Cr}(\text{CN})_6]_{2.9}\cdot n\text{H}_2\text{O}$ and thin films of $\text{Rb}_{0.7}\text{Ni}_{4.0}[\text{Cr}(\text{CN})_6]_{2.9}\cdot n\text{H}_2\text{O}$ are shown in Figure 6-9, with both parallel and perpendicular orientations with respect to the applied magnetic field shown for the film samples. Bulk material is expressed per mole and film samples are expressed per unit area. All samples show clear saturation indicative of ferromagnetic interactions in the complex. Thin films show anisotropy persisting up to the largest available field of 70 kG.

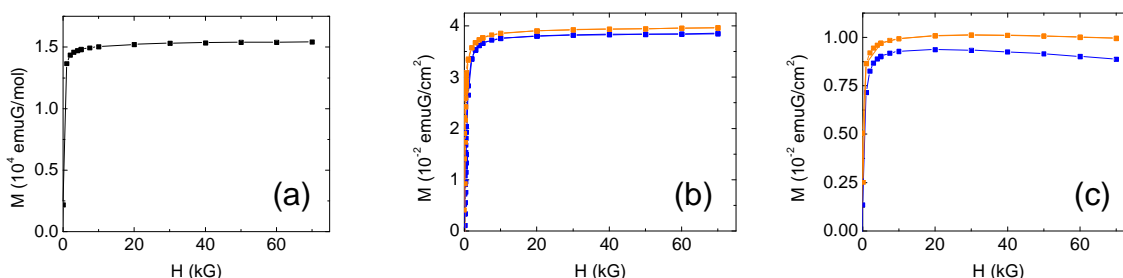


Figure 6-9. Field dependent magnetization of Ni-Cr materials. The field dependences of the low temperature, 2 K, magnetizations are shown for $\text{Rb}_{0.7}\text{Ni}_{4.0}[\text{Cr}(\text{CN})_6]_{2.9}\cdot n\text{H}_2\text{O}$ (a) powder (■), (b) 400 cycle thin film, parallel (■) and perpendicular FC (■), (c) 40 cycle thin film, parallel (■) and perpendicular FC (■). The negative high field slope of the magnetization in the 40 cycle film can be attributed to the diamagnetic substrate. Lines connecting discrete data points are guides to the eye.

6.2.2.4 Magnetization Process

The field dependence during the magnetization process, $H = 0$ to $H = 2.5$ kG, was mapped at many temperatures, from 10 K to 70 K in 10 K increments. This series of scans was performed on the bulk powder of $\text{Rb}_{0.7}\text{Ni}_{4.0}[\text{Cr}(\text{CN})_6]_{2.9}\cdot n\text{H}_2\text{O}$ (Figure 6-10), 40 cycle $\text{Rb}_{0.7}\text{Ni}_{4.0}[\text{Cr}(\text{CN})_6]_{2.9}\cdot n\text{H}_2\text{O}$ thin films (Figure 6-11), and 400 cycle $\text{Rb}_{0.7}\text{Ni}_{4.0}[\text{Cr}(\text{CN})_6]_{2.9}\cdot n\text{H}_2\text{O}$ thin films (Figure 6-12), with both parallel and perpendicular orientations with respect to the applied field measured for the films.

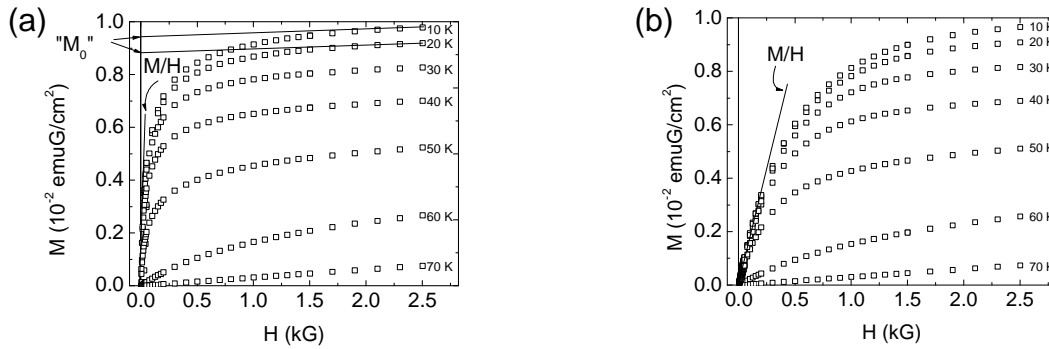


Figure 6-10. Magnetizing process of thin Ni-Cr film. Magnetization as a function of external field for 40 cycle film of $\text{Rb}_{0.7}\text{Ni}_{4.0}[\text{Cr}(\text{CN})_6]_{2.9}\cdot n\text{H}_2\text{O}$ in (a) parallel and (b) perpendicular orientations with respect to the applied magnetic field. Here the field dependence of the low field data is fit to a linear model, $M = \chi H$, where $\chi = M/H$. In a similar manner, the high field data can be fit to $M = M_0 + \chi_E H$. These fits are relevant to understanding the magnetization process and more specifically to understand the potential roles of demagnetizing fields in the materials.

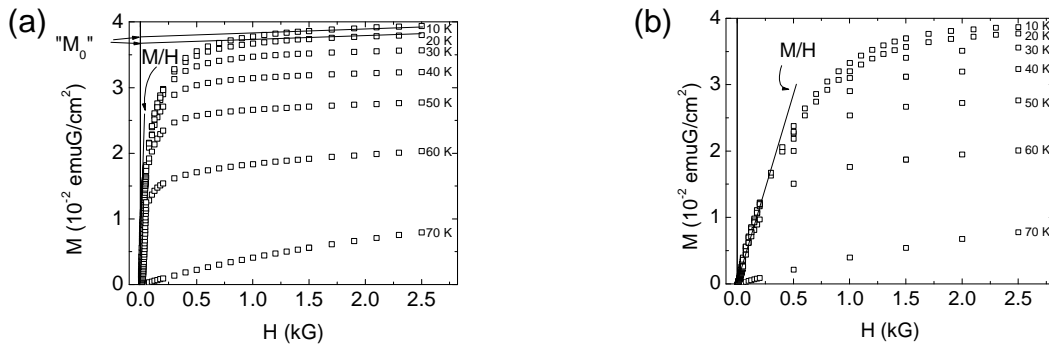


Figure 6-11. Magnetizing process of thick Ni-Cr film. Magnetization as a function of external field for 400 cycle film of $\text{Rb}_{0.7}\text{Ni}_{4.0}[\text{Cr}(\text{CN})_6]_{2.9}\cdot n\text{H}_2\text{O}$ in (a) parallel and (b) perpendicular orientations with respect to the applied magnetic field. The meaning of the fitting lines are described in the figure caption of Figure 6-10.

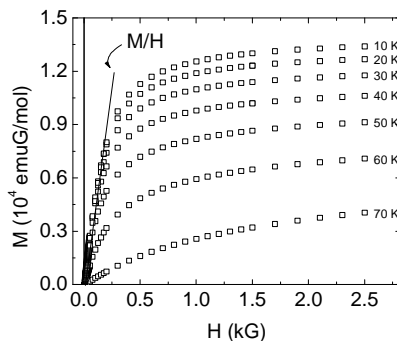


Figure 6-12. Magnetizing process of Ni-Cr powder. Magnetization as a function of external field for $\text{Rb}_{0.7}\text{Ni}_{4.0}[\text{Cr}(\text{CN})_6]_{2.9}\cdot n\text{H}_2\text{O}$ bulk powder. The meaning of the fitting lines are described in the figure caption of Figure 6-10.

6.2.2.5 DC Magnetization Angular Dependence

In order to determine the functional form of the angular dependent magnetic anisotropy, in-situ rotation measurements were performed in a SQUID magnetometer using a custom made rotation probe [28]. Measurements were performed on 40 cycle and 400 cycle thin films of $\text{Rb}_{0.7}\text{Ni}_{4.0}[\text{Cr}(\text{CN})_6]_{2.9}\cdot n\text{H}_2\text{O}$ at $T = 10\text{ K}$ and $H = 40\text{ kG}$, Figure 6-13. These field and temperature values were chosen to be compared to $f \sim 116\text{ GHz}$ microwave electron magnetic resonance experiments. Both films show clear anisotropy, with an in-plane easy axis.

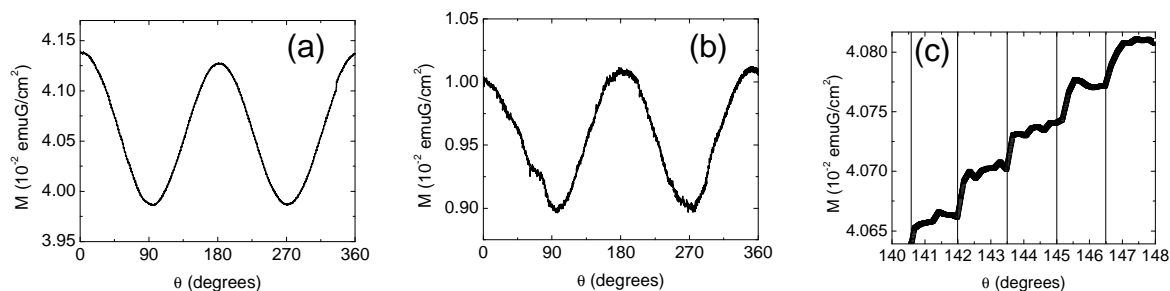


Figure 6-13. Angle dependence of magnetization in Ni-Cr materials. (a) Magnetization as a function of angle, at $T = 10\text{ K}$ and $H = 40\text{ kG}$, for (a) 400 cycle $\text{Rb}_{0.7}\text{Ni}_{4.0}[\text{Cr}(\text{CN})_6]_{2.9}\cdot n\text{H}_2\text{O}$ thin films and (b) 40 cycle $\text{Rb}_{0.7}\text{Ni}_{4.0}[\text{Cr}(\text{CN})_6]_{2.9}\cdot n\text{H}_2\text{O}$ thin films. Both data sets are raw magnetization from the SQUID, without any additional processing. A detail of the 400 cycle film data shows the discrete 1.5° steps used during rotation, as data was taken continuously. The difference in the signal to noise for the two measurements may be due to the different amount of sample present in a 40 versus 400 cycle film.

6.2.3 Electron Magnetic Resonance

To further probe the magnetic transitions in the $\text{Rb}_{0.7}\text{Ni}_{4.0}[\text{Cr}(\text{CN})_6]_{2.9}\cdot n\text{H}_2\text{O}$ magnets, and particularly the anisotropic thin films, electron magnetic resonance experiments were performed on powders and films. Continuous wave absorption measurements were performed using a resonant cavity technique at the NHMFL in Tallahassee. Temperature dependence, angular dependence and frequency

dependence of the microwave absorption will be presented in the following sections. Previously, EMR researchers at the NHMFL have studied powders of the charge transfer Mn-Fe Prussian blue analogue [112bis].

6.2.3.1 EMR Temperature Dependence

The temperature dependence of the microwave absorption for a $\text{Rb}_{0.7}\text{Ni}_{4.0}[\text{Cr}(\text{CN})_6]_{2.9}\cdot n\text{H}_2\text{O}$ powder was measured at a continuous frequency of ~ 116 GHz, Figure 6-14. One clear absorption peak can be seen, with an effective g-factor of 2.05. The full-width half-maximum of the line-width, the position, and the area of the peak all show dependences on the magnetic order parameter, Figure 6-15. More specifically, the change in the shape of the curves, near 90 K, is the temperature at which the magnetization curves also have a change in shape, which has been assigned to the development of long-range magnetic order in the samples.

The temperature dependence of the microwave absorption for a $\text{Rb}_{0.7}\text{Ni}_{4.0}[\text{Cr}(\text{CN})_6]_{2.9}\cdot n\text{H}_2\text{O}$ 40 cycle film was measured perpendicular to the applied magnetic field at $f \sim 116$ GHz, Figure 6-16. In contrast with the powder, two clear absorption peaks can be seen, with effective g-factors of 1.97 and 2.05 at 10 K. These shifts in effective g-factors (and those in the following paragraphs) may not actually be associated with changing g-factors, but are merely stated to give an additional frame of reference for the magnitude of the shifts of the lines. The full-width half-maximum of the line-widths, the position of the peaks, and the area of the peaks all show dependences on the magnetic order parameter, Figure 6-17. Just as in the powder resonance experiment, the lines are showing changes in behavior near 90 K, which is the magnetic ordering temperature of the sample for external fields of 40 kG.

The temperature dependence of the microwave absorption for a $\text{Rb}_{0.7}\text{Ni}_{4.0}[\text{Cr}(\text{CN})_6]_{2.9}\cdot n\text{H}_2\text{O}$ 40 cycle film was measured parallel to the applied magnetic field at $f \sim 116$ GHz, Figure 6-18. Similar to the perpendicular orientation, two clear absorption peaks can be seen. However, effective g-factors of 2.11 and 2.05 are observed at 10 K. The full-width half-maximum of the line-widths, the position of the peaks, and the area of the peaks all show dependence on the magnetic order parameter, Figure 6-19, with a change in shape of the temperature dependence happening near the magnetic ordering temperature of 90 K.

The temperature dependence of the microwave absorption for a $\text{Rb}_{0.7}\text{Ni}_{4.0}[\text{Cr}(\text{CN})_6]_{2.9}\cdot n\text{H}_2\text{O}$ 400 cycle film was measured perpendicular to the applied magnetic field at $f \sim 116$ GHz, Figure 6-20. Similar to the 40 cycle film measured perpendicularly, two peaks are seen, with effective g-factors of 1.97 and 2.05 at 10 K. The full-width half-maximum of the line-widths, the position of the peaks, and the area of the peaks all show dependence on the magnetic order parameter, Figure 6-21, in the same manner as the thinner films.

The temperature dependence of the microwave absorption for a $\text{Rb}_{0.7}\text{Ni}_{4.0}[\text{Cr}(\text{CN})_6]_{2.9}\cdot n\text{H}_2\text{O}$ 400 cycle film was measured parallel to the applied magnetic field at $f \sim 116$ GHz, Figure 6-22. Similar to the 40 cycle film measured parallel to the field, two peaks are seen, with effective g-factors of 2.11 and 2.05 at 10 K. The full-width half-maximum of the line-widths, the position of the peaks and the area of the peaks all show dependence on the magnetic order parameter, Figure 6-23, in the same manner as the thinner films.

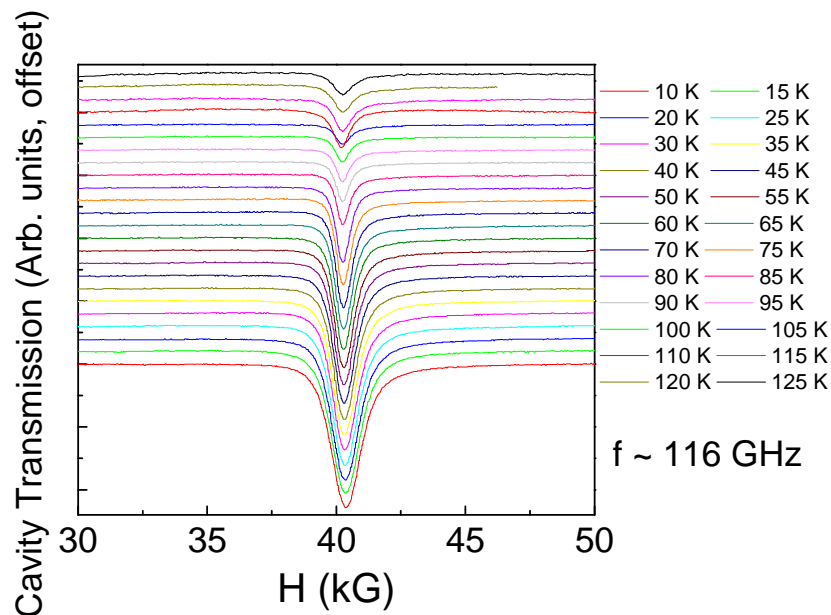


Figure 6-14. EMR lines of Ni-Cr powder. The field dependence of the microwave transmission through the resonance cavity as a function of temperature, measured at a constant frequency of ~ 116 GHz, for $\text{Rb}_{0.7}\text{Ni}_{4.0}[\text{Cr}(\text{CN})_6]_{2.9}\cdot n\text{H}_2\text{O}$ powder. Here the data have been offset to more clearly display the evolution of the line.

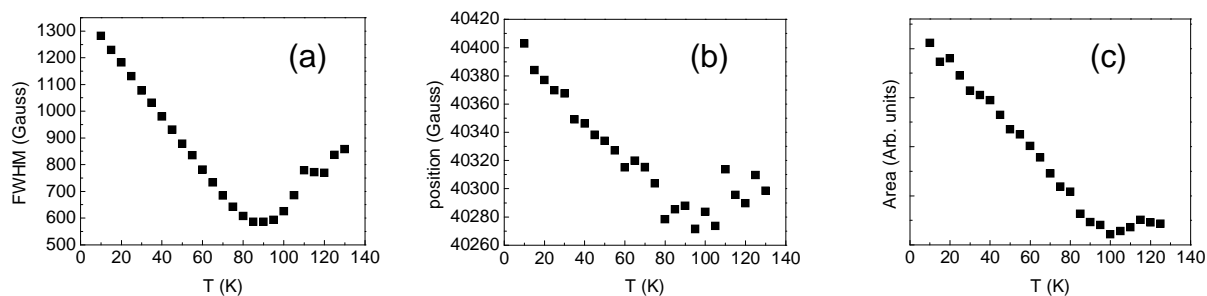


Figure 6-15. Results of fitting EMR lines of Ni-Cr powder. Fitting the temperature dependence in Figure 6-14 to a Lorentzian line yields (a) the full-width half-maximum (FWHM) of the line, (b) the center position of the absorption line and (c) the relative area of the absorption peak as a function of temperature.

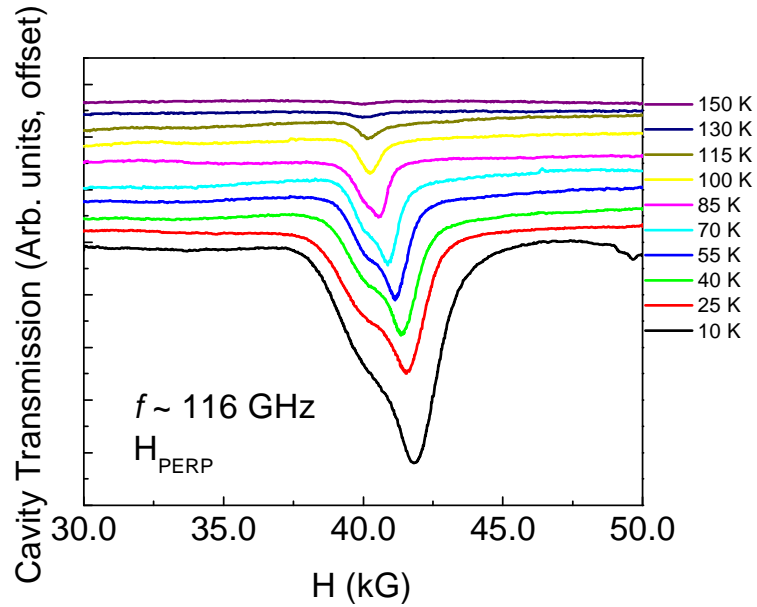


Figure 6-16. EMR lines of Ni-Cr thin film perpendicular. The field dependence of the microwave transmission through the resonance cavity as a function of temperature, measured at $f \sim 116$ GHz, for $\text{Rb}_{0.7}\text{Ni}_{4.0}[\text{Cr}(\text{CN})_6]_{2.9} \cdot n\text{H}_2\text{O}$ 40 cycle films perpendicular to the applied field. Here the data have been offset to more clearly display the evolution of the line.

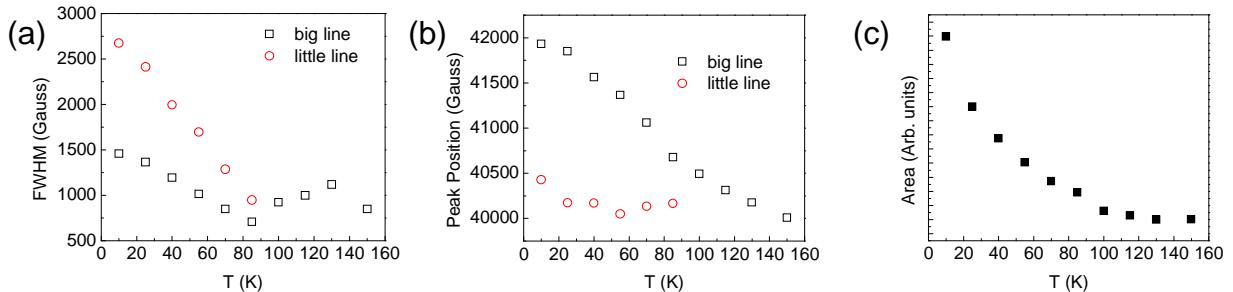


Figure 6-17. Results of fitting EMR lines of Ni-Cr thin film perpendicular. Fitting the temperature dependence in Figure 6-16 to Lorentzian lines yield (a) the full-width half-maximum (FWHM) of the lines, (b) the center positions and (c) the relative area of both peaks as a function of temperature.

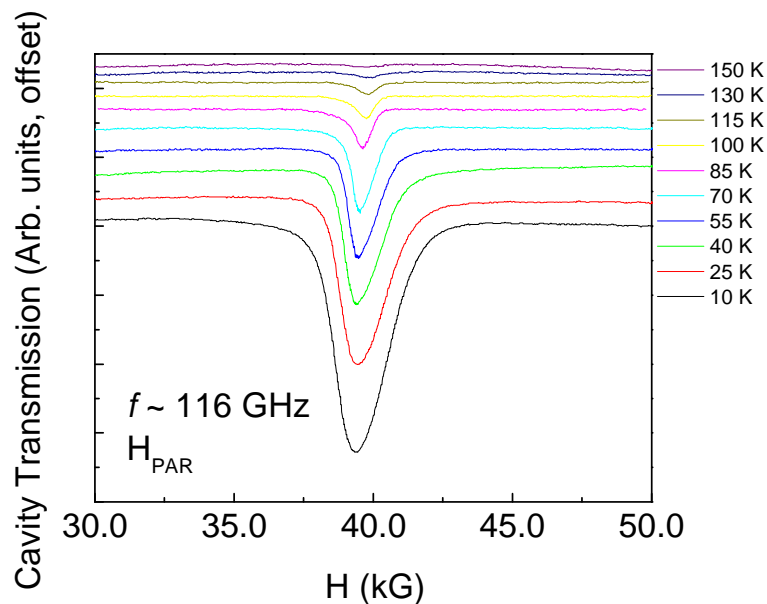


Figure 6-18. EMR lines of Ni-Cr thin film parallel. The field dependence of the microwave transmission through the resonance cavity as a function of temperature, measured at $f \sim 116$ GHz, for $\text{Rb}_{0.7}\text{Ni}_{4.0}[\text{Cr}(\text{CN})_6]_{2.9} \cdot n\text{H}_2\text{O}$ 40 cycle films parallel to the applied field. Here the data have been offset to more clearly display the evolution of the line.

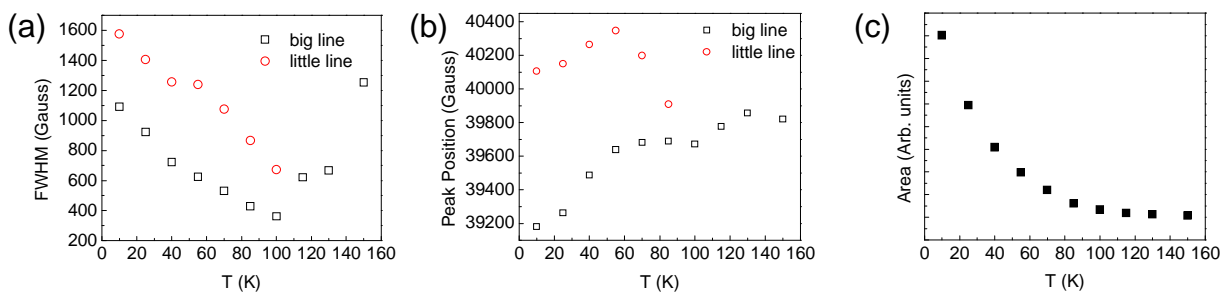


Figure 6-19. Results of fitting EMR lines of Ni-Cr thin film parallel. Fitting the temperature dependence in Figure 6-18 to Lorentzian lines yield (a) the full-width half-maximum (FWHM) of the lines, (b) the center positions and (c) the relative area of both peaks as a function of temperature.

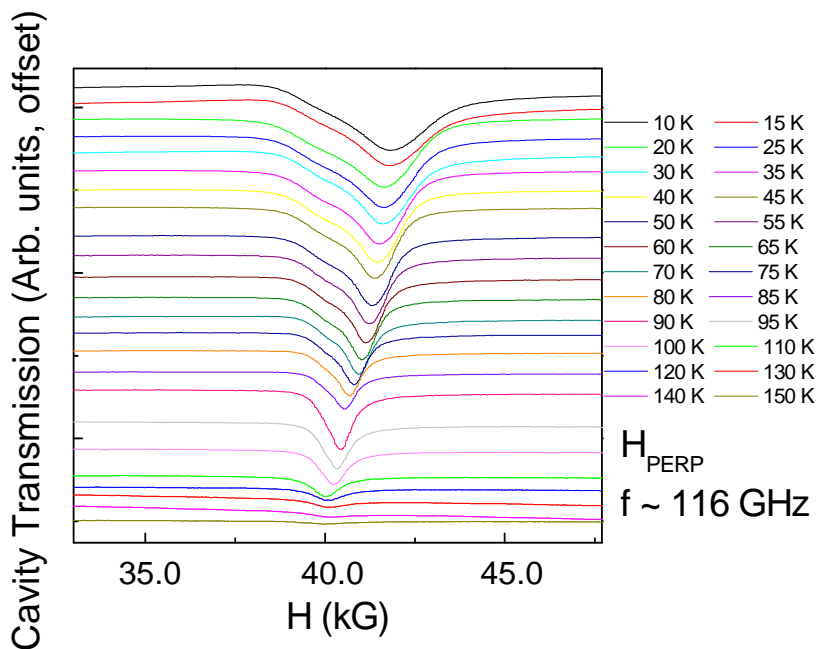


Figure 6-20. EMR lines of Ni-Cr thick film perpendicular. The field dependence of the microwave transmission through the resonance cavity as a function of temperature, measured at $f \sim 116 \text{ GHz}$, for $\text{Rb}_{0.7}\text{Ni}_{4.0}[\text{Cr}(\text{CN})_6]_{2.9} \cdot n\text{H}_2\text{O}$ 400 cycle films perpendicular to the applied field. Here the data have been offset to more clearly display the evolution of the line.

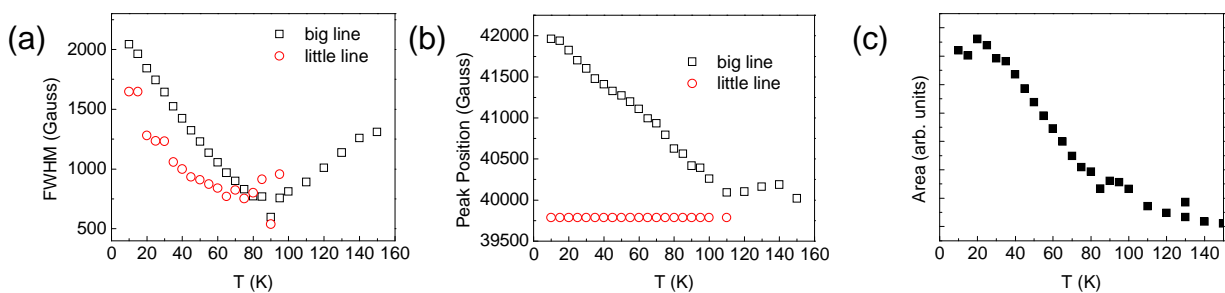


Figure 6-21. Results of fitting EMR lines of Ni-Cr thick film perpendicular. Fitting the temperature dependence in Figure 6-20 to Gaussian lines yield (a) the full-width half-maximum (FWHM) of the lines, (b) the center positions and (c) the relative area of both peaks as a function of temperature.

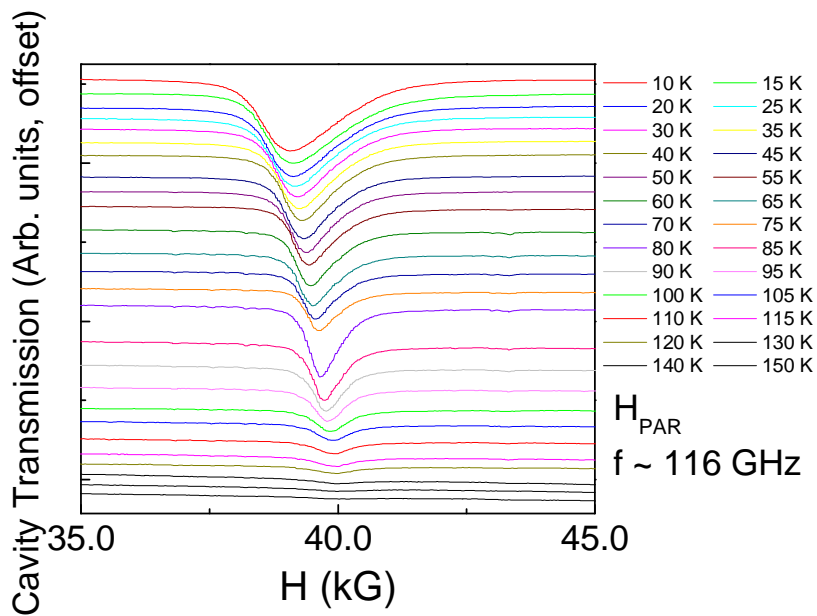


Figure 6-22. EMR lines of Ni-Cr thick film parallel. The field dependence of the microwave transmission through the resonance cavity as a function of temperature, measured at $f \sim 116$ GHz, for $\text{Rb}_{0.7}\text{Ni}_{4.0}[\text{Cr}(\text{CN})_6]_{2.9} \cdot n\text{H}_2\text{O}$ 400 cycle films parallel to the applied field. Here the data have been offset to more clearly display the evolution of the line.

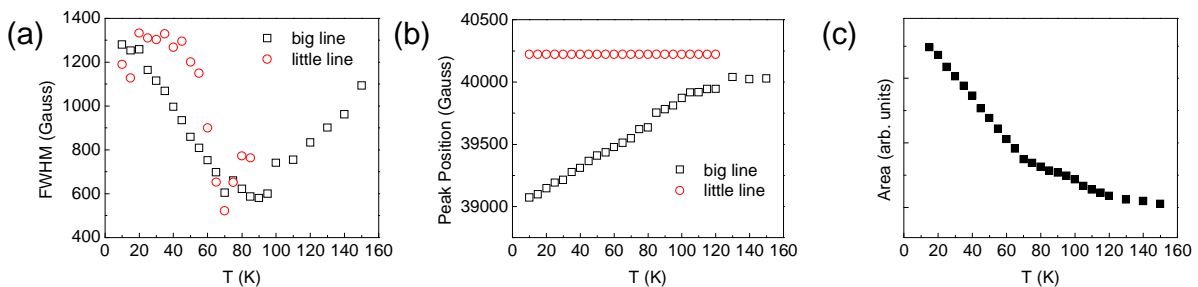


Figure 6-23. Results of fitting EMR lines of Ni-Cr thick film parallel. Fitting the temperature dependence in Figure 6-22 to Gaussian lines yield (a) the full-width half-maximum (FWHM) of the lines, (b) the center positions and (c) the relative area of both peaks as a function of temperature.

6.2.3.2 EMR Angular Dependence

The angular dependence of the microwave absorption was measured for 40 cycle thin films of $\text{Rb}_{0.7}\text{Ni}_{4.0}[\text{Cr}(\text{CN})_6]_{2.9}\cdot n\text{H}_2\text{O}$ in ~ 116 GHz radiation at a temperature of 10 K, Figure 6-24, which is well within the magnetically ordered state for the material. Angle dependence of the peak position and line-width show a planar anisotropy, Figure 6-25 (a) and (b), which cannot be resolved above the ordering temperature, Figure 6-25 (c).

The angular dependence of the microwave absorption was measured for 400 cycle thin films of $\text{Rb}_{0.7}\text{Ni}_{4.0}[\text{Cr}(\text{CN})_6]_{2.9}\cdot n\text{H}_2\text{O}$ in ~ 116 GHz radiation at a temperature of 10 K, Figure 6-26, which is well within the magnetically ordered state for the material. Analogous to the angle dependence of the 40 cycle films, the 400 cycle films show planar anisotropy in the peak position and line-width, Figure 6-27 (a) and (b), which cannot be resolved above the ordering temperature, Figure 6-27 (c).

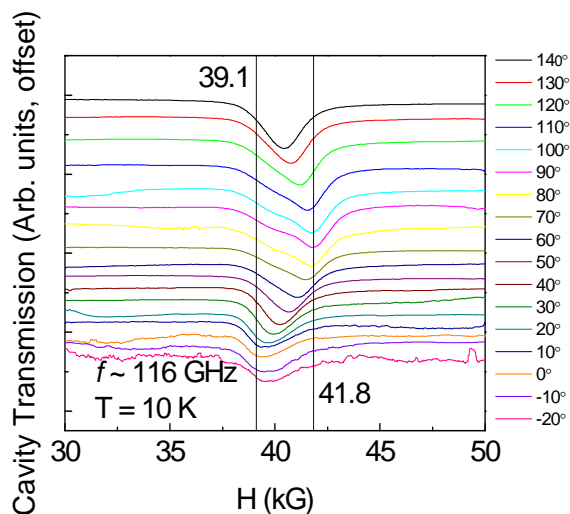


Figure 6-24. EMR lines of Ni-Cr thin film as a function of angle. The field dependence of the microwave transmission through the resonance cavity as a function of angle, measured at $f \sim 116$ GHz and $T = 10$ K, for $\text{Rb}_{0.7}\text{Ni}_{4.0}[\text{Cr}(\text{CN})_6]_{2.9} \cdot n\text{H}_2\text{O}$ 40 cycle films. Here the data have been offset to more clearly display the evolution of the line. The vertical lines delineate the extremum values of the big line, labeled by the numbers near each line in units of kG.

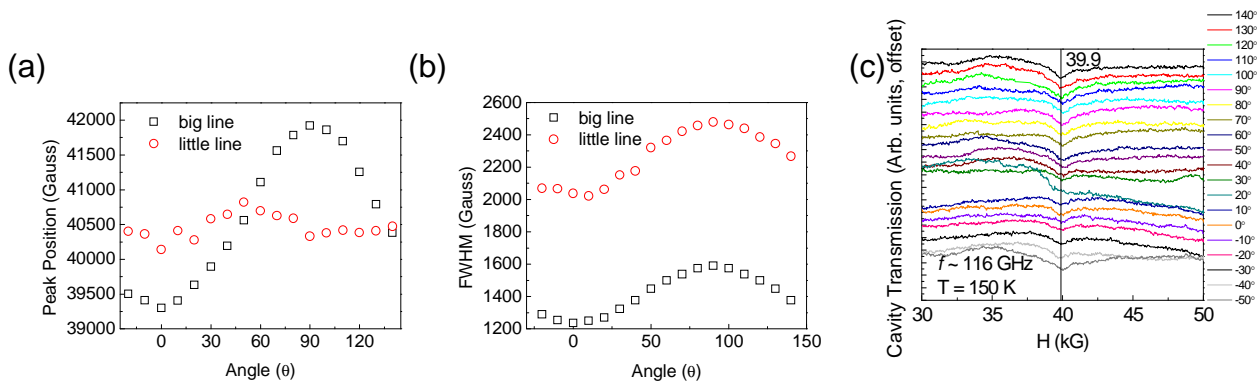


Figure 6-25. Results of fitting EMR lines of Ni-Cr thin film as a function of angle. Fitting the temperature dependence in Figure 6-24 to Lorentzian lines yield (a) the center positions and (b) the full-width half-maximum (FWHM) of the lines. (c) The angular dependence above the ordering temperature. Here the data have been offset to more clearly display the evolution of the line. The vertical line delineates the peak position, labeled by the number at the top in units of kG.

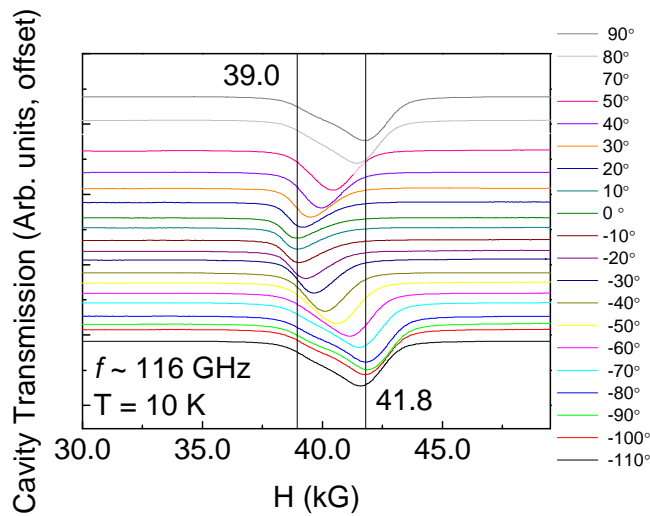


Figure 6-26. EMR lines of Ni-Cr thick film as a function of angle. The field dependence of the microwave transmission through the resonance cavity as a function of angle, measured at $f \sim 116$ GHz and $T = 10$ K, for $\text{Rb}_{0.7}\text{Ni}_{4.0}[\text{Cr}(\text{CN})_6]_{2.9} \cdot n\text{H}_2\text{O}$ 40 cycle films. Here the data have been offset to more clearly display the evolution of the line. The vertical lines delineate the extremum values of the big line, labeled by the numbers near each line in units of kG.

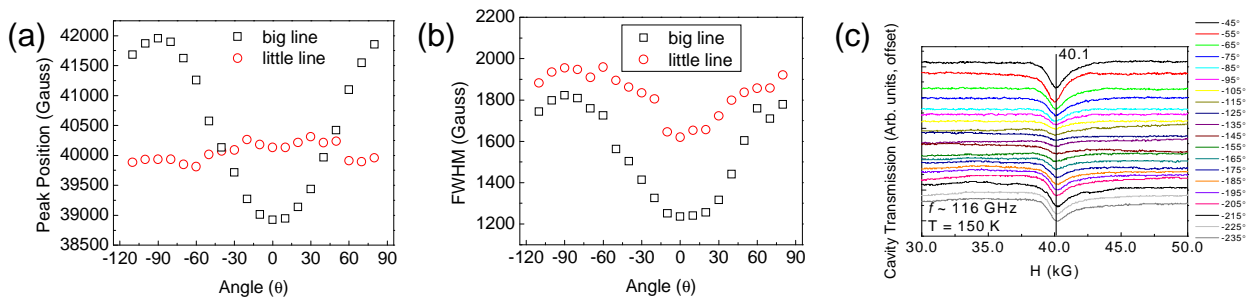


Figure 6-27. Results of fitting EMR lines of Ni-Cr thick film as a function of angle. Fitting the temperature dependence in Figure 6-26 to Gaussian lines yield (a) the center positions and (b) the full-width half-maximum (FWHM) of the lines. (c) The angular dependence above the ordering temperature. Here the data have been offset to more clearly display the evolution of the line. The vertical line delineates the peak position, labeled by the number at the top in units of kG.

6.2.3.3 EMR Frequency Dependence

The angular dependence of the microwave absorption was measured for 400 cycle thin films of $\text{Rb}_{0.7}\text{Ni}_{4.0}[\text{Cr}(\text{CN})_6]_{2.9}\cdot n\text{H}_2\text{O}$ in 50 GHz radiation at a temperature of 10 K, Figure 6-28, which is well within the magnetically ordered state for the material. The observed behavior is reminiscent of the $f \sim 116$ GHz data, again showing planar anisotropy in the peak position and line-width, Figure 6-29 (a) and (b), with similar splitting of the lines at both frequencies, Figure 6-29 (c).

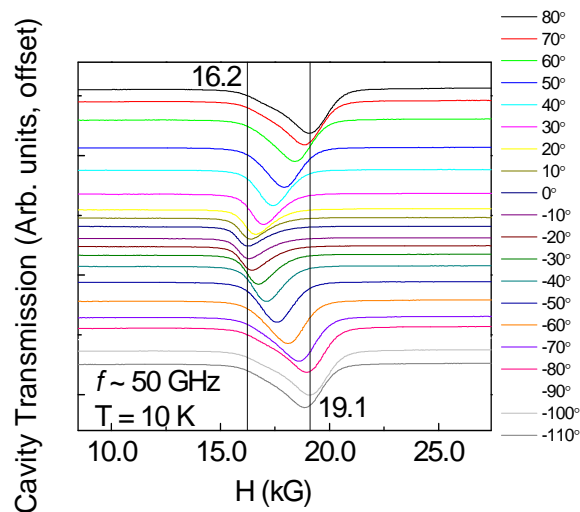


Figure 6-28. EMR lines of Ni-Cr thick film as a function of angle in lower field. The field dependence of the microwave transmission through the resonance cavity as a function of angle, measured at $f \sim 50$ GHz and $T = 10$ K, for $\text{Rb}_{0.7}\text{Ni}_{4.0}[\text{Cr}(\text{CN})_6]_{2.9}\cdot n\text{H}_2\text{O}$ 400 cycle films. Here the data have been offset to more clearly display the evolution of the line.

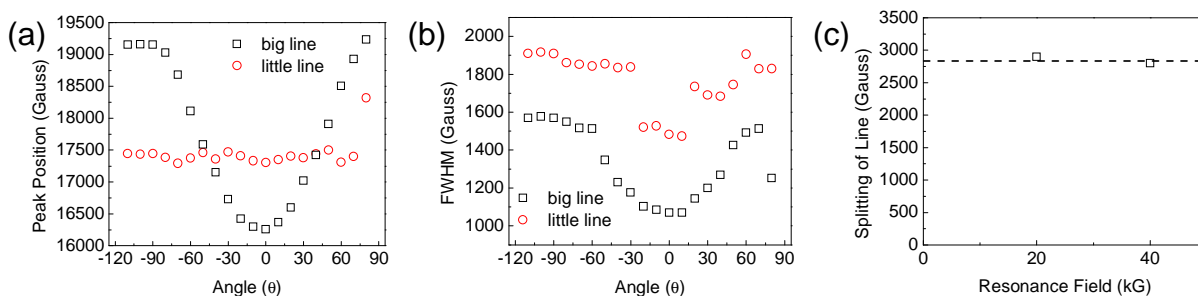


Figure 6-29. Results of fitting EMR lines of Ni-Cr thick film as a function of angle in lower field. Fitting the temperature dependence of the 400 cycle film shown in Figure 6-28 to Lorentzian lines yield (a) the center positions and (b) the full-width half-maximum (FWHM) of the lines. (c) The difference between parallel and perpendicular resonance as a function of frequency shows the lack of field dependence for the splitting of the line. This lack of field dependence rules out g-factor anisotropy as the source of the observed splitting. The dotted line is a guide to the eye.

6.2.4 X-ray Diffraction

X-ray diffraction experiments are currently underway. After room temperature experiments were performed at MAIC with the standard setup, samples were sent to Professor Stefan Kycia at the University of Guelph, and his research group is in the process of looking for structural distortions as a function of temperature.

6.3 Additional Prussian Blue Analogue Thin Films

In addition to the detailed study of $\text{Rb}_{0.7}\text{Ni}_{4.0}[\text{Cr}(\text{CN})_6]_{2.9}\cdot n\text{H}_2\text{O}$ thin films, an array of 3-d block transition metal Prussian blue analogue thin films were studied. Films were synthesized with the sequential adsorption technique, using Co^{2+} , Ni^{2+} , Cu^{2+} and Zn^{2+} for the divalent nitrogen coordinated metal site and hexacyanometallic Cr^{3+} and Fe^{3+} for the trivalent, carbon coordinated site of the network, Table 6-1. All thin films synthesized display magnetic anisotropy, which can be tuned depending upon the constituent metals. Details of magnetization studies on each material, as well as additional modeling and experimental probes will be discussed in the following sections.

Table 6-1. Molecular formulas of films measured and techniques used.

constituent ions		chemical formula	measurements
$\text{Co}^{2+}(\text{S} = 3/2)$	$\text{Cr}^{3+}(\text{S} = 3/2)$	$\text{Rb}_{0.6}\text{Co}_{4.0}[\text{Cr}(\text{CN})_6]_{2.9}\cdot n\text{H}_2\text{O}$	magnetization
$\text{Cu}^{2+}(\text{S} = 1/2)$	$\text{Cr}^{3+}(\text{S} = 3/2)$	$\text{Rb}_{0.7}\text{Cu}_{4.0}[\text{Cr}(\text{CN})_6]_{2.9}\cdot n\text{H}_2\text{O}$	magnetization, UV-Vis
$\text{Zn}^{2+}(\text{S} = 0)$	$\text{Cr}^{3+}(\text{S} = 3/2)$	$\text{Rb}_{0.3}\text{Zn}_{4.0}[\text{Cr}(\text{CN})_6]_{2.8}\cdot n\text{H}_2\text{O}$	magnetization
$\text{Ni}^{2+}(\text{S} = 1)$	$\text{Fe}^{3+}(\text{S} = 1/2)$	$\text{Rb}_{0.9}\text{Ni}_{4.0}[\text{Fe}(\text{CN})_6]_{2.8}\cdot n\text{H}_2\text{O}$	magnetization
$\text{Cu}^{2+}(\text{S} = 1/2)$	$\text{Fe}^{3+}(\text{S} = 1/2)$	$\text{Rb}_{0.5}\text{Cu}_{4.0}[\text{Fe}(\text{CN})_6]_{2.7}\cdot n\text{H}_2\text{O}$	magnetization, thickness dependence, EMR
$\text{Co}^{2+}(\text{S} = 3/2)$	$\text{Fe}^{3+}(\text{S} = 1/2)$	$\text{Rb}_{0.7}\text{Co}_{4.0}[\text{Fe}(\text{CN})_6]_{2.8}\cdot n\text{H}_2\text{O}$	magnetization, photoinduced magnetization, <i>in situ</i> rotation
$\text{Zn}^{2+}(\text{S} = 0)$	$\text{Fe}^{2+}(\text{S} = 0)$	$\text{Rb}_{0.5}\text{Zn}_{4.0}[\text{Fe}(\text{CN})_6]_{2.8}\cdot n\text{H}_2\text{O}$	magnetization

6.3.1 $\text{Rb}_{0.6}\text{Co}_{4.0}[\text{Cr}(\text{CN})_6]_{2.9}\cdot n\text{H}_2\text{O}$ Thin Films

Thin films of $\text{Rb}_{0.6}\text{Co}_{4.0}[\text{Cr}(\text{CN})_6]_{2.9}\cdot n\text{H}_2\text{O}$ generated with 200 sequential adsorption cycles on a Melinex solid support were characterized by SEM to obtain their chemical formula [93]. Similar to the nickel based films, these materials can be thought of as consisting of $\text{Co}(\text{NC})_6$ and $\text{Cr}(\text{CN})_6$ molecular building blocks. The single-ion ground states of these building blocks are important to understand the magnetization of the sample, and be calculated using ligand field multiplet calculations with known spectroscopic and nephelauxetic parameters, Figure 6-30 [5]. The results show a Co^{2+} ground state with $\text{S} = 3/2$ and unquenched orbital angular momentum and a Cr^{3+} ground state with $\text{S} = 3/2$ and no orbital angular momentum contributions.

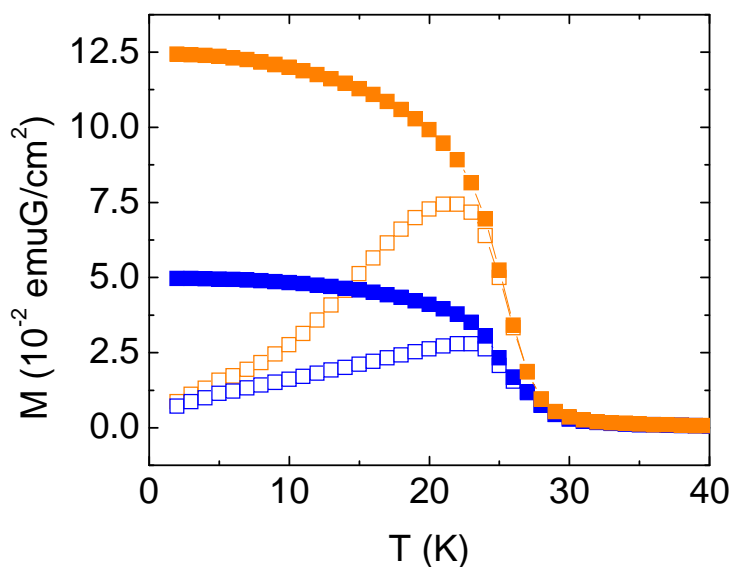


Figure 6-31. Magnetic susceptibility of Co-Cr thin film. The temperature dependences of the low field, 100 G, magnetizations are shown for 200 cycle $\text{Rb}_{0.6}\text{Co}_{4.0}[\text{Cr}(\text{CN})_6]_{2.9}\cdot n\text{H}_2\text{O}$ thin films, parallel ZFC (\square), parallel FC (\blacksquare), perpendicular ZFC (\square) and perpendicular FC (\blacksquare). Here connecting lines of orange and blue are guides to the eye.

6.3.2 $\text{Rb}_{0.7}\text{Cu}_{4.0}[\text{Cr}(\text{CN})_6]_{2.9}\cdot n\text{H}_2\text{O}$ Thin Films

Thin films of $\text{Rb}_{0.7}\text{Cu}_{4.0}[\text{Cr}(\text{CN})_6]_{2.9}\cdot n\text{H}_2\text{O}$ generated with 200 sequential adsorption cycles on a Melinex solid support were characterized by SEM to obtain their chemical formula [93]. The single-ion ground states have calculated using ligand field multiplet calculations with known spectroscopic and nephelauxetic parameters, Figure 6-32 [5]. The results show a Cu^{2+} ground state with $S = 1/2$ and unquenched orbital angular momentum and a Cr^{3+} ground state with $S = 3/2$ and no orbital angular momentum contributions.

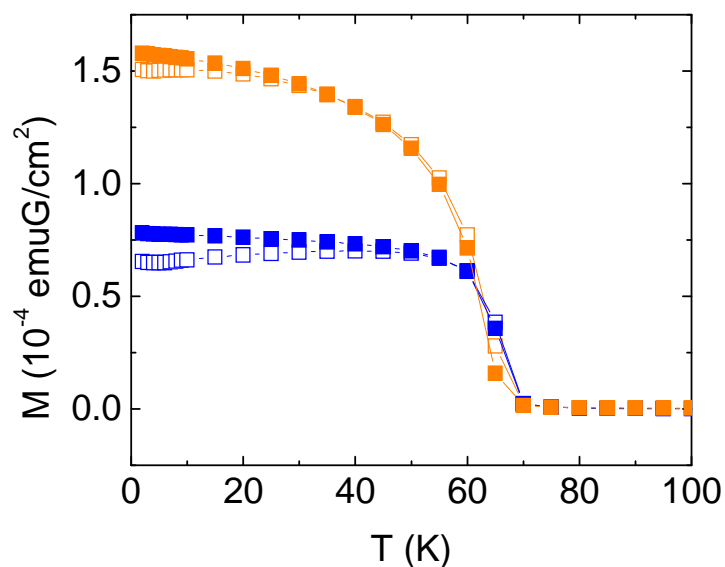


Figure 6-33. Magnetic susceptibility of Cu-Cr thin film. The temperature dependences of the low field, 100 G, magnetizations are shown for 200 cycle $\text{Rb}_{0.7}\text{Cu}_{4.0}[\text{Cr}(\text{CN})_6]_{2.9}\cdot n\text{H}_2\text{O}$ thin films, parallel ZFC (□), parallel FC (■), perpendicular ZFC (□) and perpendicular FC (■). Here connecting lines of orange and blue are guides to the eye.

Temperature dependent ultraviolet and Visible spectroscopy of an 80 cycle $\text{Rb}_{0.7}\text{Cu}_{4.0}[\text{Cr}(\text{CN})_6]_{2.9}\cdot n\text{H}_2\text{O}$ thin film on a quartz solid support was performed to study the electronic structure of the Cr^{3+} ion. The highly transmitting quartz was used instead of Melinex, which has many UV-Vis transitions that make transmission experiments impossible with the available setups. An absorption peak at $\sim 24,000\text{ cm}^{-1}$ may be assigned to a ${}^4\text{A}_{2g}(\text{F}) \rightarrow {}^4\text{T}_{2g}(\text{F})$ type transition on the chromium ion. A shift and sharpening of the absorption line can be seen in the background subtracted spectra of the film, Figure 6-34 (a), and even more clearly when taking differences between room temperature and low temperature scans, Figure 6-34 (b).

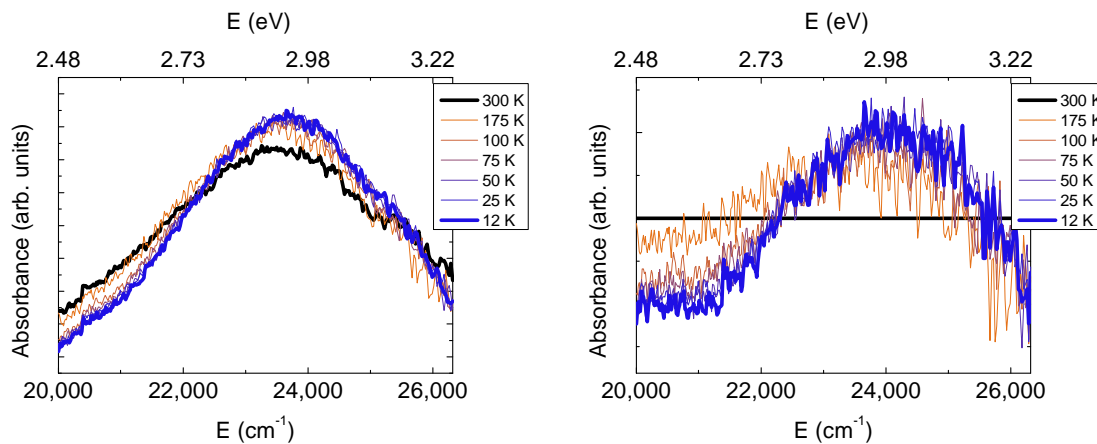


Figure 6-34. UV-Vis of Cu-Cr thin film. (a) Temperature dependent UV-Vis spectroscopy measurements of an ${}^4A_{2g}(F) \rightarrow {}^4T_{2g}(F)$ type transition on the Cr^{3+} ion of an 80 cycle $Rb_{0.7}Cu_{4.0}[Cr(CN)_6]_{2.9} \cdot nH_2O$ thin film on a quartz solid support. (b) A difference plot of the UV-Vis absorption, displaying the temperature dependent shift and sharpening of the line.

6.3.3 $Rb_{0.3}Zn_{4.0}[Cr(CN)_6]_{2.8} \cdot nH_2O$ Thin Films

Thin films of $Rb_{0.3}Zn_{4.0}[Cr(CN)_6]_{2.8} \cdot nH_2O$ generated with 200 sequential adsorption cycles on a Melinex solid support were characterized by SEM to obtain their chemical formula [93]. The single-ion ground states have calculated using ligand field multiplet calculations with known spectroscopic and nephelauxetic parameters, Figure 6-35 [5]. The results show a Zn^{2+} ground state with $S = 0$ and no orbital angular momentum and a Cr^{3+} ground state with $S = 3/2$ and no orbital angular momentum contributions.

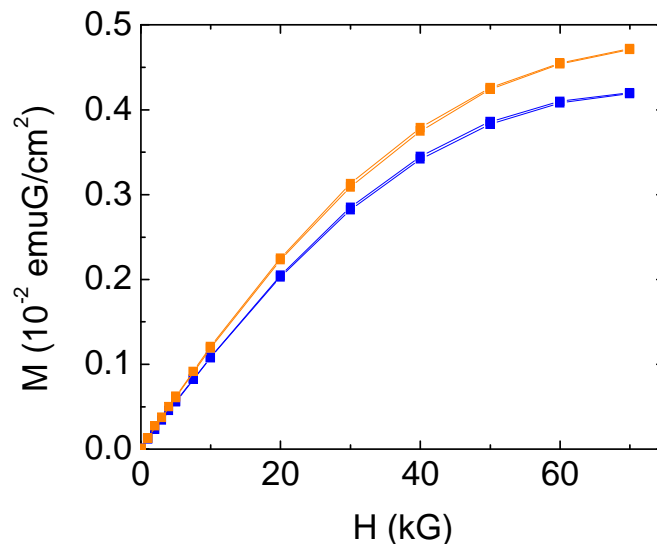


Figure 6-36. Magnetization of Zn-Cr versus field. The magnetic field dependences of the low temperature, 2 K, magnetizations are shown for $\text{Rb}_{0.3}\text{Zn}_{4.0}[\text{Cr}(\text{CN})_6]_{2.8}\cdot n\text{H}_2\text{O}$ thin films in parallel (■) and perpendicular (■) orientations. Here connecting lines of orange and blue are guides to the eye.

6.3.4 $\text{Rb}_{0.9}\text{Ni}_{4.0}[\text{Fe}(\text{CN})_6]_{2.8}\cdot n\text{H}_2\text{O}$ Thin Films

Thin films of $\text{Rb}_{0.9}\text{Ni}_{4.0}[\text{Fe}(\text{CN})_6]_{2.8}\cdot n\text{H}_2\text{O}$ generated with 200 sequential adsorption cycles on a Melinex solid support were characterized by SEM to obtain their chemical formula [93]. Similar to the hexacyanochromate based films, these materials can be thought of as being made up of $\text{Ni}(\text{CN})_6$ and $\text{Fe}(\text{CN})_6$ molecular building blocks. The single-ion ground states of these building blocks are important to understand the magnetization of the sample, and be calculated using ligand field multiplet calculations with known spectroscopic and nephelauxetic parameters, Figure 6-37 [5]. The results show a Ni^{2+} ground state with $S = 1$ and no orbital angular momentum and a Fe^{3+} ground state with $S = 1/2$ and unquenched orbital momentum contributions.

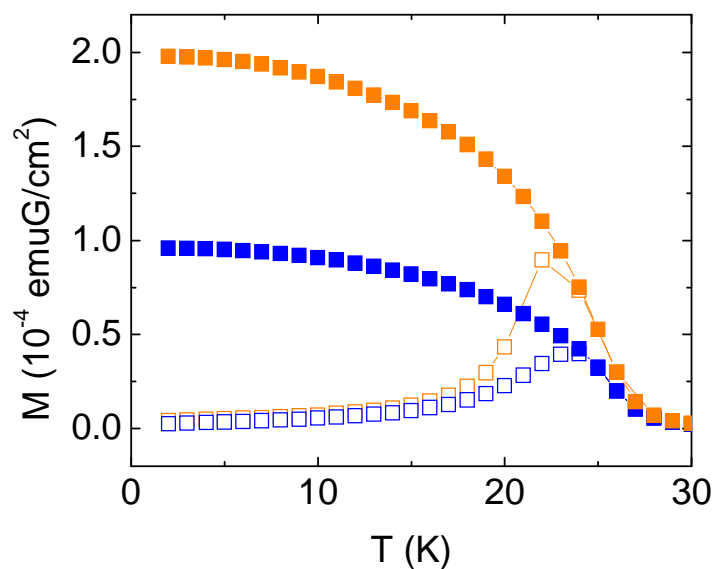


Figure 6-38. Magnetic susceptibility of Ni-Fe thin films. The temperature dependences of the low field, 100 G, magnetizations are shown for 200 cycle $\text{Rb}_{0.9}\text{Ni}_{4.0}[\text{Fe}(\text{CN})_6]_{2.8}\cdot n\text{H}_2\text{O}$ thin films, parallel ZFC (\square), parallel FC (\blacksquare), perpendicular ZFC (\square) and perpendicular FC (\blacksquare). Here connecting lines of orange and blue are guides to the eye.

6.3.5 $\text{Rb}_{0.7}\text{Co}_{4.0}[\text{Fe}(\text{CN})_6]_{2.8}\cdot n\text{H}_2\text{O}$ Thin Films

Thin films of $\text{Rb}_{0.7}\text{Co}_{4.0}[\text{Fe}(\text{CN})_6]_{2.8}\cdot n\text{H}_2\text{O}$ have already been studied in detail, both for their photoinduced anisotropy [10] and for the thickness dependence of that photoinduced anisotropy [103]. The photoinduced magnetism in $\text{Rb}_{0.7}\text{Co}_{4.0}[\text{Fe}(\text{CN})_6]_{2.8}\cdot n\text{H}_2\text{O}$ Prussian blue analogue is due to bistabilities of oxidation states in the material, which may be changed with external stimuli, but this tunability also serves to make interpretation of experimental data more complicated. Therefore, two oxidation states for each ion must be considered when interpreting experimental data, and when performing ligand field multiplet calculations, Figure 6-39. Known values of spectroscopic and nephelauxetic parameters give energy level schemes for the $\text{Co}^{3+}/\text{Fe}^{2+}$ dark state and the $\text{Co}^{2+}/\text{Fe}^{3+}$ light state. Results give well separated

diamagnetic ground states in the $\text{Co}^{3+}/\text{Fe}^{2+}$ dark state and Co^{2+} $S = 3/2$, Fe^{3+} $S = 1/2$ ground states with unquenched orbital angular momentum for the $\text{Co}^{2+}/\text{Fe}^{3+}$ light state.

Although parallel and perpendicular magnetization and photoinduced magnetization has already been reported, the development of a SQUID magnetometer probe that is capable of performing *in situ* photoexcitation and sample rotation allowed for a new twist on the previous results [28].

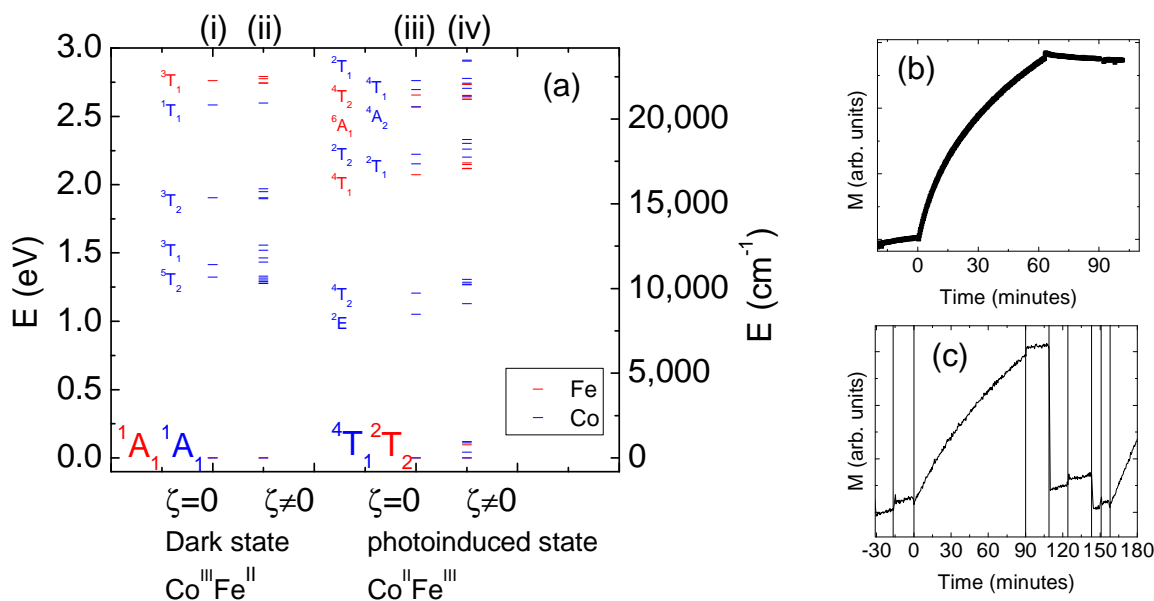


Figure 6-39. Ligand field energy levels and rotational magnetism of Co-Fe. (a) A multiplet calculation can be performed to show the electronic energy levels for the $\text{Co}^{2+}/\text{Co}^{3+}$ and $\text{Fe}^{3+}/\text{Fe}^{2+}$ ions in the Prussian blue network. On the left, $\text{Co}^{3+}/\text{Fe}^{2+}$ energy levels are shown for (i) no spin-orbit coupling and (ii) using reported values of spin-orbit coupling for the free ions [5]. On the right, $\text{Co}^{2+}/\text{Fe}^{3+}$ energy levels are shown for (iii) no spin-orbit coupling and (iv) using reported values of spin-orbit coupling for the free ions [5]. (b) Rotating the Co-Fe powder after photoirradiation at 5 K and 100 G has little effect on the magnetism. (c) Rotating the Co-Fe film after photoirradiation at 5 K and 100 G reduces the magnetism.

6.3.6 $\text{Rb}_{0.5}\text{Cu}_{4.0}[\text{Fe}(\text{CN})_6]_{2.7}\cdot n\text{H}_2\text{O}$ Thin Films

Thin films of $\text{Rb}_{0.5}\text{Cu}_{4.0}[\text{Fe}(\text{CN})_6]_{2.7}\cdot n\text{H}_2\text{O}$ generated with 200 sequential adsorption cycles on a Melinex solid support were characterized by SEM to obtain their chemical formula [93]. The single-ion ground states have calculated using ligand field multiplet

calculations with known spectroscopic and nephelauxetic parameters, Figure 6-40 [5]. The results show a Cu^{2+} ground state with $S = 1/2$ and unquenched orbital angular momentum and a Fe^{3+} ground state with $S = 1/2$ and unquenched orbital angular momentum contributions.

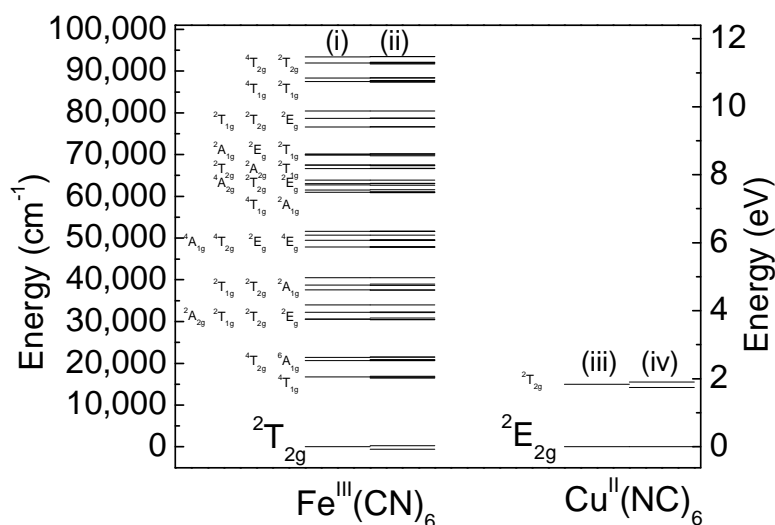


Figure 6-40. Ligand field energies of Cu-Fe. A multiplet calculation can be performed to show the electronic energy levels for the Cu^{2+} and Fe^{3+} ions in the Prussian blue network. On the left, iron energy levels are shown for (i) no spin-orbit coupling and (ii) using reported values of spin-orbit coupling for the free ion [5]. On the right, copper energy levels are shown for (iii) no spin-orbit coupling and (iv) using reported values of spin-orbit coupling for the free ion [5].

The low field magnetization as a function of temperature for thin films of $\text{Rb}_{0.5}\text{Cu}_{4.0}[\text{Fe}(\text{CN})_6]_{2.7}\cdot n\text{H}_2\text{O}$ are shown in Figure 6-41, in both parallel and perpendicular orientations with respect to the applied magnetic field. The ZFC data were obtained after cooling in zero applied field from 300 K, while the FC data were taken after cooling in 100 G from 300 K. The films show a change in the inflection of the magnetization versus temperature, indicative of the three dimensional magnetic order. In addition, a clear anisotropy in the low field susceptibility is present below the magnetic ordering temperature.

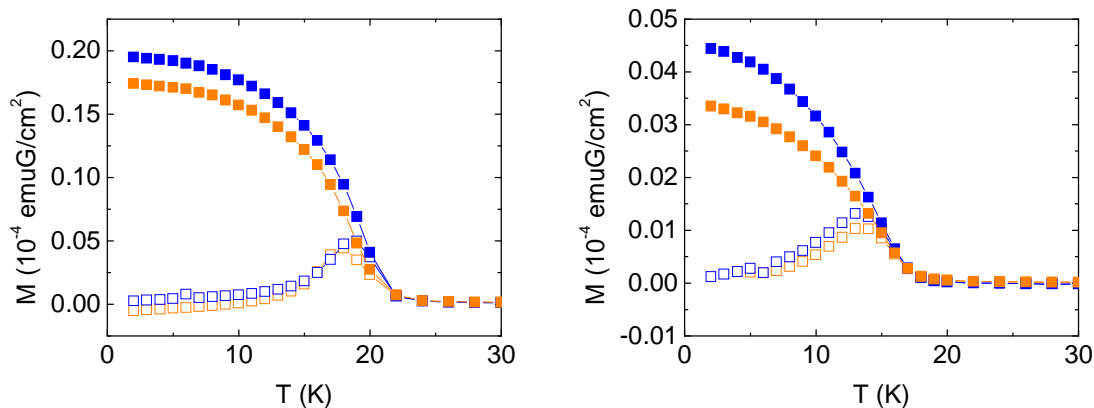


Figure 6-41. Magnetic susceptibility of Cu-Fe thin films. The temperature dependences of the low field, 100 G, magnetizations are shown for (a) 200 cycle $\text{Rb}_{0.5}\text{Cu}_{4.0}[\text{Fe}(\text{CN})_6]_{2.7}\cdot n\text{H}_2\text{O}$ thin films and (b) 20 cycle $\text{Rb}_{0.5}\text{Cu}_{4.0}[\text{Fe}(\text{CN})_6]_{2.7}\cdot n\text{H}_2\text{O}$ thin films, parallel ZFC (\square), parallel FC (\blacksquare), perpendicular ZFC (\square) and perpendicular FC (\blacksquare). Here connecting lines of orange and blue are guides to the eye.

6.3.7 $\text{Rb}_{0.5}\text{Zn}_{4.0}[\text{Fe}(\text{CN})_6]_{2.8}\cdot n\text{H}_2\text{O}$ Thin Films

This film is expected to be diamagnetic, and various measurements have shown that to be true. It is useful to have a diamagnetic sample available if magnetically quiet capping layers are to be used for heterostructured films.

6.4 Discussion

The principle result of the thin film studies is that films of Prussian blue analogues show magnetic anisotropy not present in the bulk solid state. This anisotropy manifests itself in magnetization and microwave spectroscopy experiments. However, no clear trends are observed in vibrational infrared and UV-Vis electron spectroscopy measurements. The functional form of the fundamental source of the anisotropy has been determined, and good candidates for the fundamental source of the anisotropy are presented. The state of what is known and unknown about the newfound anisotropies will be discussed in the following.

6.4.1 Rb_{0.7}Ni_{4.0}[Cr(CN)₆]_{2.9}·nH₂O Thin Films

Since the Rb_{0.7}Ni_{4.0}[Cr(CN)₆]_{2.9}·nH₂O Prussian blue analogues are of primary interest due to their high ordering temperature and their large magnetic anisotropy, they were studied in the most detail. Four types of anisotropy are possible in the Prussian blue analogue films, namely magnetostatic, superexchange, magnetocrystalline, and g-factor [113]. Frequency dependent magnetic resonance experiments have ruled out g-factor anisotropy, Figure 6-29 (c). Temperature dependent x-ray diffraction has shown no departure from cubic structure, even in the ordered stated, making magnetocrystalline effects highly unlikely [113bis]. Superexchange anisotropy cannot be present as no change in the ordering temperature is observed for different film orientations, a fact that will be reiterated in the following discussion section. Consequently, anisotropy magnetostatic effects, especially those associated with demagnetization within magnetic domains, will be the focus of the present discussion of the anisotropy in the Rb_{0.7}Ni_{4.0}[Cr(CN)₆]_{2.9}·nH₂O films.

The low field temperature dependence of the magnetization is where the magnetic anisotropy of the films was first observed as a difference between the magnetic susceptibility when the surface of the films was oriented parallel or perpendicular to the applied magnetic fields. The simplest Hamiltonian for a magnetic system with superexchange coupling is

$$\mathcal{H} = -2 \sum_{i,j=n.n} J_{ij} S_i \cdot S_j + g \mu_B H \sum_i S_i \quad , \quad 6.1$$

where J is the superexchange parameter, S is an electron spin, g is the parameter that scales the magnetic field dependence of the energy, μ_B is the Bohr magneton, and H is

the applied field. Anisotropy may be introduced into Equation 6.1 through either the first or second term, however, changing the superexchange parameter, J , changes the ordering temperature, which is not experimentally observed. On the other hand, a modification of the internal field due to demagnetizing effects may scale the magnetization without modifying the ordering temperature. A demagnetizing field consists of modifying the applied field to be

$$H_{eff} = H_{lab} - NM \quad , \quad 6.2$$

where H_{eff} is the effective field, H_{lab} is the applied field, M is the magnetization, and N is the demagnetizing factor. Immediately, this functional form is attractive because it is observed that once magnetic order begins to take place in the films while cooling, an anisotropy develops that depends upon the macroscopic magnetization. To begin, the magnetic fields produced by a 1 cm x 1 cm x 2 μm film, analogous to the 400 cycle nickel hexacyanochromate film, may be considered from a theoretical perspective. Using the magnetic charge formalism [3], calculations of internal fields are straightforward for both parallel and perpendicular orientations of films. In the absence of electric current, Maxwell's equations for magnetostatics have a reduced number of degrees of freedom that allow all of the information for magnetic fields to be tabulated in the same way as electric fields so that vector quantities are simply gradients of scalars. Thus,

$$H_z = \frac{d}{dz} \psi_M \quad , \quad 6.3$$

where ψ_M is the magnetic potential, which is determined from an analogue of Poisson's equation, and magnetic dipoles may be modeled as dumb-bells with a positive magnetic

charge on one end and a negative magnetic charge on the other. First, the potential of the oppositely, magnetically charged upper and lower surfaces of the film is calculated, and then a derivative is taken to find the field along the z-axis, so

$$H_z = \frac{d}{dz} \left(\int_{-b/2}^{b/2} \int_{-a/2}^{a/2} \frac{\mu_0 M_0 dx dy}{4\pi\mu_0 \sqrt{x^2 + y^2 + \left(z + \frac{c}{2}\right)^2}} - \int_{-b/2}^{b/2} \int_{-a/2}^{a/2} \frac{\mu_0 M_0 dx dy}{4\pi\mu_0 \sqrt{x^2 + y^2 + \left(z - \frac{c}{2}\right)^2}} \right), \quad 6.4$$

where for parallel orientations, $a = 1$ cm, $b = 1$ μ m, and $c = 1$ cm, and for perpendicular orientations, $a = 1$ cm, $b = 1$ cm, and $c = 1$ μ m, with the permanent magnetization along the z-axis for both cases. These calculations are performed using a permanent magnetization with no applied field, although applied fields are easily considered using the superposition principle. (Note: for this subsection calculations will use SI units by which $[B] = \text{T}$, $[H] = \text{A/m}$, and $[\mu_0] = 4\pi \times 10^{-7}$, and volume susceptibility for clarity, and the units are explained in Appendix A.) In the perpendicular orientation, the field produced is small, Figure 6-42 (a) and (b) and the H field is actually negative within the sample and equal to M_0 , Figure 6-42 (c). The integral and subsequent differentiation for the parallel orientations is less well behaved and was computationally more expensive, so less data were calculated. However, it is clear that the B fields produced are much larger in the parallel orientation compared to the perpendicular orientation, Figure 6-43 (a), and that there is no demagnetizing H field in the parallel orientation, Figure 6-43 (b).

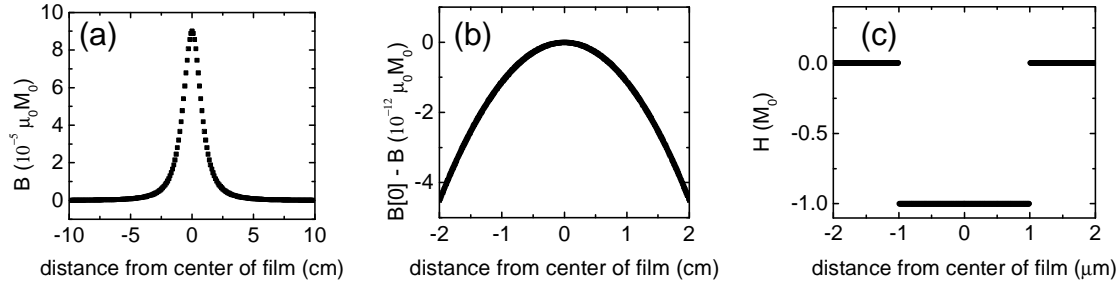


Figure 6-42. Demagnetizing fields in films uniformly magnetized perpendicular to the surface. (a) The change in the B field in and outside the $2\ \mu\text{m}$ high film with respect to the value at the center of the film. (b) The B field is small compared to $\mu_0 M_0$, and continuous across the film boundary. (c) Inside the film, the H field opposes the magnetization with maximum demagnetization. This maximum demagnetization is equivalent to $N = 1$ in Equation 6.2.

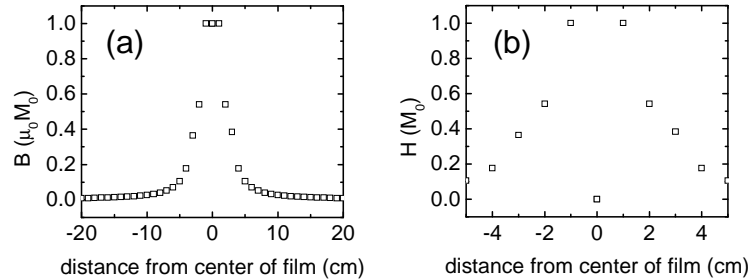


Figure 6-43. Demagnetizing fields in films uniformly magnetized parallel to the surface. (a) The B field in and outside the $1\ \text{cm}$ long film. (b) Inside the film, there is no demagnetizing H field. This lack of demagnetization is equivalent to $N = 0$ in Equation 6.2.

The effect of the demagnetizing fields on the magnetization can be seen by assuming a functional form for the magnetization in 100 G, namely,

$$M = \chi_{low} H_{eff} \quad , \quad 6.5$$

where χ_{low} is the low field volume susceptibility. This assumption of linearity is customary for fields that are small compared to temperature, and is clearly justified by the magnetization data, Figures 6-10, 6-11, and 6-12. Plugging Equation 6.5 into Equation 6.2 yields

$$M = \chi_{low} (H_{lab} - NM) \quad , \quad 6.6$$

Equation 6.6 can be solved self-consistently to give an expression for the magnetization in the presence of a demagnetizing field,

$$M = \frac{\chi_{low} H_{lab}}{1 + \chi_{low} N} \quad , \quad 6.7$$

Therefore, to calculate the magnetization in the presence of a demagnetizing field, one needs to estimate χ_{low} and N . The low field susceptibility may be found by using

$$\chi_{low} = \frac{M}{H_{eff}} \quad 6.8$$

to fit the magnetization data between 20 G (2 mT) and 100 G (10 mT) and N may be kept as a fitting parameter. Practically, to estimate the low field susceptibility, the powder data may be used, under the assumption that the magnetization at 70 kG (7 T) and 2 K reaches the theoretical saturation value of

$$\frac{M_{sat}}{V} = \frac{g\mu_B S}{V} = \frac{2.05(9.27 \times 10^{-24} J/T)(4 \times 1 + 3 \times 1.5)}{(10.33 \times 10^{-10} m)^3} = 1.47 \times 10^5 A/m^2 \quad . \quad 6.9$$

Impressive agreement of calculated and measured magnetization in the perpendicular orientation of the films at low field is seen for $N = 0.45$, which is less than the expected value of $N = 1$ for a fully magnetized film, Figure 6-44. However, the smaller demagnetizing value is consistent with an oblate spheroid [113], which is likely to be the shape of the magnetic domains present in these low fields.

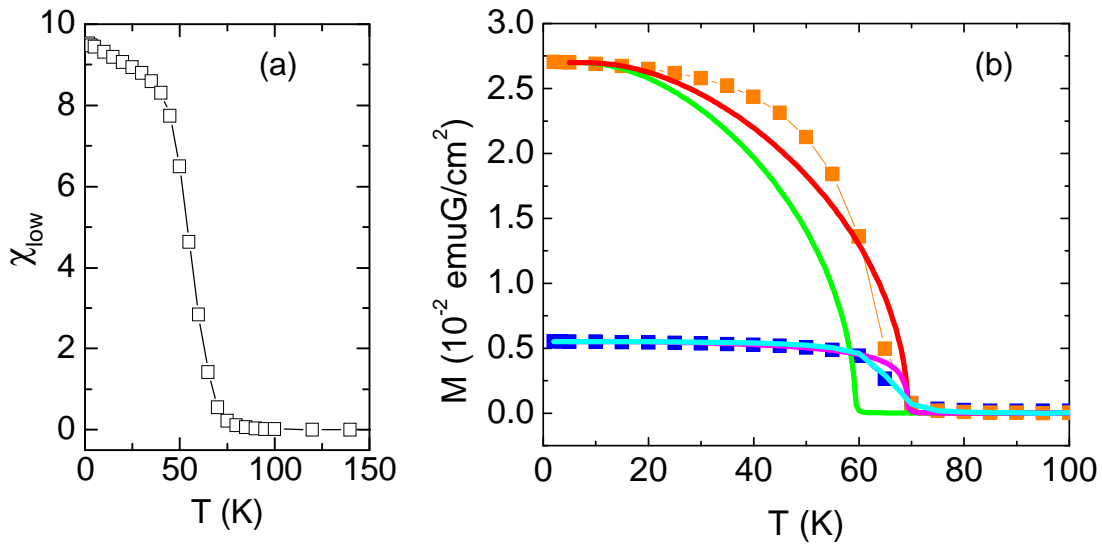


Figure 6-44. Fitting magnetization of Ni-Cr thin films in low field. (a) The low field volume susceptibility used for modeling magnetization with Equation 6.6. (b) The magnetization at $H = 100$ G of a thin film of $\text{Rb}_{0.7}\text{Ni}_{4.0}[\text{Cr}(\text{CN})_6]_{2.9}\cdot n\text{H}_2\text{O}$ in parallel (-■-) and perpendicular (-■-) orientations is modeled with mean-field theory (-), an anisotropic superexchange constant (-), mean-field theory with a demagnetizing factor (-), and the raw parallel data adjusted with a demagnetizing factor to approximate the perpendicular orientation (-).

In a similar way as for the $H = 100$ G temperature dependence, the $H = 40$ kG temperature dependent magnetization may be modeled. First, it is clear that the increase in the ordering temperature is reproduced in the mean-field model, due to increased spin-spin correlations in a high magnetic field, Figure 6-45. An important difference between the two regimes is the functional form of the field dependence of the magnetization. For the high field limit,

$$M = M_0 + \chi_{high} H_{eff} \quad , \quad 6.10$$

where M_0 and χ_{high} are empirical parameters, and the introduction of a demagnetizing factor, Equation 6.2, gives

$$M = M_0 + \chi_{high}(H_{lab} - NM) \quad , \quad 6.11$$

and solving self-consistently as before yields

$$M = \frac{M_0 + \chi_{high}H_{lab}}{1 + \chi_{high}N} \quad , \quad 6.12$$

To find M_0 and χ_{high} , the magnetization of the powder data scaled to the theoretical maximum (Equation 6.9) was fit between 20 kG and 40 kG, Figure 6-45 (a) and (b).

The magnetization data for the thin films in the perpendicular orientation can then be fit using $N = 1$, Figure 6-45 (c), however an additional scaling of the χ_{high} by a factor of 5 is necessary to achieve the magnitude of magnetic anisotropy observed, which may simply be experimental uncertainty in the determination of χ_{high} .

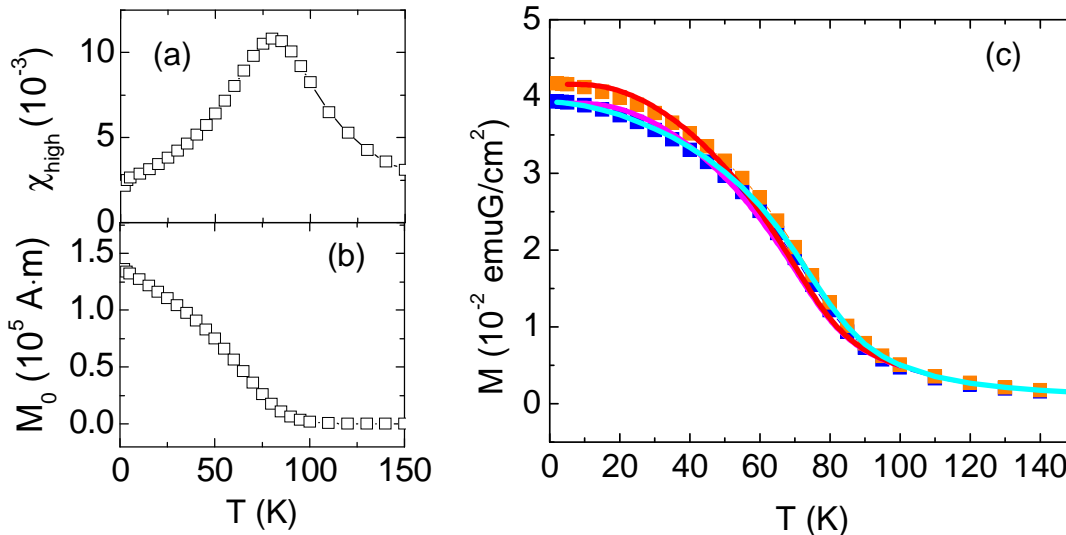


Figure 6-45. Fitting magnetization of Ni-Cr thin films in high field. (a) The high field volume susceptibility (raw from fitting experimental data without any additional factor of 5) and (b) the high field constant magnetization used for modeling magnetization with Equation 6.12. (c) The magnetization at $H = 40$ kG of a thin film of $Rb_{0.7}Ni_{4.0}[Cr(CN)_6]_{2.9} \cdot nH_2O$ in parallel (-■-) and perpendicular (-■-) orientations is modeled with mean-field theory (-), an anisotropic superexchange constant (-), mean-field theory with a demagnetizing factor (-), and the raw parallel data adjusted with a demagnetizing factor to approximate the perpendicular orientation (-).

It is also worth noting the effect of film thickness on the anisotropy of the low field susceptibilities, Figure 6-46 (a), where the anisotropy persists, even in the thickest films, albeit at slightly reduced levels. Perhaps even more startling is that anisotropy is present even in the caustically manufactured spin cast films [93]. The reduction in anisotropy may be attributed to a departure from an ideal thin film geometry, since films of increasing thickness also have an increasing presence of powder-like features on the surface, Figure 6-46 (b) and (c) [93].

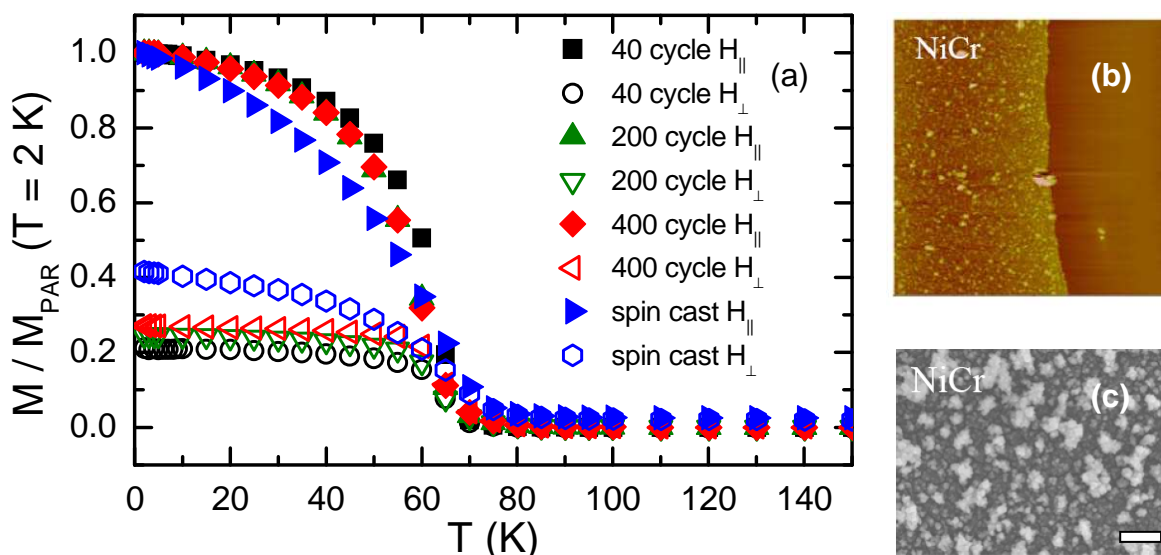


Figure 6-46. Thickness dependence of thin films. (a) The thickness dependence of the anisotropy measured in 100 G at 2 K for $Rb_{0.7}Ni_{4.0}[Cr(CN)_6]_{2.9} \cdot nH_2O$ thin films. (b) An AFM measurement showing powder-like features growing on the surface of a 40 cycle film. (c) An SEM measurement showing powder-like features growing on the surface of a 200 cycle film, analogous to the 400 cycle films studied in detail.

The complex cyanides are ideal candidates for resonance experiments because their high resistivity eliminates complications coming from potential skin effects that plague metallic magnets. For the resonance data, the powdered sample is a logical place to begin as it has the simplest spectrum. The presence of only one line in the powder spectrum of $Rb_{0.7}Ni_{4.0}[Cr(CN)_6]_{2.9} \cdot nH_2O$ indicates that only one species is in

resonance, which might be a well-coupled Ni²⁺ and Cr³⁺ line, a single Cr³⁺ line, or a Ni²⁺ line. The possibility that the signal is due to an impurity can be ruled out because the area of the line as a function of temperature, which is proportional to the magnetization, tracks the measured magnetization in the SQUID magnetometer at 40 kG. In addition, the full-width-half-maximum of the absorption peak decreases as the temperature is lowered, until the magnet becomes ordered, where the line width increases. These changes can be understood quite well in terms of the simple expression

$$\Delta H = 2\alpha H_{\text{eff}} \quad , \quad 6.13$$

where α is the damping parameter and H_{eff} is the effective field seen by the spin [113]. The general decrease above the ordering temperature may be attributed to reduction in spin-lattice relaxation as the number of phonons decreases with temperature. The increase in width of the line from the onset of magnetic order and down to the coldest temperatures may be associated with an increased spin-spin relaxation as the sample enters more deeply into the magnetically ordered state. The position of the peak as a function of temperature may be analyzed in a similar demagnetization formalism as the magnetization data was analyzed. To begin, the same functional form of the demagnetization effects is assumed

$$H_x = H_{\text{lab},x} + N_x M_x \quad , \quad H_y = H_{\text{lab},y} + N_y M_y \quad , \quad H_z = H_{\text{lab},z} + N_z M_z \quad , \quad 6.14$$

where for resonance experiments all principle axes of the magnet and magnetic field are important. Using the equations of motion for a spin in an applied magnetic field along the z-axis, the resonance condition may be written [113],

$$\omega_0^2 = g^2 \mu_0^2 [H_{\text{lab},z} + (N_y - N_z)M_z][H_{\text{lab},z} + (N_x - N_z)M_z] \quad . \quad 6.15$$

For a perfect sphere, $N_x = N_y = N_z = 1/3$, so the resonance condition should be isotropic and have no magnetization dependence,

$$\omega_{0,sphere} = g\mu_0 H_{lab,z} \quad . \quad 6.16$$

In practice, there may be small deviations from spherical symmetry for the powder, and the resonance condition may be written as

$$\omega_{0,powder} = g\mu_0 [H_{lab,z} - \delta M_z] \quad , \quad 6.17$$

where δ takes care of deviations from spherical symmetry. For the powder data of $\text{Rb}_{0.7}\text{Ni}_{4.0}[\text{Cr}(\text{CN})_6]_{2.9} \cdot n\text{H}_2\text{O}$, a shift of ~ 100 G is observed in the fully magnetized state compared to the paramagnetic state, and this is consistent with a value of $\delta \sim 0.05$.

Compared to the powder, things begin to get more complicated in the resonance experiments of the thin films. The variation of the line thickness with temperature is reminiscent of the bulk powder, however, the most striking feature is the evolution of two resonance conditions in the films when cooled below the magnetic ordering temperature. The two lines, most clearly seen in the parallel and perpendicular orientations, cannot reproduce the powder line when integrated over the angular degree of freedom, as can be clearly demonstrated by observing that the lines in the powder are actually sharper than the lines in the films, Figure 6-47 (a). It is also worth noting that the magnitudes of the absorption lines for different orientations may be different due to the complicated coupling term between the modes of the cavity and the sample. More clearly than the magnetic susceptibility measurements, this experimental fact confirms that there is magnetic anisotropy in the films that is not present in the bulk.

Restated, the thin film samples have a magnetic anisotropy that is induced by their thin film character.

A quantitative treatment of the resonance in the thin films can be carried out using the demagnetization formalism used to analyze the magnetization data of the thin films and the general resonance condition in Equation 6.15. For a film oriented perpendicular to an applied field, $N_x = N_y = 0$ and $N_z = 1$ in the limit that the film is uniformly magnetized, and the resonance condition for the perpendicular orientation is

$$\omega_{0,perp} = g\mu_0[H_{lab,z} - M_z] \quad . \quad 6.18$$

For the parallel orientation of the film, $N_x = N_z = 0$ and $N_y = 1$ in the limit that the film is uniformly magnetized, and the resonance condition for the parallel orientation is

$$\omega_{0,par} = g\mu_0[H_{lab,z}(H_{lab,z} + M_z)]^{1/2} \quad . \quad 6.19$$

Just as in the modeling of the magnetization data, M_z will be taken from the powder magnetization scaled to reach the theoretical value at 2 K and 70 kG (7 T). The results of these calculations can be seen in Figure 6-47 (b). The quantitative agreement between model and the position of the largest absorption line is striking. One may argue that qualitative agreement breaks down above approximately 100 K, and this may be explained as a breakdown of the applicability of the model. One potential problem as temperature increases is the loss of the single-domain state, which gave $N_x = N_y = 0$ and $N_z = 1$ in the perpendicular orientation and $N_x = N_z = 0$ and $N_y = 1$ in the parallel orientation.

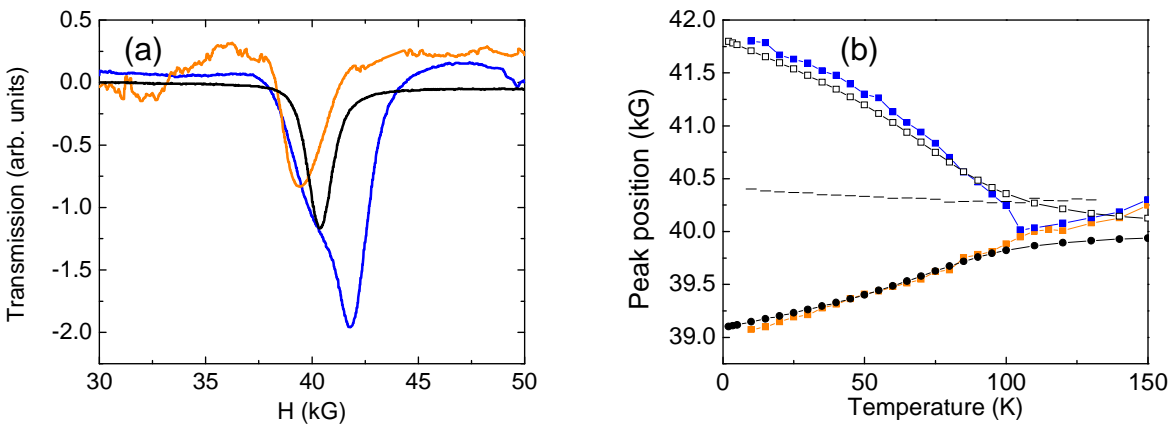


Figure 6-47. EMR lines of Ni-Cr thin films and powder. (a) A superposition of 40 cycle $\text{Rb}_{0.7}\text{Ni}_{4.0}[\text{Cr}(\text{CN})_6]_{2.9}\cdot n\text{H}_2\text{O}$ thin film EMR lines in parallel (orange) and perpendicular (blue) orientations, and a bulk powder line. All data was taken at 10 K and $f \sim 116$ GHz. (b) Observed peak positions for powder (—), 400 cycle film parallel to the applied field (■), and 400 cycle film perpendicular to the applied field (■). Peak positions using the demagnetizing formalism for the 400 cycle film parallel to the applied field (●), and 400 cycle film perpendicular to the applied field (□).

Another potential discrepancy between the model and experimental data is the existence of two absorption lines in the resonance experiments of the films. While demagnetization may produce inhomogeneous internal fields for some samples, giving rise to such a behavior, calculations of the internal field showed a high degree of homogeneity for the chosen geometries, Figure 6-42 and Figure 6-43. However, the same powder-like component that explains the observed thickness dependence of the magnetization can also explain the smaller absorption line that does not shift. A portion of the Prussian blue analogue material in the film actually exists as a powder-like phase on the surface, and therefore has a weak temperature dependence in the resonance experiments that is different than the temperature dependence of the film-like material.

The angular dependence of the resonance line provides further confirmation of the uniaxial, $\sim \sin^2(\theta)$, nature of the anisotropy that was deduced from the angular

dependent magnetization measurements. Just as in the temperature sweeps, two lines are seen, one that moves with angle and another that remains still. The angular dependence of the line width shows wider lines in the perpendicular compared to the parallel orientations, consistent with previous resonance experiments on thin films [105].

Finally, the resonance data for the thin films looks similar whether 40 cycle films or 400 cycle films were used. One key difference, however, is that in the thin films, a Lorentzian fits the line-shape better, while in the thicker films, a Gaussian fits the line-shape better. This observation implies that the disorder increases as the films become thicker and is consistent with the magnetization data.

6.4.2 Additional Prussian Blue Analogue Thin Films

Taking what has been learned from the $\text{Rb}_{0.7}\text{Ni}_{4.0}[\text{Cr}(\text{CN})_6]_{2.9}\cdot n\text{H}_2\text{O}$ films as a fixed point for understanding magnetostatic effects in these materials, the other films may be analyzed to see if additional anisotropy may be present.

The $\text{Rb}_{0.6}\text{Co}_{4.0}[\text{Cr}(\text{CN})_6]_{2.9}\cdot n\text{H}_2\text{O}$ film shows a large anisotropy in the low field magnetization, reminiscent of the $\text{Rb}_{0.7}\text{Ni}_{4.0}[\text{Cr}(\text{CN})_6]_{2.9}\cdot n\text{H}_2\text{O}$ film. While both films are ferromagnets, one difference between them is that Ni^{2+} is a $L = 0$, $S = 1$ ion, while Co^{2+} is a $L = 1$, $S = 3/2$ ion (in the unquenched limit). If the anisotropy was magnetostatic, one would expect a larger anisotropy in the $\text{Rb}_{0.6}\text{Co}_{4.0}[\text{Cr}(\text{CN})_6]_{2.9}\cdot n\text{H}_2\text{O}$ compound compared to the $\text{Rb}_{0.7}\text{Ni}_{4.0}[\text{Cr}(\text{CN})_6]_{2.9}\cdot n\text{H}_2\text{O}$, as the moments in $\text{Rb}_{0.6}\text{Co}_{4.0}[\text{Cr}(\text{CN})_6]_{2.9}\cdot n\text{H}_2\text{O}$ are larger. In fact, the nickel based film is found to have a larger angular dependence of susceptibility. In addition, Co^{2+} is known to be a highly anisotropy ion, due to the large amount of orbital momentum. Therefore additional measurements may be required to fully understand the cobalt film.

The $\text{Rb}_{0.7}\text{Cu}_{4.0}[\text{Cr}(\text{CN})_6]_{2.9}\cdot n\text{H}_2\text{O}$ film is in a different class than the Ni or Co films, as a tetragonal structure has been resolved in x-ray diffraction measurements [106]. This distortion from simple cubicity is understood within the confines of the classic Jahn-Teller distortion that lowers the electronic energy by elongating or compressing the coordinating octahedral, also relieving the orbital degeneracy of the upper crystal field split doublet [5]. In light of this distortion, it is not surprising that thin films would be anisotropic, as both single ion anisotropy of the Cr^{3+} ions, and g-factor anisotropy of the Cu^{2+} are expected to be first order effects in such a compound, in addition to magnetostatic effects. Further evidence changes in the electron energy levels in the ordered state are shown in the temperature dependent UV-Vis spectroscopy studies.

The final hexacyanochromate material studied was the zinc analogue. As Zn^{2+} has a full d-shell, the $\text{Rb}_{0.3}\text{Zn}_{4.0}[\text{Cr}(\text{CN})_6]_{2.8}\cdot n\text{H}_2\text{O}$ material remains paramagnetic down to the lowest temperature measured, which was 2 K. Anisotropy is observed, which becomes enhanced at higher fields when the magnetization is greater, showing the familiar dependence upon the sample magnetization. Therefore, the $\text{Rb}_{0.3}\text{Zn}_{4.0}[\text{Cr}(\text{CN})_6]_{2.8}\cdot n\text{H}_2\text{O}$ film anisotropy is probably magnetostatic.

In addition to chromate cyanides, iron cyanides were also studied. The magnetization of $\text{Rb}_{0.9}\text{Ni}_{4.0}[\text{Fe}(\text{CN})_6]_{2.8}\cdot n\text{H}_2\text{O}$ thin films is actually quite similar to $\text{Rb}_{0.7}\text{Ni}_{4.0}[\text{Cr}(\text{CN})_6]_{2.9}\cdot n\text{H}_2\text{O}$ thin films. The only difference, besides the ordering temperature, is the magnitude of the difference between the parallel and perpendicular low field susceptibilities. The $\text{Rb}_{0.7}\text{Co}_{4.0}[\text{Fe}(\text{CN})_6]_{2.8}\cdot n\text{H}_2\text{O}$ thin films actually add confusion instead of enlightenment. It was found with the new probe setup that rotation in field causes a change in the magnetization, the mechanism of which is still unclear.

The $\text{Rb}_{0.5}\text{Cu}_{4.0}[\text{Fe}(\text{CN})_6]_{2.7}\cdot n\text{H}_2\text{O}$ films are also different than the other films studied, and of acute interest for this reason. Unlike all other analogues, the $\text{Rb}_{0.5}\text{Cu}_{4.0}[\text{Fe}(\text{CN})_6]_{2.7}\cdot n\text{H}_2\text{O}$ has the less common out-of-plane anisotropy. Although it has yet to be observed, the $\text{Rb}_{0.5}\text{Cu}_{4.0}[\text{Fe}(\text{CN})_6]_{2.7}\cdot n\text{H}_2\text{O}$ analogue is expected to have a tetragonal structure analogous to the $\text{Rb}_{0.7}\text{Cu}_{4.0}[\text{Cr}(\text{CN})_6]_{2.9}\cdot n\text{H}_2\text{O}$. However, since both copper and iron ions are $S = 1/2$, no zero-field splittings are possible. Therefore, the only first order effects should be g-factor anisotropy, which may explain the out-of-plane anisotropy. It is much more difficult to explain out-of-plane anisotropy with demagnetization as the source. One possibility would be if the $\text{Rb}_{0.5}\text{Cu}_{4.0}[\text{Fe}(\text{CN})_6]_{2.7}\cdot n\text{H}_2\text{O}$ film had a spire-like structure on the surface. However, atomic force microscopy measurements actually show $\text{Rb}_{0.5}\text{Cu}_{4.0}[\text{Fe}(\text{CN})_6]_{2.7}\cdot n\text{H}_2\text{O}$ films to be the smoothest of all studied [93].

6.5 Conclusions

In conclusion, all Prussian blue analogue thin films studied show magnetic anisotropy. The $\text{Rb}_{0.7}\text{Ni}_{4.0}[\text{Cr}(\text{CN})_6]_{2.9}\cdot n\text{H}_2\text{O}$ films have been studied in the most detail and show a uniaxial, $\sin^2(\theta)$ dependence to the anisotropy that can be well understood within the context of a demagnetization model. Other noteworthy results are an out-of-plane anisotropy in $\text{Rb}_{0.5}\text{Cu}_{4.0}[\text{Fe}(\text{CN})_6]_{2.7}\cdot n\text{H}_2\text{O}$, and a field rotation induced change in susceptibility in $\text{Rb}_{0.7}\text{Co}_{4.0}[\text{Fe}(\text{CN})_6]_{2.8}\cdot n\text{H}_2\text{O}$. It is important that each transition metal film be examined in detail, as multiple sources of magnetic anisotropy are likely to be present. Additional probes of the films might include Lorentz microscopy to analyze the domain structure of the films, or dispersive x-ray spectroscopy to look for anisotropy of the fundamental parameters, specifically in spin-orbit coupling.

CHAPTER 7 HETEROSTRUCTURES OF PRUSSIAN BLUE ANALOGUES

One of the most compelling features of molecular-magnets is their ability to be rationally designed, giving both increased understanding of fundamental physical phenomenon as well as new or enhanced physical effects. Prussian blue analogues (PBAs) are the class of molecular-magnets in which metals are bridged by cyanide in order to generate simple cubic structures.

The $\text{Rb}_a\text{Co}_b[\text{Fe}(\text{CN})_6]_c \cdot n\text{H}_2\text{O}$ (Co-Fe) PBA has been of particular interest because it shows long-lived persistent photoinduced magnetism at temperatures below nominally 100 K, with long-range magnetic order appearing below ~ 20 K [1]. Unfortunately, from a practical standpoint, 20 K is still undesirable because of the need for expensive cryogenics to reach such cold temperatures. In attempt to address this problem, Co-Fe was incorporated into heterostructures including other Prussian blue analogues. First, studies of an atomically mixed ternary Prussian blue analogues containing Co-Fe will be presented, and then thin film heterostructures containing layers of Co-Fe will be presented. The results demonstrate a novel method to increase the photoinduced ordering temperature and to tune the sign of the photoinduced magnetization.

7.1 Solid Solutions of Cobalt Hexacyanoferrate

7.1.1 Introduction

The ability to purposefully tune magnetic properties of synthetic materials has motivated progress in the area of molecule based magnets. A new class of magnetic coordination compounds was opened when long-range magnetic order was discovered in Prussian blue [61] [62] [63] [64], and when its atomic and magnetic structures were

elucidated [65] [55], leading to the notion that properties could be controlled by changing transition metal ions within the parent cubic framework. Binary metal Prussian blue analogues (PBAs), $A_\alpha M' [M(CN)_6]_\beta \cdot nH_2O$ (where A is an alkali metal ion, M' and M are transition metal ions, and the values of α , β , and n depend upon the stoichiometry) and similar materials, have been the subject of extensive research due to their diverse and exciting range of magnetic properties [59] [60] [114]. Room temperature magnetic order [54] [115-117], photoinduced magnetization [1] [57] [68] [81] [82] [87] [90] [118-124], thermal charge transfer induced spin transitions (CTIST) [83] [84] [125], photoinduced tuning of magnetic coupling [126], anisotropic photoinduced magnetism in thin films [10] [100-103], and linkage isomerism [127-132], are among the phenomena observed in this class of compounds.

The photoinduced magnetism, discovered by Hashimoto and coworkers in $K_{0.2}Co_{1.4}[Fe(CN)_6] \cdot 6.9H_2O$, has proven to be one of the more fascinating features of PBAs [1]. Briefly, at low enough temperatures, incident light can cause an electron to transfer from Fe^{2+} (LS, $S = 0$) to Co^{3+} (LS, $S = 0$), yielding long-lived metastable Fe^{3+} (LS, $S = 1/2$)–CN– Co^{2+} (HS, $S = 3/2$) pairs that couple antiferromagnetically and give rise to an observed increase in magnetization. An impressive body of work has elucidated the details of the thermal and optical CTIST effects in this series of compounds, $A_\alpha Co [Fe(CN)_6]_\beta \cdot nH_2O$ ($A = Na, K, Rb, Cs$) [1] [57] [68] [81] [82] [87] [90] [118-124].

There has been previous interest in the so-called ternary metal PBAs of the form $A_\alpha M''_{1-x} M'_x [M(CN)_6]_\beta \cdot nH_2O$ (where M'' and M' occupy similar lattice sites as determined by x) stemming from the additional effects that are sometimes observed, such as

photoinduced magnetic pole inversion [133] [134], dilution of spin-crossover [135], and magnets having different types of Neél order [136-138]. This ability to substitute different transition metals in the compound is due to the similar lattice parameters of the cubic binary PBAs. In addition to novel function, new insight into the underlying physical properties of the compounds can be obtained through a study of these mixed PBAs.

In this section, the ternary Prussian blue analogue of the form $\text{Na}_\alpha\text{Ni}_{1-x}\text{Co}_x[\text{Fe}(\text{CN})_6]_\beta \cdot n\text{H}_2\text{O}$ will be discussed. The proposed structure is one in which a cubic iron sublattice interpenetrates a cubic sublattice containing a statistical mixture of cobalt and nickel ions, Figure 7-1. The use of the sodium cation allows for clear thermal hysteresis [84], and the presence of Ni^{2+} gives rise to ferromagnetic superexchange pathways between Ni^{2+} and Fe^{3+} with an exchange constant that is similar in magnitude to the $\text{Co}^{2+}\text{--NC--Fe}^{3+}$ exchange [139]. The role of the ferromagnetic species in the photodecrease can be illustrated by considering the Ni rich ($x \approx 0$) and Ni poor ($x \approx 1$) substitution regimes, Figure 7-1 (a) and (b). Although a similar mix of materials yielding $\text{Co}_{0.75}\text{Ni}_{0.75}[\text{Fe}(\text{CN})_6] \cdot 6.8\text{H}_2\text{O}$ has already been reported elsewhere [140], the thermally and optically induced bistabilities of the spin states are not present due to the stoichiometry.

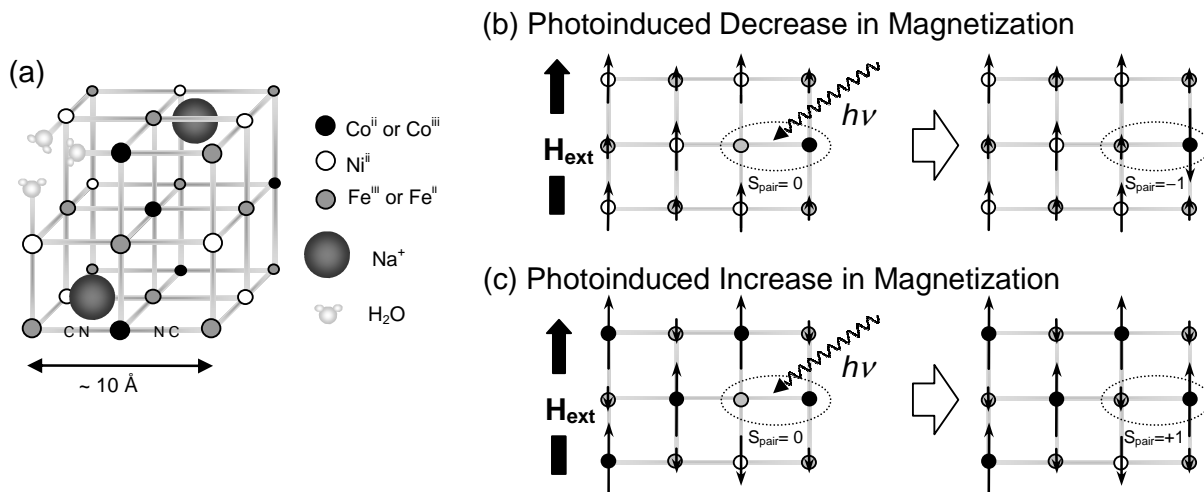


Figure 7-1. The $\text{Na}_\alpha\text{Ni}_{1-x}\text{Co}_x[\text{Fe}(\text{CN})_6]_\beta \cdot n\text{H}_2\text{O}$ material. (a) Structural model for $\text{Na}_\alpha\text{Ni}_{1-x}\text{Co}_x[\text{Fe}(\text{CN})_6]_\beta \cdot n\text{H}_2\text{O}$. (b) A decrease in the magnetization with photoexcitation of a Ni dominated material when there is atomic mixing, and spins are in an ordered state dictated by the exchange interactions $J_{\text{NiFe}} > 0$ and $J_{\text{CoFe}} < 0$. (c) The usual increase in the magnetization with photoexcitation of a sufficiently Co dominated material.

The studies reported in this section show $\text{Na}_\alpha\text{Ni}_{1-x}\text{Co}_x[\text{Fe}(\text{CN})_6]_\beta \cdot n\text{H}_2\text{O}$ bulk powder displays photoinduced magnetism that can be either *positive* or *negative* depending upon the cobalt fraction, $x = [\text{Co}]/([\text{Co}] + [\text{Ni}])$, the applied magnetic field, and the temperature. These observations are only the second report of a photoinduced *decrease* in magnetization in this class of photoswitchable coordination compounds. For the first time, the sign of the photoinduced change in magnetization can be controlled by tuning chemical composition. Additionally, an x dependence is found for the ordering temperature, the coercive field, the amount of photoactive material, the magnitude of the thermal CTIST, and the width of the thermal CTIST hysteresis loop. Qualitative understanding of these results can be obtained through the use of simple molecular field theories.

It is important to note that these materials are analyzed with the assumption of antiferromagnetic interactions in the binary $\text{Na}_\alpha\text{Co}[\text{Fe}(\text{CN})_6]_\beta \cdot n\text{H}_2\text{O}$ material, as is preceded by the majority of the literature. However, additional modeling of the binary materials by the author suggests that the current assignment of ferrimagnetism is ambiguous. As a result, the microscopic origin of the J_{CoFe} may be due to other interactions, such as single-ion effects on the nickel. Alternatively, the current understanding of the material may be correct, and the J_{CoFe} energy may indeed be due to superexchange. This situation is one in which more experimental data is required, and upcoming neutron scattering experiments are scheduled to address these issues. This work was published, in part, in the *Journal of the American Chemical Society* [141]. Those sections contained within the JACS article are copyright of the ACS (copyright release form in Appendix C).

7.1.2 Synthesis and Chemical Composition

Prussian blue analogues $\text{Na}_\alpha\text{Ni}_{1-x}\text{Co}_x[\text{Fe}(\text{CN})_6]_\beta \cdot n\text{H}_2\text{O}$ were synthesized by Dr. Justin E. Gardner by varying the relative cobalt fraction, $[\text{Co}^{2+}_{(\text{aq})}]/([\text{Co}^{2+}_{(\text{aq})} + [\text{Ni}^{2+}_{(\text{aq})}])$, present during synthesis from 0.0 to 1.0 in steps of 0.2 [93] [141]. Energy dispersive x-ray spectroscopy (EDS) was performed on a JOEL 2010F instrument to establish transition metal composition. Samples were deposited as methanol suspensions onto 400 mesh copper grids with holey carbon support films, purchased from Ted Pella, Inc. Combustion analysis to determine carbon, hydrogen, and nitrogen (CHN) percentages was performed by the University of Florida Spectroscopic Services laboratory. The resultant chemical formulas given in Table 7-1 were determined from EDS, FT-IR, and CHN analyses. The Co, Ni, and Fe ratios were explicitly taken from the EDS results,

because the signals for these ions are clean and reproducible. The percentages of C, H, and N were taken directly from combustion analyses. By using the combustion results for the hydrogen content, the amount of oxygen was calculated by assuming all hydrogen and oxygen are in H₂O molecules.

Table 7-1. Molecular formulas and unit cell parameters for Na_αCo_xNi_{1-x}[Fe(CN)₆]_β·nH₂O. [23]

x	Proposed molecular formula	Unit cell length
0.0	Na _{0.27} Ni ²⁺ _{1.0} [Fe ³⁺ (CN) ₆] _{0.73} [Fe ²⁺ (CN) ₆] _{0.02} · 5.0 H ₂ O	10.23(9)
0.22	Na _{0.31} Co ²⁺ _{0.22} Ni ²⁺ _{0.78} [Fe ³⁺ (CN) ₆] _{0.74} [Fe ²⁺ (CN) ₆] _{0.03} · 4.4 H ₂ O	10.24(9)
0.45	Na _{0.34} Co ²⁺ _{0.45} Ni ²⁺ _{0.55} [Fe ³⁺ (CN) ₆] _{0.71} [Fe ²⁺ (CN) ₆] _{0.05} · 4.9 H ₂ O	10.25(6)
0.66	Na _{0.33} Co ²⁺ _{0.66} Ni ²⁺ _{0.34} [Fe ³⁺ (CN) ₆] _{0.67} [Fe ²⁺ (CN) ₆] _{0.08} · 4.6 H ₂ O	10.26(8)
0.87	Na _{0.27} Co ²⁺ _{0.87} Ni ²⁺ _{0.13} [Fe ³⁺ (CN) ₆] _{0.63} [Fe ²⁺ (CN) ₆] _{0.10} · 3.8 H ₂ O	10.28(9)
1.0	Na _{0.31} Co ²⁺ _{1.0} [Fe ³⁺ (CN) ₆] _{0.72} [Fe ²⁺ (CN) ₆] _{0.04} · 4.4 H ₂ O	10.30(7)

7.1.3 Transmission Electron Microscopy

Transmission electron microscopy (TEM) was performed on a JOEL 2010F instrument to establish particle size. Samples were deposited as methanol suspensions onto 400 mesh copper grids with holey carbon support films, purchased from Ted Pella, Inc. Particle sizes were determined from the TEM images by measuring the edge length of more than 50 particles for each composition through the use of ImageJ imaging software [73]. For identical synthesis protocols, excepting the ratio of Co²⁺ to Ni²⁺, the equilibrium size of the particles evolves continuously, with particles becoming smaller as more Ni²⁺ ions are introduced into the lattice, Figure 7-2. Finally, some control over particle size for a given x value is possible by varying the concentration and

the amount of time that the particles are in solution before isolation. However, there are no observable changes in the magnetization, for given values of x , as a function of size within the regime studied [8] [72] [142].

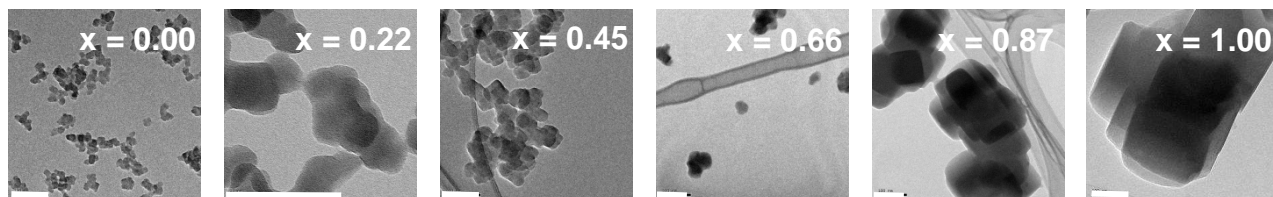
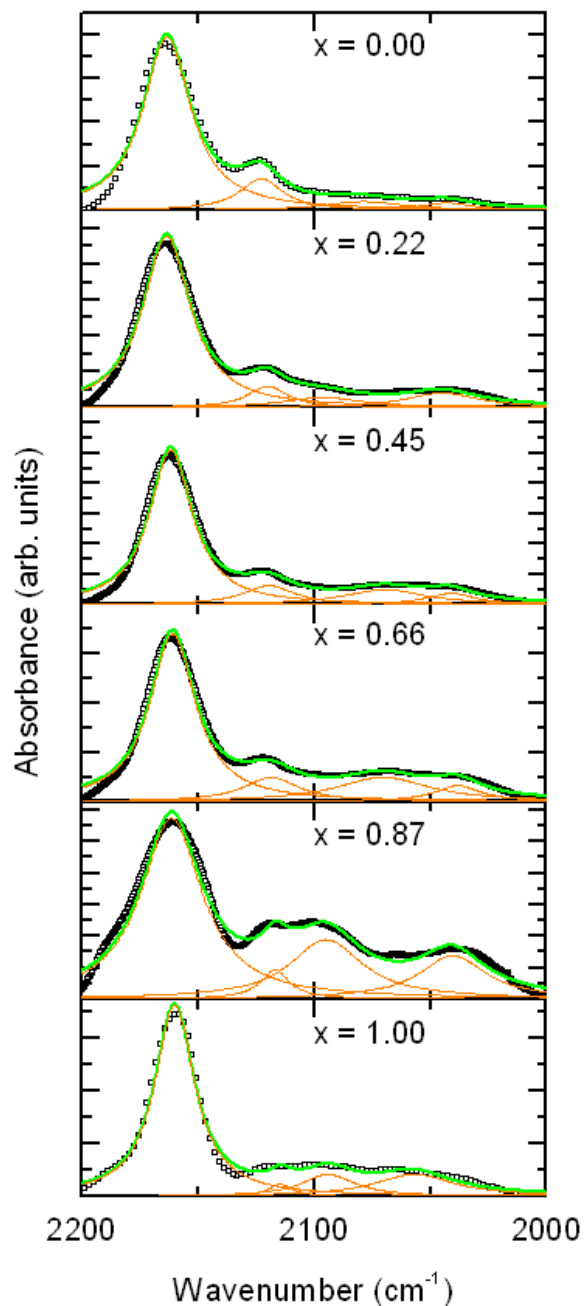


Figure 7-2. Typical TEM micrographs for samples reported in Table 7-1 for different values of x . All scale bars shown are 100 nm. A continuous increase in equilibrium particle edge length is observed when cobalt ions are added to the extended networks. The average particle sizes, in nanometers, from left to right are: 15.6 ± 3.4 , 26.5 ± 5.3 , 28.7 ± 6.9 , 38.7 ± 7.7 , 117.2 ± 22.7 , and 237.8 ± 40.1 .

7.1.4 Infrared Spectroscopy

A Thermo Scientific Nicolet 6700 spectrometer was used to record Fourier transform infrared (FT-IR) spectra, using KBr pellets or powder samples spread between NaCl plates. The relative ratios of Fe^{2+} and Fe^{3+} were estimated by fitting and subsequently integrating the cyanide stretching peaks in the FT-IR spectra associated with each species. Extinction coefficients of the cyanide stretching bands of the ternary Prussian blue analogue compounds were estimated from those measured for $\text{Ni}^{2+}\text{Fe}^{3+}$ and $\text{Ni}^{2+}\text{Fe}^{2+}$ Prussian blue analogue species [93] [141]. The FT-IR spectrum of the pure cobalt hexacyanoferrate displays peaks at 2163, 2120, 2090, and 2040 cm^{-1} , corresponding to the cyanide stretches of the $\text{Co}^{2+}\text{Fe}^{3+}$ (HS), $\text{Co}^{3+}\text{Fe}^{2+}$ (LS), $\text{Co}^{2+}\text{Fe}^{2+}$, and linkage isomerized $\text{Co}^{2+}\text{Fe}^{2+}$ phases, respectively [75]. The FT-IR spectrum of the pure nickel hexacyanoferrate displays peaks at 2160 and 2125 cm^{-1} corresponding to the bridged and terminal cyanide of $\text{Ni}^{2+}\text{Fe}^{3+}$ Prussian blue analog, as well as, peaks at 2079 and 2043 cm^{-1} corresponding to the same assignments for the reduced $\text{Ni}^{2+}\text{Fe}^{2+}$

sites [143]. As the concentration of Ni^{2+} in the lattice is increased at the expense of Co^{2+} ions, the intensities of the three peaks at 2120, 2090, and 2040 cm^{-1} decrease, while that of the peak at 2163 cm^{-1} remains relatively unchanged and a peak at 2125 cm^{-1} emerges. These intensity changes indicate both the reduction in the number of cobalt-iron pairs and the subsequent formation of nickel-iron pairs. FT-IR spectra and the peak fitting results can be found in Figure 7-3.



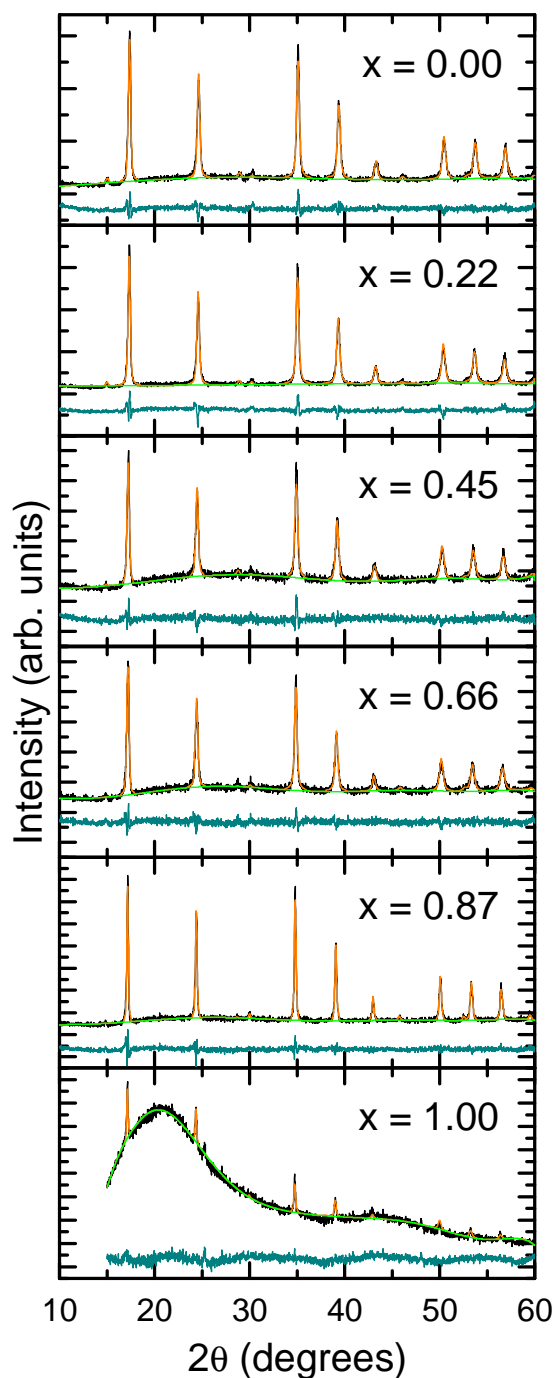
$$I = \sum_{i=1}^4 \frac{2A_i}{\pi} \frac{W_i}{4(\omega - \omega_{0,i})^2 + W_i^2}$$

	ω_0 (cm ⁻¹)	W (cm ⁻¹)	A (l cm ⁻¹)
x = 0.00	2163.2	24.7	30.7
	2122.9	22.3	5.0
	2043.0	26.9	1.4
	2078.6	40.5	2.5
x = 0.22	2163.3	24.6	9.2
	2120.1	20.6	1.0
	2095.9	42.1	0.9
	2044.8	38.1	1.2
x = 0.45	2161.5	22.1	8.9
	2119.6	26.6	1.3
	2069.5	42.8	1.6
	2041.0	25.2	0.7
x = 0.66	2160.7	23.7	6.3
	2118.6	29.0	1.1
	2070.3	48.1	1.9
	2038.2	24.4	0.6
x = 0.87	2161.2	31.8	5.7
	2116.9	15.2	0.4
	2094.8	38.3	2.3
	2040.5	35.1	1.5
x = 1.00	2159.9	20.8	23.7
	2114.5	12.3	0.9
	2094.0	27.9	3.6
	2056.8	41.6	5.5

Figure 7-3. FT-IR spectra and fitting parameters of $\text{Na}_x\text{Ni}_{1-x}\text{Co}_x[\text{Fe}(\text{CN})_6]_\beta \cdot n\text{H}_2\text{O}$ as a function of x . Fits (green) were done using four Lorentzian lines (orange). Gaussian line-shapes were also tried, but the results with the Lorentzian fits had smaller residuals. A standard Levenberg-Marquardt algorithm was employed for simultaneous fitting of the four lines until no observable change in χ^2 was detected.

7.1.5 X-Ray Diffraction

To investigate the lattice constants and crystal structure, a Philips APD 3720 powder diffractometer, housed in the Major Analytical Instrument Center at the University of Florida, was used to perform room temperature x-ray diffraction (XRD) using a Cu K_{α} source. Between 10-20 mg of the same samples used for all other characterizations including magnetometry, except for the $x = 1.00$ sample that only had 0.6 mg left by the time XRD was performed, were mounted on glass slides and pressed onto squares of double-sided cellophane tape of $\sim 2.3 \text{ cm}^2$. The resulting diffractograms, Figure 7-4 and Figure 7-5, were used to model the structure by a Rietveld refinement using the EXPGUI [53] interface for GSAS [52]. In order to approximate the complicated Prussian blue analogue structure, a single-phase model with $Fm\bar{3}m$ (No. 225) space group symmetry was used. Specifically, the cobalt and nickel atoms were forced to occupy the same site. Atomic occupancies were set by the experimentally determined chemical formulas, excepting the oxygen atoms of the interstitial waters that were allowed to vary as the samples may have dehydrated or hydrated between synthesis and diffraction. The same site symmetries as in Prussian blue were used, where the iron vacancies were replaced by the six coordinated oxygen atoms of the ligand water molecules [65]. Placement of the oxygen atoms of the interstitial water molecules at the $32f$ Wyckoff position [68] and a relatively small percentage at the $192i$ position was found to yield a robust local minima during refinement procedure. As clearly displayed by the $(4, 0, 0)$ reflection, the unit cell constants change continuously when changing from $x = 0$ to $x = 1$, Figure 7-6.



Space group: $Fm\bar{3}m$ (No. 225)

	Wyckoff position	g	x	y	z
x = 0.00,	Na	8c	0.27	0.25	0.25
	Ni	4b	1	0.5	0.5
	Co	4b	0	0.5	0.5
	Fe	4a	0.75	0.0	0.0
	C	24e	0.75	0.196(4)	0.0
	N	24e	0.75	0.296(5)	0.0
	O1	24e	0.25	0.216(2)	0.0
x = 0.22,	OA	32f	0.23	0.283(7)	0.283(7)
	OB	192i	0.06	0.243(3)	0.076(9)
	Na	8c	0.31	0.25	0.25
x = 0.45,	Ni	4b	0.78	0.5	0.5
	Co	4b	0.22	0.5	0.5
	Fe	4a	0.77	0.0	0.0
	C	24e	0.77	0.211(7)	0.0
	N	24e	0.77	0.294(0)	0.0
	O1	24e	0.23	0.205(0)	0.0
	OA	32f	0.23	0.283(2)	0.283(2)
x = 0.66,	OB	192i	0.06	0.206(4)	0.078(1)
	Na	8c	0.34	0.25	0.25
	Ni	4b	0.55	0.5	0.5
	Co	4b	0.45	0.5	0.5
	Fe	4a	0.76	0.0	0.0
	C	24e	0.76	0.204(1)	0.0
	N	24e	0.76	0.290(6)	0.0
x = 0.87,	O1	24e	0.24	0.207(6)	0.0
	OA	32f	0.23	0.282(2)	0.282(2)
	OB	192i	0.06	0.206(4)	0.078(2)
	Na	8c	0.33	0.25	0.25
	Ni	4b	0.34	0.5	0.5
	Co	4b	0.66	0.5	0.5
	Fe	4a	0.75	0.0	0.0
x = 1.00,	C	24e	0.75	0.204(5)	0.0
	N	24e	0.75	0.292(6)	0.0
	O1	24e	0.25	0.218(0)	0.0
	OA	32f	0.23	0.282(1)	0.282(1)
	OB	192i	0.06	0.206(4)	0.078(2)
	Na	8c	0.27	0.25	0.25
	Ni	4b	0.13	0.5	0.5
x = 0.87,	Co	4b	0.87	0.5	0.5
	Fe	4a	0.73	0.0	0.0
	C	24e	0.73	0.197(0)	0.0
	N	24e	0.73	0.279(0)	0.0
	O1	24e	0.27	0.212(7)	0.0
	OA	32f	0.23	0.285(6)	0.285(6)
	OB	192i	0.06	0.178(6)	0.070(2)
x = 1.00,	Na	8c	0.31	0.25	0.25
	Ni	4b	0.00	0.5	0.5
	Co	4b	1.00	0.5	0.5
	Fe	4a	0.76	0.0	0.0
	C	24e	0.76	0.197(0)	0.0
	N	24e	0.76	0.279(0)	0.0
	O1	24e	0.27	0.212(7)	0.0
x = 1.00,	OA	32f	0.23	0.285(6)	0.285(6)
	OB	192i	0.06	0.178(6)	0.070(2)

Figure 7-1. Full XRD diffractograms of $\text{Na}_\alpha\text{Ni}_{1-x}\text{Co}_x[\text{Fe}(\text{CN})_6]_\beta \cdot n\text{H}_2\text{O}$. XRD data (black), fitting parameters and fits (orange), with residuals displayed below the peaks (dark cyan), and the fitted background Visible as a thin line (green). Organic parameters were not of a particular interest and many degenerate solutions consisting of slight perturbations to the quoted solutions are possible.

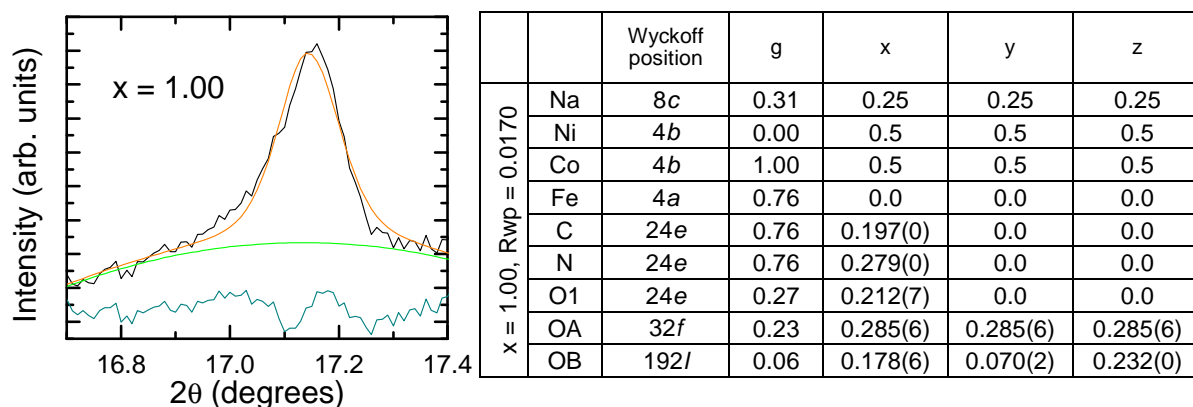


Figure 7-5. XRD of the $x = 1$ $\text{Na}_\alpha\text{Ni}_{1-x}\text{Co}_x[\text{Fe}(\text{CN})_6]_\beta \cdot n\text{H}_2\text{O}$. Since only 0.59 mg of the $x = 1.00$ sample was available for the XRD studies, as opposed to the 10-20 mg used for x-ray powder diffraction experiments on the other samples, a much weaker signal to noise ratio resulted. In addition, the background curve resulting from the sample holder is seen to be comparable to the signal, Figure 7-4. For these reasons, additional data were acquired for the (2,0,0) reflection near 17.1° . While a value of $10.3051(9)$ Å was obtained for the original fit, a value of $10.3072(6)$ Å was generated by fitting this single reflection, with better statistics, using the parameters for the structure from the original fit, and simply refining the unit cell. The fit peak (orange) is displayed, with residuals displayed below the peaks (dark cyan), and the fitted background is shown as a thin line (green).

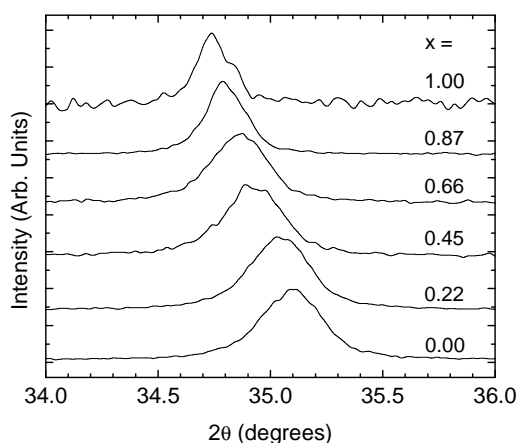


Figure 7-6. Room temperature XRD reflection with background subtracted and intensity normalized to show the continuous evolution with x . The peak position shifts as x decreases and the line width broadens, reflecting the smaller particle size of the pure Ni-Fe analogue.

7.1.6 Mean-Field Calculations

Using simple mean-field approximations, investigations of the possible effects to be observed in the magnetization were performed first, and subsequently refined the model after completing a series of experiments. In order to model the magnetic interactions, an approximation in which superexchange energies act as effective magnetic fields, so-called Weiss fields, was employed in a manner akin to previous works in similar materials [132-138]. In order to model the cooperative thermally active CTIST event, a Bethe-Peierls-Weiss approximation to a phenomenological spin-crossover Hamiltonian was implemented [97]. These numerical studies extend the previous work of others by allowing the high-spin fraction, n_{HS} , which is experimentally controlled by irradiation and temperature, to vary along with the relative metal concentration, x , which is dictated by the synthesis. Details of the calculations, including how x and n_{HS} are utilized to provide numerical results that are directly comparable to the experimental data.

7.1.6.1 Low Temperature Magnetization in the Mean-Field

Calculations were performed to investigate effects on the low temperature magnetic susceptibility due to the substitution of Ni atoms for Co in $\text{Na}_\alpha\text{Ni}_{1-x}\text{Co}_x[\text{Fe}(\text{CN})_6]_\beta \cdot n\text{H}_2\text{O}$. For simplicity, consider only superexchange of spins associated with nearest transition metal neighbors, designated as *n.n.*, under the influence of an applied magnetic field, and thus the Hamiltonian has the form

$$H = -2 \sum_{i,j=n.n.} J_{ij} S_i \cdot S_j + g\mu_B H \sum_i S_i, \quad 7.1$$

where J is an exchange constant, g is the Landé factor, μ_B is the Bohr magneton, S is the electronic spin, and H is the applied field. One method of investigating Equation 7.1 is the usual mean-field expansion of the spin operator.

For the system in question, three magnetic ions must be considered: (a) Fe^{3+} , which can superexchange with either Ni^{2+} or Co^{2+} , (b) Ni^{2+} , which only superexchanges with Fe^{3+} , and (c) Co^{2+} , which also only superexchanges with Fe^{3+} . Two parameters, x and n_{HS} , are introduced to keep track of the magnetic species present when calculating the temperature dependence of the magnetization, where x is the molar fraction of Co, $x = [\text{Co}]/([\text{Co}] + [\text{Ni}])$, and n_{HS} tracks the amount of material that has undergone CTIST. It is important to note that the high-spin fraction, n_{HS} , is representative of the amount of material that is actually magnetic. Expressions for the average spin polarization values of the constituent ions can be derived by minimizing the free energy with respect to simultaneous variation of the spin polarizations of the different sublattices, yielding,

$$\langle S_{\text{Ni}} \rangle = S_{\text{Ni}} B_S \left(\frac{g\mu_B S_{\text{Ni}} H_{\text{ext}}}{k_B T} + \frac{2Z_{\text{NiFe}} J_{\text{NiFe}}}{k_B T} S_{\text{Ni}} \langle S_{\text{Fe}} \rangle \right), \quad 7.2$$

$$\langle S_{\text{Co}} \rangle = S_{\text{Co}} B_S \left(\frac{g\mu_B S_{\text{Co}} H_{\text{ext}}}{k_B T} + \frac{2Z_{\text{CoFe}} J_{\text{CoFe}}}{k_B T} S_{\text{Co}} \langle S_{\text{Fe}} \rangle \right), \text{ and} \quad 7.3$$

$$\langle S_{\text{Fe}} \rangle = S_{\text{Fe}} B_S \left(\frac{g\mu_B S_{\text{Fe}} H_{\text{ext}}}{k_B T} + \frac{2Z_{\text{FeCo}} J_{\text{FeCo}}}{k_B T} S_{\text{Fe}} \langle S_{\text{Co}} \rangle + \frac{2Z_{\text{FeNi}} J_{\text{FeNi}}}{k_B T} S_{\text{Fe}} \langle S_{\text{Ni}} \rangle \right), \quad 7.4$$

where B_S is the Brillouin function, k_B is the Boltzmann constant, and $\langle \dots \rangle$ denotes an average. Total spin numbers of $S_{\text{Ni}} = 1$ for Ni^{2+} , $S_{\text{Fe}} = 1/2$ for Fe^{3+} , and $S_{\text{Co}} = 3/2$ for Co^{2+} were used, with other species being diamagnetic. There is an explicit dependence of Z upon both x and n_{HS} that can be resolved by considering statistical mixing and using the chemical formula, that is to say, $Z_{\text{NiFe}} = 4.0(1-x) + 3.3x \cdot n_{\text{HS}}$, $Z_{\text{CoFe}} = 4.0(1-x) + 3.3x \cdot n_{\text{HS}}$,

$Z_{FeCo} = 2.7x + 3.3x \cdot n_{HS}$, and $Z_{FeNi} = 6.0(1-x)$. Subsequent to simultaneous solution of Equations 7.3-7.5, the magnetization can be calculated from

$$M_{Ni} = 4.00(1-x)Ng\mu_B \langle S_{Ni} \rangle, \quad 7.5$$

$$M_{Co} = (1.83x + 2.17x n_{HS})Ng\mu_B \langle S_{Co} \rangle, \quad 7.6$$

$$M_{Fe} = (3.26x n_{HS} + 4.00(1-x))Ng\mu_B \langle S_{Fe} \rangle, \quad 7.7$$

$$\text{and } M_{total} = D(M_{Ni} + M_{Co} + M_{Fe}), \quad 7.8$$

where an additional parameter D accounts for the presence of magnetic domains after the onset of long-range magnetic order. In practice, D is chosen to be 100, as estimated by fitting the pure materials. At low temperature, given the mostly quenched orbital momentum, values of $g \sim 2$ are reasonable for all species.

7.1.6.2 Mean-field Magnetic Susceptibility and Spin-Crossover

To understand how the magnitude and hysteresis of the thermally induced CTIST are affected by the introduction of Ni atoms to the lattice, an analytical model was employed [75]. This solution exploits the mapping between the extensively studied Ising Hamiltonian and the phenomenological spin-crossover Hamiltonian to be considered,

$$H = -J_{SCO} \sum_{\langle i,j \rangle} \sigma_i \sigma_j - \left(\frac{k_B T}{2} \ln \left(\frac{g_+}{g_-} \right) - \Delta \right) \sum_i \sigma_i, \quad 7.9$$

where g_+ and g_- are the degeneracies of the high-spin (HS) and low-spin (LS) states, J_{SCO} is the intermolecular interaction energy associated with the different spin states, Δ is the octahedral splitting energy, σ is a pseudo-spin keeping track of the spin state, T is

temperature, k_B is the Boltzmann constant, and $\langle i, j \rangle$ refers to a summation over nearest neighbors.

In a manner similar to that employed by Hoo *et al.* [97], it is straightforward to calculate the HS fraction. For these calculations, it is assumed that the entropy content of the different states, the intermolecular interaction, and the energy difference between the HS and LS states are unchanged as x is changed. A small effect on the onset of the transition is expected to arise from the slightly varying Na content in the samples, even while the width of the hysteresis loop is unchanged [84], but this effect is not considered. The number of nearest neighbors to be considered in the spin-crossover event for the different samples is taken from the chemical formulas by taking the minimum occupation necessary for the charge transfer. Specifically, $z_{SCO}(x = 1.00) = 4.32$, $z_{SCO}(x = 0.87) = 3.8$, and $z_{SCO}(x = 0.66) = 4.0$, each determined from the switchable Fe content, $z_{SCO}(x = 0.45) = 2.7$, and $z_{SCO}(x = 0.22) = 1.3$, each determined from the amount of Co, and $z_{SCO}(x = 0.00) = 0$ because there are no Co ions in this sample. Values of $J_{SCO} = 150$ K, $\ln(g_+/g_-) = 250$, and $\Delta = 550$ K are used for all calculations and are determined by fitting the $x = 1.00$ data. Simultaneous fitting of the data above 250 K for all samples gives $g_{Co} = 2.7$, $g_{Fe} = 2.2$, and $g_{Ni} = 2.3$. These $g > 2$ values arise from the incomplete quenching of orbital moments on the ions at high temperatures [5]. Mean-field fits for each sample can then be performed in order to calculate n_{HS} above and below the spin transition.

7.1.7 Magnetic Measurements

Magnetic measurements were performed using a Quantum Design MPMS XL superconducting quantum interference device (SQUID) magnetometer. A room

temperature halogen light source (~1-2 mW) was used to introduce light into the sample chamber of the SQUID through a bundle of ten optical fibers, ~270 μm OD (Ocean Optics Model 200), for photomagnetic measurements. Powders were mounted on pieces of cellophane tape around plastic drinking straws to increase the optical cross-section for the photomagnetic studies. High temperature data ($T > 100$ K) were taken using gelcaps as the sample holders to accommodate additional sample mass. Backgrounds were subtracted from the data by using the measured mass susceptibility of similar sample holders. The same demagnetizing protocol, during which the magnet field is oscillated to zero by successive ramps starting at 20 kG, was used for all low field measurements in ~10 G. Additionally, the magnet was allowed to relax for more than two hours subsequent to demagnetization and prior to data taking. By using a commercial Hall sensor, an in-house calibrated Toshiba THS118E, it is likely that there may be differences of up to ~1 G in the external fields applied to different samples, but for each specimen, the field was not changed between light and dark states for the temperature sweeps, ensuring any resulting effects are not a result of slight perturbations of the external field.

7.1.7.1 Low Temperature DC Susceptibility

The time dependences of the DC magnetic susceptibilities, $\chi = M/H$, during photoirradiation of the samples are shown in Figure 7-7 (a). The temperature dependences of the DC magnetic susceptibilities, $\chi(T)$, in ~10 G between 2 K and 30 K for various x values, both before and after photoirradiation, are shown in Figure 7-7 (b). A clear bifurcation of the field-cooled (FC) and zero-field-cooled (ZFC) curves, with a peak in the χ_{ZFC} versus T plots, is observed for all samples. The results of the Weiss

mean-field calculations, as described in Section 7.1.4, are shown in Figure 7-7 (c). For the mean-field calculated susceptibilities of the dark states, the value of the high-spin fraction, n_{HS} , is dictated by the amount of material measured to undergo spin-crossover, whereas the calculated susceptibilities of the photoirradiated states use $n_{\text{HS}} = 1$, where all available material is in the high-spin state by definition.

All samples with $x > 0$ show a change in magnetization due to applied light. Strikingly, at 5 K and in 10 G, the $x = 0.66$ sample shows a clear decrease in magnetization with photoirradiation in both the calculations and the experimental results. To a weaker extent, a photoinduced decrease in magnetization is also observed in the $x = 0.45$ sample. Expanded photoirradiation versus time plots for the $x = 0.66$ and $x = 0.45$ samples are shown in Figure 7-8.

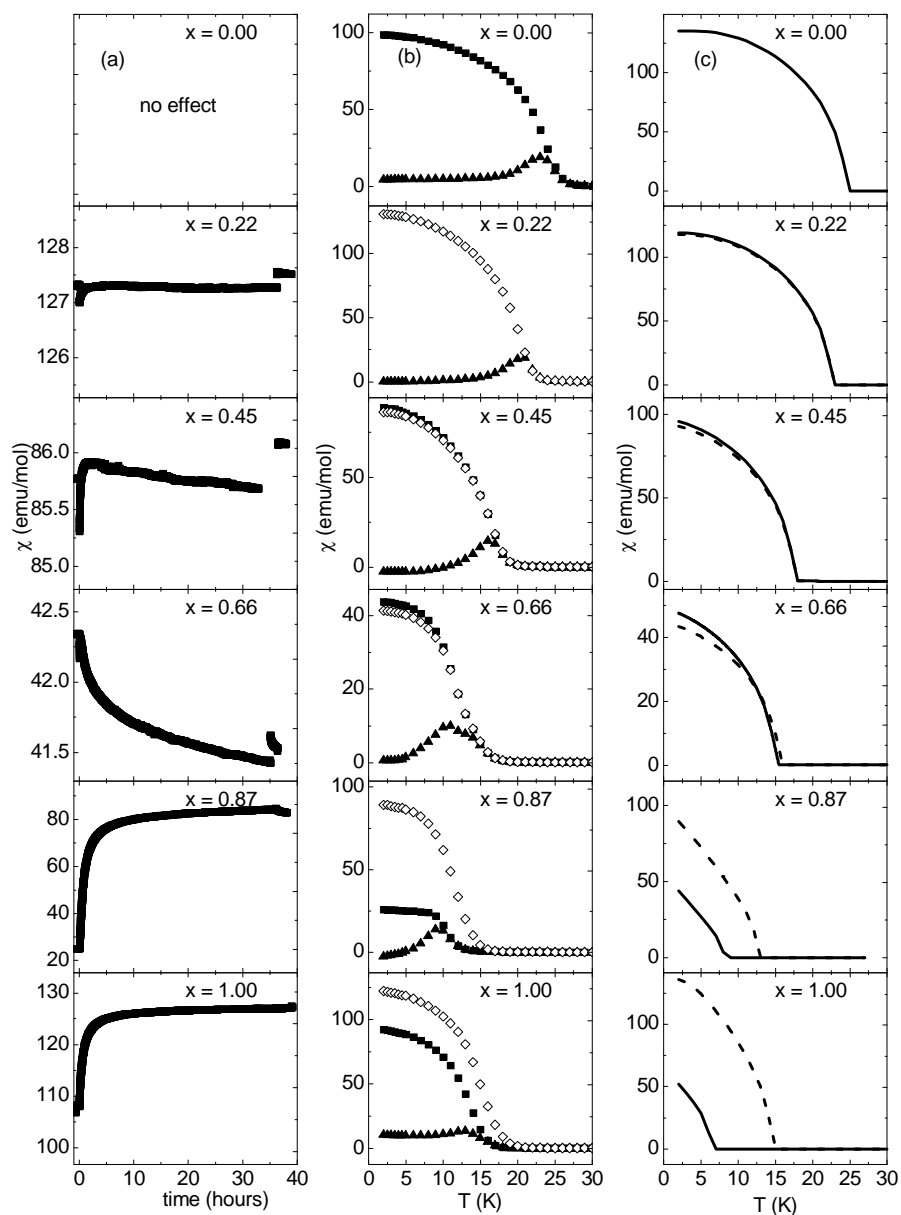


Figure 7-7. Photoinduced magnetization of $\text{Na}_\alpha\text{Ni}_{1-x}\text{Co}_x[\text{Fe}(\text{CN})_6]_\beta \cdot n\text{H}_2\text{O}$. (a) Molar magnetic susceptibility as a function of time irradiated at 5 K and 10 G, measured in a SQUID. Discontinuities in magnetization when the light is turned on and off are due to a subtle heating effect from the applied light. (b) Molar magnetic susceptibility as a function of temperature in both the dark FC (\blacksquare), ZFC (\blacktriangle) and photoirradiated states (\diamond), measured in a SQUID at 10 G. (c) Mean-field calculations of molar magnetic susceptibilities at 10 G as a function of temperature in both the dark state (solid line), where the high-spin fraction, n_{HS} , is determined from fitting high temperature susceptibility, and photoirradiated states (dashed line), where $n_{\text{HS}} = 1$. The magnetic signals are expressed per mole of sample using the chemical formulas in Table 7-1.

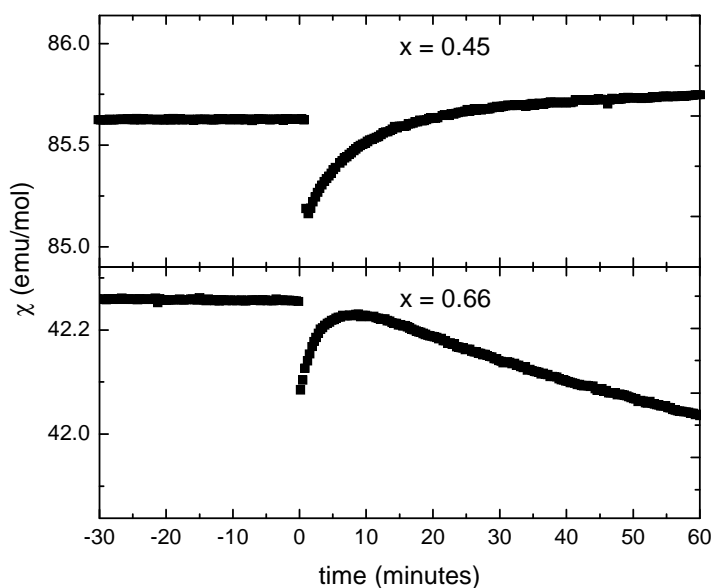


Figure 7-8. Molar magnetic susceptibility of $\text{Na}_\alpha\text{Ni}_{1-x}\text{Co}_x[\text{Fe}(\text{CN})_6]_\beta \cdot n\text{H}_2\text{O}$ as a function of time irradiated at 5 K and 10 G, measured in a SQUID. The samples are irradiated continuously for time > 0 , where the step in χ at $t = 0$ is associated with a small heating effect. For the $x = 0.66$ sample, the magnetization has a small initial increase for 10 minutes followed by the large photoinduced decrease.

7.1.7.2 DC Magnetization

Magnetization as a function of the applied magnetic field was measured for all compounds at $T = 2$ K and up to 70 kG, Figure 7-9. A scaling of the coercive fields with the mixing fraction, x , was seen. In addition, at the high fields, all samples were seen to have photoinduced increases in magnetization. A check for symmetry of the hysteresis loops as a potential contributing factor to the change in the coercive field was made, Figure 7-10.

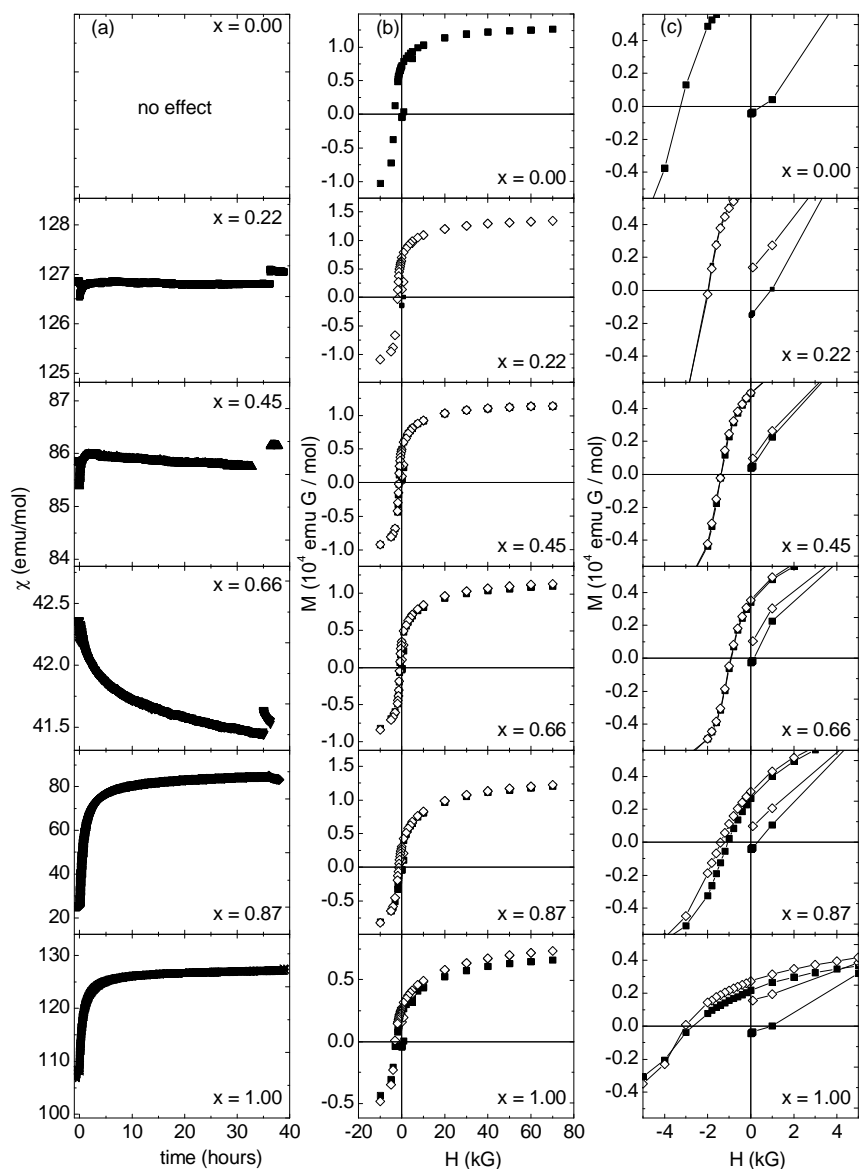


Figure 7-9. Magnetization versus field for $\text{Na}_\alpha \text{Ni}_{1-x} \text{Co}_x [\text{Fe}(\text{CN})_6]_\beta \cdot n\text{H}_2\text{O}$. (a) Molar magnetic susceptibility as a function of time irradiated at 5 K and 10 G, measured in a SQUID. Molar magnetization for both (b) high field (c) and low field, as a function of magnetic field in both the dark (\blacksquare), and photoirradiated states (\diamond), measured in a SQUID at 2 K. High field magnetization always increases after photoirradiation, even for samples showing a photodecrease at low fields. The smallest field on the field sweeps is 100 G.

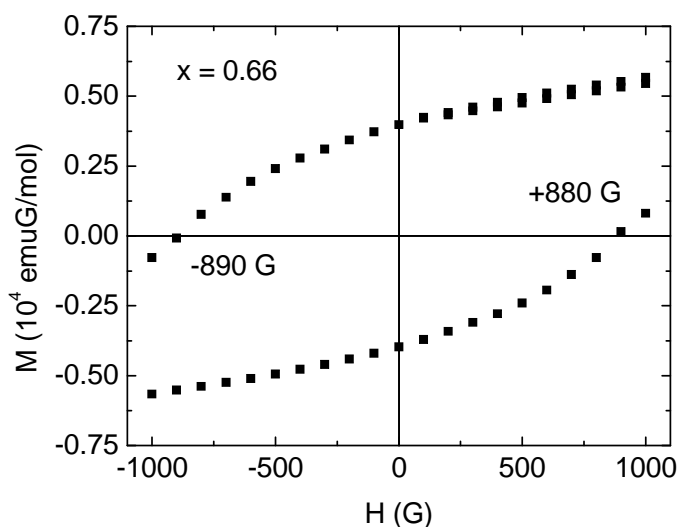


Figure 7-10. Checking for asymmetry in the hysteresis loop as a possible explanation of the reduction in H_C for the $x = 0.66$ sample. Field was swept from 100 G to 70 kG to -70 kG and back to 70 kG, all at 2 K. No asymmetry is observed within experimental uncertainty.

7.1.7.3 High Temperature DC Susceptibility

The temperature dependences of the DC magnetic susceptibility temperature product, χT , in 5 kG and between 100 K and 300 K for various x values are shown in Figure 7-11 (a). To help ensure equilibrium during the spin-crossover, a sweep rate of less than 0.5 K/min was employed. The combined Bethe-Peierls-Weiss spin-crossover and Weiss mean-field magnetization calculations, as described in Section 7.1.4, are shown in Figure 7-11 (b). For clarity, the calculated temperature dependence of the high-spin fraction, n_{HS} , is also shown, Figure 7-11 (c).

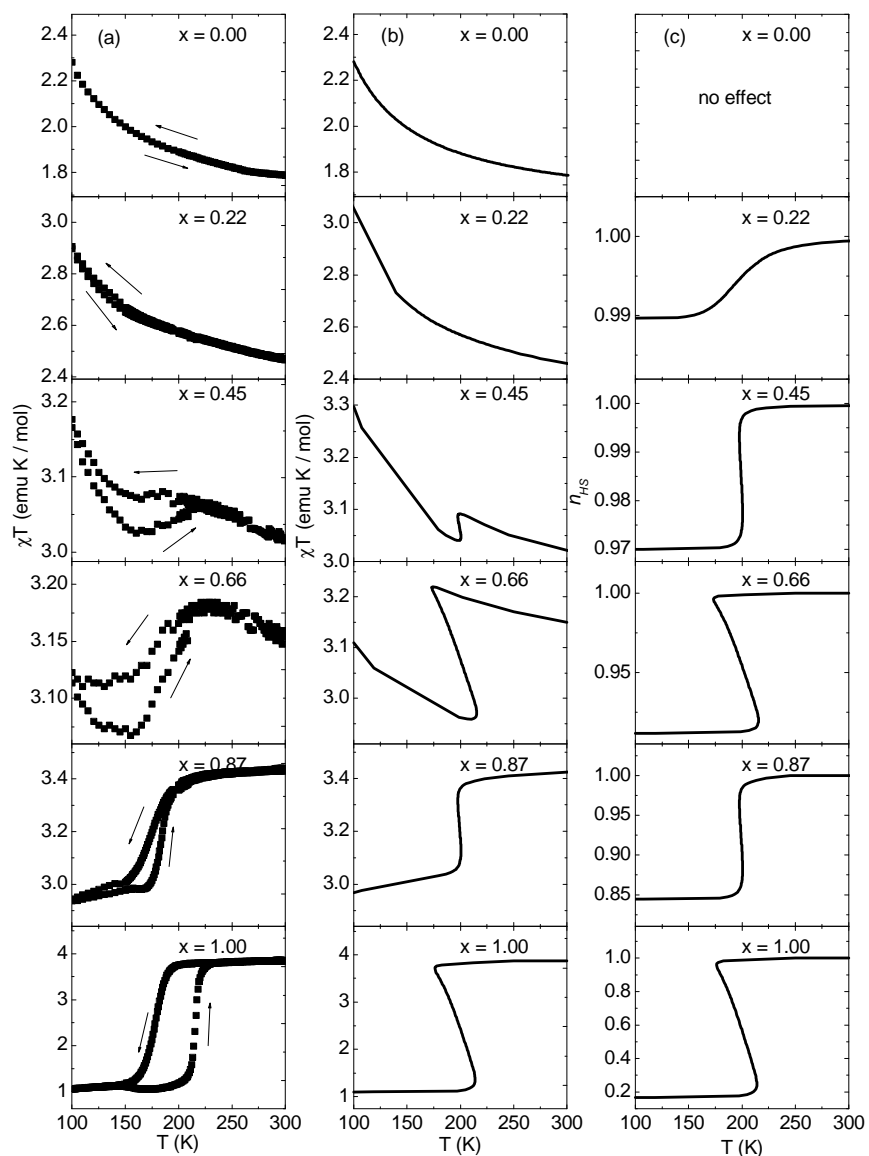


Figure 7-11. Thermal induced changes in magnetization of $\text{Na}_\alpha\text{Ni}_{1-x}\text{Co}_x[\text{Fe}(\text{CN})_6]_\beta \cdot n\text{H}_2\text{O}$. (a) χT versus T as measured in a SQUID magnetometer with 5 kG applied field. The results of mean-field calculations are shown for (b) χT versus T and (c) the high-spin fraction, n_{HS} , versus T . The magnetic signals are expressed per mole of sample using the chemical formulas listed in Table 7-1.

All samples with $x > 0$ appear to show thermally induced CTIST, as evidenced by the abrupt reduction of the magnetic susceptibility upon cooling below ~ 170 K. These CTIST events can be cycled with temperature and exhibit hysteresis that is characteristic of the cooperativity of the transition. Additionally, an evolution of the ferromagnetic slope in χT , characteristic of the $\text{Na}_\alpha\text{Ni}[\text{Fe}(\text{CN})_6]_\beta \cdot n\text{H}_2\text{O}$ compound, can be seen as more Ni is introduced to the lattice in both the numerical and experimental studies. Furthermore, the samples show a decrease of the width of the thermal hysteresis, as the amount of Co decreases, and a drastic decrease in the amount of material that undergoes CTIST, when Ni is introduced into the lattice.

7.1.7.4 Physically Mixed $x = 0.66$ Compound

To make sure that the observed behavior is not due to a physical mixture of the parent compounds on a macroscopic level, a manually mixed sample of separately synthesized nickel hexacyanoferrate and cobalt hexacyanoferrate powders was prepared and studied, Figure 7-12 and Figure 7-13. For this type of synthesis, the TEM data reveal a bimodal distribution clearly associated with the two distinct sizes of the $\text{Na}_\alpha\text{Ni}[\text{Fe}(\text{CN})_6]_\beta \cdot n\text{H}_2\text{O}$ and $\text{Na}_\alpha\text{Co}[\text{Fe}(\text{CN})_6]_\beta \cdot n\text{H}_2\text{O}$ powders. The magnetic orderings of both binary species are clearly visible in $\chi(T)$, and the magnetization only increases with irradiation, even though the chemical composition is the same as the $x = 0.66$ sample showing a photodecrease.

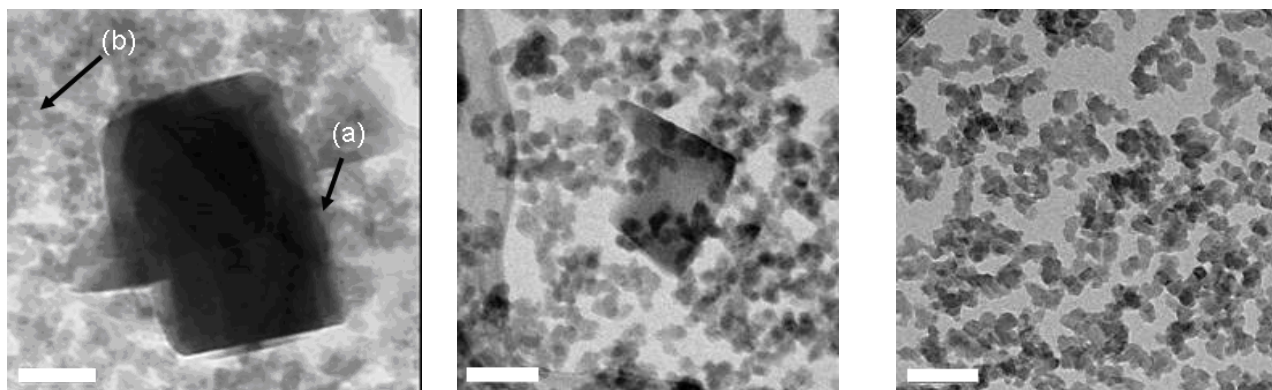


Figure 7-12. Microscopic versus macroscopic mixing. TEM images of the manually mixed powder with $x = 0.60$ showing the presence of both (a) Co-Fe and (b) Ni-Fe powders in the material with the same sizes reported for the $x = 0.00$ and $x = 1.00$ materials, respectively (Figure 7-2). All scale bars shown are 100 nm.

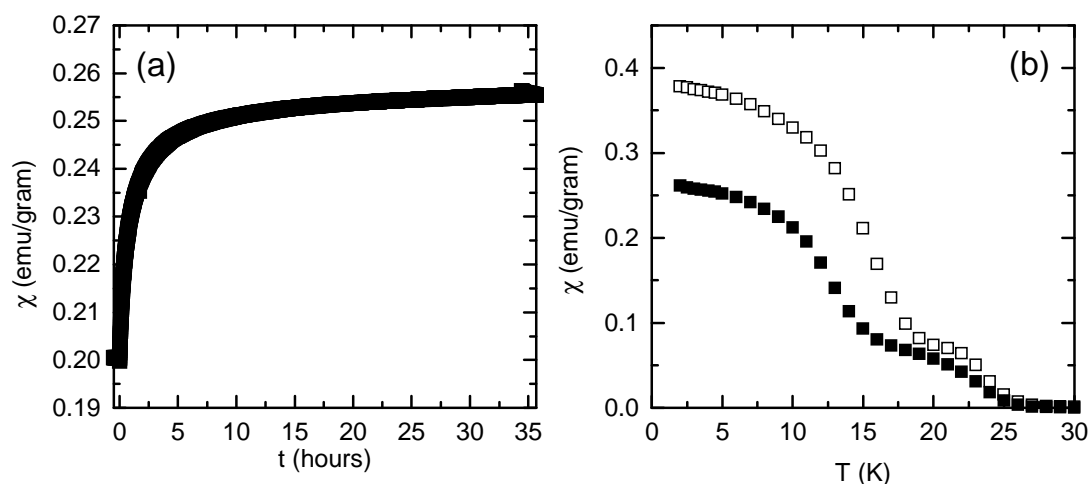


Figure 7-13. Magnetization of macroscopically mixed $\text{Na}_\alpha\text{Ni}_{1-x}\text{Co}_x[\text{Fe}(\text{CN})_6]_\beta \cdot n\text{H}_2\text{O}$. Susceptibility measurements of manually mixed powder with $x = 0.60$ in ~ 10 G showing (a) no decrease in the magnetization with photoirradiation over time, but rather a clear increase and (b) two well defined ordering temperatures present in the material as well as an overall increase in the magnetization at all temperatures from the dark (■) compared to the photoirradiated (□) states. The small change in the susceptibility above ~ 17 K is due to the slightly different measuring fields arising from the fact that these data predate the careful procedure described in the text ensuring the same measuring field for photoirradiated and dark states.

7.1.8 Discussion

In the following subsections, the three main results of the experimental and numerical work performed on the ternary transition metal Prussian blue analog, $\text{Na}_\alpha\text{Ni}_{1-x}\text{Co}_x[\text{Fe}(\text{CN})_6]_\beta \cdot n\text{H}_2\text{O}$, are discussed. Highlighted are, first, the observation of a photoinduced decrease in magnetization, second, the scaling of magnetic properties as a function of x , and third, the dependence of the observed CTIST effect upon dilution of the parent cobalt hexacyanoferrate material. Finally, aspects and potential future extensions of the mean-field calculations are examined in light of the experimental results.

7.1.8.1 Photoinduced Decrease in Magnetization

The results of the mean-field calculations predict a decrease in magnetization within the ordered state with increasing high-spin fraction for $\text{Na}_\alpha\text{Ni}_{1-x}\text{Co}_x[\text{Fe}(\text{CN})_6]_\beta \cdot n\text{H}_2\text{O}$ powders with enough ferromagnetic Ni^{2+} constituent ions. These predictions are compared to low temperature magnetic susceptibility experiments as a function of x . All samples show an increase in magnetization at high field, Figure 7-9, even those showing the photodecrease at low field, Figure 7-7. This increase in magnetization at high field, regardless of x , proves that additional spins are being generated, rather than destroyed, during photoirradiation. These results also indicate that the mechanism for the photoinduced magnetization, present in all samples having $x > 0$, is the same CTIST leading to the persistent long-lived metastable states seen in the pure $\text{Rb}_\alpha\text{Co}[\text{Fe}(\text{CN})_6]_\beta \cdot n\text{H}_2\text{O}$ material. The photoeffect can be reproduced and reversed with thermal cycling above approximately 150 K. The ability of the mean-field calculations to predict whether a material will have a photoincrease or decrease based

upon its composition, Figure 7-7, substantiates the claim that the observed photoinduced decreases in magnetization can be understood as an interplay between ferromagnetic and antiferromagnetic superexchange interactions, as was hypothesized in Figure 7-1.

These points can be further elucidated by focusing on the $x = 0.66$ sample. This sample has enough ferromagnetically interacting nearest neighbors to begin driving the Fe sublattice parallel to the applied field, while it simultaneously possesses enough Co–NC–Fe switchable pairs to still show an appreciable CTIST effect. In the low field limit, newly photoexcited Co–NC–Fe pairs align antiparallel to the applied field due to the antiferromagnetic superexchange between Co and Fe ions. Since the Fe ions are already parallel to the field due to the presence of Ni, a net photodecrease in magnetization is observed, Figure 7-14. If a sufficient external magnetic field is applied, the energy reduction gained by aligning Co–NC–Fe pairs with the applied field is larger than the superexchange, so a net photoincrease in magnetization is measured, Figure 7-14. The temperature dependence of both experimental and numerical magnetizations in the low field limit show a decrease in the measured susceptibility below approximately 12 K, above which an increase is observed since the thermal energy is now able to populate the excited states having Co spins parallel to the applied field.

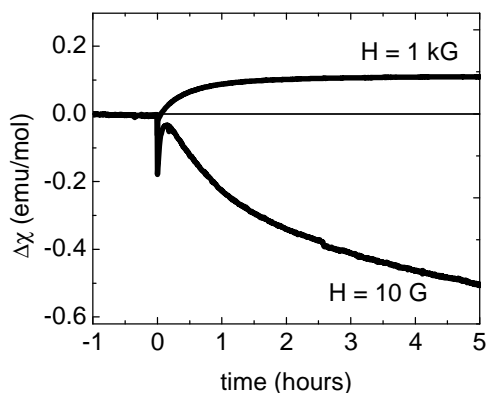


Figure 7-14. Field dependence of photoinduced magnetization for $\text{Na}_\alpha\text{Ni}_{1-x}\text{Co}_x[\text{Fe}(\text{CN})_6]_\beta \cdot n\text{H}_2\text{O}$. Photoinduced change in susceptibility for the $x = 0.66$ sample at $T = 5$ K measured at low field ($H = 10$ G) and high field ($H = 1$ kG). Photoirradiation is continuous for time > 0 .

In addition, there is a time dependence of the photoinduced magnetic effect on the scale of weeks. For example, when the samples were measured again after one month in a freezer at $T \sim 248$ K, the photodecrease was found to be slightly stronger by a few percent. This evolution of the magnetic properties may be due to an increase of atomic mixing of the samples arising from solid state diffusion or to the stabilization of the positions of interstitial counterions to regions more prone to induce bistabilities in the spin states.

As a final point, the expectation of a photoeffect having the opposite sign compared to the pure Prussian blue analogue material due to a mixing of ferromagnetic and antiferromagnetic superexchange interactions is similar to the photoinduced magnetic pole inversion reported for $\text{Fe}_{1-x}\text{Mn}_x[\text{Cr}(\text{CN})_6] \cdot n\text{H}_2\text{O}$ Prussian blue analogue [134]. A fundamental difference, however, is that in the $\text{Fe}_{1-x}\text{Mn}_x[\text{Cr}(\text{CN})_6] \cdot n\text{H}_2\text{O}$ system, the applied light is destroying exchange pathways,

whereas additional moments are being generated in the $\text{Na}_\alpha\text{Ni}_{1-x}\text{Co}_x[\text{Fe}(\text{CN})_6]_\beta \cdot n\text{H}_2\text{O}$ system reported here.

7.1.8.2 Scaling of Magnetic Properties

All $\text{Na}_\alpha\text{Ni}_{1-x}\text{Co}_x[\text{Fe}(\text{CN})_6]_\beta \cdot n\text{H}_2\text{O}$ samples studied show spin glass-like long-range magnetic order, as evidenced by the bifurcation of the FC and ZFC curves, Figure 7-7 (b). The peak in the ZFC susceptibility is a fingerprint of the spin glass-like nature of the order in both parent compounds [78] [146-150], the presence of which hints at the complicated nature of the magnetism in the samples investigated. It is noteworthy that local minima are present near $x \sim 0.8$ in the scaling of the magnetic ordering temperature, the coercive field, and the absolute value of the Curie-Weiss temperature as a function of x , Figure 7-15.

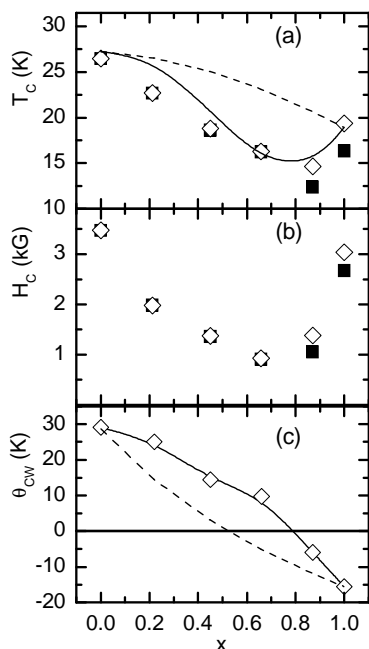


Figure 7-15. Scaling of magnetic properties of $\text{Na}_\alpha\text{Ni}_{1-x}\text{Co}_x[\text{Fe}(\text{CN})_6]_\beta \cdot n\text{H}_2\text{O}$. (a) The magnetic critical temperature, T_C , (b) the coercive field, H_C , and (c) the Curie-Weiss temperature, θ_{CW} , for both “low-spin” (■) and “high-spin” (◇) states, as a function of x . Dashed lines are a mean-field interpolation between the two pure materials. Solid lines are from mean-field fits of θ_{CW} that allow for a modification of exchange constants as the M–NC–M' distance changes as a function of x ; superexchange constants were empirically scaled to 80 % of their fit value for comparison to the low temperature T_C values. Coercive fields were obtained at $T = 2$ K after sweeping to 70 kG. Curie-Weiss temperatures, θ_{CW} , were obtained by fitting from 250 K to 300 K, where n_{HS} and μ_{eff} are essentially constant.

The observed scaling of magnetic properties in $\text{Na}_\alpha\text{Ni}_{1-x}\text{Co}_x[\text{Fe}(\text{CN})_6]_\beta \cdot n\text{H}_2\text{O}$ can be compared with previous work on ternary transition metal Prussian blue analogues [136-138][149-151]. In ternary materials of $\text{Cu}[\text{Co}_x\text{Fe}_{1-x}(\text{CN})_6]$, $\text{Ni}[\text{Co}_x\text{Fe}_{1-x}(\text{CN})_6]$ and $\text{Fe}[\text{Co}_x\text{Fe}_{1-x}(\text{CN})_6]$, a clear monotonic scaling of the transition temperature with x was observed, and these results are dominated by the changing number of magnetic nearest neighbors, since Co^{3+} on the M site is LS and therefore diamagnetic [149]. Similar monotonic scaling was observed in $\text{Ni}[\text{Cr}_x\text{Fe}_{1-x}(\text{CN})_6]$ and $\text{Fe}[\text{Cr}_x\text{Fe}_{1-x}(\text{CN})_6]$ [150], where the substitution of Cr^{3+} ($S = 3/2$) for Fe^{3+} ($S = 1/2$) provides a threefold increase of the number of superexchange pathways, as the number of unpaired electrons on the M site changes from $(t_{2g})^1$ to $(t_{2g})^3$. Finally, the most cogent example is $\text{Ni}_x\text{Mn}_{1-x}[\text{Cr}(\text{CN})_6] \cdot n\text{H}_2\text{O}$, which displays a clear dip in the ordering temperature and a peak in the coercive field on the background of a linear dependence interpolating between the values of the parent compounds as x was changed [136-138].

A few similarities are obvious when comparing $\text{Na}_\alpha\text{Ni}_{1-x}\text{Co}_x[\text{Fe}(\text{CN})_6]_\beta \cdot n\text{H}_2\text{O}$ and $\text{Ni}_x\text{Mn}_{1-x}[\text{Cr}(\text{CN})_6] \cdot n\text{H}_2\text{O}$, particularly in the context of simple empirical rules for superexchange [38]. First, both contain a Ni^{2+} ion that has a ferromagnetic superexchange pathway (e_g to t_{2g}). Second, the interaction between Mn^{2+} and Cr^{3+} is analogous to the Co^{2+} interaction with Fe^{3+} in $\text{Na}_\alpha\text{Ni}_{1-x}\text{Co}_x[\text{Fe}(\text{CN})_6]_\beta \cdot n\text{H}_2\text{O}$, as there is a competition between ferromagnetic and antiferromagnetic interactions, Figure 7-16 (a). It is plausible that when two superexchange energies of opposite sign compete, the net magnetic interaction is particularly susceptible to perturbation when the inter-ion distance is changed. The non-monotonicities observed in the ordering temperatures, as a function of metal substitution, may therefore be due to a net superexchange that

depends strongly on these small distance changes that are introduced with the substitution. In order to reproduce the experimental data, it was necessary to introduce a distance dependence to the $\text{Co}^{2+}(\text{HS})\text{-NC-Fe}^{3+}(\text{LS})$ superexchange interaction, Figure 7-16 (b).

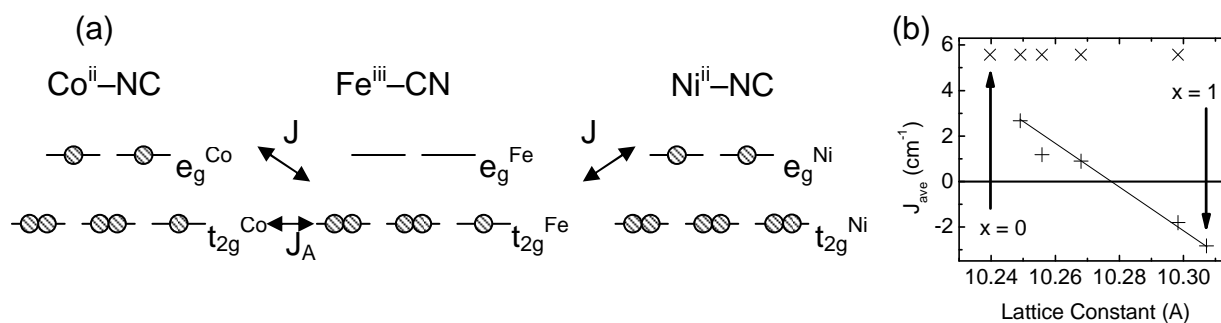


Figure 7-16. Superexchange in $\text{Na}_\alpha\text{Ni}_{1-x}\text{Co}_x[\text{Fe}(\text{CN})_6]_\beta \cdot n\text{H}_2\text{O}$. (a) Energy levels and diagram for the superexchange interactions considered in the material. The Co^{2+} (HS) ion notably has both ferromagnetic ($J_F > 0$) and antiferromagnetic ($J_{AF} > 0$) superexchange interactions with Fe^{3+} (LS), in contrast with the Ni^{2+} . (b) Average values of the exchange constants, J_{ave} , for the $\text{Ni}^{2+}\text{-NC-Fe}^{3+}$ (x) and $\text{Co}^{2+}\text{-NC-Fe}^{3+}$ (+) exchange bonds used in order to reproduce the scaling in Figure 7-15. The line is merely a guide for the eye.

The need to introduce distance dependence to the superexchange interaction in order to reproduce the data may seem drastic, but other methods to reproduce the scaling of the magnetic properties were unsuccessful. Two remarkable features are present in the data: the dip in the ordering temperature near $x = 0.8$ and the unexpectedly large ferromagnetic character of the mixed samples. This increase in ferromagnetic character manifests itself in the lack of a compensation point for the mixed ferro-ferrimagnetic system and in the high temperature slope of χT for the mixed samples. Specifically, from 250 K to 300 K, χT for the $x = 0.66$ sample is *increasing* as temperature decreases, where a model using the binary magnetic interactions predicts a clear *decrease* as temperature decreases. For powder samples containing ions in

similar environments to ours, the introduction of single-ion anisotropy and spin-orbit coupling terms can only give rise to a decrease in χT as temperature decreases [38] [153] [154]. Finally, there are precedents in the literature for such a modification of the superexchange energy. In $\text{Cs}_\alpha\text{Co}[\text{Cr}(\text{CN})_6]_\beta \cdot n\text{H}_2\text{O}$ ferromagnetic compounds having competing ferromagnetic and antiferromagnetic pathways, a dependence of the superexchange energy on the lattice constant was found [155]. Additionally, an $\text{A}_\alpha\text{Co}[\text{Fe}(\text{CN})_6]_\beta \cdot n\text{H}_2\text{O}$ material was reported in which ferromagnetic coupling, as opposed to the usual *antiferromagnetic* coupling leading to a ferrimagnet, was inferred based upon the high-temperature inverse susceptibility [139].

7.1.8.3 Spin-Crossover Dilution

The width of the thermal hysteresis, as represented by $T_{\text{up}} - T_{\text{down}}$, decreases when the cobalt hexacyanoferrate material is diluted, and this trend is correlated with the number of active CTIST nearest neighbors, z_{SCO} , Figure 7-17. As described in Section 7.1.4.2, z_{SCO} can be calculated from the chemical formula, and the observed narrowing of the hysteresis is an expected result when z_{SCO} decreases. It is worth noting that while the changing number of nearest neighbors is a dominant effect, additional perturbations due to the changing of the local environments of the active species are also present. Experimentally, the dilution of spin-crossover species has been investigated intensively after being first realized in $[\text{Fe}_x\text{Zn}_{1-x}(\text{2-pic})_3]\text{Cl}_2 \cdot \text{EtOH}$ [156] [157], where a gradual reduction in the width of the hysteresis loop was attributed to the many-body elastic interactions innate to these transitions. With respect to CTIST in Prussian blue analogues, the field is not as mature and studies are still ongoing. Recently, a CTIST diluted

Rb_{0.70}Cu_{0.22}Mn_{0.78}[Fe(CN)₆]_{0.86}·2.05H₂O sample was compared to its undiluted parent compound Rb_{0.81}Mn[Fe(CN)₆]_{0.95}·1.24H₂O, and no appreciable change in the width of the hysteresis loop was observed [158].

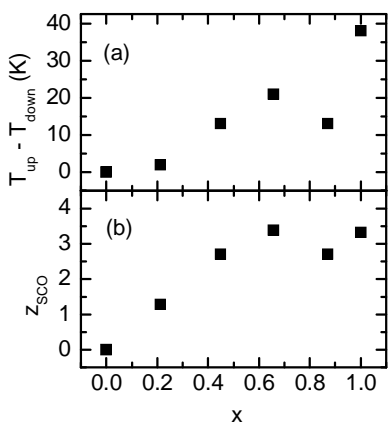


Figure 7-17. Charge transfer induced spin transition parameters for Na_αNi_{1-x}Co_x[Fe(CN)₆]_β·nH₂O. (a) The width of the thermal hysteresis, T_{up}-T_{down}, and (b) the number of spin-crossover active nearest neighbors, z_{SCO}, as a function of x. Here, T_{up}-T_{down} is defined by the difference in the temperature at which half of the spin-crossover active material is high-spin when sweeping up in temperature, and the temperature at which half of the spin-crossover active material is high-spin when sweeping down in temperature.

Furthermore, there is a striking reduction in the amount of CTIST active material once nickel is introduced into the lattice, Figure 7-18 (a). More specifically, the x = 1.00 material transitions 83% of the amount expected from the chemical formula when sweeping from 300 K to 100 K, whereas the x = 0.87 material transitions 16%, and less than 10% transitions in the remainder of the samples with lower x-values. The percent of CTIST active material can be established by considering the chemical formula, the room temperature FT-IR, and the change in χT as the samples are cooled. Although a detailed investigation of the microscopic origins of the observed reduction in spin-crossover active material is warranted, the author conjectures that the reduction is related to a Ni-induced stabilization of Co-NC-Fe HS pairs arising from subtle variations of the unit cell parameters, Figure 7-18 (b). The lattice constants are observed to scale with x in a monotonic fashion that is consistent with changes seen in other ternary metal Prussian blue analogues [136-138][149-151]. However, the

nonlinear nature of the scaling implies an actual changing of the bond energies in the system as the different systems are mixed. The FT-IR data also provide evidence supporting the stabilization of the coordination bond with the incorporation of Ni^{2+} . Using the cyanide stretch associated with the divalent metal to iron bond, plots of the stretching frequency and an effective spring constant as a function of x can be made, Figure 7-19, implying a stabilization of the bond and an increased rigidity of the lattice with the introduction of nickel ions. Therefore, it may no longer be energetically favorable for Co–NC–Fe pairs in $\text{Na}_\alpha\text{Ni}_{1-x}\text{Co}_x[\text{Fe}(\text{CN})_6]_\beta \cdot n\text{H}_2\text{O}$ to undergo CTIST due to the added strain that would result for the Ni–NC–Fe bonds in the system. More specifically, the LS phase of $\text{Na}_\alpha\text{Co}[\text{Fe}(\text{CN})_6]_\beta \cdot n\text{H}_2\text{O}$ has a lattice constant of 9.9721 Å, whereas the HS phase has a lattice constant of 10.3033 Å [68], which is comparable to the $x = 1.00$ sample that has a lattice constant of 10.30(7) Å. In contrast, the $x = 0.00$ nickel hexacyanoferrate species has a lattice constant of 10.23(9) Å, which is comparable to the previously reported value of 10.229 Å for $\text{Ni}_3[\text{Fe}(\text{CN})_6]_2$ [139].

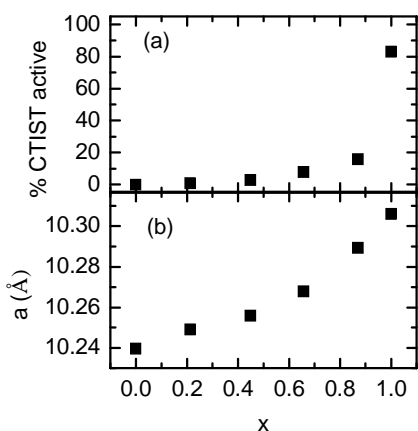


Figure 7-18. Amount of CTIST materials in $\text{Na}_\alpha\text{Ni}_{1-x}\text{Co}_x[\text{Fe}(\text{CN})_6]_\beta \cdot n\text{H}_2\text{O}$. (a) The percentage of CTIST active material, %CTIST active, and (b) the unit cell lattice constant, a , as a function of x .

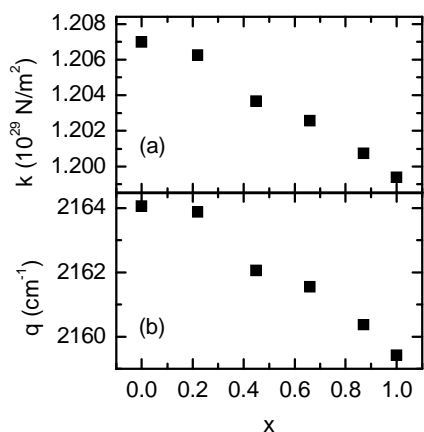


Figure 7-19. FT-IR parameters in $\text{Na}_\alpha\text{Ni}_{1-x}\text{Co}_x[\text{Fe}(\text{CN})_6]_\beta \cdot n\text{H}_2\text{O}$. (a) The effective spring constant and (b) FT-IR frequency for $\text{M}^{2+}\text{-C-N-Fe}^{3+}$ as a function of x .

Comparisons of this observation of the reduction of CTIST active material to a recent work studying the dilution of cobalt hexacyanoferrate by diamagnetic Zn^{2+} at the divalent metal site or by diamagnetic Co^{3+} at the cyanometallate site [135] are useful. In particular, a similar sensitivity of the CTIST effect with the substitution of metals is seen by Cafun *et al.*, [135] and the reduction in the magnitude of the effect in their samples is also larger than expected by a simple reduction in the spin-crossover active species on a molecule by molecule level. It was previously shown by Ksenofontov *et al.* that by application of hydrostatic pressure to $\text{A}_\alpha\text{Co}[\text{Fe}(\text{CN})_6]_\beta \cdot n\text{H}_2\text{O}$ powders, a stabilization of the LS phase could be induced in the samples [2]. This pressure sensitivity leads to the obvious contention that the stabilization of the high-spin phase for $\text{Na}_\alpha\text{Ni}_{1-x}\text{Co}_x[\text{Fe}(\text{CN})_6]_\beta \cdot n\text{H}_2\text{O}$ may simply be due to an effective “negative pressure.” Cafun *et al.* [135] argue that the observed stabilization with metal substitution cannot be due to such an effect because their starting material has a cell size of $\sim 10.32 \text{ \AA}$, while the 100% Zn^{2+} doped material should have a negative pressure due to its cell size of $\sim 10.40 \text{ \AA}$ and the 100% $\text{Co}^{3+}(\text{CN})_6$ doped material should have a positive pressure owing to lattice constant of $\sim 10.23 \text{ \AA}$. However, these room temperature values all deal with the high-spin lattice constants, and with respect to the low-spin lattice constants,

the alien species are still larger than the LS Co–NC–Fe state, and in fact closer in size to the HS Co–NC–Fe state than the LS Co–NC–Fe state, suggesting that chemical pressure may still be a valid argument for the effect. Finally, more subtle effects on the energy of the cobalt-iron charge transfer arising from the presence of neighboring nickel ions may also be present.

7.1.8.4 Mean-Field Predictions versus Observations

The mean-field calculations were able to predict whether the magnetization of the chosen samples would increase or decrease with photoirradiation. Upon completion of the experiments, the lack of a compensation point and subsequent negative magnetization, as well as the general scaling of magnetic properties, was surprising. However, a better agreement between calculations and experiment was found if a distance dependence was introduced for the superexchange constant. In addition, discrepancies between predictions and experiment may stem from the need to choose the simplest Hamiltonian that could capture the spirit of the problem, having only Zeeman and superexchange terms, in order to make the number of free parameters tractable. Future studies with more parameters may be possible once neutron spectroscopy is performed to fix the parameter values to experimental data.

Using the machinery described in the previous subsections, magnetization as a function of temperature can be calculated. For the first attempt, the superexchange constants for all materials were taken from the nickel to iron and cobalt to iron interactions of the $x = 0.00$ and $x = 1.00$ samples, respectively. This method is appealing because it is predictive and limits the number of model parameters. However, some discrepancies between model and experiment were found, Figure 7-20.

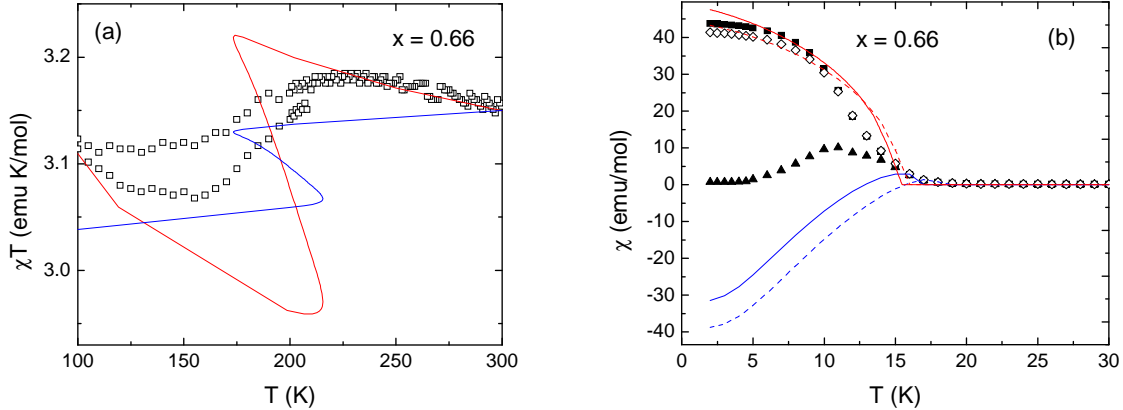


Figure 7-20. Comparison of ferromagnetic versus antiferromagnetic Co-Fe components. (a) Comparison of χT versus T for SQUID magnetometer data (\square), mean-field calculation ($-$) using J_{CoFe} and J_{NiFe} values from the binary materials, and mean-field calculation ($-$) fitting $\langle J_{CoFe} \rangle$ from 250 K to 300 K without modifying J_{NiFe} . (b) Comparison of χ versus T for SQUID magnetometer data (\diamond = FC photoinduced, \blacksquare = FC dark, \blacktriangle = ZFC dark), mean-field calculation ($-$ = FC dark, $-$ = FC photoinduced) using J_{CoFe} and J_{NiFe} values from the binary materials, and mean-field calculation ($-$ = FC dark, $-$ = FC photoinduced) fitting $\langle J_{CoFe} \rangle$ from 250 K to 300 K without modifying J_{NiFe} .

A few additional parameters were tried, with a distance dependent superexchange energy being the most successful at capturing the features observed in the magnetization. The calculations then took on a flavor of fitting the data, with the predictive role already having been fulfilled. First, the susceptibility data from 250 K to 300 K were fit using the mean-field solutions described previously, yielding values for $\langle J_{NiFe} \rangle$ and $\langle J_{CoFe} \rangle$. The nickel to iron superexchange was fixed, and the cobalt to iron superexchange was allowed to vary as a function of lattice constant due to the presence of both antiferromagnetic and ferromagnetic superexchange pathways. The distribution of superexchange energies was binned into two populations, CTIST active and CTIST inactive, the fractions of both being determined from high temperature susceptibility

data (Figure 7-21). The CTIST active superexchange value was associated with the population having the closest lattice constant to the $x = 1.00$ material.

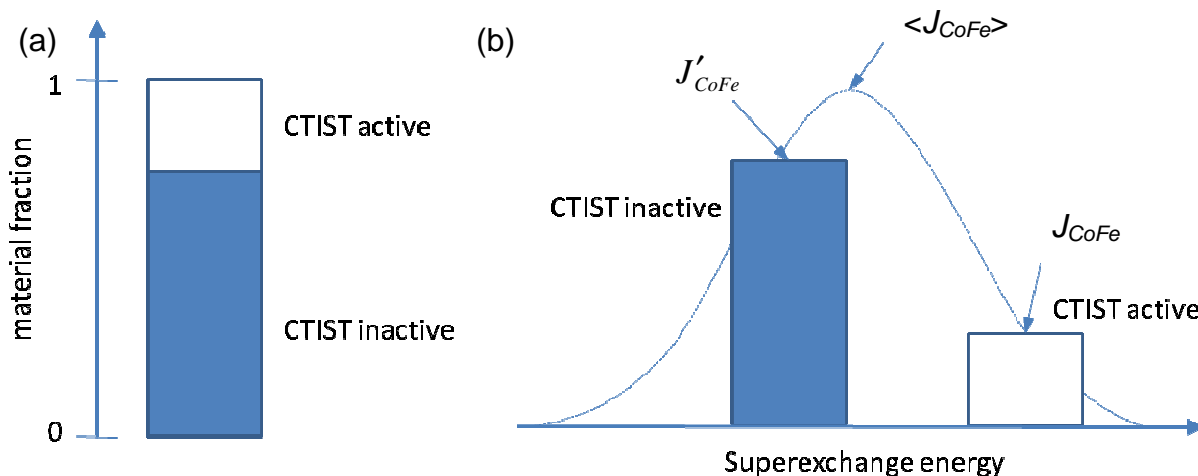


Figure 7-21. Modification of superexchange energy in $\text{Na}_\alpha\text{Ni}_{1-x}\text{Co}_x[\text{Fe}(\text{CN})_6]_\beta \cdot n\text{H}_2\text{O}$. (a) The ternary metal $\text{Na}_\alpha\text{Ni}_{1-x}\text{Co}_x[\text{Fe}(\text{CN})_6]_\beta \cdot n\text{H}_2\text{O}$ compounds were found experimentally to have CTIST active and CTIST inactive populations, as approximated from the high temperature magnetic susceptibility and the room temperature FT-IR data. (b) A sketch of the superexchange energy distribution showing $\langle J_{CoFe} \rangle$, which is determined by fitting χT versus T from 250 K to 300 K. The CTIST inactive portion, J'_{CoFe} , can actually have ferromagnetic character in some samples. For simplicity, it is assumed that the electronic structure of the CTIST active portion is most similar to the pure $x = 1.00$ material and thus the magnetic interactions, J_{CoFe} , are similar.

7.1.9 Conclusions

It has been demonstrated that the ternary transition metal Prussian blue analogue $\text{Na}_\alpha\text{Ni}_{1-x}\text{Co}_x[\text{Fe}(\text{CN})_6]_\beta \cdot n\text{H}_2\text{O}$ shows a photoinduced decrease in magnetization for certain values of x , temperature, and applied magnetic field. Furthermore, the $\text{Na}_\alpha\text{Ni}_{1-x}\text{Co}_x[\text{Fe}(\text{CN})_6]_\beta \cdot n\text{H}_2\text{O}$ system is the first example of a compound in which superexchange energies control whether incident light increases or decreases CTIST magnetization. As a result, the sign of the photoeffect can be changed by stoichiometry. Although a photoinduced decrease in magnetization while

increasing the number of spins has also been seen in $A_\alpha\text{Co}[\text{Fe}(\text{CN})_6]_\beta \cdot n\text{H}_2\text{O}$ thin films [10], the microscopic origins are different. In addition, the width of the thermal hysteresis of the CTIST is reduced upon dilution of the active spin-crossover species in the ternary mixture. The origins of the experimental observations are nicely explained using mean-field calculations.

7.2 Heterostructured Films Containing Cobalt Hexacyanoferrate

7.2.1 Introduction

Recently, there has been interest not only in three-dimensional systems, but also in two-dimensional and quasi-two-dimensional structures, some of which have been shown to display phenomenon different than that seen in the analogous three-dimensional materials [10] [29] [76] [93] [94][98-112]. Work on thin films of Co-Fe was originally motivated by the functional need to increase the light cross-section of the photoactive material, but it is noteworthy that anisotropy in the photoinduced magnetization is seen in the quasi-two-dimensional geometry [10].

Originally, the previous student in Professor Meisel's lab, Dr. Ju-Hyun Park, had the idea that, by layering the lower ordering temperature Co-Fe photomagnet between layers of a higher ordering magnet that is not photoactive, a transition between two-dimensional and three-dimensional behavior in the heterostructure might be seen after photoirradiation [76]. This transition was hypothesized to occur as Co-Fe spins become magnetic and contribute additional exchange pathways between the higher ordering temperature layers. Upon surveying the different possible high- T_C magnets, nickel hexacyanochromate (Ni-Cr) was chosen because of its robustness and similar lattice constant to Co-Fe [54] [56]. Heterostructured films may be generated with a

synthesis technique similar to that used for pure phase films, sequential adsorption (Figure 7-22).

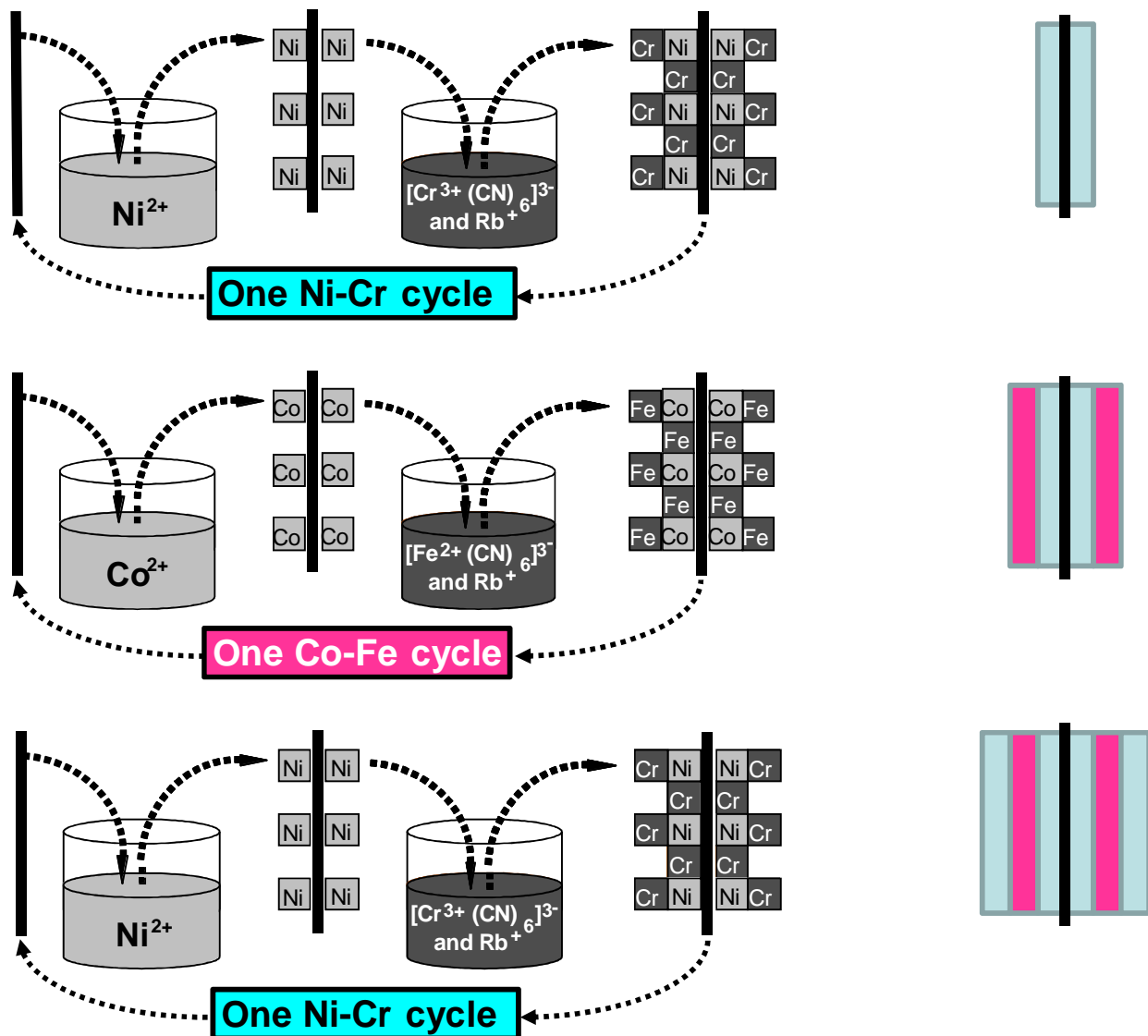


Figure 7-22. A scheme showing synthesis of a heterostructured thin film using multiple sequential adsorption cycles.

Exploration of Co-Fe/Ni-Cr heterostructures in various geometries eventually led to the realization of the desired effect, although in a different manner than originally hypothesized. Heterostructures with sufficiently thick regions of unadulterated high- T_C magnets and photoactive Co-Fe, so as to retain bulk-like features but sufficiently thin

layers so as to have strong inter-layer interactions, show photoinduced modification of long-range magnet order up to the limit of the photoinduced structural transition of the Co-Fe molecule, ~ 100 K. These high- T_C photoeffects are due to a propagation of photoinduced structural changes in the Co-Fe layer propagating to the Ni-Cr layers. In the following subsections, these discoveries will be discussed. First, the evolution of studies of Co-Fe/Ni-Cr thin film heterostructures will be presented, leading up to the structures having the largest photo-response. Second, the optimized heterostructure will be dissected in detail, and the current understanding of the phenomenon will be presented. Finally, heterostructures with different chromate Prussian blue analogues will be presented. Elements of the chapter have recently been published in JACS communications [159] and elsewhere.

7.2.2 Synthesis

Synthesis of the desired heterostructure of Ni-Cr and Co-Fe is possible by a sequential deposition method (SD), in which PBA films are generated by sequentially dipping a solid-support into aqueous solutions containing the desired constituent metals. One such dipping process will often be referred to as one “cycle” in the following sections. The attractiveness of the SD approach comes from its combination of simplicity with fine thickness control for generation of homogeneous films of arbitrary PBAs with tunable chemical compositions on a variety of substrates. The synthesis of a heterostructured film is made possible by alternating protocols for the SD films of the sought after component PBAs, the details of which are discussed in Dr. Franz Frye’s thesis [94]. The shorthand notation used to refer to samples first lists the repeat cycle, then the total number of repeats, and finally the constituent magnets. For example, a film with every other cycle of Co-Fe and Ni-Cr repeated 40 times will be referred to as

1/1 x 40 Co-Fe/Ni-Cr, and a film with 40 cycles of Ni-Cr followed by 40 cycles of Co-Fe followed by 40 cycles of Ni-Cr will be referred to as 40/40/40 Ni-Cr/Co-Fe.

7.2.3 Magnetization of Nickel Hexacyanochromate and Cobalt Hexacyanoferrate Heterostructures

Due to similar lattice constants and the high ordering temperature of the Ni-Cr material, most of the heterostructured films studied were of Ni-Cr and Co-Fe layers. A brief summary of all films to be presented can be found in Table 7-2.

Table 7-2. Nickel hexacyanochromate and cobalt hexacyanoferrate heterostructures studied.

Number of cycles	Order of deposition	Deposition Speed
1/1 x 40	Ni-Cr/Co-Fe/Ni-Cr/Co-Fe/...	Slow
5/5 x 20	Ni-Cr/Co-Fe/Ni-Cr/Co-Fe/...	Slow
40/40	Ni-Cr/Co-Fe	Slow
10/10	Ni-Cr/Co-Fe	Fast
10/10	Co-Fe/Ni-Cr	Fast
10/5/10	Ni-Cr/Co-Fe/Ni-Cr	Fast
10/10/10	Ni-Cr/Co-Fe/Ni-Cr	Fast
40/40/40	Ni-Cr/Co-Fe/Ni-Cr	Fast
20/40/20	Ni-Cr/Co-Fe/Ni-Cr	Fast
40/20/40	Ni-Cr/Co-Fe/Ni-Cr	Fast
40/40/40	Ni-Cr/Co-Fe/Ni-Cr	Fast

7.2.3.1 Slow Deposition Multilayer Films

A series of films having the same total number of cycles, but with different numbers of cycles between the alternation of Co-Fe and Ni-Cr depositions, was studied

in the SQUID magnetometer. Unlike the rest of the samples to be presented, these were generated using a “slow” deposition method that included extra washing of the film after deposition [94]. Exemplary samples are a 1/1 x 40 Co-Fe/Ni-Cr, 5/5 x 20 Co-Fe/Ni-Cr, and 40/40 Co-Fe/Ni-Cr. The temperature dependence of the DC magnetic susceptibilities, $\chi = M/H$, are shown in Figure 7-23 for temperatures between 2 K and 100 K and an external field of 100 G. The magnetic signals are expressed per cm^2 .

A clear evolution of the magnetic order in the samples can be seen as a progression is made from separate behaviors of the Co-Fe and Ni-Cr magnets to an overall combined magnet that has the addition of superexchange between Co and Cr as well as superexchange between Ni and Fe. The disparity between the changes in magnetization with photoirradiation can be explained by poor transfer ratios causing less Co-Fe content in the film.

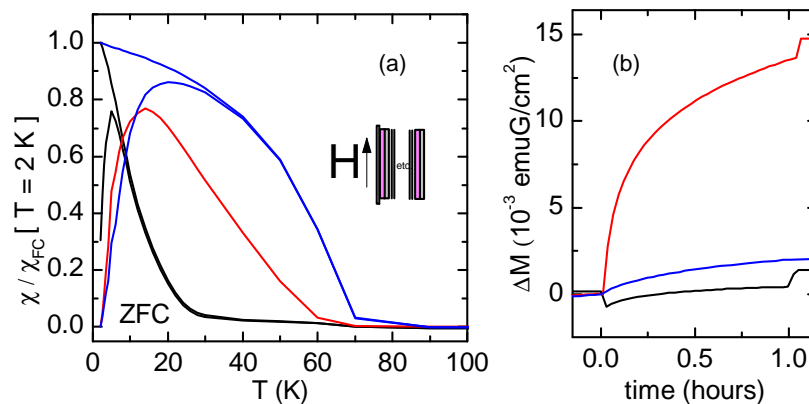


Figure 7-23. Magnetization of slow deposition multilayer films. (a) Plots of FC and ZFC DC magnetic susceptibilities of 1/1 x 40 Co-Fe/Ni-Cr (—), 5/5 x 20 Co-Fe/Ni-Cr (—), and 40/40 Co-Fe/Ni-Cr (—) films. The lines are guides to the eye connecting the data points, taken every 10 K. (b) ΔM versus time irradiated, are shown for parallel orientations of films 1/1 x 40 Co-Fe/Ni-Cr (—), 5/5 x 20 Co-Fe/Ni-Cr (—), and 40/40 Co-Fe/Ni-Cr (—) with applied magnetic field of 100 G and at 5 K.

7.2.3.2 Stacked Films

Simpler, stacked films of 10/10 Co-Fe/Ni-Cr and of 10/10 Ni-Cr/CoFe were measured to investigate their magnetic and photomagnetic character. The temperature dependence of the DC magnetic susceptibilities, $\chi = M/H$, for temperatures between 2 K and 100 K, and ΔM versus time irradiated at 5 K and 100 G, are shown in Figure 7-24 (a), Figure 7-25 (a), Figure 7-26 (a), and Figure 7-27 (a). ΔM versus time irradiated is shown in Figure 7-24 (b), Figure 7-25 (b), Figure 7-26 (b), and Figure 7-27 (b). The magnetic signals are all expressed per cm^2 of sample.

The presence of the Ni-Cr component can clearly be seen by the ordering onset at ~ 70 K and the large magnetic anisotropy exists below this temperature. The increase of magnetization with photoirradiation is clearly coming from the Co-Fe component. In addition, two ordering temperatures can be seen for both films, with an additional onset at ~ 10 K. Differences between the stacked films are also apparent, where the anisotropy of the photoeffect is stronger for the 10/10 Co-Fe/Ni-Cr film, which has the Co-Fe deposited first, as opposed to the 10/10 Ni-Cr/CoFe film, which has the Ni-Cr deposited first. A slightly different ordering temperature is also observed for the Co-Fe component in the films, with the 10/10 Co-Fe/Ni-Cr film having a lower ordering temperature than the 10/10 Ni-Cr/CoFe film. These effects can be explained by low transfer ratios for the first few cycles and by the proximity of the solid support being a key factor in the sign of the photoeffect of the Co-Fe.

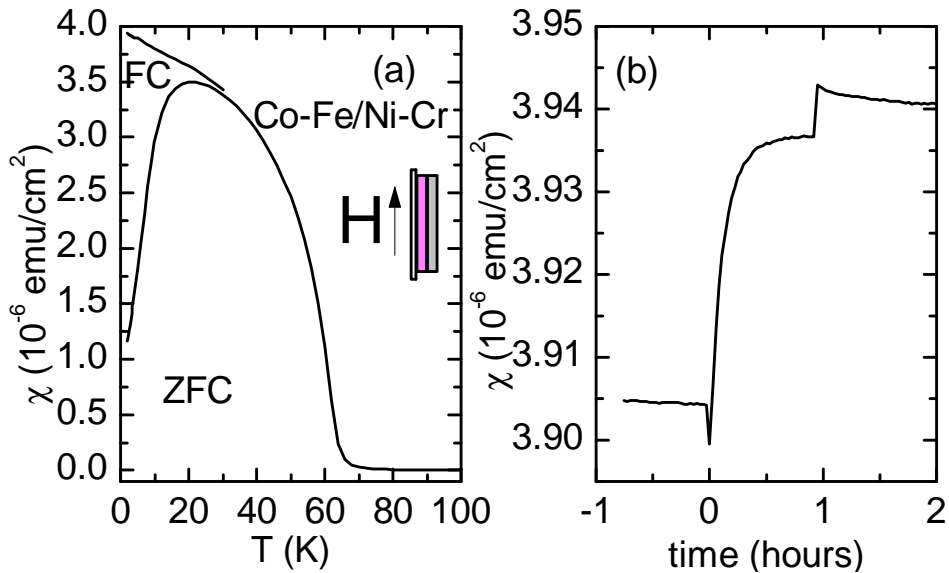


Figure 7-24. Magnetization of 10/10 Co-Fe/Ni-Cr thin film oriented parallel. (a) Plots of FC and ZFC DC magnetic susceptibilities versus temperature for the 10/10 Co-Fe/Ni-Cr thin film in $H = 100$ G parallel to the planes of the films are shown. (b) ΔM versus time irradiated is shown at 5 K and 100 G parallel to the film.

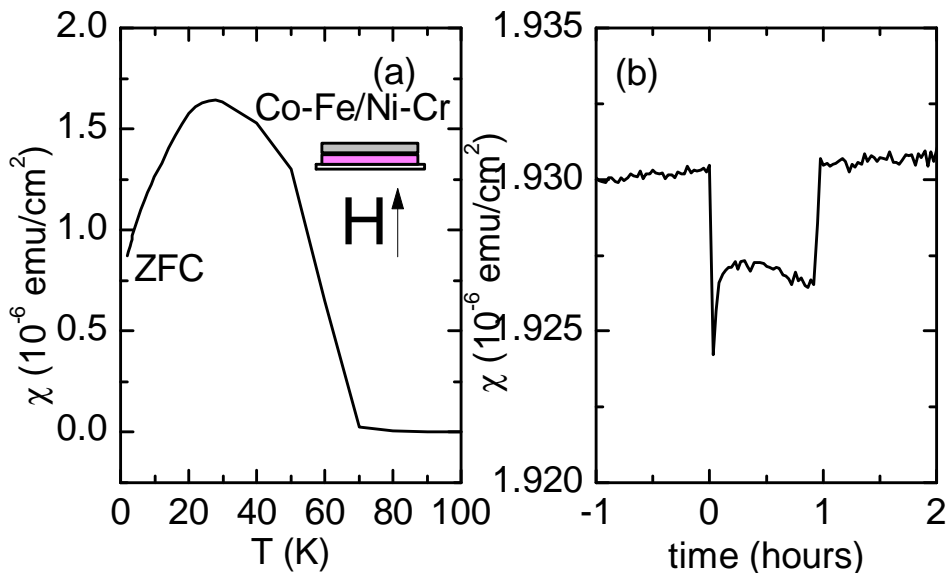


Figure 7-25. Magnetization of 10/10 Co-Fe/Ni-Cr thin film oriented perpendicular. (a) Plots of ZFC DC magnetic susceptibility versus temperature for the 10/10 Co-Fe/Ni-Cr thin film in $H = 100$ G perpendicular to the planes of the films are shown. (b) ΔM versus time irradiated is shown at 5 K and 100 G perpendicular to the film.

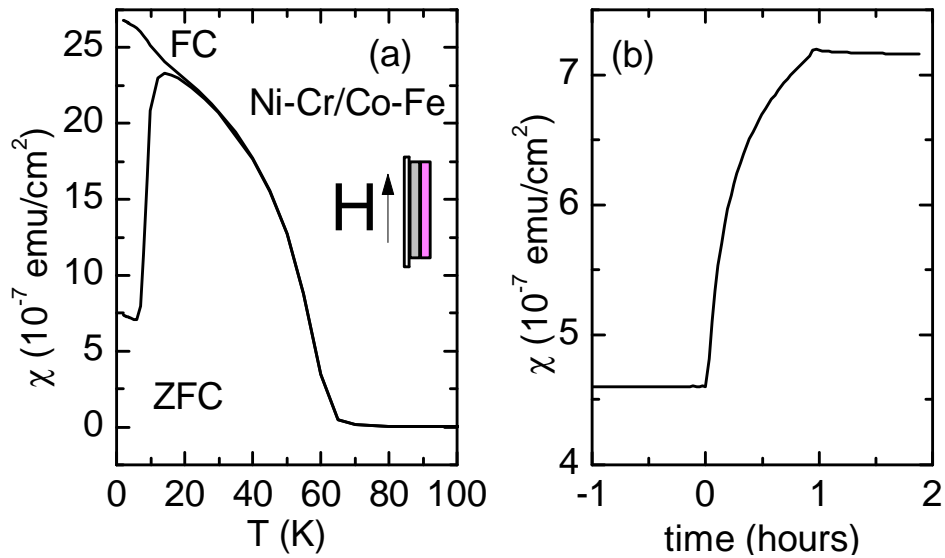


Figure 7-26. Magnetization of 10/10 Ni-Cr/Co-Fe thin film oriented parallel. (a) Plots of FC and ZFC DC magnetic susceptibilities versus temperature for the 10/10 Ni-Cr/Co-Fe thin film in $H = 100$ G parallel to the planes of the films are shown. (b) ΔM versus time irradiated is shown at 5 K and 100 G parallel to the film.

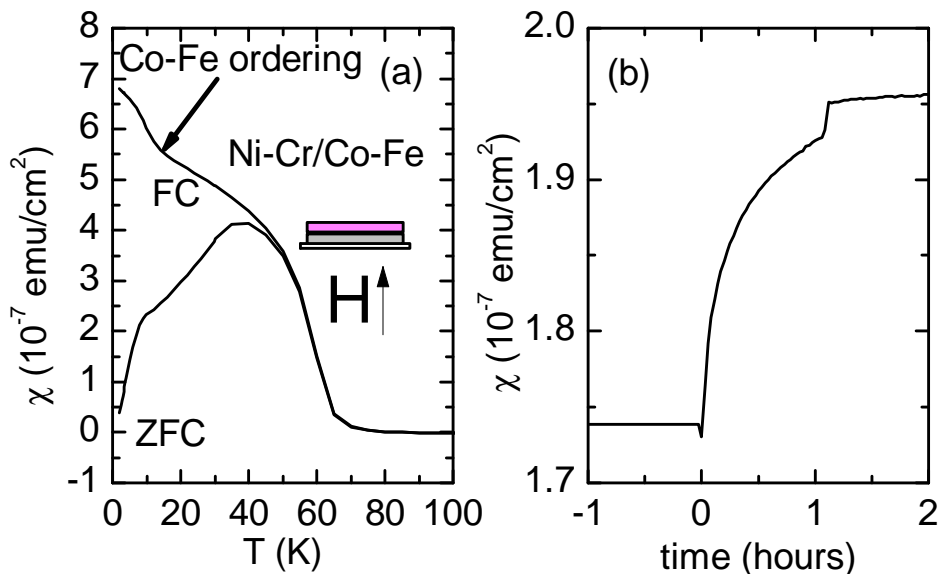


Figure 7-27. Magnetization of 10/10 Ni-Cr/Co-Fe thin film oriented perpendicular. (a) Plots of FC and ZFC DC magnetic susceptibilities versus temperature for the Ni-Cr/Co-Fe thin film in $H = 100$ G perpendicular to the planes of the films are shown. (b) ΔM versus time irradiated is shown at 5 K and 100 G perpendicular to the film.

7.2.3.3 Thin Sandwiched Films

A third set of films, in which a thin layer of Co-Fe PBA is deposited between two thin layers of Ni-Cr PBA, is the so-called thin sandwich geometry. Two different heterostructures are presented, 10/5/10 and 10/10/10, where both are Ni-Cr/Co-Fe/Ni-Cr, so the additional nomenclature for constituent makeup will be dropped to ease discussion. The temperature dependence of the DC magnetic susceptibilities, $\chi = M/H$, are shown in Figure 7-28 (a), Figure 7-29 (a) and Figure 7-30 for temperatures between 2 K and 100 K and an external field of 100 G. For the film 10/5/10, ΔM versus time irradiated is shown in Figure 7-28 (b) for H parallel, and Figure 7-29 (b) for H perpendicular, both in fields of 100 G. ΔM versus time irradiated at 5 K and fields of 100 G and 1 kG is shown in Figure 7-31 and Figure 7-32 for both parallel and perpendicular orientations of the 10/10/10 film with respect to the applied magnetic field. The magnetic signals are expressed per cm^2 of sample.

The susceptibility data again show the strong presence of Ni-Cr magnetism in the samples as well as photoinduced magnetism from the Co-Fe moieties. However, the most striking feature of the data for the sandwich films is that for the 10/10/10 film, and to a lesser extent for the 10/5/10 film, a clear *decrease* in magnetization with photoirradiation is seen in an applied field of 100 G in both film orientations. When going to higher external fields of 1 kG, the 10/10/10 film no longer shows a decrease with photoexcitation, but rather an increase for both orientations.

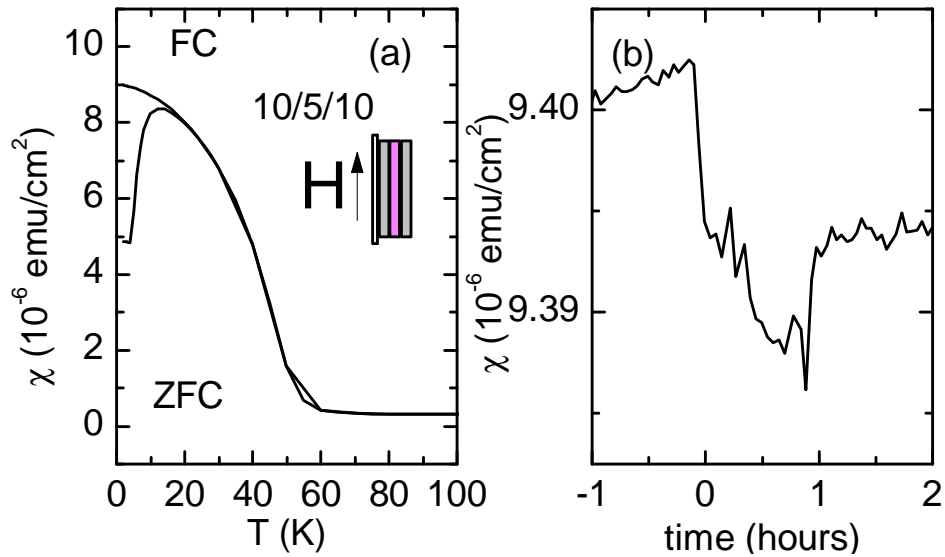


Figure 7-28. Magnetization of 10/5/10 Ni-Cr/Co-Fe/Ni-Cr thin film oriented parallel. (a) Plots of FC and ZFC DC magnetic susceptibilities versus temperature of the sandwich 10/5/10 Ni-Cr/Co-Fe/Ni-Cr PBA thin film in $H = 100$ G parallel to the planes of the films are shown. (b) ΔM versus time irradiated is shown at 5 K and 100 G parallel to the film.

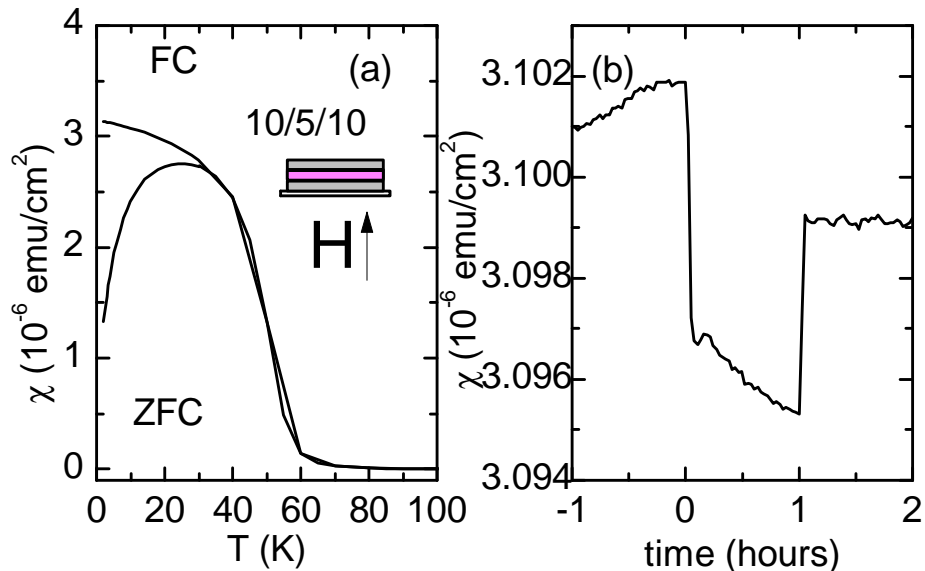


Figure 7-29. Magnetization of 10/5/10 Ni-Cr/Co-Fe/Ni-Cr thin film oriented perpendicular. (a) Plots of FC and ZFC DC magnetic susceptibilities versus temperature of the sandwich 10/5/10 Ni-Cr/Co-Fe/Ni-Cr PBA thin film in $H = 100$ G perpendicular to the planes of the films are shown. (b) ΔM versus time irradiated is shown at 5 K and 100 G perpendicular to the film.

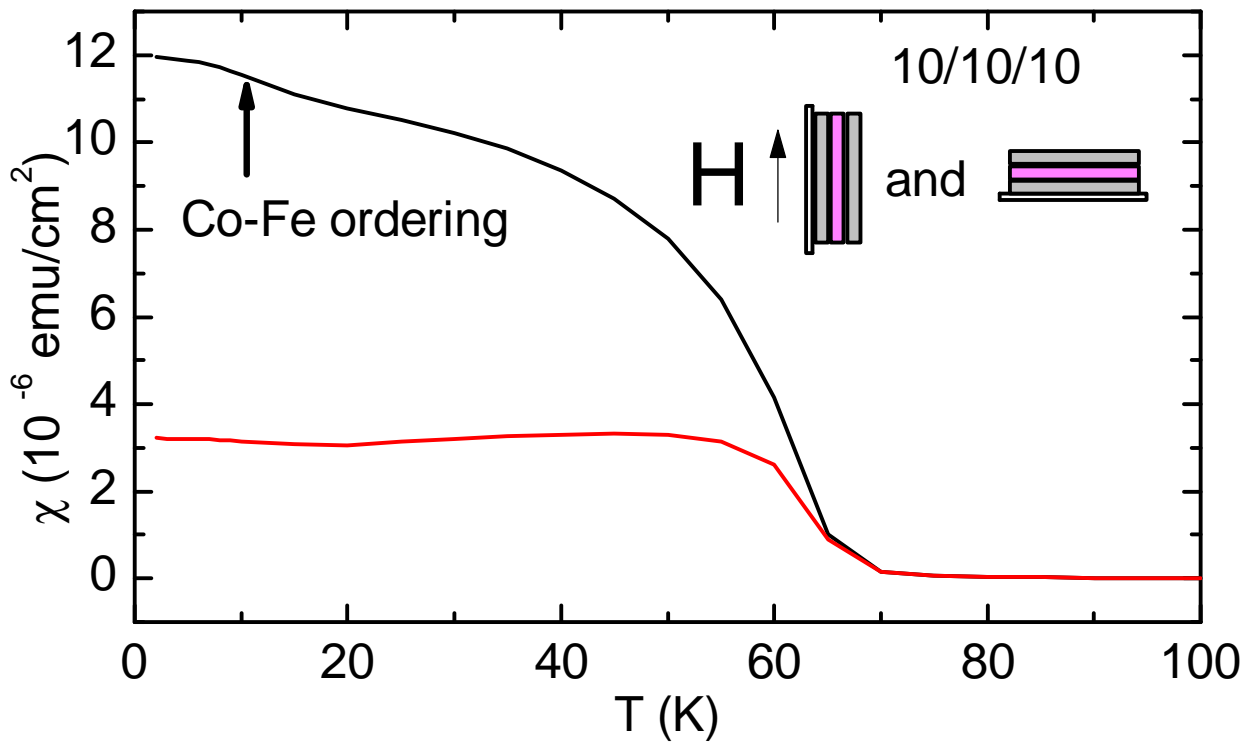


Figure 7-30. Magnetization of 10/10/10 sandwich film versus temperature. Plots of FC DC magnetic susceptibility versus temperature for the 10/10/10 sandwich Ni-Cr/Co-Fe/Ni-Cr PBA thin film in $H = 100$ G are shown for parallel (—) and perpendicular (—) orientations of the plane of the film with respect to the applied field.

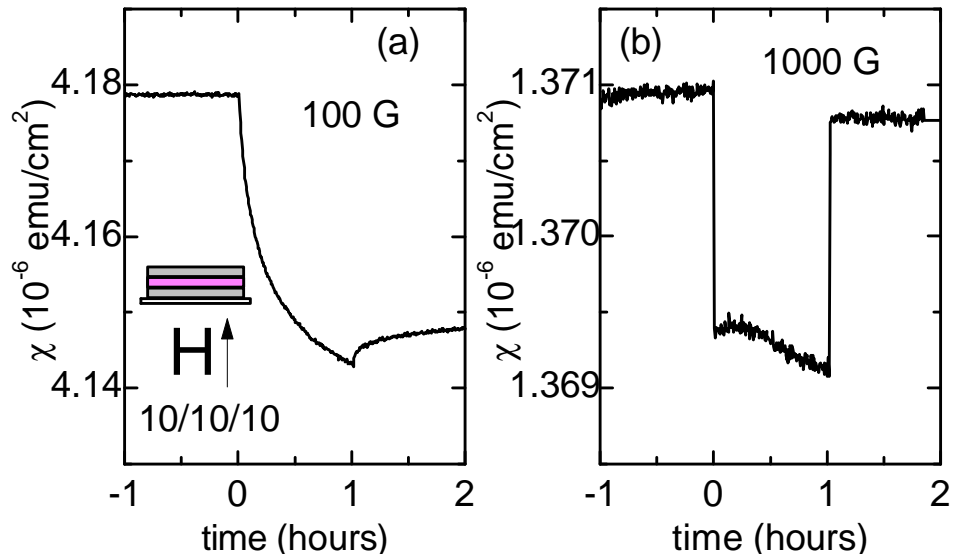


Figure 7-31. Photoinduced magnetization of 10/10/10 film oriented perpendicular. ΔM versus time irradiated is shown for perpendicular orientations of the 10/10/10 sandwich Ni-Cr/Co-Fe/Ni-Cr PBA thin film with respect to the applied magnetic field of (a) 100 G and (b) 1 kG, at 5 K.

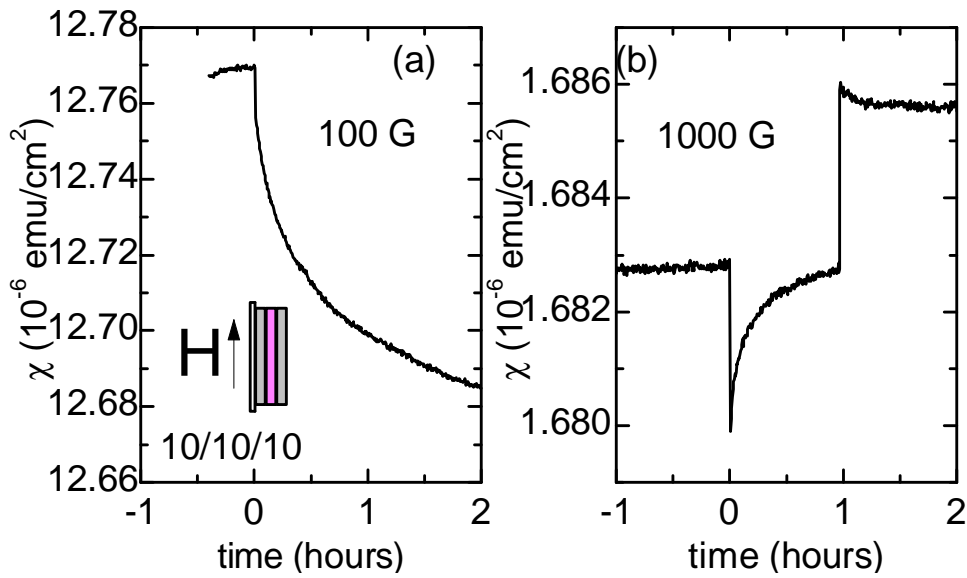


Figure 7-32. Photoinduced magnetization of 10/10/10 film oriented perpendicular. ΔM versus time irradiated is shown for parallel orientations of the 10/10/10 sandwich Ni-Cr/Co-Fe/Ni-Cr PBA thin film with respect to the applied magnetic field of (a) 100 G and (b) 1 kG, at 5 K.

7.2.3.4 Thick Sandwiched Films

At this point, it is worth mentioning that a novel new effect had been seen in the thin sandwiched films, and to help understand the effect, a more easily modeled, solid solution with a similar set of constituents, $\text{Ni}_x\text{Co}_{1-x}[\text{Fe}(\text{CN})_6]_{3/4} \cdot n\text{H}_2\text{O}$, was studied [141]. Since intimate mixing of foreign species with Co-Fe strongly damped the photomagnetic bistability, the sandwich geometry was reinvestigated with thicker layers that were conjectured to possess a larger photoeffect. A larger photoeffect was observed and, in fact, photoinduced changes could be observed as a function of field and temperature in the heterostructures for the first time. Three different heterostructures are presented here, 40/40/40, 20/40/20, and 40/20/40, where all are Ni-Cr/Co-Fe/Ni-Cr, so the additional nomenclature for the constituent makeup will be dropped to ease discussion.

For the 40/40/40 film, the temperature dependence of the DC magnetic susceptibilities, $\chi = M/H$, are shown for parallel and perpendicular orientations in Figure 7-33 (a) and Figure 7-33 (b), respectively, for temperatures between 2 K and 75 K and an external field of 100 G. Field dependence of the magnetization is shown for parallel and perpendicular orientations in Figure 7-33 (c) at 2 K. While kinks in the temperatures sweeps can be associated with ordering of the pure Co-Fe and Ni-Cr phases, the heterostructures show two striking features not observed in the homogeneous phases. First, there is a significant increase in the temperature, from 18 K to 70 K, at which persistent photoinduced changes in the magnetically ordered state are observed. Second, like the thin sandwich heterostructures, the magnetization decreases with light, in contrast to the normal photoinduced increases known for pure Co-Fe compounds. The increase in magnetization at high field is an indication that

there is the usual diamagnetic to magnetic transition of the Co-Fe spins. In addition, aside from an overall scale factor between parallel and perpendicular orientations, the photoinduced effects are the same.

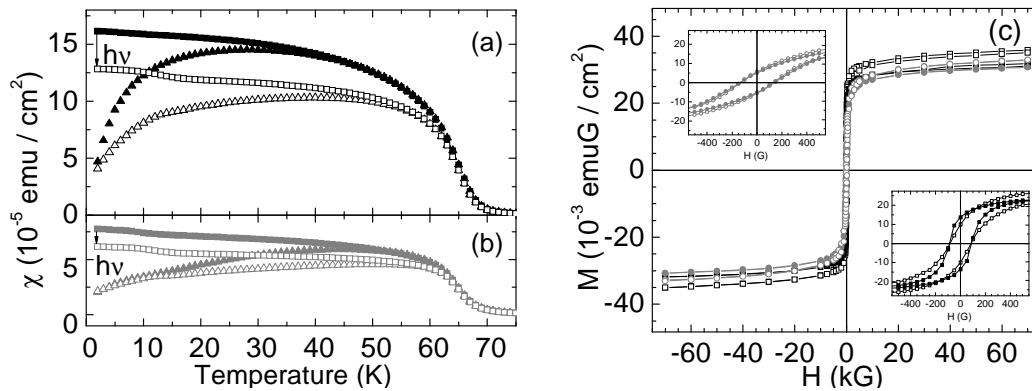


Figure 7-33. Magnetization of 40/40/40 Ni-Cr/Co-Fe/Ni-Cr heterostructure. The $\chi(T)$ data, normalized to the area of the 40/40/40 sandwich Ni-Cr/Co-Fe/Ni-Cr PBA film, are plotted when the externally applied field of 100 G is oriented (a) parallel (black) and (b) perpendicular (grey) to the surface of the film. The closed symbols represent the data prior to irradiation (i.e. dark state), and the open symbols designate the data acquired after 5 hrs of irradiation with white light, but with the light subsequently off, (i.e. PPIM state). (c) The magnetization, M , versus magnetic field, H , loops at 2 K are shown when $H \parallel$ film (black) and $H \perp$ film (grey). The closed symbols are before irradiation and the open symbols are after photoexcitation but with the light off. The insets show an expanded region at low magnetic fields, and the coercive fields, H_C , are 85 G for $H \parallel$ film and 140 G for $H \perp$ film.

For the 20/40/20 film, the temperature dependence of the DC magnetic susceptibilities, $\chi = M/H$, are shown for parallel orientation in Figure 7-34 (a), for temperatures between 2 K and 75 K and an external field of 100 G. Field dependence of the magnetization is shown for parallel orientation in Figure 7-34 (b) at 2 K. These films behave similarly to the 40/40/40 films, except that the relative photoinduced decrease is less, so much so that when the Co-Fe is in the ordered state, an overall increase is observed on the background of the decrease, even in 100 G.

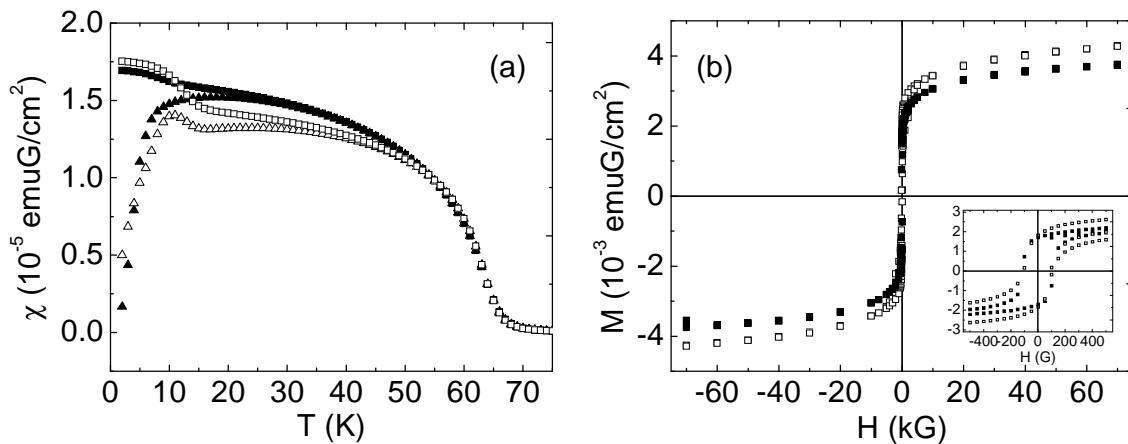


Figure 7-34. Magnetization of 20/40/20 Ni-Cr/Co-Fe/Ni-Cr heterostructure. (a) The $\chi(T)$ data, normalized to the area of the 20/40/20 sandwich Ni-Cr/Co-Fe/Ni-Cr PBA film, are plotted when the externally applied field of 100 G is oriented parallel to the surface of the film. The closed symbols represent the data prior to irradiation (i.e. dark state), and the open symbols designate the data acquired after 5 hrs of irradiation with white light, but with the light subsequently off, (i.e. PPIM state). (b) The magnetization, M , versus magnetic field, H , loops at 2 K are shown when $H \parallel$ film. The closed symbols are before irradiation and the open symbols are after photoexcitation but with the light off.

For the 40/20/40 film, the temperature dependence of the DC magnetic susceptibilities, $\chi = M/H$, are shown for parallel orientation in Figure 7-35 (a), for temperatures between 2 K and 75 K and an external field of 100 G. Field dependence of the magnetization is shown for parallel orientation in Figure 7-35 (b) at 2 K. Again, these films behave similarly to the 40/40/40 films, but here the photoinduced decrease at low fields and increase at high fields are relatively smaller.

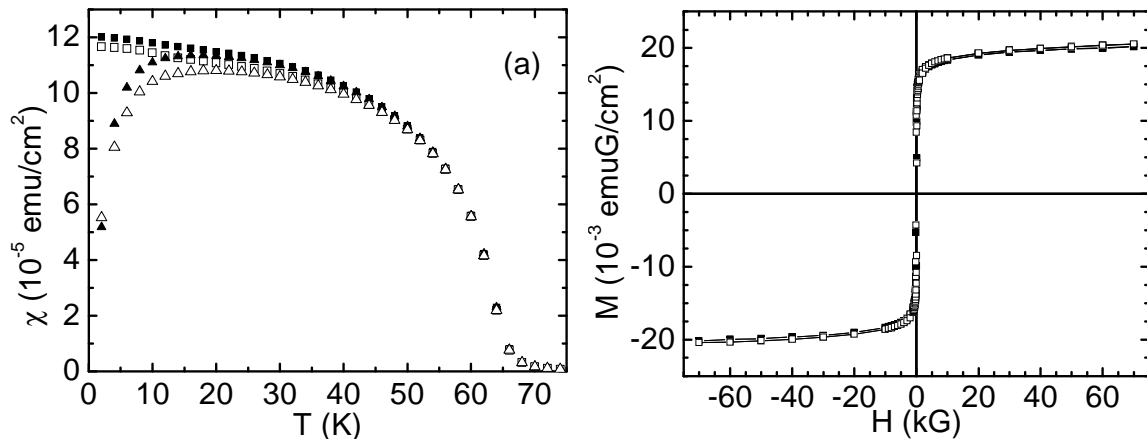


Figure 7-35. Magnetization of 40/20/40 Ni-Cr/Co-Fe/Ni-Cr heterostructure. (a) The $\chi(T)$ data, normalized to the area of the 40/20/40 sandwich Ni-Cr/Co-Fe/Ni-Cr PBA film, are plotted when the externally applied field of 100 G is oriented parallel to the surface of the film. The closed symbols represent the data prior to irradiation (i.e. dark state), and the open symbols designate the data acquired after 5 hrs of irradiation with white light, but with the light subsequently off, (i.e. PPIM state). (b) The magnetization, M , versus magnetic field, H , loops at 2 K are shown when $H \parallel$ film. The closed symbols are before irradiation and the open symbols are after photoexcitation but with the light off.

7.2.4 40/40/40 Heterostructure

Even better than the thin sandwich films showing a novel photoeffect, the thick sandwich films showed a novel photoeffect clearly resolvable at temperatures much higher than in the pure material, which is particularly clear in the 40/40/40 film, Figure 7-36. Therefore, to glean the underlying nature of the effect observed in all

heterostructures, the optimized 40/40/40 film was studied in further detail. These studies include additional measurements in a SQUID magnetometer, Figure 7-37. Transmission electron microscopy was performed to resolve the nanostructure of the sample, Figure 7-38. Nanometer resolved high-resolution inelastic x-ray scattering, EDS, was performed to resolve the chemical makeup as a function of film position, Figure 7-39. Elastic x-ray powder diffraction resolved the lattice constants present in the heterostructure, Figure 7-40. Fourier transform infrared spectroscopy of the cyanide stretches in the heterostructure, compared to the stretches in the pure constituent materials, also provides evidence for the structure and chemical content of the heterostructures, Figure 7-41.

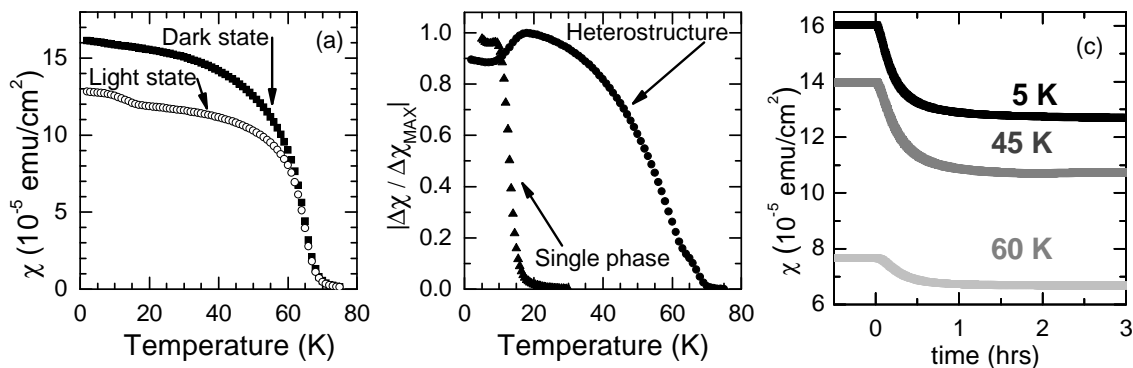


Figure 7-36. Magnetization data of the 40/40/40 sandwich Ni-Cr/Co-Fe/Ni-Cr PBA film. (a) The field-cooled magnetic susceptibility $\chi(T)$ in 100 G oriented parallel to the surface of the film, where $\chi(T)$ is normalized to the area of the film. The closed symbols represent the data prior to irradiation (i.e. dark state), and the open symbols designate the data acquired after 5 hrs of irradiation with white light, but with the light subsequently off, (i.e. PPIM state). (b) The absolute value of the photoinduced changes of χ , $\Delta\chi = \chi(\text{dark}) - \chi(\text{light})$, normalized to the maximum value. The data for the heterostructure is from the left panel, whereas the data for the single phase Co-Fe PBA thin film is taken from Ref. [103]. (c) An expanded view of the temporal evolution of the magnetic response is shown during irradiation at 5 K, 45 K, and 60 K, with $H \parallel$ film and $H = 100$ G. The irradiation begins at time = 0.

7.2.4.1 40/40/40 film, 10 kG Temperature Sweeps

To test the nature of the photoinduced effect, temperature sweeps were performed in high fields of 10 kG for both the light and dark states, Figure 7-37 (a). Difference plots between the light and dark states show that 10 kG is sufficient to overcome the photoinduced decrease when the temperature is less than approximately 60 K, Figure 7-37 (b).

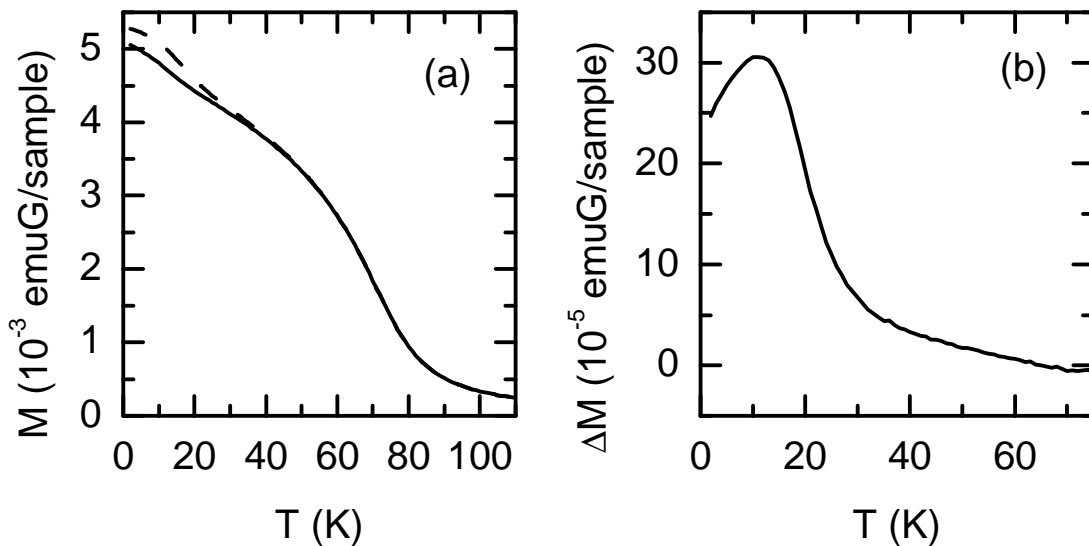


Figure 7-37. High magnetic field, 10 kG temperature sweeps of 40/40/40 Ni-Cr/Co-Fe/Ni-Cr. (a) The $\chi(T)$ data of a 40/40/40 Ni-Cr/Co-Fe/Ni-Cr film are plotted when the externally applied field of 10 kG is oriented parallel to the surface of the film. The solid line represents the data prior to irradiation (i.e. dark state), and the dashed line designates the data acquired after 5 hrs of irradiation with white light, but with the light subsequently off, (i.e. PPIM state). (b) Difference plots of the light state minus the dark state, ΔM , showing a photoinduced increase at high fields, 10 kG, and temperatures.

7.2.4.2 40/40/40 film, Transmission Electron Microscopy

To investigate the structure of the 40/40/40 Ni-Cr/Co-Fe/Ni-Cr heterostructure, samples were microtomed and mounted on a transmission electron microscope. Contrast differences in the transmission can be assigned to the different Prussian blue analogue lattices, Figure 7-38 (a) and (b). While discrete regions are clear, interfacial surfaces have roughnesses on the order of 20 nm. It is worth mentioning that additional experiments were done, where the microtome process incited a fracture at the interface between the Co-Fe and Ni-Cr layers, presumably due to the high strain induced by the lattice mismatch, Figure 7-38 (c).

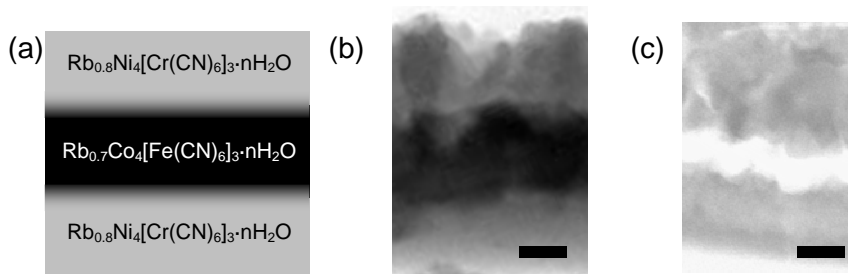


Figure 7-38. Transmission electron microscopy of the 40/40/40 Ni-Cr/Co-Fe/Ni-Cr heterostructure. (a) A schema of the heterostructure using a shading gradient between layers to illustrate regions at the interfaces where there can be mixing of the two phases. (b) A TEM micrograph shows a cross-section of a microtomed sample. The scale bar is 100 nm. The Melinex solid support is located at the bottom in the image. (c) A TEM micrograph showing a fracture at the Co-Fe/Ni-Cr interface.

7.2.4.3 40/40/40 film, Energy Dispersive X-ray Spectroscopy

While transmission electron microscopy provides clear evidence for the proposed structure, the chemical composition as a function of the height of the film can provide additional details about the heterogeneous atomic makeup. Energy dispersive x-ray spectroscopy (EDS) were performed on a JOEL 2010F super-probe. By line-scanning an electron beam across the microtome heterostructure, position dependence of the Co-Fe fraction can be plotted and directly compared to the model structure, Figure 7-39. Practically, the Co-Fe fraction is found by integrating Co and Fe peaks together and integrating Ni and Cr peaks together. The Co-Fe fraction is then the total amount of Co and Fe divided by the total amount of Co, Fe, Ni and Cr.

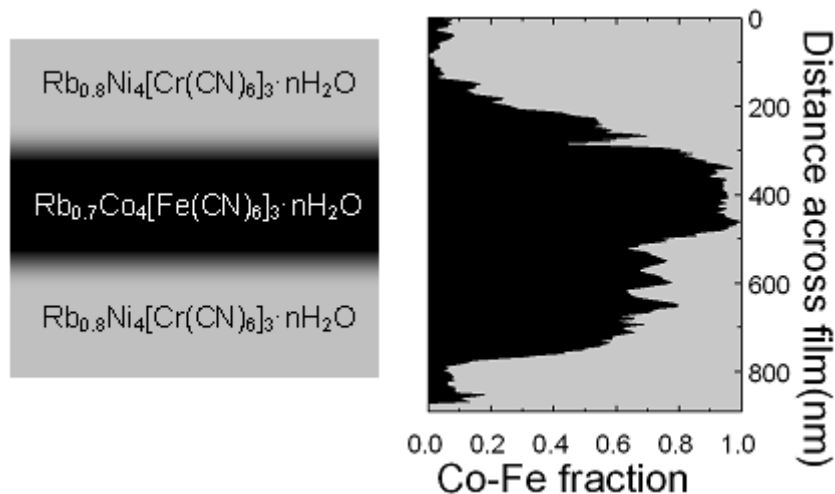


Figure 7-39. An energy dispersive x-ray line scan of the 40/40/40 heterostructure. (left) A schema of the heterostructure using a shading gradient between layers to illustrate regions at the interfaces where there can be mixing of the two phases. (b) A linescan from the EDS provided the Co-Fe fraction across the film, and the apparently high Co-Fe fraction deep into the bottom Ni-Cr layer arises because the films become rougher with increasing thickness. The solid support of Melinex is located at the top of the image and the free surface of the heterostructure is located at the bottom.

7.2.4.4 40/40/40 film, X-ray Powder Diffraction

A Philips APD 3720 powder diffractometer was used to perform room temperature x-ray diffraction (XRD) using a Cu K_{α} source with a primary wavelength of 1.5418 Å. Despite a large background due to the Melinex from the solid support, two clear peaks can be seen, Figure 7-40. Two important conclusions can be drawn from these data. First, the x-ray powder diffraction provides additional microscopic evidence of the existence of both Prussian blue analogues in the heterostructure, in proportions consistent with other microscopic measurements. Second, unlike substitutional solids of Co-Fe [141], the heterostructures possess two distinct lattice constants, showing that, while bonded at the interface, the majority of the constituents remain in structures similar to their pure states.

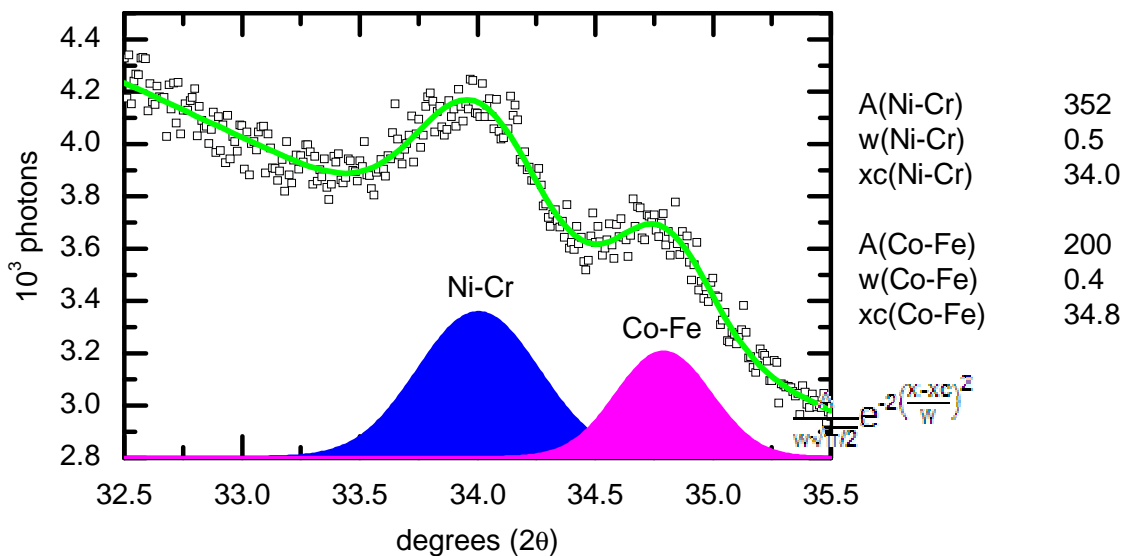


Figure 7-40. X-ray powder diffraction of a 40/40/40 heterostructure. To investigate the crystal structure of the heterostructures, reflections of the (4, 0, 0) plane were measured. Experimental intensities are shown (\square), as well as fits to Lorentzian lines for Co-Fe (—) and Ni-Cr (—) lattices to extract the relative intensities and positions. The peak at 34.8° corresponding to a cubic lattice constant of 10.3 Å is consistent with the Co-Fe analogue in the high spin state [68], whereas the peak at 34.0° corresponding to a cubic lattice constant of 10.5 Å can be assigned to the Ni-Cr analogue.

7.2.4.5 40/40/40 film, Infrared Spectroscopy

Fourier transform spectroscopy was performed on the 40/40/40 heterostructure, as well as the constituent pure materials, Figure 7-41. The heterostructure shows discrete peaks corresponding to the cyanide stretches of the constituents.

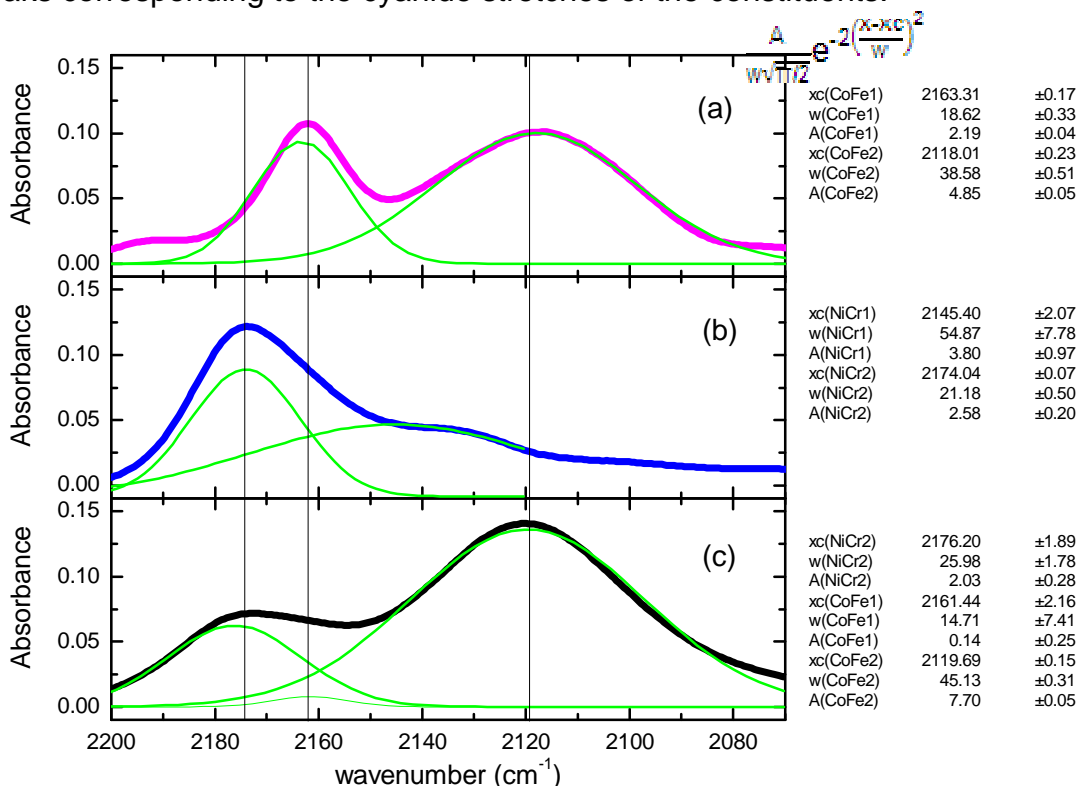


Figure 7-41. Cyanide stretching energies in the infrared. Spectra and fits are shown at left and fitting parameters (the center position, xc, the width, w, and the area, A) are shown at right. (a) The FT-IR spectrum of pure cobalt hexacyanoferrate is known to display peaks at 2163, 2120, 2090, and 2040 cm^{-1} corresponding to the cyanide stretches of the $\text{Co}^{2+}\text{-NC-Fe}^{3+}$ (HS), $\text{Co}^{3+}\text{-NC-Fe}^{2+}$ (LS), $\text{Co}^{2+}\text{-NC-Fe}^{2+}$, and linkage-isomerized $\text{Co}^{2+}\text{-NC-Fe}^{2+}$ phases, respectively [7]. The experimental data can be fit well with two lines, CoFe1, which is assigned to $\text{Co}^{2+}\text{-NC-Fe}^{3+}$ (HS) and CoFe2, which is assigned to $\text{Co}^{3+}\text{-NC-Fe}^{2+}$ (LS). (b) The FT-IR spectrum of pure nickel hexacyanochromate displays peaks at 2160 and 2125 cm^{-1} corresponding to the bridged $\text{Ni}^{2+}\text{-NC-Cr}^{3+}$ pairs and terminal cyanides. The experimental data can be fit to two lines, NiCr1, which is assigned to $\text{Ni}^{2+}\text{-NC-Cr}^{3+}$, and NiCr2, which is assigned to terminal cyanides. (c) In the heterostructured thin film, discrete peaks corresponding to each of the constituents can be seen. The experimental data fit well to three lines, CoFe1 ($\text{Co}^{2+}\text{-NC-Fe}^{3+}$ (HS)), CoFe2 ($\text{Co}^{3+}\text{-NC-Fe}^{2+}$ (LS)), and NiCr2 ($\text{Ni}^{2+}\text{-NC-Cr}^{3+}$). The observation of these peaks is further evidence for the proposed structure of the 40/40/40 film.

7.2.5 Capping Layers of Cobalt and Chromium Hexacyanochromates

In order to further explore the novel photoeffect, most prominently present in the 40/40/40 Ni-Cr/Co-Fe/Ni-Cr heterostructure, different capping layers of $\text{Rb}_a\text{Co}_b[\text{Cr}(\text{CN})_6]_c \cdot n\text{H}_2\text{O}$ (Co-Cr) and $\text{Rb}_a\text{Cr}_b[\text{Cr}(\text{CN})_6]_c \cdot n\text{H}_2\text{O}$ (Cr-Cr) were used. The Co-Cr analogue is known to be a ferromagnet with an ordering temperature near 30 K [155], and the Cr-Cr is a ferrimagnet with an ordering temperature near 200 K [116]. Hexacyanoferrate based capping layers were not used in order to avoid additional charge transfer between the Fe in the Co-Fe layer and Fe in the capping layer.

7.2.5.1 Magnetization of Cobalt Hexacyanochromate and Cobalt Hexacyanoferrate Sandwich Heterostructures

Two Co-Cr/Co-Fe/Co-Cr heterostructures are presented, a 40/40/40 and 40/60/40 layering scheme. The temperature dependence of the DC magnetic susceptibilities, $\chi = M/H$, are shown for 40/40/40 and 40/60/40 Co-Cr/Co-Fe/Co-Cr in Figure 7-42 (a) and Figure 7-42 (b), respectively, for temperatures between 2 K and 50 K and an external field of 100 G oriented parallel to the plane of the films. Time dependence during irradiation is shown in the inset of 7.20 (b), showing clear increase below the ordering temperature of Co-Fe and decrease above the ordering temperature of Co-Fe. Sharp increases in the temperature sweeps can be associated with ordering of the pure Co-Fe and Co-Cr phases, at ~10 K and ~30 K, respectively. Clear photoinduced magnetization can be observed well above the ordering temperature of the Co-Fe, and up to the ordering temperature of the Co-Cr. The photoeffect is seen to be negative, excepting when dominated by ordered Co-Fe magnetization.

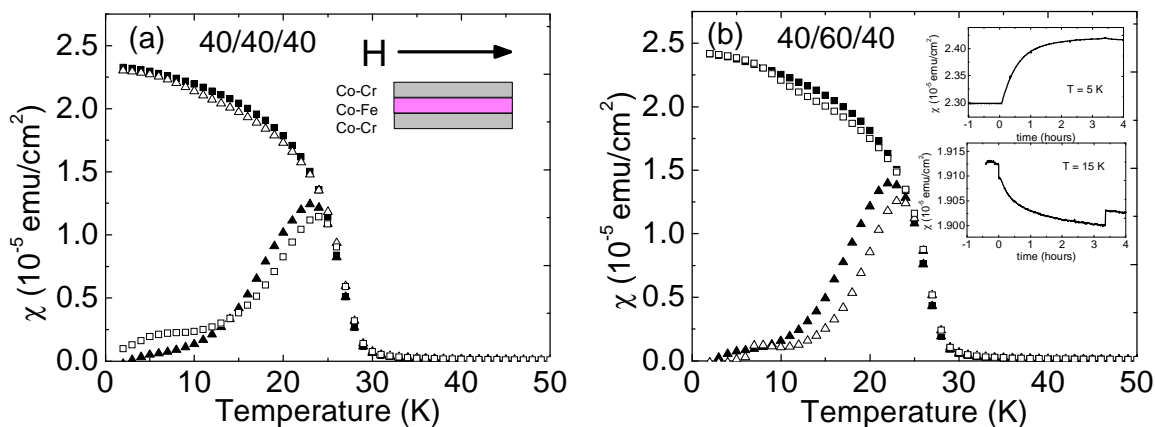


Figure 7-42. Magnetization data of Co-Cr/Co-Fe/Co-Cr heterostructures. (a) For a 40/40/40 Co-Cr/Co-Fe/Co-Cr heterostructure, the $\chi(T)$ data, normalized to the area of the film, are plotted when the externally applied field of 100 G is oriented parallel to the surface of the film. The closed symbols represent the data prior to irradiation (i.e. dark state), and the open symbols designate the data acquired after 3 hrs of irradiation with white light, but with the light subsequently off, (i.e. PPIM state). (b) Analogous $\chi(T)$ data for a 40/60/40 Co-Cr/Co-Fe/Co-Cr heterostructure is shown. Insets are the time dependences of the magnetization for temperatures above and below the ordering temperature of the Co-Fe layer.

7.2.5.2 Magnetization of Chromium Hexacyanochromate and Cobalt Hexacyanoferrate Sandwich Heterostructures

Two Cr-Cr/Co-Fe/Cr-Cr heterostructures are presented, a 40/40/40 and 60/40/60 layering scheme. The temperature dependence of the DC magnetic susceptibilities, $\chi = M/H$, are shown for 40/40/40 and 60/40/60 Cr-Cr/Co-Fe/Cr-Cr in Figure 7-43 (a) and Figure 7-43 (b), respectively, for temperatures between 2 K and 300 K and an external field of 100 G oriented parallel to the plane of the films. The difference between the irradiated and dark sample for the 60/40/60 Cr-Cr/Co-Fe/Cr-Cr film is shown in the inset of Figure 7-43 (b), showing detectable changes in the magnetization at temperatures well above the liquid point of nitrogen. Sharp increases in the temperature sweeps can be associated with ordering of the pure Co-Fe and Cr-Cr phases, at ~ 10 K and ~ 230 K, respectively. The photoeffect is again observed to be negative.

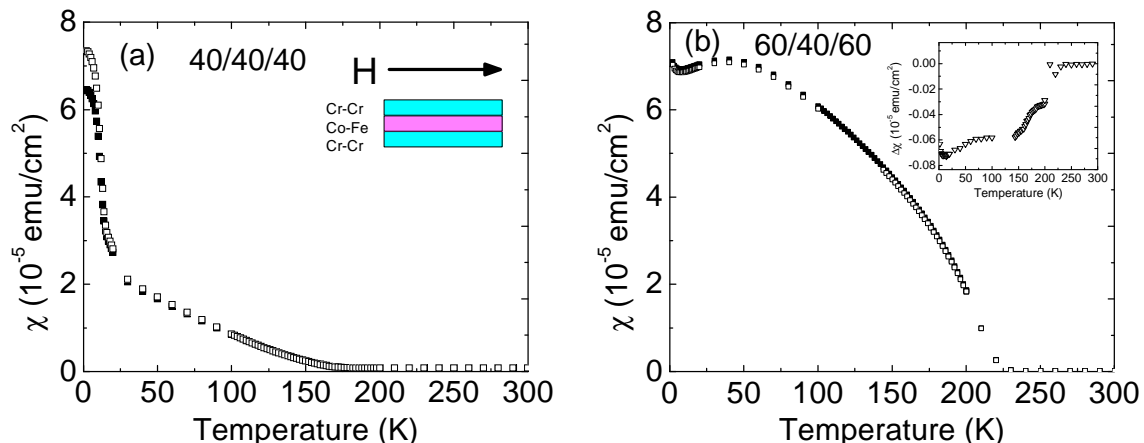


Figure 7-43. Magnetization data of Cr-Cr/Co-Fe/Cr-Cr heterostructures. (a) For a 40/40/40 Cr-Cr/Co-Fe/Cr-Cr heterostructure, the $\chi(T)$ data, normalized to the area of the film, are plotted when the externally applied field of 100 G is oriented parallel to the surface of the film. The closed symbols represent the data prior to irradiation (i.e. dark state), and the open symbols designate the data acquired after 3 hrs of irradiation with white light, but with the light subsequently off, (i.e. PPIM state). (b) Analogous $\chi(T)$ data for a 60/40/60 Cr-Cr/Co-Fe/Cr-Cr heterostructure is shown. The inset shows the difference between the photoinduced and dark states, $\Delta\chi$, showing modification of the magnetization at temperatures well above liquid nitrogen.

7.2.6 Discussion

This chapter describes the characterization of cyanometallate Prussian blue analogue heterostructured films, specifically with photomagnetic Co-Fe as a constituent. The heterostructure geometry leads to two striking new behaviors, an increase in the ordering temperature of the photomagnetic effect compared to Co-Fe and a change in the sign of the photomagnetic effect compared to Co-Fe. The synthesis technique is elegant in its simplicity, allowing fine control over thickness and constituents, while using room temperature and pressure wet chemistry. The magnetism data presented suggest a new mechanism for PPIM, whereby photoinduced changes in one lattice alter the magnetic response of the other.

Many samples were studied to arrive at the current understanding of the effect. Slow deposition multilayer films formulated with slow deposition techniques showed too much intermixing of the lattices and insufficient material transferred to the solid supports. The problems with slow deposition led to fast deposition techniques to be tried, with stacked films showing promise due to a modification of the photoeffect, which remained a small fraction of the total magnetization. A small breakthrough came with a sandwich geometry, in which clear decreases in susceptibility were seen for films, although the effect was small on the background of the total magnetization. The big break came with the thick sandwich geometry, where the effect was found to be large enough to be resolved as a function of temperature and field. In fact, thick sandwich structures were the first example showing a clear increase of the photoinduced modification of long-range magnetic order, much higher than the pure Co-Fe material. These geometries were engineered to give the optimal effect, observed in a 40/40/40 Ni-Cr/Co-Fe/Ni-Cr heterostructure. This sample was studied with additional probes, to explore the nanostructure and atomic character. Finally, different capping layers, of Co-Cr and Cr-Cr, were fabricated and studied for their photomagnetic effects.

The structural probes clearly display the multi-layer character of the 40/40/40 Ni-Cr/Co-Fe/Ni-Cr heterostructure. The lattice constants and cyanide stretches of the heterostructure are consistent with those observed in the homogeneous precursor Ni-Cr and Co-Fe materials, and EDS line scans show an evolution of the chemical formula with film height. Finally, TEM images show difference in contrast that can be associated with the different layers of Co-Fe and Ni-Cr.

All studies come back to the novel photoeffect observed in the heterostructures and the search to understand the fundamental origins of the photoeffect. To this end, the well documented photoeffect in Co-Fe must first be considered. To begin, the mechanism of PPIM in bulk Co-Fe PBA involves light induced electron transfer from Fe^{2+} (LS, $S = 0$) to Co^{3+} (LS, $S = 0$), yielding long-lived metastable Fe^{3+} (LS, $S = 1/2$)– CN-Co^{2+} (HS, $S = 3/2$) pairs that couple antiferromagnetically, giving rise to a net increase in magnetization in the ferrimagnetic state below 18 K [1] [78] [81]. The electron transfer and change in spin state also lead to a change in lattice constant, increasing $\sim 0.2 \text{ \AA}$ upon transitioning from the low-spin state to the high-spin state, Figure 7-44 [160] [161].

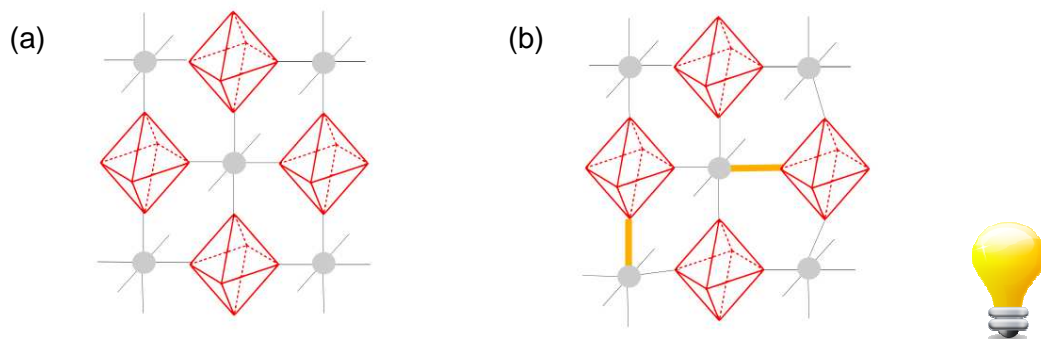


Figure 7-44. Photoexcitation of Co-Fe. In these schema of a Co-Fe lattice, the ferricyanide molecules are represented as red octagons and the cobalt ions are represented by gray circles. Bonds between the atoms are represented by gray lines. (a) The low-spin Co-Fe sample has a lattice constant of $\sim 10 \text{ \AA}$ [160] [161]. (b) From EXAFS measurements [96] it was shown that under photoirradiation, the structural change in the Co-Fe, increasing the unit cell to $\sim 10.3 \text{ \AA}$, takes place in the Co-N bonds, while the Fe-C bonds remain rigid. Photoexcited bonds are represented as thicker, longer yellow lines. This has the effect that Co ligand fields are found to be distorted in different states of photoexcitation.

When Co-Fe layers are fabricated to be in intimate contact with another analogue that is not photoactive, these structural distortions propagate through the heterostructure, Figure 7-45. The hexacyanochromate based networks have been shown to have a dependence of the magnetic susceptibility upon pressure, with the divalent nickel analogue have the greatest pressure dependence. For Ni-Cr, decreases of the magnetization of ~ 50% can be induced by the application of hydrostatic pressure of 0.8 GPa [162].

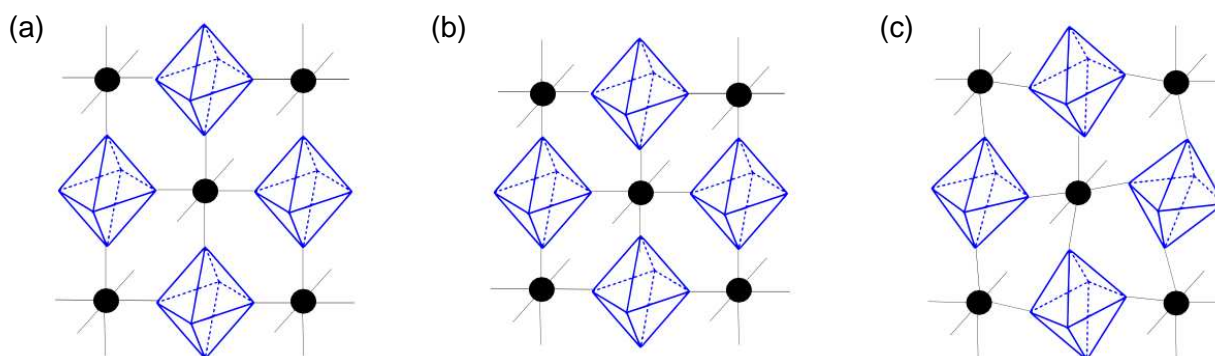


Figure 7-45. Distortions in Ni-Cr. In these schema of a Ni-Cr lattice, the hexacyanochromate molecules are represented as blue octagons and the nickel ions are represented by black circles. Bonds between the atoms are represented by gray lines. (a) While in the bulk Ni-Cr, simple cubicity is the most energetically favorable, (b) in thin films there may be a tetragonal distortion of the Ni coordination. This distortion gives rise to the anisotropy seen in the dark state of films and is only of ancillary interest to the discussion of the photoeffect, as it was discussed in detail previously in Chapter 6. (c) In heterostructures, where Ni-Cr is in intimate contact with Co-Fe, structural distortions induce by photoirradiation in the Co-Fe can propagate to the Ni-Cr lattice, distorting the Ni octahedra.

The photomagnetic response of the heterostructure indicates that the structural change in the Co-Fe PBA layer couples to the M-Cr PBA (where M = Co, Cr, or Ni), leading to the change in magnetization due to distortion of the divalent metal octahedral, Figure 7-46. The interesting aspect exists because the other Prussian blue analogue

has a much greater ordering temperature compared to the Co-Fe. The dependence of the high- T_C photoeffect in the heterostructures on capping layer can be clearly correlated to the pressure dependence of the capping layer. The Ni-Cr has the most pressure dependence, and therefore the photoeffect in the heterostructure is the most dramatic. The end result is a meta-magnet, with long-range magnetic order, that exhibits large changes in magnetization with the application of light, at unprecedented temperatures for this class of compounds, due to photoinduced structural distortions in the Co-Fe layer propagating to the previously non-photoactive capping layer.

Finally, it is tantalizing that, in materials with capping layers containing antiferromagnetic exchange pathways (Co-Cr and Cr-Cr), small modifications of the ordering temperature can be seen, suggesting a photoinduced modification of the exchange coupling in the samples. Unfortunately, an ideal candidate to further probe this idea, a 40-40-40 Mn-Cr/Co-Fe/Mn-Cr heterostructure, was unable to be synthesized, presumably due to the large lattice mismatch between the two materials and different space groups [163]. In the future, an interesting set of experiments could study the Mn-NC-Fe molecule as opposed to the Co-NC-Fe, and therefore synthesize a Mn-Cr/Mn-Fe/Mn-Cr heterostructure and look for photoinduced changes in the magnetic coupling of the Mn-Cr layer.

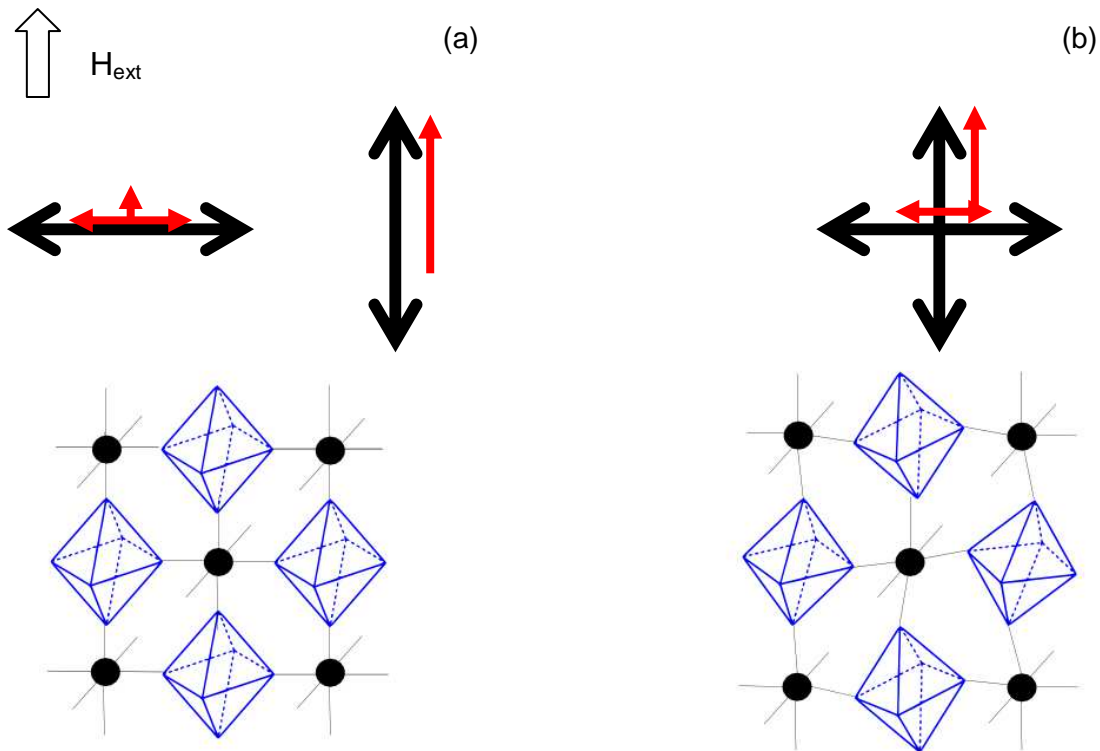


Figure 7-46. Anisotropy in Ni-Cr. The lower figures are analogous to those presented in Figure 7-45. The upper figures are representing the anisotropy axes present and the subsequent preferred orientation of the spin momentum in an applied field of the same energy scale as the anisotropy. (a) For a sample with correlated anisotropy, black arrows, macroscopic differences in the magnetization, red arrows, can be seen for different orientations. At the furthest left, a perpendicular orientation of the anisotropy axis and the applied field is shown, with the tendency for spin momentum to lie along the anisotropy axis, and not necessarily along the applied field. Just to the right, a parallel orientation of the anisotropy axis and the applied field is shown, showing the tendency of both energies to align the spins along the field axis. (b) For a sample with random anisotropy, black arrows, there is no angular dependence of the magnetization. However, a reduction of the magnetization, red arrows, compared to the case of no anisotropy is expected for sufficiently low fields, as some moments always prefer to point away from the applied field.

7.2.7 Conclusion

In summary, heterostructured films consisting of two different Prussian blue analogues, one with a high- T_C and the other photoactive, have been fabricated for the first time, and this novel arrangement leads to persistent photoinduced changes in magnetization at elevated temperatures. The new behavior is not seen in either pure phase and requires the unique heterostructure arrangement that generates an interface between them. Simple mixing of ions in a three-dimensional lattice does not give the same result, and in fact, serves to greatly suppress the amount of Co-Fe material that is bistable [141] [135]. Heterostructures based on coordination polymers are largely unexplored, and these results provide an example of new phenomena arising from engineered coordination polymer based structures that may motivate the rational design of further systems with new applications.

CHAPTER 8 SUMMARY AND CONCLUSIONS

While each chapter of this thesis has been presented in such a way as to be largely self-contained, a more general summary and set of conclusions will be made in this chapter. The motivation of the preceding experimental and theoretical investigations had two, main driving factors, the investigation of previously unknown science and education of the author and all interested parties. These goals will be explicitly considered as a final contemplation of the dissertation is made.

In Chapter 2, the experimental techniques are outlined for the purpose of understanding the experimental data presented. Although most of the information is a compilation of existing literature and “word-of-mouth” sources, the original contributions of the author are included in detail. In fact, portions of apparatus development have not been included, since these efforts did not pertain directly to the photoinduced magnetism of Prussian blue nanostructures. One specific example not included is the development of a low temperature, high pressure magnetometer, which was utilized for tunnel diode penetration depth studies of superconductors and in high pressure susceptibility measurements of a single molecule magnet [164]. These tunnel diode, pressure cell, and other low temperature studies were exceedingly effective in expanding the experimental and fabrication repertoire of the author.

The major apparatus development included in this thesis is related to bringing Visible light to sample measurement spaces. First, a rotation probe with fiber optics was designed and constructed for use with a commercial SQUID magnetometer, and this device was essential for studying thin film magnetization and photoinduced magnetization. It is particularly noteworthy that this custom probe represents the first

example of simultaneous rotation and photoirradiation in a SQUID magnetometer. Furthermore, automation with a computer controlled stepper motor makes the design tractable for the modern experimentalist. During the design process, extensive mechanical and magnetic testing was performed on potential construction materials. Second, a neutron scattering probe with a quartz light guide is still being further refined as of the writing of this thesis. While previous groups have performed photoinduced neutron scattering experiments on single crystals, the new neutron optical probe is the first to attempt photoirradiation of large quantities of bulk powder for neutron studies. A novel sample tumbler was designed in order to overcome the obstacle of opaque powders limiting photoirradiation to surface of the sample. For the future, a high pressure probe for use with the sensitive SQUID magnetometer may be made, as reports of similar probes are available [165] [166].

In Chapter 3, the relevant theoretical background was detailed. Analogous to the experimental techniques, the theoretical and numerical tools were preexisting techniques that were applied to the materials of interest, but some modifications were needed to model the photoinduced and bistable effects. While few extended Hückel calculations made it into the thesis, many were performed. These quick calculations yielded invaluable insight into the nature of the bonding in the systems, as well as the energy spectra. The author is currently in the process of applying more sophisticated semi-empirical methods, as well as density functional theory, to problems that proved intractable with the tight-binding extended Hückel theory.

Chapter 4 is more than just an extension of the theoretical methods because it begins to apply the outlined theories to relevant materials in a concrete manner. Care is

taken to understand the transition from modeling to fitting experimental data, which is important, especially since examples can be found in the literature where formulae have been applied without sufficient rigor to provide meaningful results. A thought-provoking result is the ambiguity of the sign of the superexchange interaction in $A_jCo_k[Fe(CN)_6]_nH_2O$, based upon more sophisticated modeling than is presently described in the literature. To help address this issue, neutron scattering experiments are scheduled to be performed (May 2010) on $A_jCo_k[Fe(CN)_6]_nH_2O$ samples, with the goal of searching for unequivocal evidence proving or disproving the existing assignment of antiferromagnetic Co-Fe interactions. In the future, an extension of the current codes to treat all higher level perturbations of magnetic and vibrational energies would increase understanding of the molecular based systems studied. Furthermore, a transparent, open source code for modeling magnetization of molecules and ionic crystals would be immensely beneficial to scientists throughout the world when experimental data is being analyzed.

The first set of novel materials is presented in Chapter 5, where slow cooled and thermally quenched nanoparticles of $A_jCo_k[Fe(CN)_6]_nH_2O$ were studied. The first material was $Rb_jCo_k[Fe(CN)_6]_nH_2O$ nanoparticles protected by polyvinylpyrrolidone. Photoinduced magnetization was present in all sizes studied, however the efficiency of the effect, as well as the coercive fields and ordering temperatures, could be correlated with the particle size. In addition, $K_jCo_k[Fe(CN)_6]_nH_2O$ nanoparticles showed that the amount of photoswitchable material is drastically reduced with size. The observed size dependence showed that, in addition to chemical formula, particle size is a necessary parameter for understanding the magnetism of the $A_jCo_k[Fe(CN)_6]_nH_2O$ system.

Furthermore, the data suggest that a core-shell type of distribution of states is present, with bulk-like bistable cores, and modified diamagnetic shells. In the future, a series of probes to quantify the true microscopic nature of the distribution of states, and test the hypothesis of a core-shell geometry, would be desirable.

In Chapter 6, thin films of Prussian blue analogues were discussed, with most attention paid to the $A_jNi_k[Cr(CN)_6]_nH_2O$ material. These samples were prepared with sequential adsorption techniques, which can deposit many layers, but introduce more disorder than Langmuir-Blodgett techniques. All films studied showed magnetic anisotropy, but the magnitude and sign of the anisotropy depended on the metal ions used. The underlying source of anisotropy in Prussian blue analogue films can have multiple sources, including dipolar, magnetocrystalline, and g-factor effects. In addition to the fundamental science involved, the ability to induce magnetic anisotropy in the systems by deposition onto a film is novel in itself and may have implications for materials engineering problems and future technologies. Future researchers may further refine the synthesis protocol by using flow-cells, and finally characterize the domain structure of the samples by Lorentz microscopy or magnetic force microscopy. The precise length scale of the domain structures is not yet known; however, nanostructure studies imply they are greater than ~ 50 nm, and x-ray studies of the Na-Co-Fe material have implied structural domains as large as ~ 1000 nm.

From a materials standpoint, the most interesting data arose from studying heterostructured materials presented in Chapter 7. Two new types of materials were synthesized and studied, photomagnetic solid solutions and photomagnetic thin film heterostructures. Studies of solid solutions showed that the sign and the magnitude of

the photomagnetic effect could be tuned with chemical composition. In addition, these studies allowed for investigation of the dilution effect of charge transfer induced spin transitions. The experience and understanding gained by studying photomagnetic solid solutions was central to achieving a break-through in understanding and engineering photomagnetic thin film heterostructures. Specifically, the need to have large enough unadulterated regions of photomagnetic material to observe appreciable effects was clearly demonstrated by the solid solution studies. The appreciable photoeffect finally achieved in the heterostructures was the subject of keen interest within the group, due to the unprecedented ordering temperatures of photomagnetization in a Prussian blue analogue. The largest effect was observed for a 40/40/40 Ni-Cr/Co-Fe/Ni-Cr material, but many other heterostructures were studied and presented. These studies have already spurred the study of photomagnetic core-shell nanoparticles with analogous fundamental properties.

To conclude, this dissertation has provided new insight into Prussian blue analogue nanoparticles, thin films, solid solutions, and thin film heterostructures. Portions have already been published and cited in the scientific literature, and others represent manuscripts in preparation. Finally, none of the studies in this thesis would have been possible without the synthesis of samples and characterization of compounds by collaborating chemists, who, through constant conversations, also imparted invaluable insight to the investigations for our frolicking flirtation with the vast unknown.

APPENDIX C UNITS

The system of units used throughout the majority of this thesis is based upon the literature standard used in Kahn's book on Molecular Magnetism [38]. Although magnetic susceptibility is traditionally intrinsic to volume, the molecule magnetism community prefers a molar normalization that is not dimensionless; χ_{mol} has units of emu mol^{-1} . Taking $[\chi] = \text{emu mol}^{-1}$ as a starting point, molar magnetization is expressed in emu G mol^{-1} and χT has units of emu K mol^{-1} . Finally, the H field is sometimes expressed in units of Tesla for familiarity [167], but this convention is not universal [3].

SI units of physical constants [38]

Planck constant	h	$6.6260755 \times 10^{-34} \text{ J s}$
	$h/2\pi$	$1.05457267 \times 10^{-34} \text{ J s}$
Elementary charge	e	$1.60217733 \times 10^{-19} \text{ C}$
Electron mass	m_e	$9.1093897 \times 10^{-31} \text{ kg}$
Proton mass	m_p	$1.6726231 \times 10^{-27} \text{ kg}$
Avogadro number	N	$6.0221367 \times 10^{23} \text{ mol}^{-1}$
Molar gas constant	R	$8.3145121 \text{ J mol}^{-1} \text{ K}^{-1}$
Boltzmann constant	k_B	$1.3806580 \times 10^{-23} \text{ J K}^{-1}$
Bohr magneton	μ_B	$9.27401549 \times 10^{-24} \text{ J T}^{-1}$
Nuclear magneton	$\mu_{B,N}$	$5.05078947 \times 10^{-27} \text{ J T}^{-1}$

c.g.s. - emu units of physical constants [38]

Planck constant	h	$6.6260755 \times 10^{-27} \text{ erg s}$
	$h/2\pi$	$1.05457267 \times 10^{-27} \text{ erg s}$
Elementary charge	e	$4.80320427 \times 10^{-10} \text{ esu}$
Electron mass	m_e	$5.4857990943 \times 10^{-4} \text{ amu}$
Proton mass	m_p	1.0072764667 amu
Avogadro number	N	$6.0221367 \times 10^{23} \text{ mol}^{-1}$
Molar gas constant	R	$8.3145121 \times 10^7 \text{ erg mol}^{-1} \text{ K}^{-1}$
Boltzmann constant	k_B	$1.3806580 \times 10^{-16} \text{ erg K}^{-1}$
Bohr magneton	μ_B	$9.27401549 \times 10^{-17} \text{ erg T}^{-1}$
Nuclear magneton	$\mu_{B,N}$	$5.05078947 \times 10^{-20} \text{ erg T}^{-1}$

Some mixed units as favored by Kahn [38]

Boltzmann constant	k_B	$0.69503877 \text{ cm}^{-1} \text{ K}^{-1}$
Bohr magneton	μ_B	$4.66864374 \text{ cm}^{-1} \text{ G}^{-1}$
Mol Bohr magneton	$N\mu_B$	$5585 \text{ cm}^3 \text{ G mol}^{-1}$

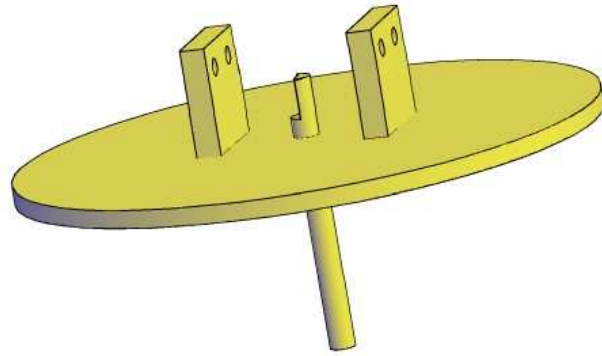
APPENDIX A
LOW TEMPERATURE ROTATION PROBE DRAWINGS

This appendix contains the machine drawings used for the optical rotation probe described in Section 2.3.1.

Assembly Drawings
Assembly Drawings detail
Slide Seal
Cell
Drive Rod
Probe Head Bracket
Probe Head Cap
Manual Bracket (Piece #1)
Manual Bracket (Piece #2)
Manual Bracket (Piece #3)
Motor Bracket
Probe Head (hidden view)
Probe Head (wireframe view)
Yoke

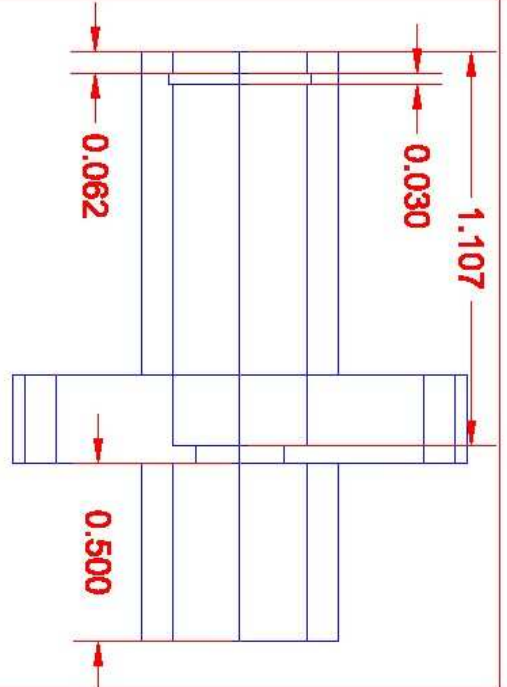
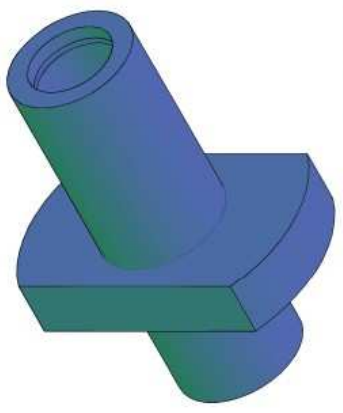
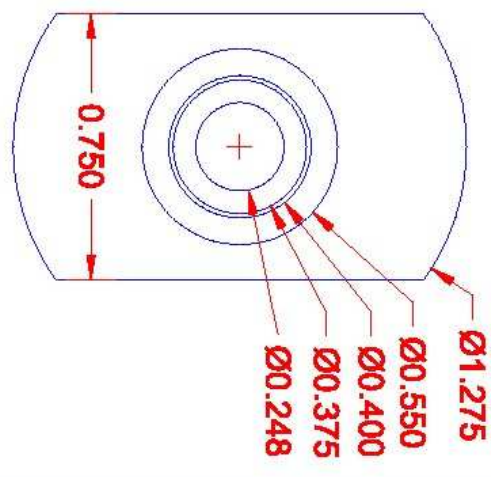
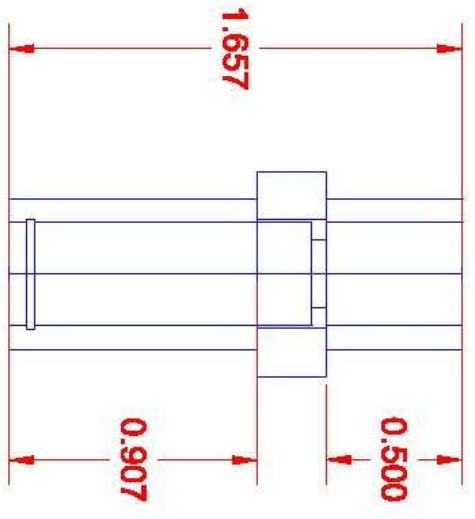


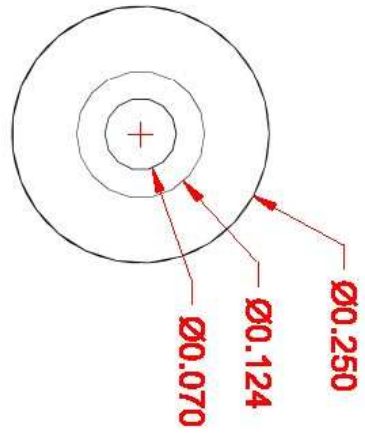
Assembly Drawings



Assembly Drawings detail

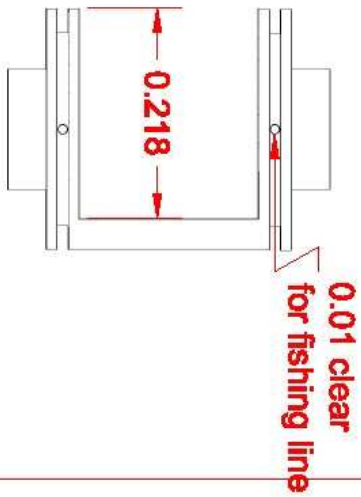
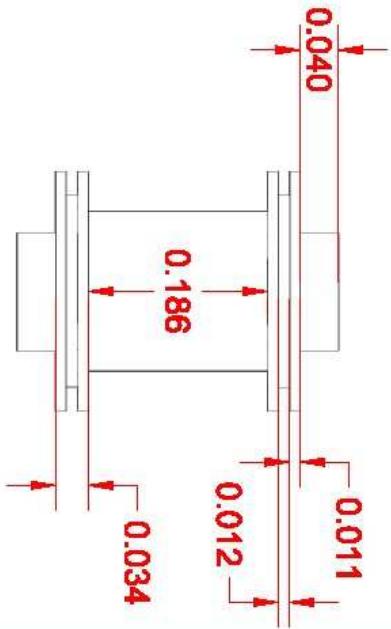
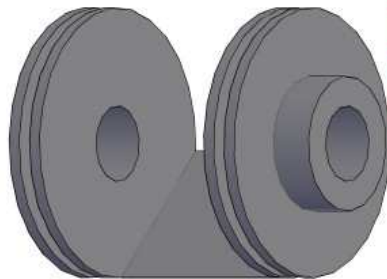
Slide Seal, Aluminum
 notes: snap ring provided for fit





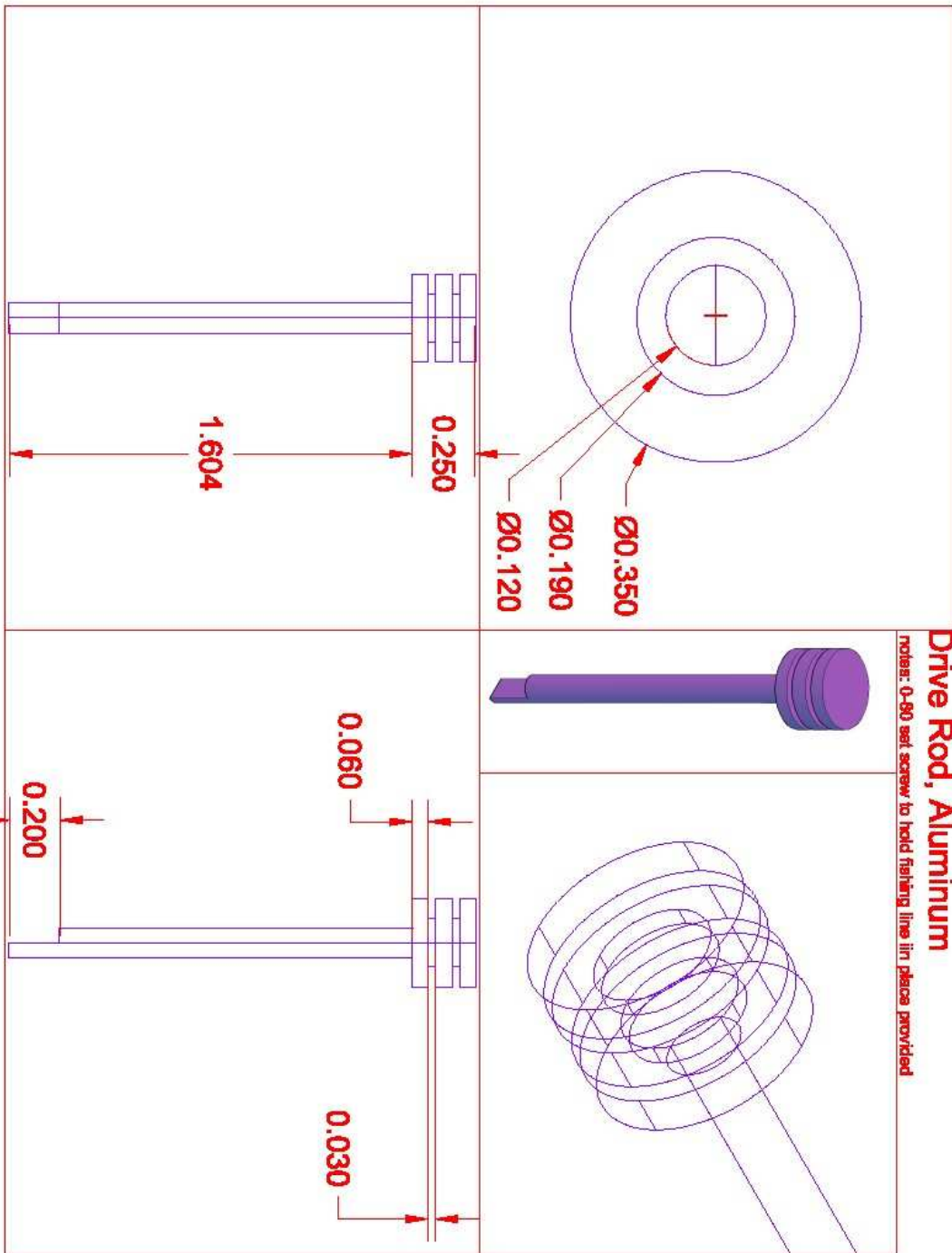
CELL, black Delrin

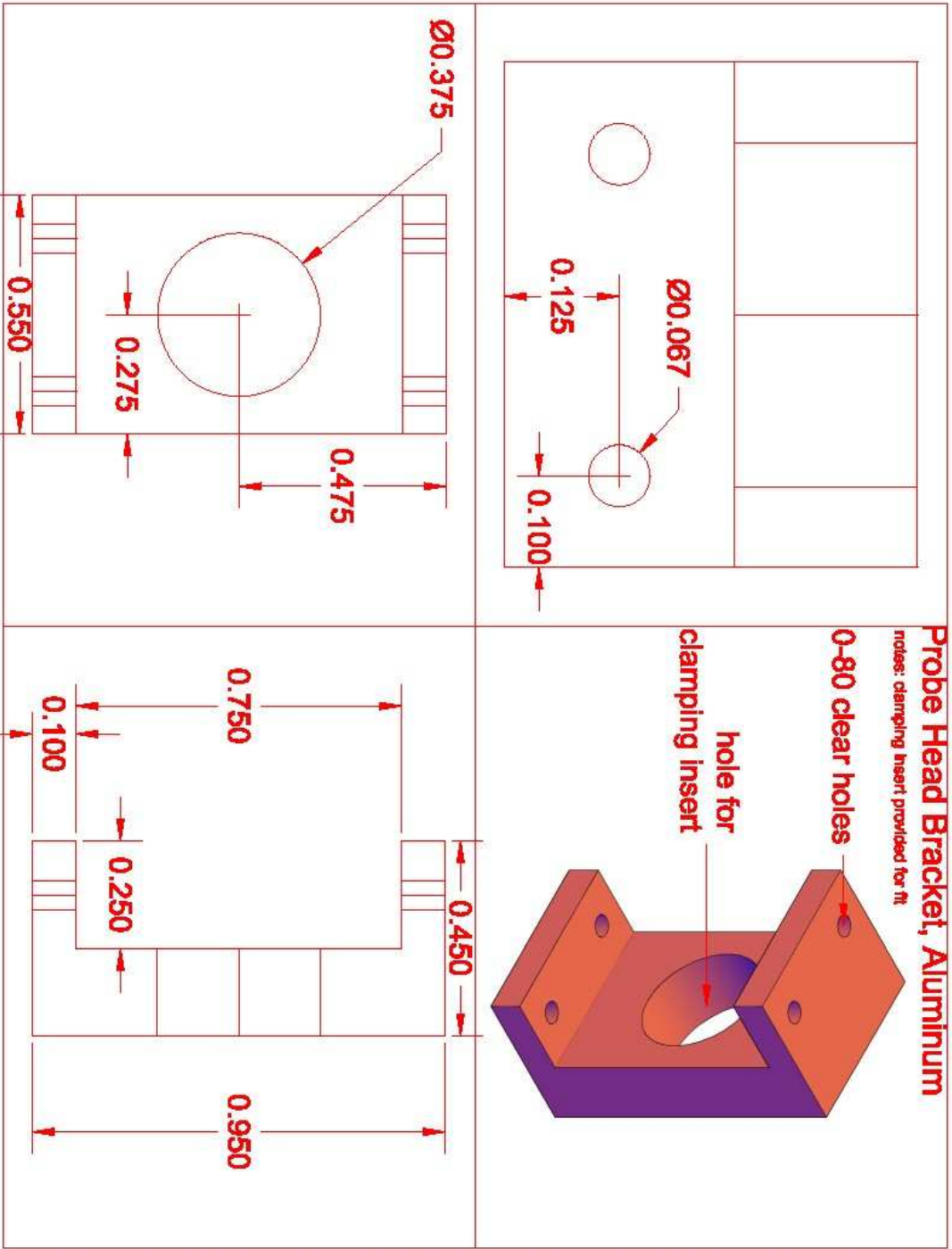
notice: tolerance is available on request



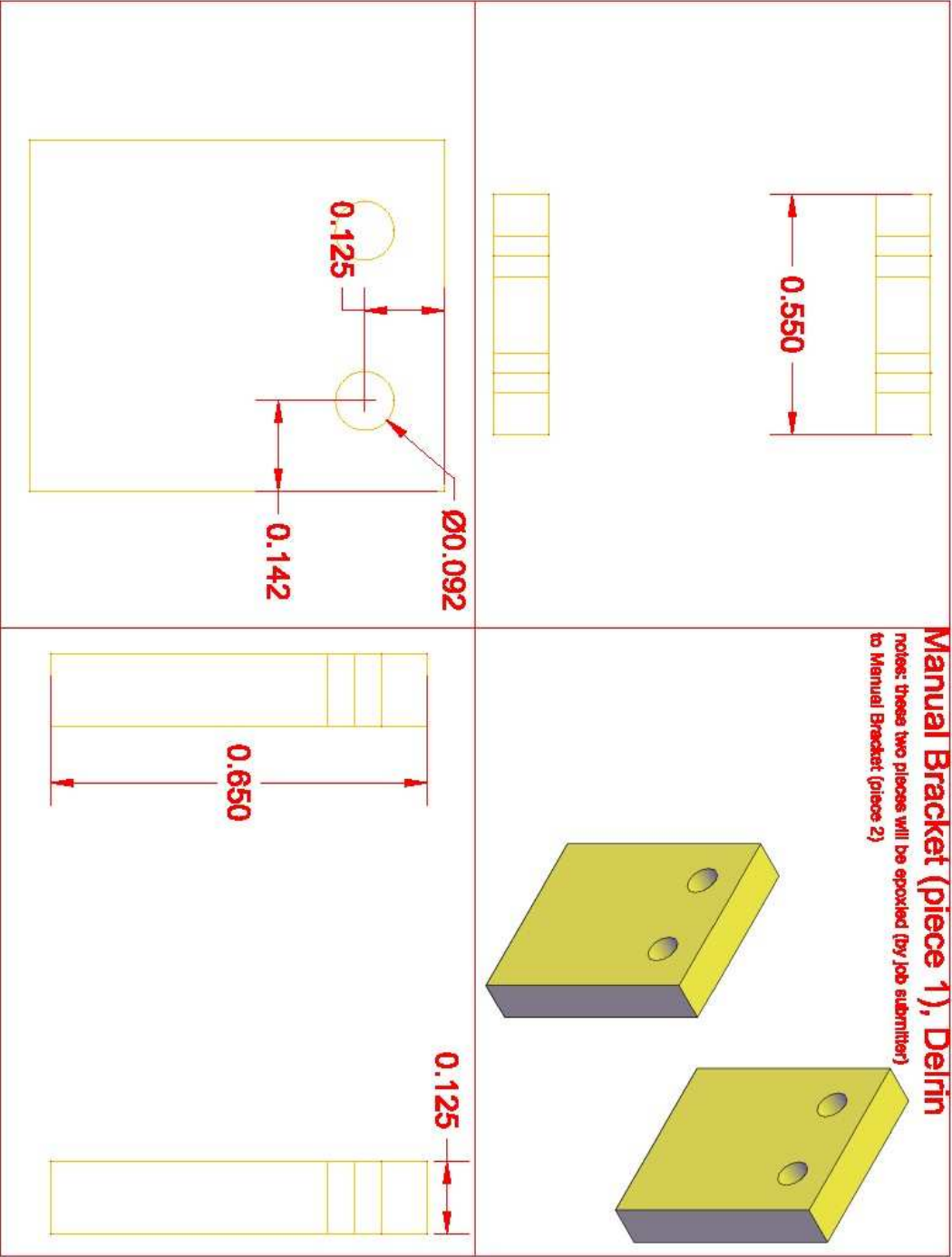
Drive Rod, Aluminum

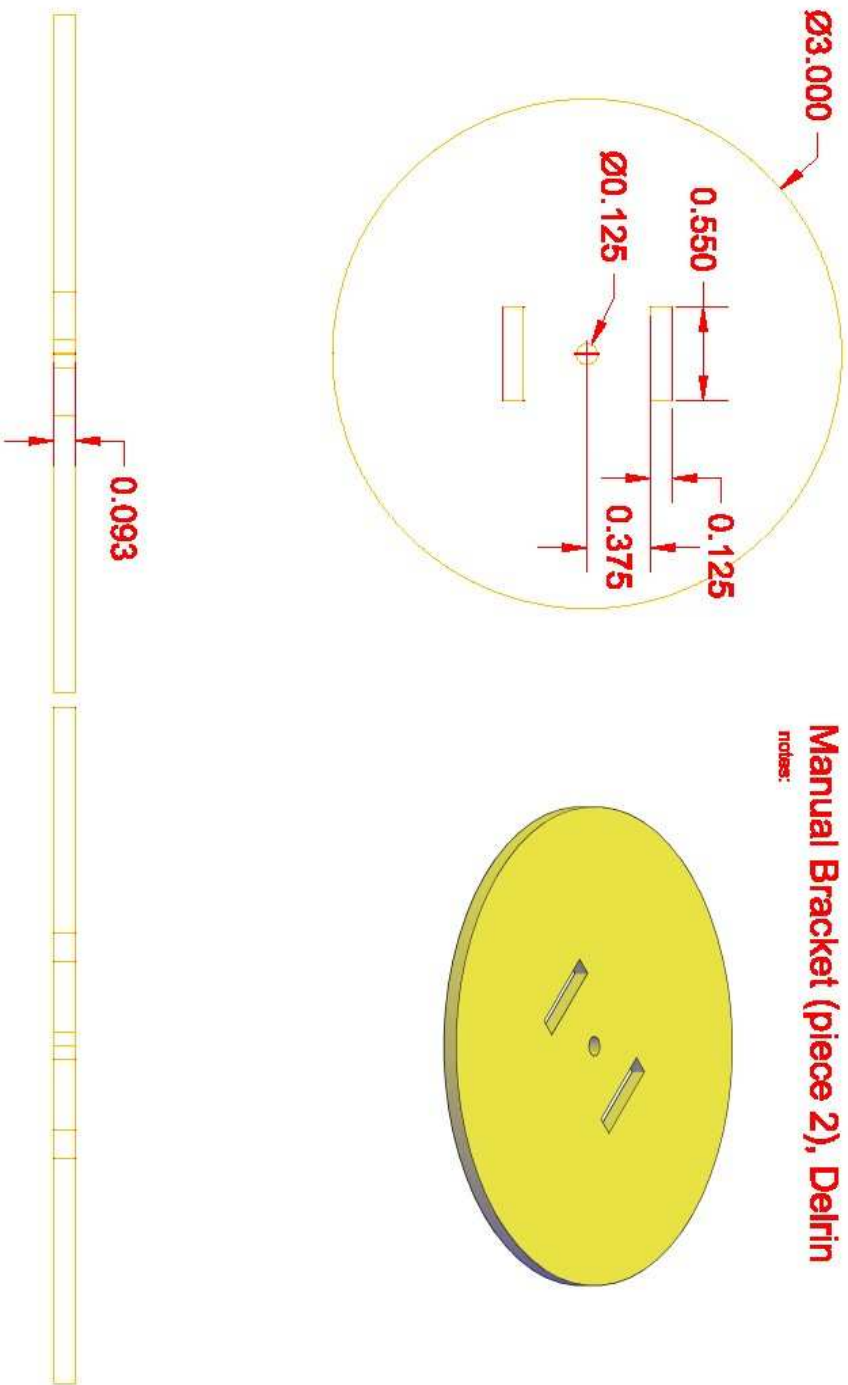
Notes: 0-90 seat screw to hold fishing line in place provided



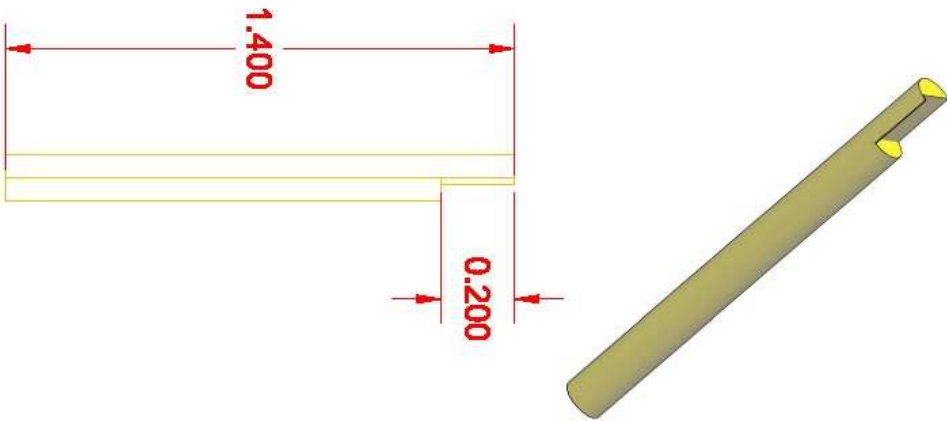
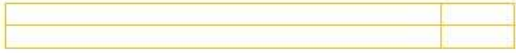


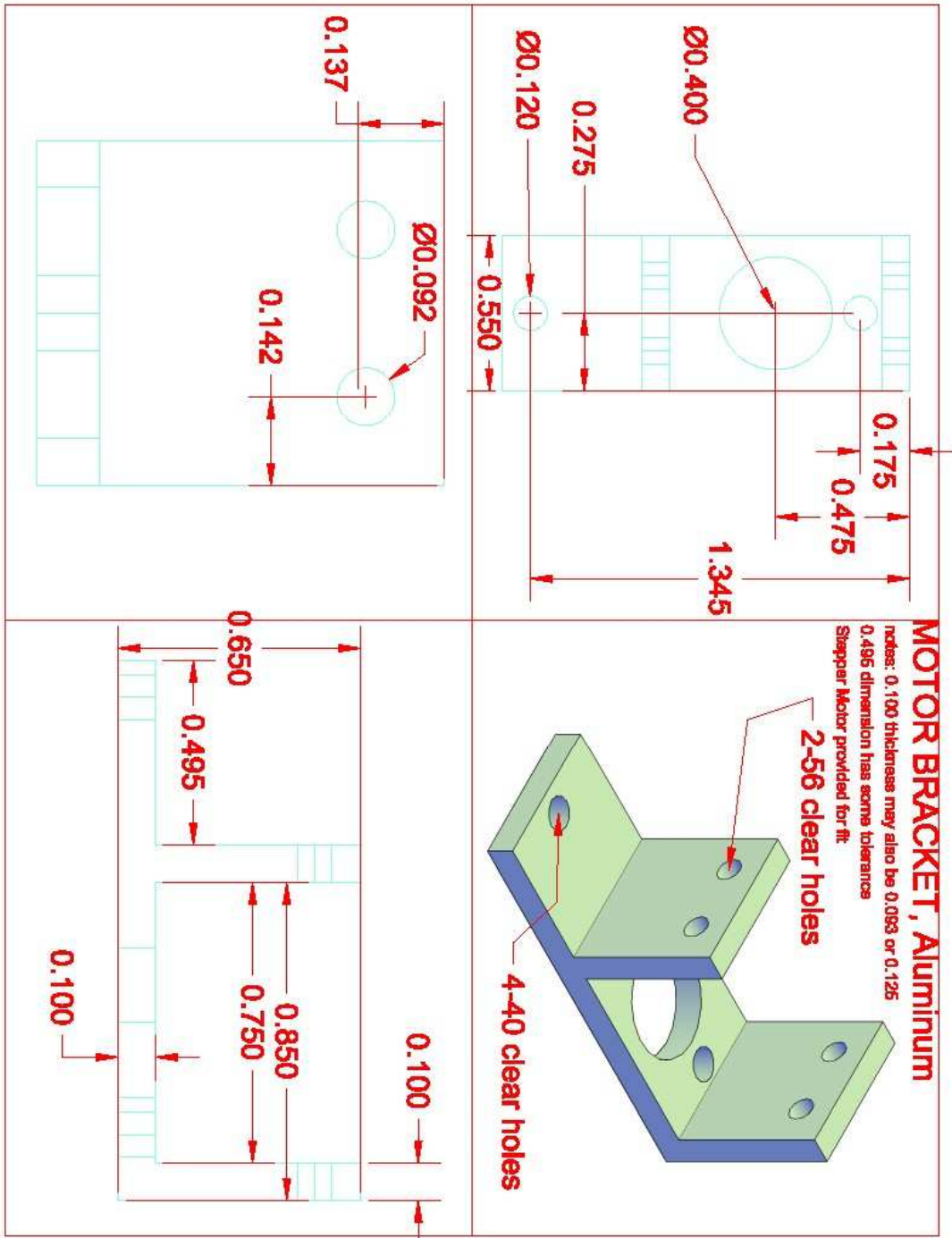
<p>Ø0.047</p> <p>0.150</p> <p>0.150</p>	
<p>0.125</p>	<p>Probe Head Cap, Clear Poly-Carbonate</p> <p>notes: 2 copies required</p> <p>clear hole for 0.80</p>

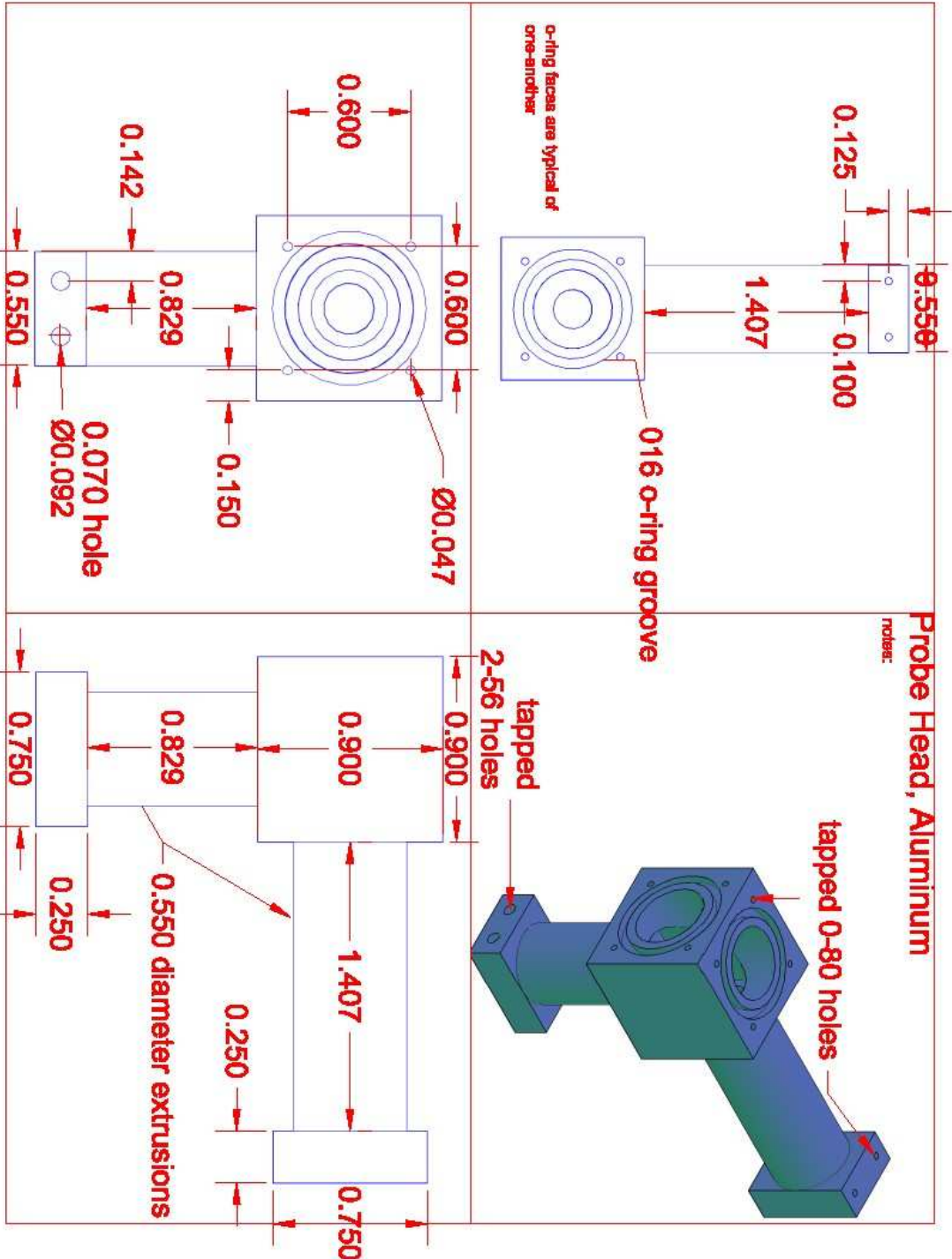


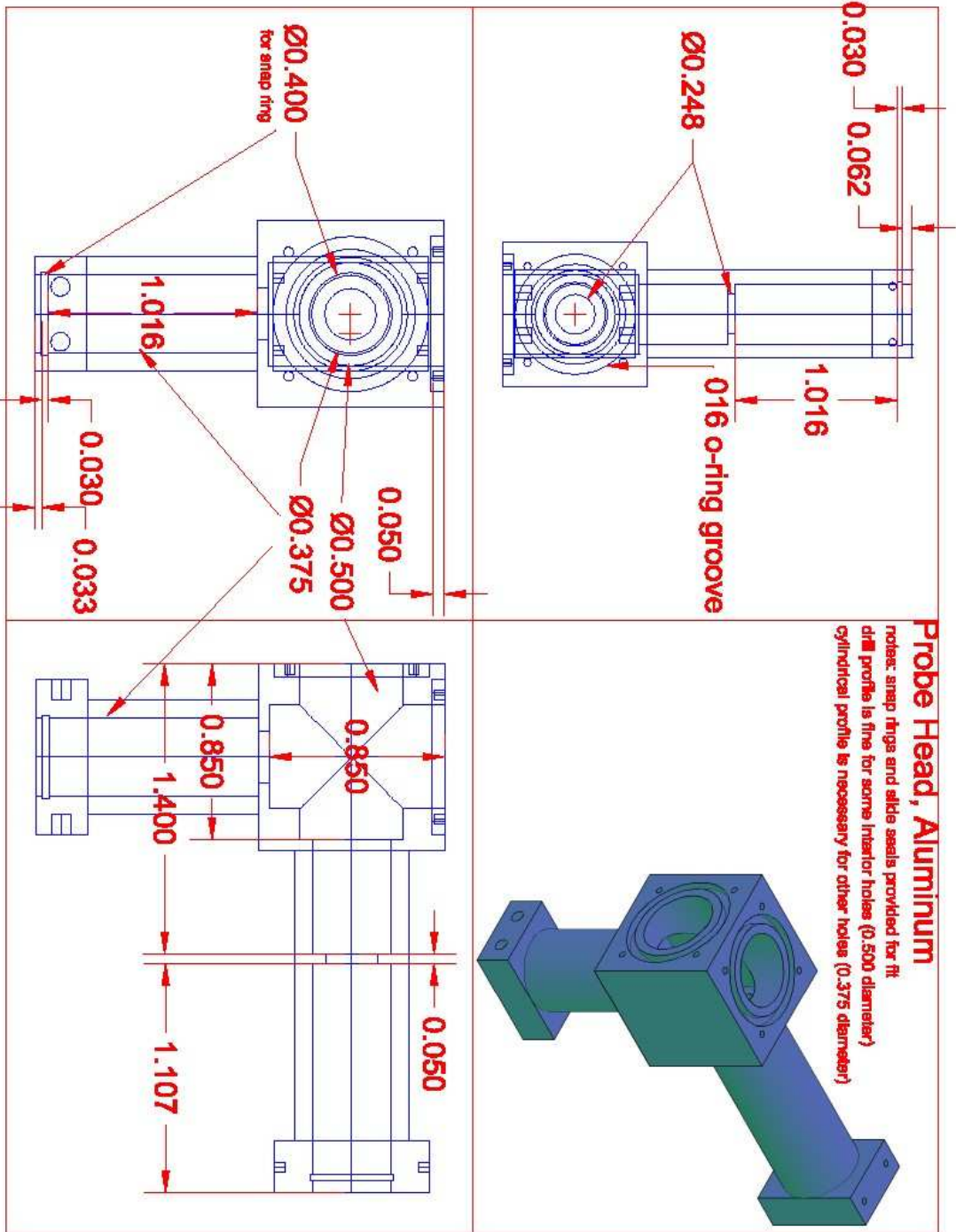


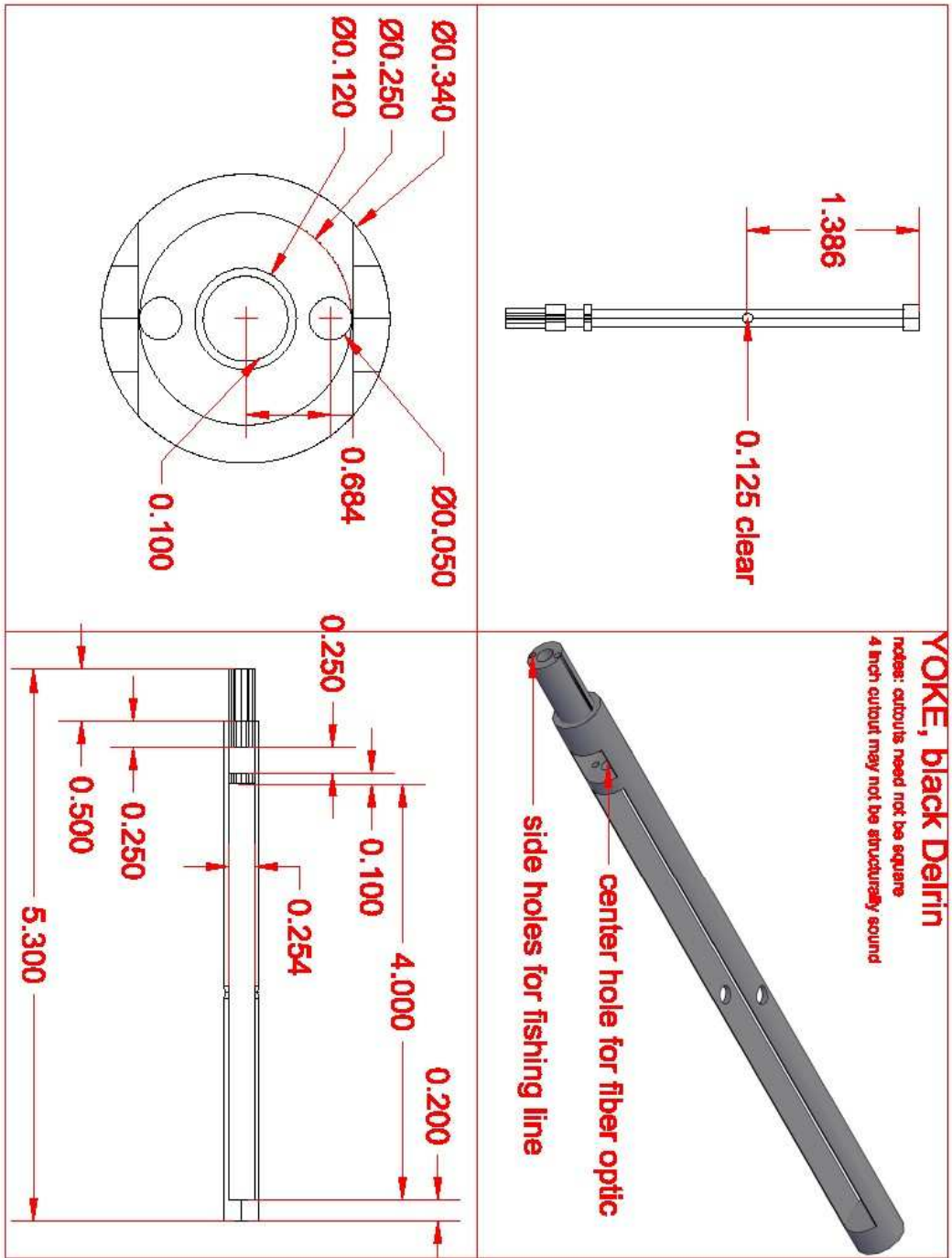
Manual Bracket (piece 3), Aluminum
notes: this (like the stepper motor) will be coupled to the drive rod
with a 0-80 screw coupling











APPENDIX B
COPYRIGHT RELEASE FORMS

Permissions/IOPP
Sent by: Jill Membrey
01/12/2009 09:11

To dpaj@phys.ufl.edu
cc
bcc
Subject Re: Fw: copyright release?



----- Forwarded by Sarah Fricker/Legal/IOPP on 25/11/2009 17:24 -----



Daniel M Pajerowski
<dpaj@phys.ufl.edu>
25/11/2009 17:05

To legal@iop.org
cc
Subject copyright release?

Hello!

I am writing my PhD dissertation and was hoping to use passages from papers I've authored.

Specifically,

D. M. Pajerowski and M. W. Meisel

Magnetometer probe with low temperature rotation and optical fibers

J. Phys.: Conf. Ser. [150](#) (2009) 012034 (4pp), [doi:10.1088/1742-6596/150/1/012034](#)

Please advise.

Best Regards,
Daniel M Pajerowski

PERMISSION TO REPRODUCE AS REQUESTED

IS GIVEN PROVIDED THAT:

~~(a) the consent of the author(s) is obtained~~

(b) the source of the material including author/editor,
title, date and publisher is acknowledged.*

IOP Publishing Ltd
Dirac House

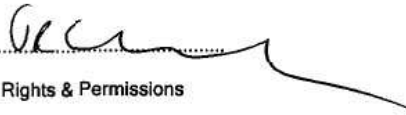
Temple Back

BRISTOL

BS1 6BE

1/12/09

Date



Rights & Permissions

* Please include the IOP Copyright line, mention the journal's homepage at:

www.iop.org/journals/jpcs

and provide a link back to the article's abstract on our website from the electronic version of your thesis (if applicable).

Thank you.



To: Permissions <permissions@iop.org>,
Cc:
Bcc:
Subject: Re: Permission request
From: Daniel M Pajeroski <dpaj@phys.ufl.edu> - Monday 08/02/2010 16:09

Dear Sarah Ryder;

Thank you for your reply to my email.

The data in

<http://www.iop.org/EJ/abstract/-search=68992789.1/1367-2630/9/7/222>

represent a large portion of one chapter of my thesis. Therefore I would like permission to reproduce the plots and text describing them. Specifically, Table 1, Figure 1, Figure 2, Figure 3, Figure 4, Figure 5, and Figure A.1. While the bulk of the text describing these figures will be different, as it is required by my University to fit the flow of the overall thesis, there are certainly subsections that I have worked hard on to reach the tightest possible wording, and rewording would not only be additional work, but would actually be a step backwards in terms of the quality of my thesis document. I hope this is sufficient detail for your records (if not please let me know), and I look forward to your reply.

Have a nice day,
Daniel Pajeroski

> *reproduction of article in thesis*
>
> *Daniel M Pajeroski * to: njp
> 01/02/2010 23:47

> From: Daniel M Pajeroski <dpaj@phys.ufl.edu>
> To: njp@iop.org
>
> -----
>
> To Whom It May Concern;
>
> I am in the process of writing my PhD thesis and was hoping to copy
> large portions of text and figures from
>
> <http://www.iop.org/EJ/abstract/-search=68992789.1/1367-2630/9/7/222>
>
> which is an article I had authored and published in your Journal.
>
> Based upon my reading of the copyright agreement between NJP and its
> publishing authors, I believe the aforementioned usage is pursuant to
> the agreement, however I was hoping for confirmation of this assumption.
>
> I look forward to your reply.
>
> Best Wished,
> Daniel M Pajeroski

PERMISSION TO REPRODUCE AS REQUESTED
IS GIVEN PROVIDED THAT:

~~(a) the consent of the author(s) is obtained~~

(b) the source of the material including author/editor,
title, date and publisher is acknowledged.

IOP Publishing Ltd
Dirac House
Temple Back
BRISTOL
BS1 6BE

11/2/2010
Date


Rights & Permissions

If your paper has already been published by ACS and you want to include the text or portions of the text in your thesis/dissertation in _____, please print the ACS copyright credit line on the first page of your article. "Reproduced (or 'Reproduced in part') with permission from [FULL REFERENCE CITATION] Copyright [YEAR] American Chemical Society." Include appropriate information.

_____ If you plan to submit your thesis to UMI or to another dissertation distributor, you should not include the unpublished ACS paper in your thesis if the thesis will be disseminated electronically, until ACS has published your paper. After publication of the paper by ACS, you may release the entire thesis (_____) for electronic dissemination through the distributor; ACS's copyright credit line should be printed on the first page of the ACS paper.

_____ The inclusion of your ACS unpublished or published manuscript is permitted in your thesis in print and microfilm formats. If ACS has published your paper you may include the manuscript in your thesis on an intranet that is not publicly available. Your ACS article cannot be posted electronically on a publicly available medium (i.e. one that is not password protected), such as but not limited to, electronic archives, Internet, library server, etc. The only material from your paper that can be posted on a public electronic medium is the article abstract, figures, and tables, and you may link to the article's DOI or post the article's author-directed URL link provided by ACS. This paragraph does not pertain to the dissertation distributor paragraph above.

v.l.1

Gratis licenses (referencing \$0 in the Total field) are free. Please retain this printable license for your reference. No payment is required.

If you would like to pay for this license now, please remit this license along with your payment made payable to "COPYRIGHT CLEARANCE CENTER" otherwise you will be invoiced within 48 hours of the license date. Payment should be in the form of a check or money order referencing your account number and this invoice number RLNK10728285.

Once you receive your invoice for this order, you may pay your invoice by credit card. Please follow instructions provided at that time.

**Make Payment To:
Copyright Clearance Center
Dept 001
P.O. Box 843006
Boston, MA 02284-3006**

If you find copyrighted material related to this license will not be used and wish to cancel, please contact us referencing this license number 2360450361649 and noting the reason for cancellation.

Questions? customercare@copyright.com or +1-877-622-5543 (toll free in the US) or +1-978-646-2777.

shall be void as if never granted. Use of materials as described in a revoked license, as well as any use of the materials beyond the scope of an unrevoked license, may constitute copyright infringement and publisher reserves the right to take any and all action to protect its copyright in the materials.

COPYRIGHT NOTICE/ DISCLAIMER

You must include the following copyright and permission notice in connection with any reproduction of the licensed material: "Reprinted ("Adapted" or "in part") with permission from REFERENCE CITATION. Copyright YEAR American Chemical Society."

WARRANTIES: NONE

Publisher makes no representations or warranties with respect to the licensed material.

INDEMNITY

You hereby indemnify and agree to hold harmless publisher and CCC, and their respective officers, directors, employees and agents, from and against any and all claims arising out of your use of the licensed material other than as specifically authorized pursuant to this license.

NO TRANSFER OF LICENSE

This license is personal to you or your publisher and may not be sublicensed, assigned, or transferred by you to any other person without publisher's written permission.

NO AMENDMENT EXCEPT IN WRITING

This license may not be amended except in a writing signed by both parties (or, in the case of publisher, by CCC on publisher's behalf).

OBJECTION TO CONTRARY TERMS

Publisher hereby objects to any terms contained in any purchase order, acknowledgment, check endorsement or other writing prepared by you, which terms are inconsistent with these terms and conditions or CCC's Billing and Payment terms and conditions. These terms and conditions, together with CCC's Billing and Payment terms and conditions (which are incorporated herein), comprise the entire agreement between you and publisher (and CCC) concerning this licensing transaction. In the event of any conflict between your obligations established by these terms and conditions and those established by CCC's Billing and Payment terms and conditions, these terms and conditions shall control.

JURISDICTION

This license transaction shall be governed by and construed in accordance with the laws of the District of Columbia. You hereby agree to submit to the jurisdiction of the courts located in the District of Columbia for purposes of resolving any disputes that may arise in connection with this licensing transaction.

THESES/DISSERTATION TERMS:

Publishing implications of electronic publication of theses and dissertation material
Students and their mentors should be aware that posting of theses and dissertation material on the Web prior to submission of material from that thesis or dissertation to an ACS journal may affect publication in that journal. Whether Web posting is considered prior publication may be evaluated on a case-by-case basis by the journal's editor. If an ACS journal editor considers Web posting to be "prior publication", the paper will not be accepted for publication in that journal. If you intend to submit your unpublished paper to ACS for publication, check with the appropriate editor prior to posting your manuscript electronically.



ACS / RIGHTSLINK TERMS & CONDITIONS THESIS/DISSERTATION

INTRODUCTION

The publisher for this copyrighted material is the American Chemical Society. By clicking "accept" in connection with completing this licensing transaction, you agree that the following terms and conditions apply to this transaction (along with the Billing and Payment terms and conditions established by Copyright Clearance Center, Inc. ("CCC"), at the time that you opened your Rightslink account and that are available at any time at <<http://myaccount.copyright.com>>).

LIMITED LICENSE

Publisher hereby grants to you a non-exclusive license to use this material. Licenses are for one-time use only with a maximum distribution equal to the number that you identified in the licensing process; any form of republication must be completed within 60 days from the date hereof (although copies prepared before then may be distributed thereafter).

GEOGRAPHIC RIGHTS: SCOPE

Licenses may be exercised anywhere in the world.

RESERVATION OF RIGHTS

Publisher reserves all rights not specifically granted in the combination of (i) the license details provided by you and accepted in the course of this licensing transaction, (ii) these terms and conditions and (iii) CCC's Billing and Payment terms and conditions.

PORTION RIGHTS STATEMENT: DISCLAIMER

If you seek to reuse a portion from an ACS publication, it is your responsibility to examine each portion as published to determine whether a credit to, or copyright notice of, a third party owner was published adjacent to the item. You may only obtain permission via Rightslink to use material owned by ACS. Permission to use any material published in an ACS publication, journal, or article which is reprinted with permission of a third party must be obtained from the third party owner. ACS disclaims any responsibility for any use you make of items owned by third parties without their permission.

REVOCATION

The American Chemical Society reserves the right to revoke a license for any reason, including but not limited to advertising and promotional uses of ACS content, third party usage, and incorrect figure source attribution.

LICENSE CONTINGENT ON PAYMENT

While you may exercise the rights licensed immediately upon issuance of the license at the end of the licensing process for the transaction, provided that you have disclosed complete and accurate details of your proposed use, no license is finally effective unless and until full payment is received from you (by CCC) as provided in CCC's Billing and Payment terms and conditions. If full payment is not received on a timely basis, then any license preliminarily granted shall be deemed automatically revoked and shall be void as if never granted. Further, in the event that you breach any of these terms and conditions or any of CCC's Billing and Payment terms and conditions, the license is automatically revoked and

**AMERICAN CHEMICAL SOCIETY LICENSE
TERMS AND CONDITIONS**

Feb 01, 2010

This is a License Agreement between Daniel M Pajeroski (" You") and American Chemical Society ("American Chemical Society") provided by Copyright Clearance Center ("CCC"). The license consists of your order details, the terms and conditions provided by American Chemical Society, and the payment terms and conditions.

All payments must be made in full to CCC. For payment instructions, please see information listed at the bottom of this form.

License Number	2360450361649
License Date	Feb 01, 2010
Licensed content publisher	American Chemical Society
Licensed content publication	Journal of the American Chemical Society
Licensed content title	Tuning the Sign of Photoinduced Changes in Magnetization: Spin Transitions in the Ternary Metal Prussian Blue Analogue Na ₀ Ni _{1-x} Co _x [Fe(CN) ₆]β·H ₂ O
Licensed content author	Daniel M. Pajeroski et al.
Licensed content date	Sep 1, 2009
Volume number	131
Issue number	36
Type of Use	Thesis/Dissertation
Requestor type	Not specified
Format	Electronic
Portion	50% or more of original article
Author of this ACS article	Yes
Order reference number	
Title of the thesis / dissertation	Photoinduced Magnetism in Synthetic Nanostructures of Prussian Blue Analogues
Expected completion date	Apr 2010
Estimated size(pages)	200
Billing Type	Invoice
Billing Address	925 NW 13th Avenue Gainesville, FL 32601 United States
Customer reference info	
Total	0,00 USD
Terms and Conditions	

LIST OF REFERENCES

- [1] O. Sato, T. Iyoda, A. Fujishima, and K. Hashimoto, *Science*, no. 272, p. 704, 1996.
- [2] V. Ksenofontov, et al., *Phys. Rev. B*, no. 68, p. 024415, 2003.
- [3] D. J. Griffiths, *Introduction to Electrodynamics*. New Jersey: Prentice Hall, 1999.
- [4] D. J. Griffiths, *Introduction to Quantum Mechanics*. Englewood Cliffs: Prentice Hall, 1995.
- [5] B. N. Figgis and M. A. Hitchman, *Ligand Field Theory and Applications*. New York: Wiley-VCH, 2000.
- [6] J. G. Moore, E. J. Lochne, C. Ramsey, N. S. Dalal, and A. E. Stiegman, *Angew. Chem.*, no. 115, p. 2847, 2003.
- [7] L. Catala, et al., *Chem. Commun.*, p. 746, 2005.
- [8] D. M. Pajerowski, F. A. Frye, D. R. Talham, and M. W. Meisel, *New J. Phys.*, no. 9, p. 222, 2007.
- [9] J.-H. Park, et al., *J. Magn. Magn. Mater.*, no. 310, p. 1458, 2007.
- [10] J.-H. Park, et al., *Appl. Phys. Lett.*, no. 85, p. 3797, 2004.
- [11] N. H. Balshaw, *Practical Cryogenics*. Oxon: Oxford Instruments Superconductivity Limited, 1996.
- [12] T. Flynn, *Cryogenic Engineering, Second Edition, ReVised and Expanded*. New York: CRC Press, 2004.
- [13] F. Pobell, *Matter and Methods at Low Temperatures*. Berlin: Springer-Verlag, 1992.
- [14] R. C. Richardson and E. N. Smith, *Experimental Techniques In Condensed Matter Physics At Low Temperatures*. New York: Westview Press, 1998.
- [15] J. Clarke and A. I. Braginski, *SQUID Handbook*. Berlin: Wiley-VCH, 2004.

- [16] O. V. Lounasmaa, *Experimental Principles and Methods Below 1K*. New York: Academic Press, 1974.
- [17] *MPMS User's Manual*. San Diego, CA: Quantum Design, 2000.
- [18] *MPMS Hardware Manual*. San Diego, CA: Quantum Design, 2000.
- [19] [Online]. <http://www.qdusa.com>
- [20] H. Buberl and H. Jenett, *Surface and thin film analysis : principles, instrumentation, applications*. Weinheim: Wiley-VCH, 2002.
- [21] F. L. Holmes, *Isis*, no. 54, no. 1, p. 50–81, 1963.
- [22] J. I. Goldstein, et al., *Scanning Electron Microscopy and X-Ray Microanalysis*. Springer, 2003.
- [23] D. C. Harris and M. D. Bertolucci, *Symmetry and Spectroscopy: An Introduction to Vibrational and Electronic Spectroscopy*. New York: Oxford University Press, 1978.
- [24] A. Montasser, *Inductively Coupled Plasma Mass Spectrometry*. Berlin: Wiley-VCH, 1998.
- [25] H. Kohl, *Transmission Electron Microscopy : Physics of Image Formation*. New York: Springer-Verlag, 2008.
- [26] R. C. Denney and R. Sinclair, *Visible and Ultraviolet Spectroscopy*, D. Mowthorpe, Ed. New York: John Wiley and Sons, 1987.
- [27] A. Guinier, *X-Ray Diffraction in Crystals, Imperfect Crystals and Amorphous Bodies*. New York: W.H. Freeman, 1963.
- [28] D. M. Pajerowski and M. W. Meisel, *J. Phys.: Conf. Ser.*, no. 150, p. 012034, 2009.
- [29] T. Yamamoto, Y. Umemura, O. Sato, and Y. Einaga, *Chem. Mater.*, no. 16, p. 1195, 2004.
- [30] A. Schuhl, S. Maegawa, M. W. Meisel, and M. Chapellier, *Phys. Rev. B*, no. 36, p. 13, 1987.
- [31] (2010, May) Spectra Fiber - Products - Honeywell Advanced Fibers and Products. [Online]. <http://www51.honeywell.com/sm/afc/products->

[details/fiber.html](#)

- [32] B. H. Bransden and C. J. Joachain, *Quantum Mechanics*, Second Edition ed. New York: Prentice Hall, 2000.
- [33] C. J. Ballhausen, *Introduction to Ligand Field Theory*. New York: McGraw-Hill Book Company, Inc., 1962.
- [34] E. U. Condon and G. H. Shortley, *The Theory of Atomic Spectra*, 2nd ed. New York: Cambridge University Press, 1953.
- [35] G. Racah, *Phys. Rev.*, no. 61, p. 438, 1942.
- [36] J. S. Griffith, *The Theory of Transition Metal Ions*. Cambridge: Cambridge University Press, 1964.
- [37] H. Bethe, *Ann. Phys.*, no. 3, p. 133, 1929.
- [38] O. Kahn, *Molecular Magnetism*. New York: Wiley-VCH, 1993.
- [39] J. B. Goodenough, *Magnetism and the Chemical Bond*. New York: Interscience-Wiley, 1963.
- [40] H. Bruus and K. Flensberg, *Many-Body Quantum Theory in Condensed Matter Physics*. New York: Oxford University Press, 2004.
- [41] H. Ibach and H. Luth, *Solid-State Physics*. New York: Springer-Verlag, 2002.
- [42] N. W. Ashcroft and N. D. Mermin, *Solid State Physics*. Harcourt College Publishers, 1976.
- [43] K. Yosida, *Theory of Magnetism*. New York: Spring-Verlag, 1996.
- [44] S. Blundell, *Magnetism in Condensed Matter*. New York: Oxford University Press, 2007.
- [45] K. H. Fischer and J. A. Hertz, *Spin Glasses*, D. Edwards and D. Melville, Eds. Cambridge: Cambridge University Press, 1999.
- [46] A. P. Young, Ed., *Spin Glasses and Random Fields*. New Jersey: World Scientific, 1997.
- [47] K. I. Ramachandran, G. Deepa, and K. Namboori, *Computational Chemistry and Molecular Modeling*. Berlin: Springer-Verlag, 2008.

- [48] N. J. Giordano, *Computation Physics*. New Jersey: Prentice Hall, 1997.
- [49] K. Levenberg, *Quart. Appl. Math.*, no. 2, p. 164, 1944.
- [50] D. Marquardt, *SIAM J. Appl. Math.*, no. 11, p. 431, 1963.
- [51] H. M. Rietveld, *J. Appl. Cryst.*, no. 2, p. 65, 1969.
- [52] A. C. Larson. and R. B. V. Dreele, *Los Alamos National Laboratory Report LAUR*, p. 86, 2000.
- [53] B. H. Toby, *J. Appl. Cryst.*, no. 34, p. 210 2001.
- [54] V. Gadet, T. Mallah, I. Castro, M. Verdaguer, and P. Veillet, *J. Am. Chem. Soc.*, no. 114, p. 9213–9214, 1992.
- [55] P. Day, et al., *Helv. Chim. Acta*, no. 63, p. 148, 1980.
- [56] M. Mihalik, et al., *J. Phys.: Conf. Ser.*, no. 200, p. 022035, 2010.
- [57] G. Champion, et al., *J. Am. Chem. Soc.*, no. 123, p. 12544, 2001.
- [58] S. Blundell, *Magnetism in Condensed Matter*. New York: Oxford University Press, 2007.
- [59] K. R. Dunbar and R. A. Heintz, *Progress in Inorganic Chemistry*, K. D. Karlin, Ed. New York: Wiley and Sons, 1997, no. 45, p. 283.
- [60] M. Verdaguer and G. Girolami, *Magnetism: Molecules to Materials V*, J. S. Miller and M. Drillon, Eds. Weinheim: Wiley-VCH, 2003, p. 283.
- [61] D. Davidson and L. Welo, *J. Phys. Chem.*, no. 32, p. 1191, 1928.
- [62] A. N. Holden, B. T. Matthias, P. W. Anderson, and H. W. Lewis, *Phys. Rev.*, no. 102, p. 1463, 1956.
- [63] R. M. Bozorth, H. J. Williams, and D. E. Walsh, *Phys. Rev.*, no. 103, p. 572, 1956.
- [64] A. Ito, M. Suenaga, and K. Ôno, *J. Chem. Phys.*, no. 48, p. 3597, 1968.
- [65] H. J. Buser, D. Schwarzenbach, W. Petter, and A. Ludi, *Inorg. Chem.*, no. 16, p. 2704, 1977.

- [66] S. Ohkoshi and K. Hashimoto, *J. Photochem. and Photobio. C: Photochem. Rev.*, no. 2, p. 71, 2001.
- [67] F. Varret, M. Nogues, and A. Goujon, *Magnetism: Molecules to Materials I*, J. S. Miller and M. Drillon, Ed. Weinheim: Wiley-VCH, 2002, p. 257.
- [68] M. Hanawa, et al., *J. Phys. Soc. Jpn.*, no. 72, p. 987, 2003.
- [69] T. Kawamoto, Y. Asai, and S. Abe, *Phys. Rev. Lett.*, no. 86, p. 348, 2001.
- [70] T. Uemura and S. Kitagawa, *J. Am. Chem. Soc.*, no. 125, p. 7814, 2003.
- [71] T. Uemura, M. Ohba, and S. Kitagawa, *Inorg. Chem.*, no. 43, p. 7339, 2004.
- [72] F. A. Frye, et al., *Polyhedron*, no. 26, p. 2273, 2007.
- [73] ImageJ. [Online]. <http://rsb.info.nih.gov/ij/>
- [74] Y. Xian, et al., *Anal. Chim. Acta*, no. 546, p. 139, 2005.
- [75] C. W. Ng, J. Ding, and L. M. Gan, *J. Solid State Chem.*, no. 156, p. 400, 2001.
- [76] J.-H. Park, Ph.D. thesis, University of Florida, 2006.
- [77] J. A. Mydosh, *Spin Glasses: An Experimental Introduction*. London: Taylor and Francis, 1993.
- [78] D. A. Pejakovič, J. L. Manson, J. S. Miller, and A. J. Epstein, *Phys. Rev. Lett.*, no. 85, p. 1994, 2000.
- [79] K. Yoshizawa, F. Mohri, G. Nussli, and T. Yamabe, *Phys. Chem. B*, no. 102, p. 5432, 1998.
- [80] T. Kawamoto, Y. Asai, and S. Abe, *Phys. Rev. Lett.*, no. 86, p. 348, 2001.
- [81] A. Bleuzen, et al., *J. Am. Chem. Soc.*, no. 122, p. 6648, 2000.
- [82] C. C. dit Moulin, et al., *J. Am. Chem. Soc.*, no. 122, p. 6653, 2000.
- [83] V. Escax, et al., *J. Am. Chem. Soc.*, no. 123, p. 12536, 2001.
- [84] N. Shimamoto, S. Ohkoshi, O. Sato, and K. Hashimoto, *Inorg. Chem.*, no. 41, p. 678, 2002.

- [85] V. Escax, et al., no. 44, p. 4798, 2005.
- [86] Z. Salman, et al., *Phys. Rev. B*, no. 73, p. 174427, 2006.
- [87] A. Goujon, F. Varret, V. Escax, A. Bleuzen, and M. Verdagner, *Polyhedron*, no. 20, p. 1347, 2001.
- [88] H. Liua, et al., *J. Magn. Magn. Mater.*, no. 322, p. 572, 2010.
- [89] M. Arai, M. Miyake, and M. Yamada, *J. Phys. Chem. C*, no. 112, p. 1953, 2008.
- [90] D. Li, et al., *J. Am. Chem. Soc.*, no. 130, p. 252, 2008.
- [91] S. Gawali, et al., *J. Phys. Chem. B*, no. 109, p. 8251, 2005.
- [92] M. Castro, et al., *Eur. Phys. Lett*, no. 79, p. 27007, 2007.
- [93] J. E. Gardner, PhD Thesis, University of Florida, 2009.
- [94] F. A. Frye, PhD Thesis, University of Florida, 2007.
- [95] T. Yokoyama, T. Ohta, O. Sato, and K. Hashimoto, *Phys. Rev. B*, no. 58, p. 8257–8266, 1998.
- [96] C. C. dit Moulin, et al., *J. Am. Chem. Soc.*, no. 122, p. 6653–6658, 2000.
- [97] B. Hoo, K. Boukheddaden, and F. Varret, *Eur. Phys. J. B*, no. 17, p. 449, 2000.
- [98] T. Yamamoto, Y. Umemura, O. Sato, and Y. Einaga, *Chem. Lett.*, no. 33, p. 500, 2004.
- [99] T. Yamamoto, Y. Umemura, O. Sato, and Y. Einaga, *Chem. Mater.*, no. 16, p. 1195, 2004.
- [100] J.-H. Park, et al., *Polyhedron*, no. 24, p. 2355, 2005.
- [101] T. Yamamoto, Y. Umemura, O. Sato, and Y. Einaga, *J. Am. Chem. Soc.*, no. 127, p. 16065, 2005.
- [102] F. A. Frye, et al., *Polyhedron*, no. 26, p. 2281, 2007.
- [103] F. A. Frye, D. M. Pajerowski, J.-H. Park, M. W. Meisel, and D. R. Talham, *Chem. Mater.*, no. 20, p. 5706, 2008.

- [104] J. Culp, J.-H. Park, D. Stratakis, M. W. Meisel, and D. R. Talham, *J. Am. Chem. Soc.*, no. 124, p. 10083, 2002.
- [105] J. Culp, J.-H. Park, I. Benitez, M. W. Meisel, and D. R. Talham, *Polyhedron*, no. 22, p. 2125, 2003.
- [106] J. Culp, et al., *Chem. Mater.*, no. 15, p. 3431, 2003.
- [107] J. Culp, J.-H. Park, M. W. Meisel, and D. R. Talham, *Inorg. Chem.*, no. 42, p. 2842, 2003.
- [108] J. Culp, et al., *Coord. Chem. Rev.*, no. 249, p. 2642, 2005.
- [109] G. Agusti, et al., *Chem. Mater.*, no. 20, p. 6721, 2008.
- [110] N. Bagkar, et al., *Thin Film Solids*, no. 513, p. 325, 2006.
- [111] O. Sato, S. Hayami, Y. Einaga, and Z.-Z. Gu, *Bull. Chem. Soc. Jap.*, no. 76, p. 443, 2003.
- [112] G. Torres, B. Agricole, P. Delhaes, and C. Mingotaud, *Chem. Mater.*, no. 14, p. 4012, 2002.
- [112bis] M. Pregelj, A. Zorko, D. Arcon, S. Margadonna, K. Prassides, H. van Tol, L.C. Brunel, and A. Ozarowski, *J. Magn. Magn. Mater.*, no. 316, p. 680, 2007.
- [113] S. V. Vonsovskii, *Ferromagnetic Resonance*. Oxford: Pergamon Press, 1966.
- [113bis] A. Gomez and S. W. Kycia, private communication, April 2010.
- [114] K. Pokhodnya, V. Dokukin, and J. Miller, *Inorg. Chem.*, no. 47, p. 2249, 2008.
- [115] S. Ferlay, T. Mallah, R. Ouahes, P. Veillet, and M. Verdaguer, *Nature*, no. 378, p. 701, 1995.
- [116] T. Mallah, S. Thiebaut, M. Verdaguer, and P. Veillet, *Science*, no. 262, p. 1554, 1993.
- [117] M. Taliferro, M. Thorum, and J. Miller, *Angew. Chem., Int. Ed.*, no. 45, p. 5326, 2006.
- [118] C. C. dit Moulin, et al., *J. Am. Chem. Soc.*, no. 122, p. 6653, 2000.
- [119] A. Goujon, et al., *Eur. Phys. J. B*, no. 14, p. 115, 2000.

- [120] A. Bleuzen, V. Escax, J.-P. Iti, P. Mensch, and M. Verdaguer, *C. R. Chimie*, no. 6, p. 343, 2003.
- [121] J.-W. Yoo, et al., *Phys. Rev. Lett.*, no. 97, p. 247205, 2006.
- [122] D. Brinzei, et al., *J. Am. Chem. Soc.*, no. 129, p. 3778, 2007.
- [123] J.-W. Yoo, R. Edelstein, D. Lincoln, N. Raju, and A. Epstein, *Phys. Rev. Lett.*, no. 99, p. 157205, 2007.
- [124] A. Bleuzen, V. Marvaud, C. Mathoniere, B. Sieklucka, and M. Verdaguer, *Inorg. Chem.*, no. 48, p. 3453, 2009.
- [125] W. Kosaka, K. Nomura, K. Hashimoto, and S.-i. Ohkoshi, *J. Am. Chem. Soc.*, no. 127, p. 8590, 2005.
- [126] S. Ohkoshi, Y. Einaga, A. Fujishima, and K. Hashimoto, *J. Electroanal. Chem.*, no. 473, p. 245, 1999.
- [127] D. F. Shriver, S. A. Shriver, and S. E. Anderson, *Inorg. Chem.*, no. 4, p. 725, 1965.
- [128] D. B. Brown, D. F. Shriver, and L. H. Schwartz, *Inorg. Chem.*, no. 7, p. 77, 1968.
- [129] D. B. Brown and D. F. Shriver, *Inorg. Chem.*, no. 8, p. 37, 1969.
- [130] J. E. House and J. C. Bailar, *Inorg. Chem.*, no. 8, p. 672, 1969.
- [131] E. Reguera, J. A. Bertrán, and L. Nuñez, *Polyhedron*, no. 13, p. 1619, 1994.
- [132] R. Martínez-García, M. Knobel, and E. Reguera, *J. Phys. Chem. B*, no. 110, p. 7296, 2006.
- [133] S.-i. Ohkoshi and K. Hashimoto, *J. Am. Chem. Soc.*, no. 121, p. 10591, 1999.
- [134] S.-i. Ohkoshi, et al., *Appl. Phys. Lett.*, no. 70, p. 1040, 1997.
- [135] J.-D. Cafun, L. Londinière, E. Rivière, and A. Bleuzen, *Inorg. Chim. Acta*, no. 361, p. 3555, 2008.
- [136] S. Ohkoshi, T. Iyoda, A. Fujishima, and K. Hashimoto, *Phys. Rev. B*, no. 56, p. 11642, 1997.

- [137] S.-i. Ohkoshi, O. Sato, T. Iyoda, A. Fujishima, and K. Hashimoto, *Inorg. Chem.*, no. 36, p. 268, 1997.
- [138] S.-i. Ohkoshi and K. Hashimoto, *Phys. Rev. B*, no. 60, p. 12820, 1999.
- [139] S. Juszczyk, C. Johansson, M. Hanson, A. Ratuszna, and G. Małeckı, *J. Phys.: Condens. Matter*, no. 6, p. 5697, 1994.
- [140] A. Kumar and S. M. Yusuf, *Physica B*, no. 362, p. 278, 2005.
- [141] D. M. Pajerowski, J. E. Gardner, D. R. Talham, and M. W. Meisel, *J. Am. Chem. Soc.*, no. 131, p. 12927–12936, 2009.
- [142] Nanoparticles of nickel hexacyanoferrate were independently measured and no appreciable size dependence as found between 15 and 35 nm.
- [143] O. Sato, *J. Solid State Electrochem.*, no. 11, p. 773, 2007.
- [144] D. A. Pejakovič, J. L. Manson, J. S. Miller, and A. J. Epstein, *J. Appl. Phys.*, no. 87, p. 6028, 2000.
- [145] D. A. Pejakovič, J. L. Manson, J. S. Miller, and A. J. Epstein, *J. Synth. Met.*, no. 122, p. 529, 2001.
- [146] D. A. Pejakovič, J. L. Manson, C. Kitamura, J. S. Miller, and A. J. Epstein, *Polyhedron*, no. 20, p. 1435, 2001.
- [147] D. A. Pejakovič, C. Kitamura, J. S. Miller, and A. J. Epstein, *J. Mol. Cryst. Liq. Cryst.*, no. 374, p. 289, 2002.
- [148] P. K. Phu, T. N. Giang, and N. Minh, *V. Commun. Phys.*, no. 18, p. 43, 2008.
- [149] A. Widmann, et al., *Inorg. Chem.*, no. 41, p. 5706, 2002.
- [150] N. Bagkar, et al., *Philos. Mag.*, no. 85, p. 3659, 2005.
- [151] A. Widmann, H. Kahlert, H. Wulff, and F. Scholz, *J. Solid State Electrochem.*, no. 9, p. 380, 2005.
- [152] D. Schwudke, R. Stösser, and F. Scholz, *Electrochem. Commun.*, no. 2, p. 301, 2000.
- [153] F. Lloret, M. Julve, J. Cano, R. Ruiz-Garcia, and E. Pardo, *Inorg. Chim. Acta*, no. 361, p. 3432, 2008.

- [154] J. Baker and B. N. Figgis, *Aust. J. Chem.*, no. 35, p. 265, 1982.
- [155] S.-i. Ohkoshi and K. Hashimoto, *Chem. Phys. Lett.*, no. 314, p. 210, 1999.
- [156] M. Sorai, J. Ensling, and P. Gütlich, *Chem. Phys.*, no. 18, p. 199, 1976.
- [157] H. Spiering, E. Meissner, H. Köppen, E. W. Müller, and P. Gütlich, *Chem. Phys.*, no. 68, p. 65, 1982.
- [158] T. T. A. Lummen, et al., *J. Phys. Chem. C*, no. 112, p. 14158, 2008.
- [159] D. M. Pajerowski, et al., *J. Am. Chem. Soc.*, no. 132, p. 4058–4059, 2010.
- [160] O. Sato, Y. Einaga, A. Fujishima, and K. Hashimoto, *Inorg. Chem.*, no. 38, p. 4405, 1999.
- [161] C. C. dit Moulin, G. Champion, J.-D. Cafun, M.-A. Arrio, and A. Bleuzen, *Angew. Chem., Int. Ed.*, no. 46, p. 1287, 2007.
- [162] M. Zentková, et al., *J. Phys.: Condens. Matter*, no. 19, p. 266217, 2007.
- [163] H. U. Güdel, H. Stucki, and A. Ludi, *Inorg. Chim. Acta*, no. 7, p. 121, 1973.
- [164] D. M. Pajerowski, et al., *Polyhedron*, no. submitted, 2010.
- [165] K. V. Kamenev, S. Tancharakorn, N. Robertson, and A. Harrison, *Rev. Sci. Instrum.*, no. 77, p. 073905, 2006.
- [166] P. L. Alireza and G. G. Lonzarich, *Rev. Sci. Instrum.*, no. 80, p. 023906, 2009.
- [167] R. M. White, *Quantum Theory of Magnetism*. New York: McGraw-Hill, 1970.

BIOGRAPHICAL SKETCH

Daniel Matthew Pajerowski was born as the third and final son of Mary I. Pajerowski and John T. Pajerowski, Jr. in Wilmington, Delaware. Daniel has attended public schools throughout his education, graduating from Brandywine High School in 2000. In 2004, Daniel graduated from the University of Delaware with a Bachelor degree in Science, with a major in physics and minors in sculpture and math. During his stay, he worked for Professor Barry C. Walker in a femtosecond laser lab for 3 years. After graduation, Daniel continued to work in the Walker lab in a limited capacity and took additional coursework to be sure that pursuing a PhD would be a career choice that would make him satisfied. In 2005, he began studies at the University of Florida and immediately joined the low temperature laboratory headed by Professor Mark W. Meisel. After graduating with his PhD in physics in the summer of 2010, he will try to continue on to a career as a research scientist. Finally, at some point he will retire.